Tuning the spin-orbit coupling in Ge for spin generation, detection and manipulation

Thomas Guillet

Université Grenoble Alpes

THÈSE

Pour obtenir le grade de

DOCTEUR DE L'UNIVERSITE GRENOBLE ALPES
Spécialité : **Physique de la matière condensée**

Arrêté ministériel : 25 mai 2016

Présentée par

Thomas GUILLET

Thèse dirigée par **Matthieu JAMET, CEA**, et
codirigée par **Alain MARTY, CEA**

préparée au sein du **Laboratoire Spintronique et Technologie des Composants (SPINTEC)**
et de l'École Doctorale de Physique de Grenoble

Tuning the spin-orbit coupling in Ge for spin generation, detection and manipulation

Thèse soutenue publiquement le **« 16 octobre 2020 »**,
devant le jury composé de :

Pr., David, Ferrand
Professeur, Université Grenoble Alpes, Président du jury
Pr., Sergio, Valenzuela
Professeur, Institut Català de Nanociència i Nanotechnologia, Rapporteur
Pr., Pierre, Renucci
Enseignant-Chercheur, INSA Toulouse, Rapporteur
Pr., Masashi, Shiraishi
Professeur, Université de Kyoto, Examinateur
Dr., Jean-Marie, George
Directeur de recherche, CNRS Thales, Examinateur
Dr., Federico, Bottegoni
Enseignant-Chercheur, Politecnico di Milano, Membre invité

Contents

Acknowledgments

First, I would like to express a deep gratitude to all the people who helped me achieving this PhD thesis during the last few years. Despite the fact that the manuscript is written in English , this particular section will be written in French.

Avant de rentrer au cœur de mes travaux de thèse, je tiens à remercier toutes les personnes qui m'ont entourés et épaulés durant ces dernières trois années.
Je remercie Lucian Prejbeanu et Olivier Fruchat, à la direction du laboratoire Spintec, pour leur accueil pendant ma thèse. Je tiens ensuite à remercier les membres du jury pour leur temps et l'intérêt qu'ils ont porté à mes travaux.
Je remercie bien évidemment Matthieu, mon directeur de thèse, qui a cru en moi et mes idées depuis le premier jour. Sa capacité à s'investir dans le travail de ses étudiants est, je pense, sans égale. J'ai énormément appris grâce à lui, autant sur les thématiques expérimentales que théoriques et je n'en serais pas là aujourd'hui sans l'échange constant qu'il y a eu entre nous. Il a toujours su me faire me sentir non pas comme un étudiant mais plutôt comme un collègue et m'a donné l'opportunité d'aller au bout de chacune de mes idées. Pour tout ce soutien et cet incroyable investissement, je l'en remercie.

Je me dois ensuite de remercier l'entièreté de mon équipe de recherche, notamment Alain qui m'a apporté beaucoup de connaissance autour de la croissance de films minces, la diffraction des rayons X et en magnétisme. Je remercie également Céline, qui m'a transmis un savoir-faire précieux autour des techniques de nanofabrication. Je tiens également à remercier Frédéric, qui a rejoint notre équipe plus récemment et avec qui j'ai toujours eu de très riches discussions.

Lors de mes trois ans de travaux, j'ai entrepris plusieurs projets en collaboration notamment avec l'unité mixte de physique CNRS-Thales. A ce titre, je remercie Jean-Marie George, Nicolas Reyren, Quentin Barbedienne et Albert Fert, avec qui j'ai passé quelques très bonnes

semaines au synchrotron et au laboratoire, toujours dans la bonne humeur.

Une autre partie importante de mes travaux s'est réalisée en collaboration avec l'équipe de spintronique des semiconducteurs du Politecnico di Milano. Je remercie donc chaleureusement Carlo Zucchetti, avec qui j'ai travaillé sur de nombreuses thématiques évoquées dans ce manuscrit. J'ai appris de son excellence dans le domaine de la magnéto-optique et lui ai transmis mon savoir-faire du magnétotransport : une belle collaboration. J'adresse également tous mes remerciements à Federico Bottegoni et Adèle Marchionni, avec qui j'ai découvert de nouveaux effets physiques et développé de nouvelles techniques de mesures.

Je tiens à spécialement remercier Paul Noël, l'encyclopédie vivante de la spintronique, qui a mené ses travaux de thèses en même temps que moi, et avec qui j'ai toujours eu d'excellentes discussions, tant sur le propos scientifique et technique que personnel.

J'exprime aussi une sincère reconnaissance pour Albin De Muer et Ilya Sheikin, mes premiers directeurs de stage, qui m'ont permis de découvrir le monde de la recherche et m'ont transmis le goût de la physique expérimentale et l'instrumentation ; sans eux, je ne serais sûrement arrivé jusqu'ici. Je remercie chaleureusement Alix McCollam, qui m'a supervisé pendant mon stage de Master 1 au Pays-Bas, et qui m'a beaucoup appris et m'a permis de perfectionner ma connaissance de l'instrumentation scientifique de pointe et de la physique de la matière condensée.

Je remercie ma mère, mon père et toute ma famille pour le support et le soutien qu'ils m'ont apporté tout au long de mes études et pendant ces trois ans de thèses. Je porte bon espoir que ce manuscrit pourra les amener à comprendre la nature de mon travail.

Je remercie mes amis, à Grenoble, Toulouse et partout ailleurs pour les bons moments partagés depuis notre rencontre. La plupart d'entre eux ont également entamé un travail de thèse et nous avons traversé les mêmes épreuves, les mêmes doutes et avons souvent su nous entraider.

Finalement, je tiens particulièrement à remercier Alice, qui m'a accompagné et soutenu comme personne d'autre, tout au long de mon travail. Elle a toujours été là, autant dans les moments de doutes et de difficultés, que dans les moments de réussite. Sa curiosité n'a d'égale que sa bienveillance et je suis très fier d'avoir rédigé l'entièreté de ce manuscrit en sa compagnie.

Introduction

Since the 1950s with the discovery of the transistor, the microelectronics industry has developed around the miniaturization of devices to increase their integration capacity on electronic chips. Many technological steps have been taken to reach the current level of miniaturization, but the basic principle has not changed, we are still dealing with an electrical manipulation of charge currents to encode information. Currently, the race for miniaturization ends its path and new lines of investigation are opening up to continue to progress. One of these approaches was born with the discovery of the giant magnetoresistance by Albert Fert's group in the 80s: it is called spin electronics or spintronics. This emerging science takes advantage of the spin degree of freedom of electrical carriers in order to improve and develop new devices.

The spintronics field experienced its first successes using metallic medium to generate, transport and detect spin currents. In 1990, S. Datta and B. Das proposed the initial semiconductor-based spin transistor architecture, where the information is carried by the electron spin instead of its charge. This proposal steered the community interest towards semiconductor spintronics.

At this stage the electrical generation and detection of spin-polarized carriers relied on the exchange interaction in ferromagnetic materials. A more recent approach consists in harnessing the spin–orbit interaction (SOI) in heavy metals such as platinum (Pt), tungsten (W) or tantalum (Ta) to produce spin currents. The so-called spin Hall effect was predicted in 1971 and experimentally observed for the first time in 2004 and stimulated the community, leading a large variety of new spin-dependent phenomenons. Recently, it was shown that the peculiar spin texture obtained at surfaces and interfaces could lead to an enhanced spin-charge interconversion efficiency. Two-dimensional electronic systems (2DEG) owing peculiar spin texture like Rashba surfaces and interfaces or topological insulators were then intensively studied.

The aim of my PhD work is to develop the generation, transport, detection and manipulation of the spin information in a semiconductor-based spintronics platform. While the three first points were well addressed by the community, the manipulation of spins with an electric field still remains a challenge as the intrinsic spin-orbit interaction is rather weak in conventional group IV-semiconductors. Our approach was to induce or enhance this interaction by growing thin films with strong SOI on a semiconductor: Ge. We aim at combining the long spin diffusion length of Ge as well as its optical properties with the spin-momentum locking property of Rashba interfaces and topological insulators.

The first chapter presents an introduction to the classical spintronics as well as the important advances of the semiconductor spintronics and the spin-orbitronics in the past 20 years. A thorough literature review lays the foundation of my work that lies in between the semiconductor spintronics and the spin-orbitronics fields.

The second chapter introduces the set of experimental techniques I employed during my PhD. In our group, we have the possibility to control the complete experimental process. I start by growing ultra-thin films by molecular beam epitaxy and/or magnetron sputtering and characterize their structural properties. Then I use micro and nano-fabrication techniques to pattern devices to ultimately, quantify electrical, optical, magnetic properties and study spin-dependent phenomena.

In the following, I focus on two approaches in order to tune the spin-orbit interaction (SOI) in a Ge-based platform. Both rely on the structural inversion asymmetry and the spin-orbit coupling at surfaces and interfaces with germanium (111). In chapter 3, I describe the epitaxial growth of the topological insulator (TI) Bi_2Se_3 on Ge (111). After characterizing the structural and electrical properties of the Bi_2Se_3/Ge heterostructure, we developed an original method to probe the spin-to-charge conversion at the interface between Bi_2Se_3 and Ge by taking advantage of the Ge optical properties. The results showed that the hybridization between the Ge and TI surface states could pave the way for implementing an efficient spin manipulation architecture.

Chapter 4 relates the results from the second approach where we try to exploit the intrinsic SOI of Ge (111). The generation of spin in Ge has been long studied in our group, and the results showed that the SOI of Ge (100) was not strong enough to generate large spin currents. Here, we show that using the spin-splitted Rashba states at the interface between Ge (111) and a metal could lead to an efficient manipulation of the spins. By investigating the electrical properties of a thin Ge (111) film epitaxially grown on Si(111), we found a large unidirectional Rashba magnetoresistance (UMR), which we ascribe to the interplay

between the externally applied magnetic field and the current-induced pseudo-magnetic field applied in the spin-splitted subsurface states of Ge (111). The unusual strength and tunability of this UMR effect open the door towards spin manipulation with electric fields in an all-semiconductor technology platform.

Finally, chapter 5 focuses on integrating perpendicularly magnetized magnetic tunnel junctions on the Ge (111) platform. I first investigated the magnetic properties of Co/Pt multilayers grown by sputtering on Ge (111) by using three magnetometry techniques simultaneously: the anomalous Hall effect, Kerr microscopy and a new original technique based on an electrical detection of the magnetic circular dichroism in Co/Pt. These MTJs were then used to perform spin generation and detection in a lateral spin valve. The perpendicular magnetic anisotropy (PMA) allows to generate spin current with a spin orientation being also perpendicular to the sample plane. In the last section, we gather all the building blocks that were studied during my PhD work to build a prototypical spin transistor. The spin accumulation was generated either optically or electrically, using optical spin orientation in germanium or the electrical generation by the magnetic tunnel junctions.

CHAPTER 1

Combining semiconductor spintronics and spin-orbitronics

This first chapter aims at introducing the field of spintronics, from the discovery of the spin to its applications in modern technologies. In a first section, I review the main discoveries that shaped the classical spintronics and explain the basics of spin-dependent physics. Then I introduce the well-established field of semiconductor spintronics, finally, I present the more emergent field of spin-orbitronics. I will show how those three domains meet to develop hybrid devices where the spins propagating in a semiconductor can be manipulated using an electric field.

1.1 Introduction to spintronics

In 1947, J. Bardeen, W. Shockley and W. Brattain discovered the transistor at Bell laboratories, this elemental brick that kick-started the electronics revolution that eventually, shapes the modern world we live in. The fundamental aspect of the transistor is to control one of the electron intrinsic properties: the electrical charge, by employing materials where the conductivity can be easily tuned by applying a voltage: the semiconductors industry was born. From this starting point, tremendous research work has been intimately conducted between the academic and the industrial world in order to miniaturize this building block. Across the decades, the transistor size decreases from the cm-range to the nanoscale, increasing the integrated density on a single chip up to several tens of billion.[1] This exponential boost in performance allowed manufacturers to propose forever-increasing processing power at constant manufacturing cost. However, this driving force, well known as the Moore's Law,[2] is reaching physical limits as the transistor size is approaching the quantum limits. One appealing alternative is based on exploiting another intrinsic property of the electron: its *spin*.[3]

1.1.1 Discovery of the spin

The spin concept was born in the early 1920's. At this time, quantum mechanics formalism was in its infancy and could not yet provide answers to contemporary experimental observations. The field of atomic physics was facing two main concerns, the first one comes from the field of spectroscopy: the anomalous Zeeman effect, which occurs when atoms emitting light in the presence of a static external magnetic field, exhibits in a typical four-lines spectra (see Fig. 1.1 a)) which was not explainable with the available theory of Bohr-Sommerfeld.

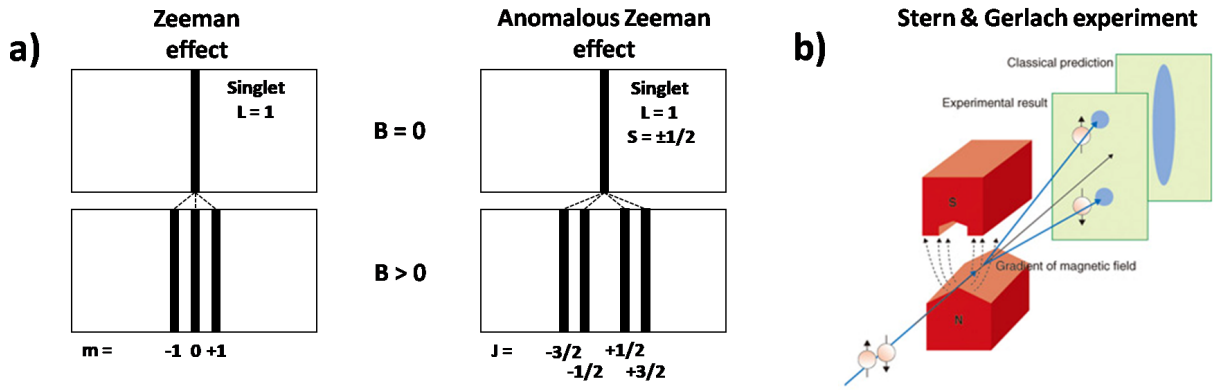

Figure 1.1 – a) Normal and anomalous Zeeman effect. b) Stern and Gerlach experiment.

The second one is the very famous Stern and Gerlach experiment. O. Stern was an experimental physicist, he worked under the close influence of A. Einstein and later on, M. Born. During his experimental odyssey, he pushed the limits of molecular beam experiments to test the atomic physics theories. First motivated by thermodynamic and kinetic theories, he moved on to magnetism and met W. Gerlach. Together they designed one of the canonical experiments that shook the emerging quantum mechanics field. The experiment objective at this time was to judge whether or not Bohr-Sommerfeld model was right by testing its predictions. In the Stern and Gerlach experiment, a beam of silver atoms passes through an inhomogeneous magnetic field (see Fig. 1.1 b)) and hits a screen. In a simplified picture, electrons are orbiting the atom's nuclei, giving rise to an orbital momentum that results in an orbital magnetic moment. In Larmor's classical approach of atomic physics, there is no preferential direction for the direction of the magnetic moment, so when the silver atoms pass through the magnetic field, there should not be deflected in a particular orientation. In the Bohr-Sommerfeld quantum theory, the magnetic moment values are fixed, leading to deterministic deflections. Stern and Gerlach did observe a spatial deflection, rejecting the classical theory and partially confirming the Bohr-Sommerfeld predictions. Indeed, they observed a two-fold figure of deflection, which was inconsistent with the picture that atoms in state $L = 0$ would not split at all and atoms in state $L = 1$ would split into three components. This was solved in 1925 when G. Uhlenbeck and S. Goudsmit proposed that the electron holds an intrinsic angular momentum or *spin*. S. Goudsmit was a spectroscopist who was

confused by some inconsistencies between the experimental hydrogen emission spectrum and the predictions of quantum mechanics. Influenced by P. Erhenfest, he partnered G. Uhlenbeck, a theoretical physicist and together, they came up with the idea that the electron must own a fourth degree of freedom: the spin, a form of angular momentum that a particle intrinsically carries. They figured out that it could only take two values: $\pm 1/2$, this concept could explain the Stern-Gerlach experimental observation: in an atom, the electron carries a total angular momentum $J = L + S$, where L is the orbital angular momentum and S is the spin of the electron. For silver atoms in the $L = 0$ state, the electron only carries a spin angular momentum leading to the beam splitting into two components.[4]

These pioneering works strongly stimulated the scientific community, and soon after this first proposition, renowned physicists like W. Pauli, E. Schrödinger W. Heisenberg developed the formalism that shaped the modern quantum mechanics. Still, the spin properties seemed to be *ad-hoc*, it looks like an ingredient that physicists used to better describe reality, but without strong fundamental foundations. This is only when P. Dirac unified quantum mechanics with A. Einstein theory of relativity that the spin properties arose naturally.

The spin possesses a profound quantum nature. In order to better visualize this peculiar object of physics, we have to rely on classical images. One common way to picture the spin property is to imagine a rotation of the electron on its own axis, acting as a subatomic coil that orientate the magnetic moment perpendicularly to the plane of rotation. This picture can help apprehending such an unconventional quantity but is fundamentally wrong as the electron tangential speed should be greater than speed of light, as forbidden by relativity.

1.1.2 Spin in solid state physics

We saw how the spin properties can lead to a variety of exotic effects when considering only a few of non-interacting atoms. In the field of condensed matter physics, we consider a very large number of atoms, usually arranged in a crystal lattice. The following section aims at showing the properties of a solid that are due to the existence of the spin. It gives a short introduction on the origins of magnetic moments and magnetic interactions.

1.1.2.1 Magnetic moment

Both spin and orbital moments can give rise to the magnetic moment of an atom, we start by defining the relation between these two observables and their magnetic moments:

$$\mu_{\mathbf{s}} = -\frac{g_s \mu_{\mathrm{B}} \mathbf{s}}{\hbar} \quad \text{and} \quad \mu_{\mathbf{l}} = -\frac{g_l \mu_{\mathrm{B}} \mathbf{l}}{\hbar} \tag{1.1}$$

where $|\mathbf{s}| = \frac{\hbar}{2}$, μ_{B} is the Bohr magneton, $g_{s(l)}$ is the Landé factor of the spin (orbital) moment ($g = 2$ for a free electron) and $\hbar$ is the reduced Planck constant.
Derived from quantum mechanics, the Hund's rules only allow atoms with partially filled orbitals to possess a net magnetic moment since spin and orbital moments cancel in filled electron shells. Most atoms carry a magnetic moment when they are isolated. However, in a solid, the formation of interatomic bonds leads to the compensation of the magnetic momenta in most cases. There are mainly two types of pure materials with nonvanishing magnetic moments: the transition metals like Fe, Co and Ni and the rare earth elements like Nd, Sm, Gd.

1.1.2.2 Itinerant magnetism

In a non-magnetic system, there are equal numbers of spin up and spin down electrons ($n_\uparrow = n_\downarrow = n$). For ferromagnetism to exist, there must be an imbalance. This is attributed to the presence of repulsive interaction. Let us consider a simple model with on-site repulsion (i.e. an energy cost U when two electrons occupy the same site). As per the Pauli exclusion principle, it is required that if two electrons were to occupy the same site, they need to have opposite spins.[5]
With this in mind, let consider the situation when δn down-spin spontaneously flip. Then the number of up spins is: $n_\uparrow = n + \delta n$ and the number of down spins is: $n_\uparrow = n - \delta n$. This redistribution of the spins leads to a change in the energy of the system. The potential energy of the system is given by $U_E = U n_\uparrow n_\downarrow$. The change in potential energy is:

$$\begin{aligned} \mathrm{d}U_E &= U\left(n + \delta n\right)\left(n - \delta n\right) - Un^2 \\ &= -U\left(\delta n\right)^2 \end{aligned} \tag{1.2}$$

The change in the kinetic energy due to the δn spins occupying higher energy states is:

$$\mathrm{d}K_E = \delta n \mathrm{d}E \tag{1.3}$$

The density of states is defined as the number of states in the energy interval $[E,\, E + \mathrm{d}E]$:

$$\rho\left(E\right) = \frac{\mathrm{d}n}{\mathrm{d}E} \tag{1.4}$$

Since the electrons occupation change happens close to the Fermi level, we can relate the variation in density δn and the change in energy $\mathrm{d}E$ through the density of states at the Fermi level.

$$\delta n = \rho\left(E_F\right)\mathrm{d}E \tag{1.5}$$

Thus the change in kinetic energy:

$$\mathrm{d}K_E = \frac{\left(\delta n\right)^2}{\rho\left(E_F\right)} \tag{1.6}$$

The change in total energy is the addition of the kinetic and potential energy changes:

$$\begin{aligned} \mathrm{d}E_{\mathrm{Tot}} &= \mathrm{d}K_E + \mathrm{d}U_E \\ &= \frac{\left(\delta n\right)^2}{\rho\left(E_F\right)}\left[1 - \rho\left(E_F\right)U\right] \end{aligned} \tag{1.7}$$

The above equation provides the Stoner criterion for itinerant ferromagnetism. When $\rho\left(E_F\right)U > 1$, the system can lower its energy by creating an imbalance in the number of up and down spins, thereby becoming ferromagnetic.

1.1.2.3 Exchange interaction

Many effects in magnetism can be explained by the competition between the different magnetic configurations. The interaction between an external magnetic field $\mathbf{H}_{\mathrm{ext}}$ and a magnetic moment is described by the so-called Zeeman energy E_Z given by:

$$E_z = -\mu_0 \mathbf{m} \cdot \mathbf{H}_{\mathrm{ext}} \tag{1.8}$$

where $\mathbf{m}$ is the magnetic moment and μ_0 is the magnetic permeability of the vacuum. Consequently the Zeeman energy is minimum when the magnetization is parallel to the applied field.

The magnetic order is due to the exchange interaction between spins. The origin of this interaction is due to the Coulomb interaction and the Pauli principle, which prohibits the

existence of two electrons in the same state. The exchange interaction depends on the exchange constant J and the orientation of the spins $\mathbf{S_i}$. An important parameter which determines J is the distance between the two spins $\mathbf{S_i}$ and $\mathbf{S_j}$ at the positions $\mathbf{r_i}$ and $\mathbf{r_j}$. The exchange energy between two moments is expressed as:

$$E_{\text{ex}} = -J\left(\mathbf{r_i} - \mathbf{r_j}\right)\mathbf{S_i} \cdot \mathbf{S_j} \tag{1.9}$$

The sign of J influences the different magnetic configurations: if $J > 0$ the minimum energy is obtained for a parallel arrangement of the two moments, $J < 0$ leads to an antiparallel arrangement of the two moments. In a solid, the exchange interaction is a short-range interaction, basically limited to first neighbor moments. It will lead to a magnetic order like ferromagnetic order or antiferromagnetic order. At finite temperature T, magnetic moments are excited by an average energy of $k_B T$ with k_B the Boltzmann constant. This excitation competes with the ordering due to the exchange interaction. At a certain critical temperature the magnetic long-range order is lost. For ferromagnetic order this critical temperature is called the Curie temperature T_C, for antiferromagnetic order it is called the Néel temperature T_N. For transition metals the exchange interaction is strong leading to high T_C ($T_C = 1043$ K for Fe and $T_C = 1388$ K for Co).

The exchange interaction lies at the heart of magnetism and it is thoroughly exploited in the field of spintronics to generate, detect and manipulate spin currents.

1.1.3 Spin current and magnetoresistance effects

This section aims at introducing the notion of spin current, which is a central aspect of the field of spintronics. We present a short review of the historical development of the field through its most important effects: the giant[6,7] and tunneling[8] magnetoresistances as well as the spin transfer torque effect.[9]

1.1.3.1 Charge and spin currents

The notion of currents is related to the flow of a certain quantity per surface unit. In conventional electronics devices, a charge current ($\mathbf{J_c}$) corresponding to a flow of charges, is manipulated to encode and transfer information. Analogously, a spin current ($\mathbf{J_s}$) corresponds to a flow of angular momentum, it is a key concept in the field of spintronics. The charge current density is defined as the flux of charges transferred through a surface S:

$$J_c = \frac{e}{S}\frac{\mathrm{d}N}{\mathrm{d}t} \tag{1.10}$$

where N is the total amount of charges. The transport of spins can be described using a two-currents model with spin-selectivity, the spin up (down) current density $J^{\uparrow}$ ($J^{\downarrow}$) is defined as the flux of spin up (down) angular momentum through a surface S, respectively. The two conduction channels are supposed to be independent from each other. This approximation holds when the spin-orbit interaction is small. We can thus define the corresponding current contributions:

$$J_{\uparrow(\downarrow)} = \frac{h}{2e}\frac{e}{S}\frac{\mathrm{d}N_{\uparrow(\downarrow)}}{\mathrm{d}t} \tag{1.11}$$

where $N^{\uparrow}$ ($N^{\downarrow}$) is the number of charges of spin up (down). The $\frac{h}{2e}\frac{e}{S}$ factor indicates that this current is a flow of angular momentum. We can write the resulting charge and spin currents as:

$$J_c = J^{\uparrow} + J^{\downarrow} \tag{1.12}$$

and

$$J_s = J^{\uparrow} - J^{\downarrow} \tag{1.13}$$

As shown in Fig. 1.2, we can distinguish three different types of current. The first one is a pure charge current with no net flow of angular momentum, this is the type of conduction that occurs in most materials. The second one is a spin-polarized current where both charge and angular momentum flow in a given direction, this is typical of the conduction in a ferromagnetic material. Interestingly, a pure spin current can be generated if there is no net flow of charges but only of angular momentum, several techniques can be used to

generate such currents like optical spin orientation, electrical spin injection or spin pumping by ferromagnetic resonance.

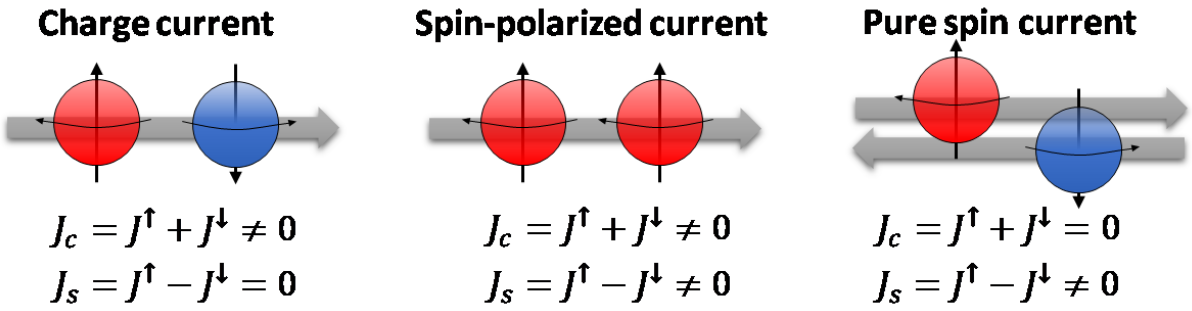

Figure 1.2 – Schematic representation of a pure charge current, of a 100 % spin polarized current and of a pure spin current.

It should be noted that contrary to the charge current which is a vectorial quantity (defined by a magnitude and a direction in space), the spin current is a tensor quantity (defined by a magnitude, a direction in space and a spin direction ↑ or ↓). Another important difference between the two types of transports is that unlike the charge current, the spin current is non-conservative as a consequence of a finite spin-flip probability during successive scattering events.
The Ohm's law can also be generalized to define the spin-dependent conductivities, accounting for the contributions from electron drift and diffusion:

$$\mathbf{j}_{\uparrow\downarrow} = \bar{\sigma}_{\uparrow\downarrow}\mathbf{E} + e\bar{D}_{\uparrow\downarrow}\nabla n_{\uparrow\downarrow} \tag{1.14}$$

where $\mathbf{E} = -\nabla\mathbf{V}$ is the electric field resulting from the potential gradient, $\nabla n_{\uparrow\downarrow}$ is the spin-dependent carrier density gradient, $\bar{\sigma}_{\uparrow\downarrow}$ is the spin-dependent electrical conductivity tensor and $\bar{D}_{\uparrow\downarrow}$ is the spin-dependent diffusion tensor. The carrier density gradient can be expressed as a function of the spin-dependent chemical potential $\nabla\nu_{\uparrow\downarrow}$:

$$\nabla n_{\uparrow\downarrow} = \rho_{\uparrow\downarrow}(E_f)\,\nabla\nu_{\uparrow\downarrow} \tag{1.15}$$

where $\rho_{\uparrow}(E_f)$ ($\rho_{\downarrow}(E_f)$) is the spin ↑ (↓) density of states at the Fermi level. We can apply the Einstein relation to the considered spin-dependent tensor quantities:

$$\bar{\sigma}_{\uparrow\downarrow} = e^2\rho_{\uparrow\downarrow}(E_f)\,\bar{D}_{\uparrow\downarrow} \tag{1.16}$$

The spin-dependent conduction can be written as:

$$\mathbf{j}_{\uparrow\downarrow} = \frac{1}{e}\bar{\sigma}_{\uparrow\downarrow}\nabla\mu_{\uparrow(\downarrow)} \tag{1.17}$$

where $\mu_{\uparrow\downarrow} = \nu_{\uparrow\downarrow} - eV$ is the electrochemical potential of spins ↑ (↓) and V the electrical

potential.
This derivation shows how the two spin channels can own different conductivities and set the basis of spin-dependent transport.

1.1.3.2 Giant magnetoresistance

We usually associate the birth of spintronics with the simultaneous discovery of the giant magnetoresistance (GMR) by A. Fert[6] and P. Grünberg[7] groups in 1988 who were awarded the Nobel Prize in 2007. This effect takes place in ferromagnetic/non-magnetic/ferromagnetic (FM/NM/FM) trilayers. When a current flows through the structure, different resistance states are observed depending on the relative orientation of the FM layer magnetizations. The thickness of the films has to be comparable with the electron characteristic lengths: the mean free path and the spin diffusion length, so they are typically a few nanometers-thick.
In non-magnetic metals like copper, the Fermi level lies within the *sp* band, and the *d* band is completely filled. In ferromagnets, the *d* band is partially filled and split into two spin sub-bands as a consequence of exchange interaction. Therefore the density of states at the Fermi level is different for the two spins orientations. The Fermi level for majority-spin electrons is located in the *sp* band, so their electrical conduction is similar in ferromagnets and non-magnetic metals. For minority-spin electrons, the *sp* and *d* bands are hybridized, and the Fermi level lies within the *d* band. The hybridized *spd* band has a high density of states, which results in stronger scattering rate and thus a shorter mean free path λ for minority-spin than majority-spin electrons.
The origin of GMR lies in spin-dependent scattering events in ferromagnetic layers as well as at their interfaces. We first consider the case where the two FM magnetizations are parallel. As shown in Fig. 1.3 a), the spin $\uparrow$ channel is parallel to the magnetization orientation, its spin-dependent conductivity $\bar{\sigma}_{\uparrow}$ is higher as a result of reduced scattering rate. Inversely, the spin $\downarrow$ channel is antiparallel to the magnetization orientation, the increased electron scattering rate results in a lower spin-dependent conductivity $\sigma_{\downarrow}$. The total resistance scheme for the parallel state is depicted in Fig. 1.3 b), the low-resistance spin $\uparrow$ channel shorts the electrical current and results in a low resistance state. At contrast, when the two FM magnetizations are antiparallel, as shown in Fig. 1.3 c), both spin channels exhibit a high and a low spin conductivity: the two channels are now equivalent. The current can no longer shorts into a low resistance path so the total resistance is high (see Fig. 1.3 d)). The GMR ratio is defined as:

$$\mathrm{GMR} = \frac{R_{\uparrow\downarrow} - R_{\uparrow\uparrow}}{R_{\uparrow\uparrow}} \tag{1.18}$$

where $R_{\uparrow\uparrow}$ ($R_{\uparrow\downarrow}$) corresponds to the parallel (antiparallel) configuration equivalent resistance. Different geometries can be used to exploit the GMR effect. First, the current can be applied perpendicularly to the trilayer plane, as illustrated in Fig. 1.3, this is the current

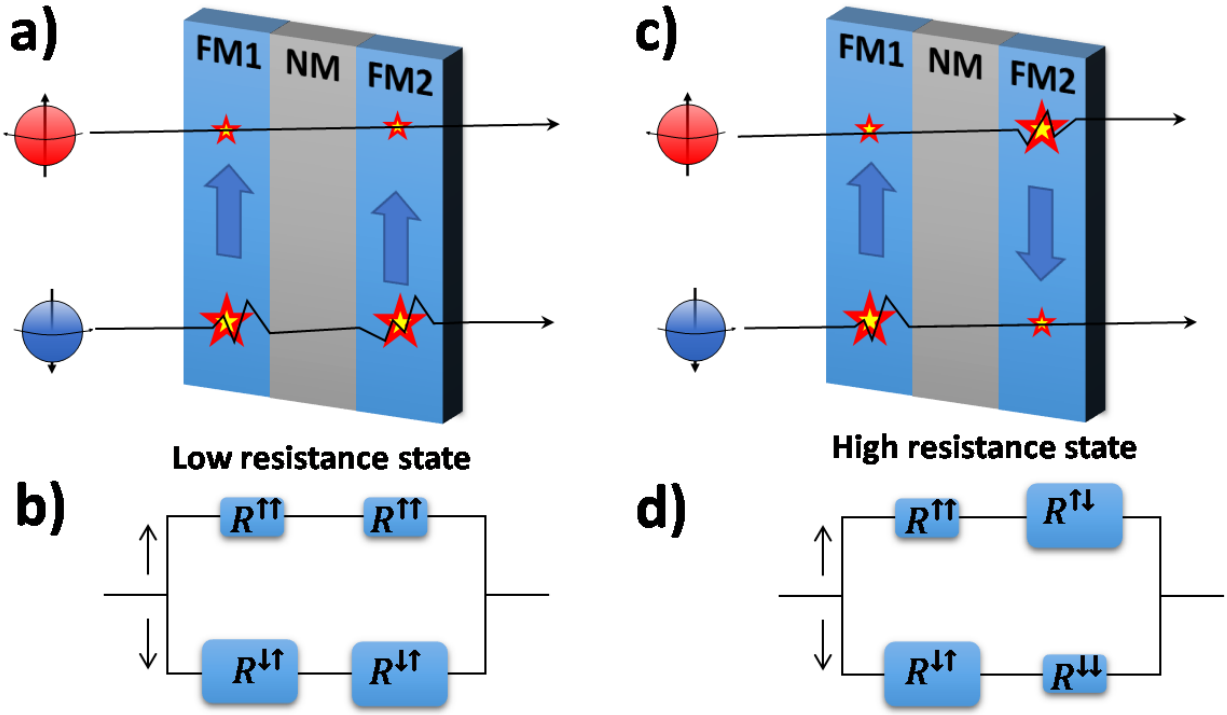

Figure 1.3 – Scheme of the conduction mechanism in a ferromagnetic/non-magnetic/ferromagnetic multilayer. a) Parallel configuration: the spin ↑ (↓) channel scattering rate is low (high) as a consequence of the spin orientation and the FM magnetization being parallel (antiparallel). b) Corresponding equivalent circuit: the low resistance channel shorts the current resulting in a low total resistance. c) Antiparallel configuration: the two spin channels exhibit a low and and a high scattering rate. d) Corresponding equivalent circuit: the resistance of the two channels is equal, resulting in a higher total resistance.

perpendicular-to-the-plane geometry or (CPP-GMR). Alternatively, the current can be applied within the trilayer plane, it is called the current-in-plane geometry(or CIP-GMR). Despite the fact that the CPP geometry leads to higher GMR, it is more difficult to measure as it requires a delicate vertical nanofabrication procedure.

The progress in thin films growth and processing along with a deeper understanding of the fundamental mechanisms allowed for a fast optimization of this effect, and the integration of GMR stacks into several applications (reading heads of hard-disks or field sensors). The non-magnetic layers were further replaced by an ultra-thin insulating film that acts as a tunnel barrier between the two FMs to form a magnetic tunnel junction. In these devices, the tunneling magnetoresistance between parallel and antiparallel states can reach several hundreds of percents, one order of magnitude larger than the GMR.

1.1.3.3 Tunneling magnetoresistance

The first experiments on spin-dependent electron transport phenomena were done by Tedrow and Meservey in the early 70s by studying the magnetoresistance of a ferromagnet / insulator / superconductor (F/I/S) junction.[10,11] Later on, Jullière extended this work to F/I/F junctions leading to the discovery of tunneling magnetoresistance (TMR)[8] (see Fig. 1.4). In magnetic tunnel junctions (MTJs), the insulating layer is thin enough (typically a few nanometers) for electrons to tunnel from one ferromagnet to the other. Like GMR, TMR is a magnetoresistive effect where the resistance of the trilayer is lower when the FMs magnetizations are parallel. Similarly to the GMR effect, the TMR ratio is phenomenologically defined as:

$$\mathrm{TMR} = \frac{R_{\uparrow\downarrow} - R_{\uparrow\uparrow}}{R_{\uparrow\uparrow}} \tag{1.19}$$

where $R_{\uparrow\uparrow}$ ($R_{\uparrow\downarrow}$) is the trilayer total resistance in the parallel (antiparallel) state. The first model to understand the TMR effect was proposed by Jullière,[8] it involves the spin polarizations of the ferromagnetic electrodes P defined after as the difference of the densities of states for spin up and spin down at the Fermi level:

$$P_{\text{Jullière}} = \frac{\rho_{\uparrow}(E_F) - \rho_{\downarrow}(E_F)}{\rho_{\uparrow}(E_F) + \rho_{\downarrow}(E_F)} \tag{1.20}$$

The TMR ratio can then be expressed as a function of the spin polarization of the two ferromagnets: P_1 and P_2 as:

$$\mathrm{TMR} = \frac{2P_1P_2}{1 - P_1P_2} \tag{1.21}$$

One can note that this model is very limited as it does not account for the tunnel barrier height and hence the tunneling probability as well as the details of the electronic band structure.

The first MTJ used by Jullière was composed of Fe/Ge/Co, yielding about 14 % of TMR,[8] this low value limited the interest of the community for this magnetoresistance effect. In 1995, Moodera used Fe/AlOx/Co junctions and reached several tens of percents.[12] Applying the Jullière model in this junction resulted in a prediction of negative TMR, as $\rho^{\uparrow}_{Co(Fe)}(E_F) < \rho^{\downarrow}_{Co(Fe)}(E_F)$, highlighting that the Jullière model is insufficient to model the TMR here. The first solution was brought by Stearns, who modified the Jullière formula of the FM spin-polarization to account for the band structure:[13]

$$P_{\text{Stearns}} = \frac{k_{\uparrow}(E_F) - k_{\downarrow}(E_F)}{k_{\uparrow}(E_F) + k_{\downarrow}(E_F)} \tag{1.22}$$

where $k_{\uparrow(\downarrow)}(E_F)$ is the Fermi wavevector for spin $\uparrow\downarrow$. This model was used with some success but still, could not account for the tunneling probability in many cases. In order to improve

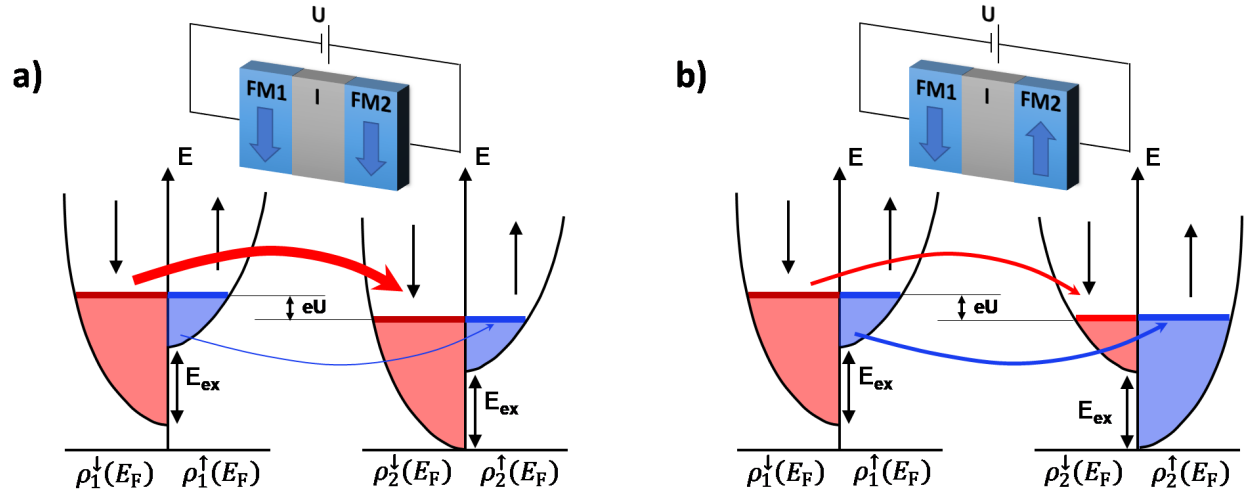

Figure 1.4 – Schematics of a FM/I/FM magnetic tunnel junction (MTJ) and illustration of the Jullière's model of TMR for a) the parallel state. b) the antiparallel state.

the understanding of TMR, one has to consider the electronics band structure of the three components of the trilayer.

J. Slonczewski provided the theoretical solution to this problem, by accounting for the tunnel barrier height, to define the FM spin-polarization as:[14]

$$P_{\text{Slonczewski}} = \left(\frac{k_\uparrow(E_F) - k_\downarrow(E_F)}{k_\uparrow(E_F) + k_\downarrow(E_F)}\right)\left(\frac{\kappa_0^2 - k_\uparrow(E_F)\,k_\downarrow(E_F)}{\kappa_0^2 + k_\uparrow(E_F)\,k_\downarrow(E_F)}\right) \tag{1.23}$$

where κ_0 is the Fermi wavevector in the tunnel barrier region. One can note that this model is equivalent to the Stearn model for high tunnel barriers ($\kappa_0 >> k_\uparrow(E_F), k_\downarrow(E_F)$). Also, by considering a free electron model: $\rho(E_F) \propto k$, we retrieve the initial Jullière formula.[15]

At this point, the tunnel barriers were mostly made of amorphous Al_2O_3 or amorphous MgO and resulted in TMR ratios below 100 %. In 2005, several groups started to grow single crystalline MgO barriers, which resulted in a large enhancement of the TMR but was puzzling from a theoretical point of view. As the barrier went from amorphous to crystalline, the band structure of MgO had to be taken into account. In short, MgO filters the tunneling transmission of electrons with a particular symmetry that are fully spin-polarized within the current flowing across body-centered cubic Fe-based electrodes.[16]

1.1.4 Spin transfer torque

In 1996, J. Slonczewski showed that magnetic tunnel junctions could be more than passive devices acting as magnetic field sensors, but that they could be actively operated to control the magnetization orientation of a FM film.

This mechanism relies on the fact that a current becomes spin-polarized when it passes through a ferromagnetic layer. By conservation of angular momentum, the spin current is

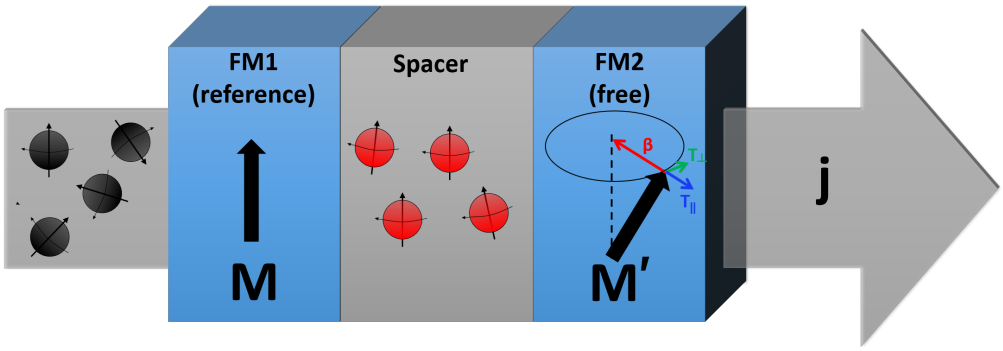

Figure 1.5 – Schematic representation of the spin transfer torque in a magnetic tunnel junction. The charge current becomes spin-polarized in FM1 (called the reference layer of magnetization $\mathbf{M}$), and exerts a torque on the magnetization $\mathbf{M}'$ in FM2 (called the free layer). The circular motion of $\mathbf{M}'$ with respect to the direction of $\mathbf{M}$ corresponds to the Larmor precession. The red vector β corresponds to the damping of the magnetization. $\mathbf{T}_{\parallel}$ (in blue) is the damping-like torque and $\mathbf{T}_{\perp}$ (in green) is the field-like torque.

transferred from a first ferromagnet named the reference layer, to the second one: the free layer, exerting a torque on the magnetization[9,17] (see Fig. 1.5). This torque can force the magnetization to precess, and ultimately, to switch. The physics of magnetization dynamics is described by the Landau Lifshitz Gilbert equation (LLG), for a material with uniform magnetization, it can be written as:

$$\frac{\mathrm{d}\mathbf{M}}{\mathrm{d}t} = -\gamma_0 \mathbf{M} \times \mathbf{H}_{eff} + \frac{\alpha}{M_s}\mathbf{M} \times \frac{\mathrm{d}\mathbf{M}}{\mathrm{d}t} \tag{1.24}$$

where γ_0 is the gyromagnetic ratio, α is the Gilbert damping and M_s is the saturation magnetization. Here, $\mathbf{H}_{eff}$ is the effective magnetic field accounting for the external magnetic field $\mathbf{H}_0$, the demagnetizing field $\mathbf{H}_D$, and the anisotropy field $\mathbf{H}_k$: $\mathbf{H}_{eff} = \mathbf{H}_0 + \mathbf{H}_D + \mathbf{H}_k$. The first term (in black) is usually known as the Larmor precession. The second term (in red) is referred to the damping term: it accounts for the dissipation of angular momentum during the precessional motion as a consequence of various mechanisms (electron-magnon or magnon-phonon scattering).

If we now consider a magnetic tunnel junction where a spin-polarized current coming from the reference layer also exerts a torque on the magnetization of the free layer, we can feed the LLG equation with additional terms:

$$\frac{\mathrm{d}\mathbf{M}'}{\mathrm{d}t} = -\gamma_0 \mathbf{M}' \times \mathbf{H}_{eff} + \frac{\alpha}{M_s}\mathbf{M}' \times \frac{\mathrm{d}\mathbf{M}'}{\mathrm{d}t} - \frac{|g_e \mu_B|}{\hbar}\left(T_{\parallel}\mathbf{M}' \times (\mathbf{M} \times \mathbf{M}') + T_{\perp}\mathbf{M} \times \mathbf{M}'\right) \tag{1.25}$$

where $\mathbf{T}_{\parallel}$ (in blue) is the parallel torque, better known as the damping-like torque as it is colinear with the damping vector β and $\mathbf{T}_{\perp}$ (in green) is the perpendicular torque, known as the field-like torque as its action on the magnetization mimics the effect of an external

magnetic field. The latter is the sum of two terms $T_{\perp}^{0}$ and $T_{\perp}^{1}(J)$, $T_{\perp}^{0}$ refers to the interlayer exchange coupling, which is current-independent and $T_{\perp}^{1}(J)$ which is current-dependent.
The STT efficiency can be derived by calculating the different transmission probabilities for spin $\uparrow$ and $\downarrow$ through the MTJ using a free electron model and gives:

$$\frac{T_{\parallel}}{J} = \frac{P_1 \sin\phi}{1 + P_1 P_2 \cos\phi} \tag{1.26}$$

where ϕ is the angle between the two FMs magnetization vectors. In the colinear case, a large spin current is generated but the torque efficiency is minimum whereas in the non-colinear case, the spin current is minimum but the torque efficiency is maximum.
STT brought a new paradigm for technological applications as a memory dot can be written using this effect.

1.1.5 Applications

1.1.5.1 Hard-drive disks

The discovery of giant magnetoresistance had a important impact in the hard disk drives (HDDs) industry. Memory bits are detected by sensing the stray magnetic fields between adjacent magnetic domains as the disk is rotated beneath a magnetic sensor. As the area of the magnetized region decreased, the read element had to scale down in size accordingly. The improvement in GMR magnitude allowed such downscaling thanks to an increased sensitivity.[18]

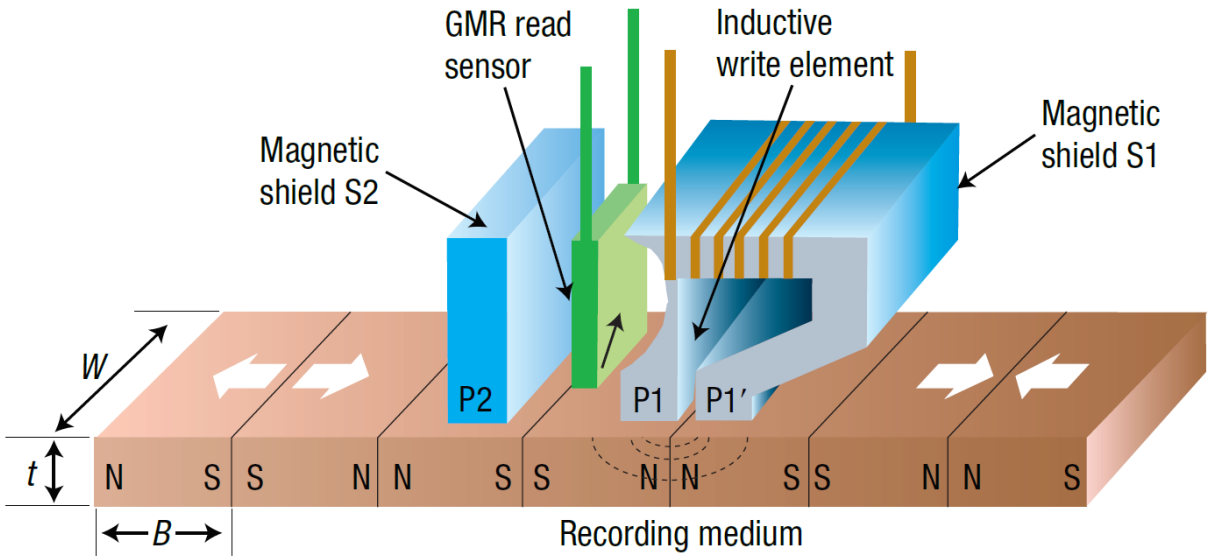

Figure 1.6 – Magnetoresistive head for hard-disk recording.

Fig. 1.6 illustrates how the magnetic states are encoded and read. Passing a current through the coil generates a magnetic field that is guided through the magnetic circuit. This magnetic

field is used to align the magnetization of the recording layer. In modern technologies, the read head is decoupled from the writing part and consists of a spin valve based on GMR or TMR. The introduction of the spin-valve head, by providing a highly sensitive and scalable read technique, contributed to increase the raw HDD areal recording density by three orders of magnitude (from 0.1 to 100 Gbit.in^{-2}) between 1991 and 2003.

1.1.5.2 Magnetic random access memory

Despite all these progresses, developing solid-state magnetic storage with no moving part was still much desirable.[19] In that sense, magnetic random access memory (MRAM) is a non-volatile read out memory, which is based on the magnetic anisotropy energy to retain information and the magnetoresistance effect to read the information. The writing and reading mechanisms have undergone various changes since the first proposal of MRAM in the late 1990s. Fig. 1.7 a) shows the initial design called the *field* MRAM as the magnetization state of the free layer was manipulated by the Oersted field generated by a large current. The switching field is inversely proportional to the area of the storing element limiting the scalability toward smaller dimensions as higher and higher currents are required.

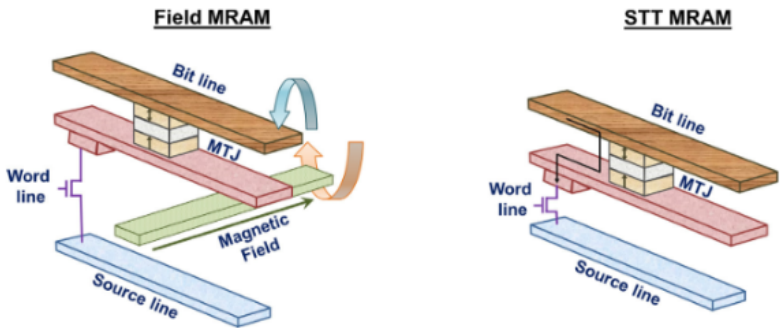

Figure 1.7 – A comparison of the architectures of MRAMs with (a) field induced switching (b) Spin Transfer Torque (STT) switching. In STT switching, the current flows through the MTJ and the final device is much simpler than the field MRAM one.

In that sense, the discovery of spin transfer torque was an awaited breakthrough for the magnetic storage research community.[20] The STT based magnetization manipulation does not require an external magnetic field, which allows both for energy-efficient writing and improves the scalability of the STT-MRAM cell. The read operation is performed by tunneling magnetoresistance. These MRAMs are now reaching industrial scale production. They can be easily embedded in CMOS technology, are faster than NAND Flash, and have a higher cyclability than phase change memories. Moreover, when compared with strandard SRAM and DRAM, they are comparable in terms of speed, but their non-volatility allows lowering the total power consumption.[18]

1.2 Semiconductor spintronics

The spintronics field experienced its first successes using metals to generate, transport and detect spin currents. In 1990, S. Datta and B. Das proposed the first semiconductor-based spin transistor architecture, where the information is carried by the electron spin instead of its charge.[21] This proposal steered the community interest towards semiconductor spintronics. Indeed, a silicon technology-compatible spintronics platform is highly desirable. In semiconductors, the spin lifetime is orders of magnitude larger than in metals. The adjustable energy bandgap allows to tune the light-matter interaction, and the optical selection rules for light absorption allow to envision spin-optoelectronics.[22] The promises of this field are numerous: a gain in working frequency, reduction in the energy consumption of devices and the possibility to design hybrid devices associating memory and logic functions taking advantage of the intrinsic non-volatility of magnetism.[23]

1.2.1 Spin transistor proposal

The spin transistor, shown in Fig. 1.8, consists of two ferromagnetic contacts (FM1 and FM2) on both sides of a two-dimensional electron gas (2DEG). This 2DEG is formed in a quantum well between two semiconducting materials, here $In_xAl_{1-x}As$ and $In_xGa_{1-x}As$. The FM1 source acts as a spin polarizer and FM2 as a spin analyzer. The spin current is injected from the FM1 contact into the 2DEG. The length of the channel L, given by the distance between the two FM contacts, is less than the spin diffusion length in the 2DEG. In order to perform the transistor operation, the spin orientation has to be manipulated while diffusing in the channel. A magnetic field is usually required to induce the precession of spins. However, this solution is not easily integrable to nanodevices. Like in the CMOS technology, a manipulation by an electric field created by a gate voltage would be highly desirable. Therefore, the interplay between a static electric field and the spin orientation is of first importance. This is achieved by the Rashba spin-orbit coupling (see sect. [1.3.3.1]). As shown in Fig. 1.8 a), if there is no gate voltage applied to the 2DEG, the spin-polarized electrons maintain their orientation and enter the analyzer, leading to a low resistance state. By applying a gate voltage, an effective magnetic field is generated by the Rashba spin-orbit interaction in the 2DEG plane. This effective magnetic field causes the electron spins to precess and the spin direction is no longer parallel to the FM magnetizations, resulting in a high resistance state as shown in Fig. 1.8 b). The precession angle of the electron spin can be controlled by the electric field. This spin field effect transistor might have a significant technological impact for a variety of new applications.[23,24]

To successfully incorporate the spin degree of freedom into existing semiconductor technology, four principal technical issues have to be addressed. First, one has to perform an efficient spin injection and detection through a ferromagnetic metal/semiconductor junction. Then, it is desirable to use materials with long spin diffusion length to carry the spin information over

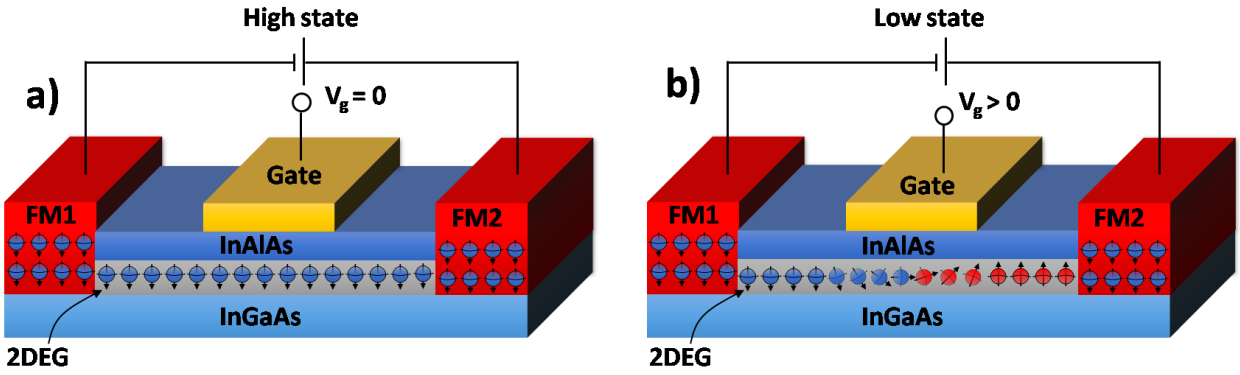

Figure 1.8 – Schematic diagram of SpinFET proposed by Datta and Das in 1990. The architecture is similar to a conventional MOSFET transistor but the information is transferred by controlling the spin orientation using ferromagnetic electrodes. a) The gate voltage is zero, the spin orientation stays aligned with the source and drain magnetizations: this is the passing state. b) By applying a gate voltage, the Rashba spin-orbit interaction results in an effective magnetic field that induce a 180° spin precession, resulting in an antiparallel state: this is the blocking state.

long distances and Si and Ge are the perfect candidates to address this point as they own a low spin-orbit interaction and crystal inversion symmetry. Finally, the most challenging aspect is to control the Rashba interaction with an electric field to allow for the manipulation of the spin orientation. In the following, we provide an historical background of the different techniques developed to generate and detect spin accumulations in semiconductors and metals.[23]

1.2.2 Electrical spin generation and detection

1.2.2.1 Spin generation in metals

The typical free electron-like band diagram of a non-magnetic metal (NM) like copper or gold is represented in Fig. 1.9 a), the amount of spins ↑ ($N_\uparrow$) and ↓ ($N_\uparrow$) is equal, resulting in zero spin-polarization P:

$$P = \frac{N_\uparrow - N_\downarrow}{N_\uparrow + N_\downarrow} \tag{1.27}$$

In ferromagnetic materials (FM), however, the exchange interaction results in an imbalance between spins ↑ and ↓ populations, leading to a spontaneous spin-polarization that can reach several tens of percents in 3d ferromagnets like Fe, Co, Ni and 100 % in Heusler alloys. This spin-polarization can be transferred into the NM under the action of an external perturbation. When passing a current through the FM/NM junction, the current becomes partially spin-polarized and both charges and angular momentum are transferred to the NM, resulting in an out-of-equilibrium magnetization δM in the NM. As a result of the finite spin diffusion

length, the amount of spins coherently oriented in the NM decays with the distance to the interface.

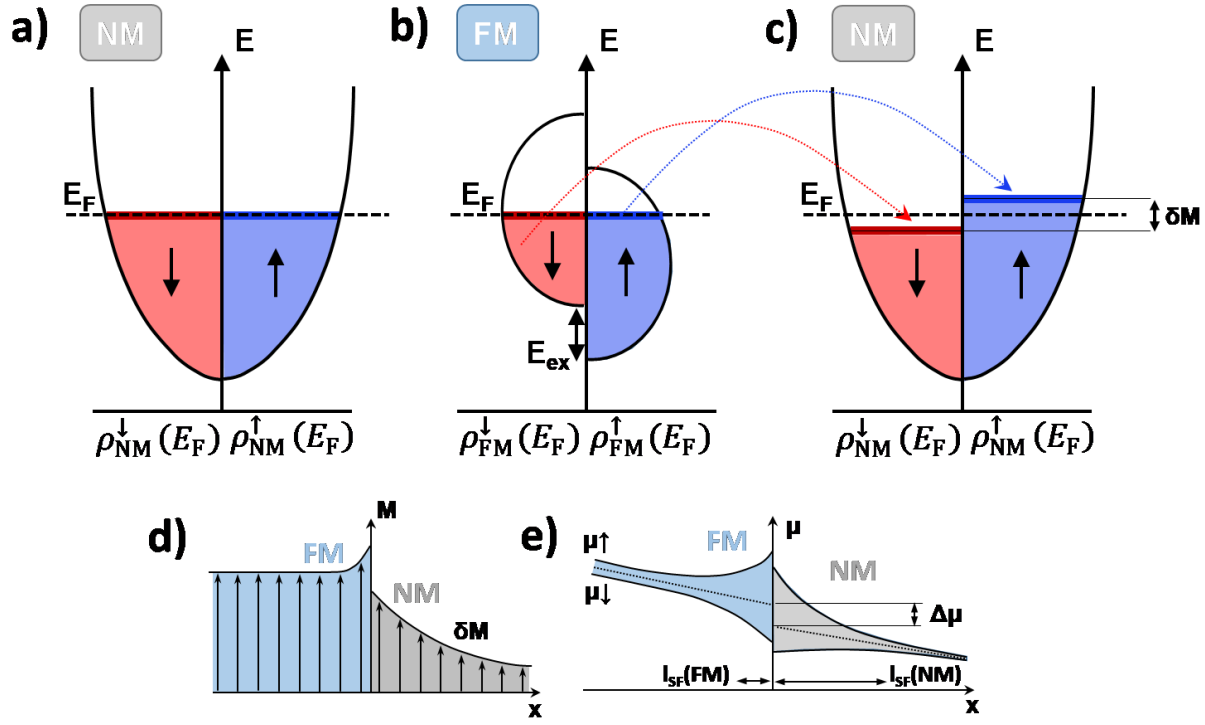

Figure 1.9 – a) Band diagram of a non-magnetic material, there is are equal numbers of spins ↑ and ↓. b) Band diagram of a FM material c) Band diagram of a non-magnetic material during the spin injection from the FM to the NM. The intrinsic spin-splitting of the FM is transferred to the NM, shifting the spin populations by δM. d) Magnetization profile of the FM/NM interface, An out-of-equilibrium spin population δM is injected and decays toward equilibrium ($\delta M = 0$) in the NM. e) Corresponding spin-dependent electrochemical potentials. We notice an accumulation of spin ↑ and a depletion of spin ↓ at the interface between the two materials. The difference of the two populations defines the accumulation of spin at the interface.

The spin polarization of the current at the ferromagnetic/non-magnetic (FM/NM) interface can be derived using the formalism developed by Valet and Fert.[25] The following derivation is adapted from the work of Jaffrès and Fert in 2001.[26] We consider a one-dimensional model, the $x < 0$ region corresponds to the FM and the $x > 0$ region to the NM. In the ferromagnet, the spin ↑ and spin ↓ electrons have different resistivities. They are given by:

$$\rho^{\mathrm{FM}}_{\uparrow(\downarrow)} = 2\left[1 - (+)\beta\right]\rho^{\mathrm{FM}}_{*} \tag{1.28}$$

where $\rho^{\mathrm{FM}}_{*} = \rho^{\mathrm{FM}}/\left(1-\beta^2\right)$ and β is the dimensionless bulk asymmetry parameter given by:

$$\beta = \frac{\rho^{\mathrm{FM}}_{\uparrow} - \rho^{\mathrm{FM}}_{\downarrow}}{\rho^{\mathrm{FM}}_{\uparrow} + \rho^{\mathrm{FM}}_{\downarrow}} \tag{1.29}$$

where electrons with spin ↑ (↓) correspond to majority (minority) carriers in the ferromagnetic

material and $\rho^{\mathrm{FM}}_{\uparrow(\downarrow)}$ are the corresponding spin-dependent resistivities. For $x > 0$, in the NM region, the resistivity is independent of the spin orientation such that:

$$\rho^{\mathrm{NM}}_{*} = \frac{1}{2}\rho^{\mathrm{NM}}_{\uparrow} = \frac{1}{2}\rho^{\mathrm{NM}}_{\downarrow} \tag{1.30}$$

By assuming that the spin flips occur on a much slower timescale than other electron scattering events, the two electrochemical potentials ($\mu_\uparrow$ and $\mu_\downarrow$) are not necessary equal. In our model, the current is supposed to be one-dimensional, it is connected to the electrochemical potentials by the resistivity and the spin diffusion length λ_{SF} by the spin drift-diffusion equation:

$$J_c = J_\uparrow + J_\downarrow \tag{1.31}$$

$$J_{\uparrow(\downarrow)} = \frac{-1}{e\rho_{\uparrow(\downarrow)}}\frac{\partial \mu_{\uparrow(\downarrow)}}{\partial x} \tag{1.32}$$

$$\frac{\partial^2 \Delta\mu}{\partial x^2} = \frac{\Delta\mu}{\lambda^2_{\mathrm{SF}}} \tag{1.33}$$

where $\Delta\mu = \mu_\uparrow - \mu_\downarrow$ is the imbalance of chemical potential due to the spin accumulation. As a consequence of the spin relaxation, the boundary conditions imposes that:

$$\Delta\mu_{\mathrm{NM(FM)}}\left(z = +(-)\infty\right) = 0 \tag{1.34}$$

Additionally, at the FM/NM interface ($z = 0$), the continuity between $j_\uparrow$ and $j_\downarrow$ gives the following condition:

$$J^{\mathrm{FM}}_c(z = 0^-) = J^{\mathrm{NM}}_c(z = 0^+) \tag{1.35}$$

If we first consider that there is no interface resistance, there is a continuity between the electrochemical potentials $\mu_\uparrow$ and $\mu_\downarrow$:

$$\mu^{\mathrm{FM}}_{\uparrow(\downarrow)}(z = 0^-) = \mu^{\mathrm{NM}}_{\uparrow(\downarrow)}(z = 0^+) \tag{1.36}$$

The solutions of the spin drift-diffusion equations in the two regions can be written as:

$$\mu^{\mathrm{FM}}_{\uparrow(\downarrow)} = e\rho^{\mathrm{FM}}_{*}\left[1 - \beta^2\right] Jx - (+)B\left[1 - (+)\beta\right]\exp\left(\frac{x}{\lambda^{\mathrm{FM}}_{\mathrm{SF}}}\right) + C \tag{1.37}$$

$$\mu^{\mathrm{NM}}_{\uparrow(\downarrow)} = e\rho^{\mathrm{NM}}_{*} Jx - (+)D\exp\left(\frac{-x}{\lambda^{\mathrm{NM}}_{\mathrm{SF}}}\right) \tag{1.38}$$

$$J^{\mathrm{FM}}_{\uparrow(\downarrow)} = \left[1 - \beta^2\right]\frac{J}{2} - (+)\frac{B}{2eR_{\mathrm{FM}}}\exp\left(\frac{x}{\lambda^{\mathrm{FM}}_{\mathrm{SF}}}\right) \tag{1.39}$$

$$J^{\mathrm{NM}}_{\uparrow(\downarrow)} = \frac{J}{2} - (+)\frac{D}{2eR_{\mathrm{NM}}}\exp\left(\frac{-x}{\lambda^{\mathrm{NM}}_{\mathrm{SF}}}\right) \tag{1.40}$$

where $R_{\mathrm{FM}} = \rho^{\mathrm{FM}}_{*}\lambda^{\mathrm{FM}}_{\mathrm{SF}}$ and $R_{\mathrm{NM}} = \rho^{\mathrm{NM}}_{*}\lambda^{\mathrm{NM}}_{\mathrm{SF}}$ are the spin resistances of the FM and NM, respectively. The constant B, C and D can be calculated from the above boundary conditions. This set of equations gives the spin accumulations in the two regions:

$$\Delta\mu^{\mathrm{FM}} = E\exp\left(\frac{x}{\lambda^{\mathrm{FM}}_{\mathrm{SF}}}\right) \tag{1.41}$$

$$\Delta\mu^{\mathrm{NM}} = F\exp\left(\frac{-x}{\lambda^{\mathrm{NM}}_{\mathrm{SF}}}\right) \tag{1.42}$$

where E and F are constants determined by the boundary conditions. For a transparent interface, the spin accumulation $\Delta\mu$ has the same magnitude on both sides of the interface and decays exponentially with the distance from the interface. As the spin diffusion length of the NM is usually larger than the one of the FM, this spin accumulation decays on a longer distance in the NM.

Finally, we can express the spin polarization of the current injected in the NM:

$$SP^{\mathrm{NM}}(x) = \frac{J^{\mathrm{NM}}_{\uparrow}(x) - J^{\mathrm{NM}}_{\downarrow}(x)}{J^{\mathrm{NM}}_{\uparrow}(x) + J^{\mathrm{NM}}_{\downarrow}(x)} = \frac{\beta}{1 + R_{\mathrm{NM}}/R_{\mathrm{FM}}} = \frac{\beta}{1 + \dfrac{\rho^{\mathrm{NM}}_{*}\lambda^{\mathrm{NM}}_{\mathrm{SF}}}{\rho^{\mathrm{FM}}_{*}\lambda^{\mathrm{FM}}_{\mathrm{SF}}}} \tag{1.43}$$

According to Eq. 1.43, the spin polarization strongly depends on the spin transport properties of the two materials and is limited by the reabsorption of the spin accumulation by the ferromagnetic material. This limitation corresponds to the impedance mismatch issue, and is explained by a much faster spin relaxation in the ferromagnetic than in the non-magnetic material. In metallic junctions like Cu/Co ($R_{\mathrm{Cu}} = 6\times10^{-15}$ $\Omega.\mathrm{m}^2$ and $R_{\mathrm{Co}} = 4.5\times10^{-15}$ $\Omega.\mathrm{m}^2$), the reduction of SP^{NM} is about 2.33, which is reasonable. In ferromagnetic/semiconductor junction (FM/SC), the large difference between the two resistances (several orders of magnitude) completely prevents any spin injection in the SC as shown in Fig. 1.10 a). The solution was proposed by E. Rashba in 2000,[27] it consists on inserting a large interface resistance (like a tunnel barrier) that decouples the FM from the SC and prevents the spin reabsorption by the FM.

1.2.2.2 Spin generation in semiconductors: impedance mismatch

The presence of an interfacial resistance in a ferromagnetic/insulator/semiconductor (FM/I/SC) junction can be accounted for by changing the boundary conditions. It has the effect of breaking the continuity between the electrochemical potentials $\mu_{\uparrow}$ and $\mu_{\downarrow}$:

$$\mu^{\mathrm{FM}}_{\uparrow(\downarrow)}(z=0^{-}) - \mu^{\mathrm{NM}}_{\uparrow(\downarrow)}(z=0^{+}) = eR^{\mathrm{I}}_{\uparrow(\downarrow)}J_{\uparrow(\downarrow)}(z=0) \tag{1.44}$$

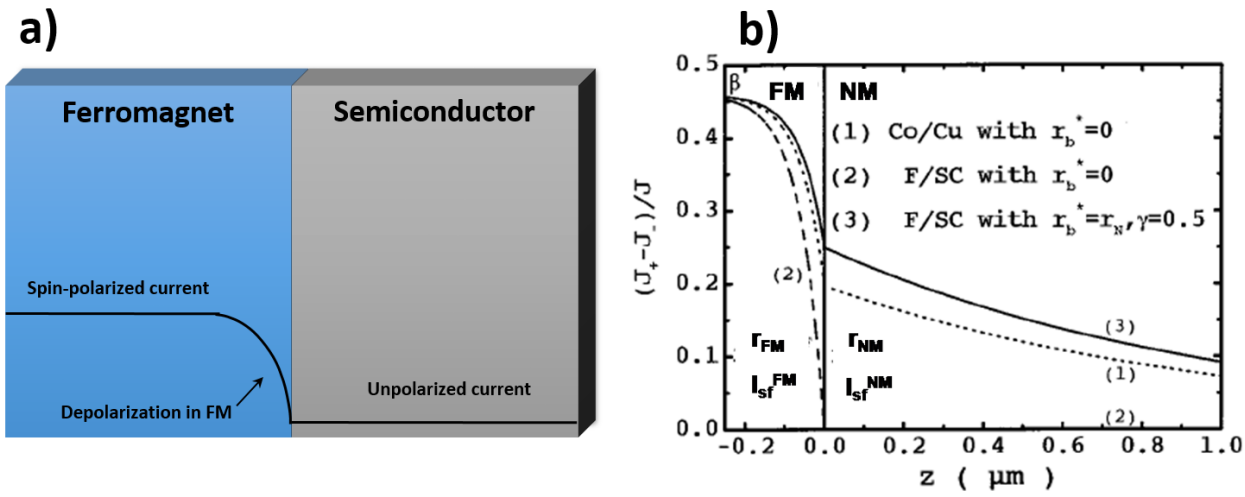

Figure 1.10 – a) Spin polarization of the current as a function of x at the FM/SC interface. b) Spin polarization of the current as a function of x at the FM/NM interface. (1) corresponds to a Co/Cu junctions without interface resistance. (2) corresponds to a FM/SC junction without interface resistance, the spin polarization drops to zero at the interface. (3) corresponds to the same FM/SC junction including a strong interface resistance (i.e. a tunnel barrier). When $R_b^* = R_{\mathrm{NM}} >> R_{\mathrm{FM}}$), the spin polarization at the interface is $\gamma/2$. Extracted from Ref. [26].

where $R^{\mathrm{I}}_{\uparrow(\downarrow)} = 2R_b^2\left[1-(+)\gamma\right]$ with R_b^* connected to the insulating barrier resistance by $R_b^* = R_b/\left(1-\gamma^2\right)$ and γ being the spin asymmetry coefficient. Taking this extra resistance term into account, the spin-polarization can now be written as:

$$SP^{\mathrm{NM}}(x) = \frac{\beta R_{\mathrm{FM}} + \gamma R_b^*}{R_{\mathrm{FM}} + R_{\mathrm{NM}} + R_b^*} \tag{1.45}$$

This expression shows that by inserting a high resistance barrier with $R_b^* > R_{\mathrm{NM}}$, it leads to higher spin-polarization. For $R_b = R_{\mathrm{NM}} >> R_{\mathrm{FM}}$, the spin-polarization SP^{NM} is equal to $\gamma/2$, as illustrated in Fig. 1.10 b). Finally, for $R_b^* >> R_{\mathrm{NM}} > R_{\mathrm{FM}}$, the spin-polarization is maximum and is given by γ, the spin asymmetry of the barrier.

Experimentally, such high resistance barriers are achieved by growing ultra-thin insulating tunnel barriers like Al_2O_3 or MgO by sputtering or molecular beam epitaxy. These theoretical advancements allowed to successfully generate spin accumulations in semiconductors like GaAs, Si and Ge, using magnetic tunnel junctions.

1.2.2.3 Lateral spin valves

The lateral spin valves (LSVs) consist of two ferromagnetic electrodes connected by a transverse non-magnetic channel. These structures played a major role in the study of spin generation, transport and detection in metals and semiconductors during the past fifteen years.

The principle was proposed by Aronov and demonstrated experimentally by Johnson and Silsbee in 1985.[28,29] Few experimental developments have been reported using lateral spin valves until recently. But the non-local detection of a spin accumulation was reported in a variety of systems: in metals,[30,31] superconductors,[32] organic[33] and inorganic III-V semiconductors (GaAs,[34] InAs,[35] ...). A few research groups successfully reported on the spin injection and detection using lateral spin valves in silicon and germanium. For silicon, the first experimental demonstration was done by OMJ Van't Erve in 2007.[36] They were followed by the works of Siraishi *et al.*[37] and Saito *et al.*[38] in 2011. In the case of germanium, early works by Zhou *et al.*[39] reported small signals at low temperature. During the last 10 years, our group subsequently reported the spin injection and detection in both *n*-type[40] and *p*-type[41] Ge (100) using lateral spin valves[42] and three-terminal devices[40,43](see next section).

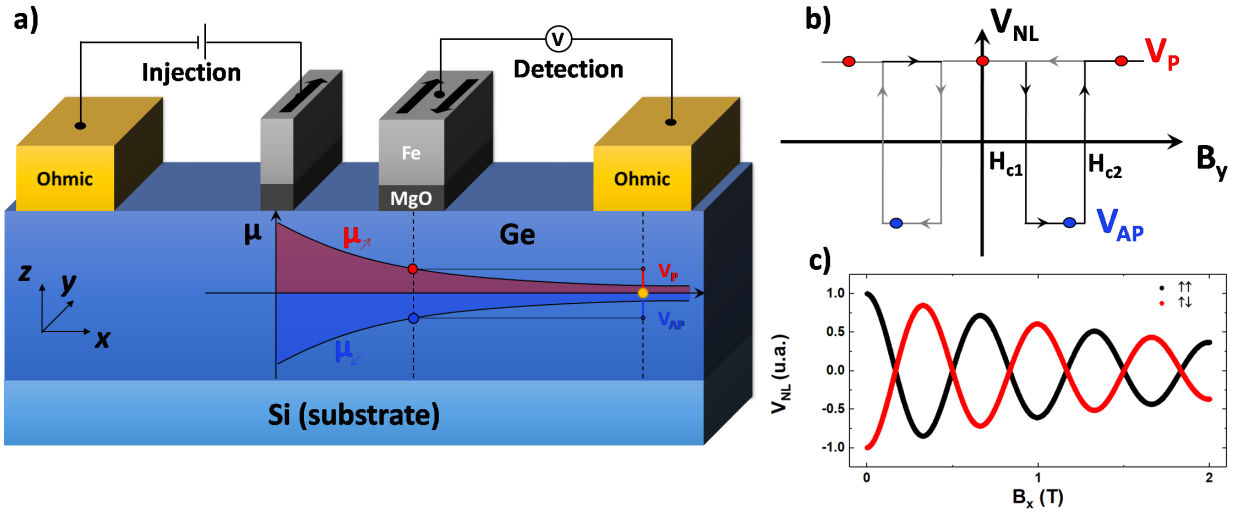

Figure 1.11 – a) Schematics of a lateral spin valve, consisting of two ohmic contacts and two magnetic tunnel junction (MTJ). (b) An external magnetic field is applied along y to set the MTJ magnetization orientations. The magnetization of the injector (left MTJ) sets the spin orientation of the spin accumulation transferred to the SC. The sign of the detected voltage depends on the relative orientation of the detector magnetization (right MTJ) and the spin orientation of the spin accumulation. This results in a characteristic two-crenel pattern as a function of the field. c) Hanle effect in non-local configuration: The injected spins precess under the action of the external magnetic field perpendicular to the MTJ magnetization ($\pm B_x$ here), the second MTJ detects the spin component according to its magnetization ($\pm M_y$ here).

The lateral layout of the two FMs allows non-local measurements, a spin accumulation is

generated by passing a current between the first MTJ and an ohmic contact. The spin accumulation diffuses in the NM channel and reaches the second MTJ as shown in Fig. 1.11 a) below. The difference of electrochemical potential $\Delta\mu = \mu_\uparrow - \mu_\downarrow$ is leads to a voltage drop between the second MTJ and ohmic contact. The separation between the electrical spin injection and detection avoids the detection of spurious magnetoresistance contributions like the local Hall effect or the anisotropic magnetoresistance of the FMs.

Similarly to GMR devices, in a lateral spin valve, we measure the resistance difference between the parallel and antiparallel magnetizations states of the two MTJs. Two different coercive fields are obtained by increasing the shape anisotropy of one electrode (left MTJ in Fig. 1.11 a).

An external magnetic field $B_y > \mu_0 H_{c2}$, the coercive field of the hard layer, is applied along the y direction, initializing the device in a parallel state. Then, an antiparallel state is achieved by sweeping the magnetic field to $-\mu_0 H_{c2} < B_y < -\mu_0 H_{c1}$, reversing the soft electrode. In this configuration, the spin accumulation is unchanged but the detection axis is reversed, therefore the measured voltage changes sign because we probe the opposite spin population or chemical potential. This is designed as blue dots in Fig. 1.11 a) and by the negative voltage V_{AP} in figure Fig. 1.11 b). Then, for larger negative magnetic field ($B_y < -\mu_0 H_{c2}$), the hard layer reverses and the parallel state is measured again corresponding to a measured voltage V_P and red dots in Fig. 1.11. By sweeping the magnetic field in the opposite direction, the same square signal is measured for positive fields. The difference in resistance between the two states depends on the initial spin accumulation and its diffusion in the semiconductor channel. It can be described using a one-dimensional model[44,45]:

$$\Delta R_{\mathrm{NL}} = \pm\frac{1}{2} P_1 P_2 R_s^{\mathrm{SC}} \exp\left(\frac{-x}{\lambda_{\mathrm{SF}}^{\mathrm{SC}}}\right) \tag{1.46}$$

where P_1 and P_2 are the tunneling spin polarizations of the injector and the detector respectively, $R_s^{\mathrm{SC}} = \frac{{\lambda_{\mathrm{SF}}^{\mathrm{SC}}}^2 \rho_{\mathrm{SC}}}{V_s}$ is the SC spin resistance (ρ_{SC} is the SC resistivity and V_s is the effective volume of spin accumulation). x is the distance between the injector and the detector and $\lambda_{\mathrm{SF}}^{\mathrm{SC}}$ the spin diffusion length in the semiconductor. By varying the distance x, one can experimentally extract the spin diffusion length and the product of the tunneling spin polarizations.

In a non-local configuration, the application of a magnetic field perpendicular to the magnetization of the MTJs results in the precession of the spins diffusing in the SC channel. If the diffusion time between the two electrodes is comparable with the spin lifetime of the carriers, the free layer detects the projection of the spin along its own magnetization as shown in Fig. 1.11 a). This measure is called the non-local Hanle effect and allows to extract the important parameters of the spin dynamics in the conduction channel (spin lifetime, spin diffusion length, ...) using a single device. This was the method developed by Johnson and Silsbee in 1985 using the first lateral spin valve measurements in aluminum.[28] The measured spin signal is a succession of oscillations as a function of the angle between the free layer

magnetization and the direction of the spin accumulated underneath. The precession angle ϕ depends on the applied magnetic field as: $\phi = \omega_L t$ where t is the electron transit time between the two MTJs and ω_L is the Larmor precession frequency directly proportional to the external magnetic field.

In the case of a very long spin lifetime, several oscillations can be detected as shown in Fig. 1.11 c). Experimentally, this type of oscillations has already been observed in intrinsic silicon.[46] The non-local Hanle effect can be formalized using the spin drift-diffusion model, detailed by Fabian *et al.* in Ref. [47]. Considering a one-dimensional system, the oscillating signal due to the precession can be fitted by the following equation:

$$\Delta R_{NL} = \frac{\Delta V_{NL}(B_\perp)}{I} = \pm \frac{P_1 P_2}{e^2 N(E_F) A} \int_0^\infty P_r(t) \cos(\omega_L t) \exp\left(\frac{-t}{\tau_{SF}^{SC}}\right) dt \tag{1.47}$$

where $P_r(t)$ corresponds to the temporal distribution of the detected spins considering a diffusive regime, it is given by:

$$P_r(t) = \frac{1}{\sqrt{4\pi D t}} \exp\left(\frac{-L}{4Dt}\right) \exp\left(\frac{-t}{\tau_{SF}^{SC}}\right) \tag{1.48}$$

where $N(E_F)$ is the carrier density at the Fermi level, A is the semiconductor channel cross-section and τ_{SF} is the spin lifetime. For the time distribution $P_r(t)$, we define: D the diffusion coefficient, L the distance between the MTJs. In the definition of ΔR_{NL}, the exponential decay is due to spin-flip events.

1.2.2.4 Three terminal devices

The generation of spin accumulation in a semiconductor using magnetic tunnel junctions is very difficult and lateral spin valves are costly devices as they necessitate five to six e-beam lithography steps (see sect. [5.2.1.2]). The need to find a simpler model system to study spin generation and detection in semiconductors has motivated the community to imagine alternative geometries. In 2007, the group of Paul Crowell demonstrated that devices consisting of only three-terminals could be used to detect a spin accumulations in GaAs.[34] Since then, many materials have been studied using this technique, however, metals are not good candidates for this measurement configuration since it is based on the Hanle effect which is difficult to measure as a result of the short spin lifetime of metals. This technique is also not suitable for materials with too long spin lifetime since it requires very weak magnetic fields below our experimental level of control to detect the Hanle effect. The figure Fig. 1.12 a) shows the geometry of the three-terminals devices where a single ferromagnetic electrode is used for spin injection and detection. A current flows between the ferromagnetic electrode and a first ohmic contact, which creates a spin accumulation below this electrode.

Again, the Hanle effect is measured to quantify the spin accumulation. A magnetic field is applied perpendicularly to the MTJ magnetization (i.e. the direction of the accumulated spins) in order to make them precess. The principle is shown schematically in Fig. 1.12

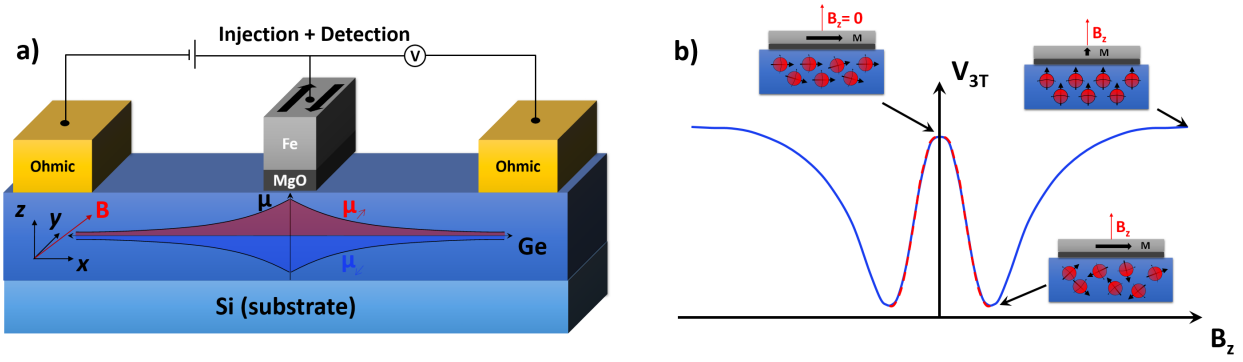

Figure 1.12 – (a) Schematic representation of a three-terminal device. b) The magnetization of the MTJ is set along the y direction by shape anisotropy, the current flows between the MTJ and the left ohmic contact, generating a spin accumulation with a spin orientation along y. The application of a transverse magnetic field causes the precession of the spins.

b). A current is passed between the MTJ and a first ohmic contact while, the spin signal is measured by recording the voltage drop between the MTJ and a second ohmic contact. By well separating the injection and detection paths, we minimize the contributions from spin-independent phenomena to the measured signal. At zero magnetic field, the spin signal is maximum since the spin accumulation orientation is parallel to the MTJ magnetization. For an intermediate magnetic field, the spin depolarization due to incoherent spin precession suppresses the spin accumulation and the spin signal drops close to zero. This decay can be fitted using a Lorentzian curve which FWHM is inversely proportional to the spin lifetime in the material[48,49] (red dashed line in Fig. 1.12 b)). The amplitude is proportional to the spin accumulation and can be written as:

$$\Delta V_{3\mathrm{T}} = \frac{\Delta V_{3\mathrm{T}}^{0}}{1 + \left(\omega_{\mathrm{L}} \tau_{\mathrm{SF}}^{\mathrm{SC}}\right)^{2}} \tag{1.49}$$

When the applied field is comparable to the out-of-plane saturation field of the ferromagnetic layer, the MTJ magnetization aligns with the external magnetic field, and a parallel state is recovered, resulting in a large spin signal.

1.2.3 Optical spin generation and detection

In the previous paragraph, we have shown that all-electrical spin injection/detection using MTJs is very difficult to achieve. An alternative method consists in taking advantage of the semiconductor optical properties. Indeed, in direct gap semiconductors, the absorption of circularly-polarized light results in a direct transfer of angular momentum from the photon to the electron-hole pair following sum rules. Using this phenomenon, one can set the spin orientation of photogenerated carriers and generate spin accumulations. Several techniques can then be used to detect the out-of-equilibrium spin accumulation: photoluminescence,[50] electroluminescence (spin-LED)[51] or magneto-optical Kerr microscopy.[52]

1.2.3.1 Magneto-optical Kerr effect detection in a lateral spin valve

In 2005, Crooker *et al.*[52] directly imaged the electrical spin accumulation in a GaAs-based lateral spin valve. Here, the spin injection is achieved using Fe/GaAs Schottky contacts (see Fig. 1.13 a)). The electrical current flows from one ferromagnetic contact to the other, and scanning Kerr microscopy is performed to image the resulting spin accumulation in the 300 µm-long GaAs channel.

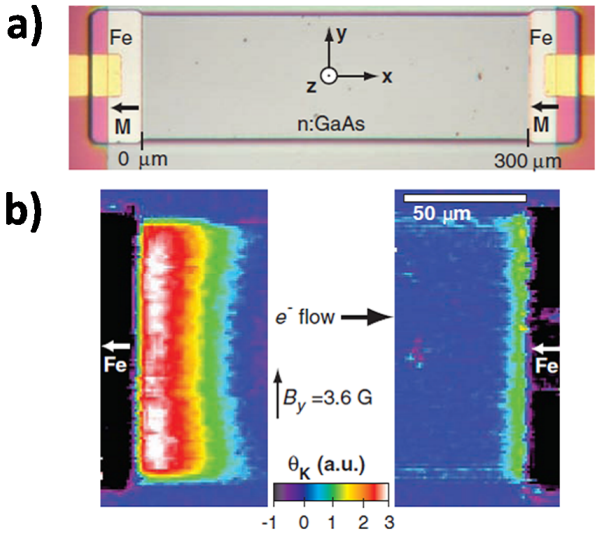

Figure 1.13 – a) Photo-micrograph of the lateral spin injection/detection device. Spins are electrically injected from the Fe electrode into the GaAs channel. b) Two-dimensional map of the perpendicular component of spin accumulation in the GaAs channel recorded using scanning Kerr microscopy.

The Fe magnetization is saturated in the sample plane, leading to the injection of a spin accumulation with an in-plane orientation. However, they optically detect the perpendicular spin component by polar Kerr effect. This out-of-plane component is obtained by applying a transverse magnetic field B_y, resulting in the precession of the spin (see Fig. 1.13 b)).

The injected spins are accumulated close to the injector contact and the spin accumulation decays with the distance due to spin relaxation in GaAs. We note that the Kerr signal corresponding to spin accumulation close to the right Fe electrode is less pronounced, this is explained by the asymmetry of the Schottky contact and the spin-selective extraction of electrons.

1.2.3.2 Optical spin orientation

A powerful alternative to the use of electrical ferromagnetic contacts to generate spin accumulations in semiconductors is the the optical spin orientation process. In chapter 3, I apply this technique to generate pure spin currents in germanium, to study spin-to-charge conversion phenomenon in a topological insulator (Bi_2Se_3) epitaxially grown on top by molecular beam epitaxy.

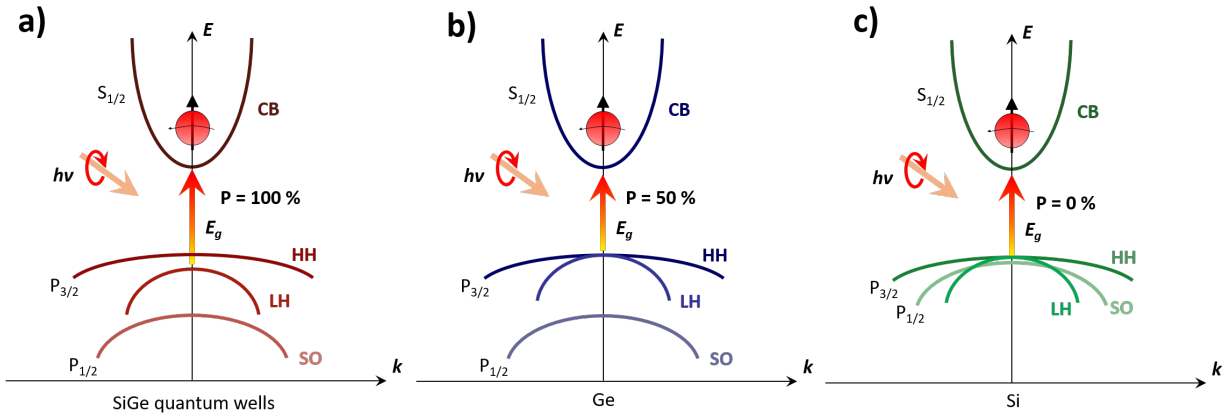

Figure 1.14 – Schematic band structure of a direct bandgap semiconductor illustrating the optical spin orientation process when circularly-polarized light is absorbed. a) Considering a SiGe quantum well where the confinement lift the LH-HH degeneracy, leading to a 100% spin polarization. b) Considering Ge, where the LH and HH bands are degenerated but the spin-orbit band is split-off leading to a 50% spin polarization. c) Considering the case of Si where the three bands are degenerated, leading to spin polarizations close to 0%.

The optical spin orientation relies on the dipole selection rules for optical transitions with circularly polarized light as shown in Fig. 1.14. It allows the excitation of an electron population in the Ge conduction band with a spin polarization P that can theoretically reach 50 %.[53] P is defined as:

$$P = \frac{n_\uparrow - n_\downarrow}{n_\uparrow + n_\downarrow} \tag{1.50}$$

where $n_{\uparrow(\downarrow)}$ are the up (down) photogenerated spin densities with respect to the quantization axis. This technique exploits the spin-orbit interaction, which allows the induction of a net spin polarization by the absorption of circularly polarized light. The spin-orbit interaction removes the energy degeneracy between heavy hole (HH) and light hole (LH) states and

split-off (SO) states of the valence band at the Γ point of the Ge Brillouin zone: a net electron spin polarization is obtained when the photon energy reaches the direct bandgap E_d (in Ge $\approx$ 0.8 eV at room temperature) and electrons coming only from HH and LH states are promoted to the conduction band. In Ge, the splitting ΔE_{SO} between the HH/LH bands and the SO band is rather large ($\Delta E_{SO} \approx 300$ meV), which is much larger than in Si, ($\Delta E_{SO} \approx 40$ meV) (see Fig. 1.14). This explains why only very small polarization values are achieved in Si.[54] In contrast, the spin-polarization obtained in Ge is comparable to that obtained in the direct-gap III-V semiconductors.[55,56]

The spin-oriented electrons excited at the bottom of the Ge conduction band at the Γ point are scattered to the L minima of the CB within $\sim$ 300 fs, partially maintaining the initial spin orientation.[50] As the hole spin lifetime is much shorter than the one of electrons(a few hundreds of femtoseconds[57]), the spin currents resulting from the diffusion of the optically generated spin accumulation consists of electrons. The spin orientation is set by the quantization axis given by the direction of the light wave vector in the absorbing material. Although optical orientation allows the generation of much higher spin polarizations in semiconductors compared to electrical spin injection with tunnel junctions, only an out-of-plane spin polarization is achieved at normal incidence. It limits the integration of spin-readout blocks, such as magnetic tunnel junctions, to those with out-of-plane magnetization.[58] Illumination at grazing incidence can comply with in-plane magnetization devices,[59] although it does not represent a convenient geometry for optical orientation. In chapter 3, I will show that we can use micro-fabrication to circumvent this issue.

Room temperature manipulation of the spin orientation with an electric field has not been demonstrated yet as the spin-orbit interaction in conventional semiconductors is rather small. In this thesis, I will attempt to enhance and control the SOI by growing ultra-thin films with large SOI on Ge. After an introduction of the main concepts of spintronics and a short review of the well established field of semiconductor spintronics, I now introduce a more emerging field that is entirely based on the spin-orbit coupling: the spin-orbitronics.

1.3 Spin-orbitronics: heavy metals, Rashba interfaces and topological insulators

At this point, we have seen that the generation and detection of spin-polarized carriers could be achieved by harnessing the exchange interaction in ferromagnetic materials. However, since fifteen years, the spin–orbit interaction (SOI) has been shown to be a very efficient mechanism to complete both operations . In 1971, Dyakonov and Perel theoretically proposed a mechanism to convert a charge current into a spin current: the spin Hall effect.[60] Much later, in 2004, the first experimental observation was reported, demonstrating the existence of the effect. By harnessing the spin-orbit coupling, it is indeed possible to obtain spin-charge current interconversion through two effects known as the spin Hall effect (SHE) in bulk materials and the Rashba-Edelstein Effect (REE) at surfaces and interfaces.[61] In both cases, thanks to the spin-orbit coupling, a charge current produces a transverse spin density, which can diffuse as a spin current in an adjacent material. The obtained spin current is transverse to the charge current and carries no charge current, which is why it is usually called a pure spin current. Conversely, it is possible to detect a charge current using the inverse mechanisms, known as the Inverse Spin Hall and Inverse Edelstein Effects (ISHE and IREE). Both the (I)SHE and (I)REE can be used as a source of spin accumulation and spin current, and as a spin current detector.

The spin currents originating from the SHE and EE have been eventually found to be large enough to allow magnetization switching in heavy-metal/FM bilayers.[62] This effect is known as the spin-orbit torque (SOT), corresponding to a torque on the magnetization originating from the spin-orbit interaction. After the demonstration of current-induced magnetization reversal, the efforts have shifted towards the optimization of these SOTs, with experiments such as current-induced magnetization switching,[63] current-induced domain walls motion[64] and skyrmions motion.[65]

1.3.1 Spin-orbit coupling

The easiest way to manipulate the spin of an electron is to use a magnetic field. It will create a magnetic torque $\mathbf{\Gamma}$ which will cause the spin to precess, this is the Larmor precession mechanism:

$$\mathbf{\Gamma} = \gamma \mathbf{S} \times \mathbf{B} \tag{1.51}$$

where γ is the gyromagnetic ratio, $\mathbf{S}$ is the spin angular momentum and $\mathbf{B}$ is the external magnetic field. This method is easy to set up, but cannot be integrated on a large scale in the framework of microelectronics. In this thesis, we will attempt to manipulate the spins with an electric field using the spin-orbit coupling. The spin-orbit interaction is a relativistic effect, a carrier moving in an electric field $\mathbf{E} = -\nabla V(\mathbf{r})$ will experience an effective magnetic field acting on the spin as a consequence of the Lorentz transformation of special relativity ($V(\mathbf{r})$ being a spherical potential resulting from the electrons orbiting the atoms nucleus). This effective field can be written as:

$$\mathbf{B}_{\text{eff}} = -\frac{\mathbf{v} \times \mathbf{E}}{c^2} \tag{1.52}$$

where $\mathbf{v}$ is the carrier speed, c is the speed of light and $\mathbf{E}$ is the electric field resulting from the Coulomb attraction of the positively charged nucleus. The effective magnetic field $\mathbf{B}_{\text{eff}}$ interacts with the spin of the carrier, resulting in an energy term $\pm g m u_{\text{B}} B_{\text{eff}}$, $\mu_{\text{B}} = \frac{e\hbar}{2m}$ being the Bohr magneton and g the Landé factor ($g = 2$ for the electron).
We can then consider the general form for the spin-orbit interaction:

$$\mathscr{H} = \mathscr{H}_{\text{SOC}} + \mathscr{H}_{\text{SE}} = -\frac{e\hbar}{4m^2c^2}\sigma \cdot [\nabla V(\mathbf{r}) \times \mathbf{p}] + \frac{e\hbar}{4m^2c^2}\sigma \cdot [\nabla V(\mathbf{r}) \times e\mathbf{A}] \tag{1.53}$$

where $\mathscr{H}_{\text{SOC}}$ (resp. $\mathscr{H}_{\text{SE}}$) represents the coupling between the electron spin and the particle orbital momentum (resp. the external electric field).
In the case of an isolated atom,

$$\mathscr{H}_{\text{SOC}} = \frac{\hbar}{4m^2c^2}\frac{1}{r}\frac{\mathrm{d}V}{\mathrm{d}r}\sigma \cdot [\mathbf{r} \times \mathbf{p}] = \frac{1}{2m^2c^2}\frac{1}{r}\frac{\mathrm{d}V}{\mathrm{d}r}\mathbf{S} \cdot \mathbf{L} = \lambda_{\text{SO}}\mathbf{S} \cdot \mathbf{L} \tag{1.54}$$

where $\mathbf{L} = \mathbf{r} \times \mathbf{p}$ is the orbital momentum, λ_{SO} is the spin-orbit coupling constant that depends on the atomic number Z. In the hydrogenoic picture, it scales with Z^4, a more realistic model taking in account the screening of the core electrons results in $\lambda_{\text{SO}} \propto Z^2$. In both cases, a strong spin-orbit interaction is expected for heavy metals like W ($Z = 74$), Pt ($Z = 78$) or Bi ($Z = 83$).

1.3.2 The spin Hall effect

This interaction between the spin orientation and its momentum leads to the spin-charge interconversion phenomena: flowing a charge current in a material with significant spin-orbit coupling will result in a spatial separation of the two spin orientations: it generates a transverse pure spin current.

1.3.2.1 General picture

The name of Spin Hall effect was introduced by Hirsch in 1999,[66] by analogy to the ordinary Hall Effect. The direct spin Hall Effect was later measured in 2004 in the semiconductor GaAs by Kerr effect microscopy,[67] and was detected in metals only in 2006 in Aluminum[68] and Platinum.[69] Since its detection at room temperature and its possible applications in electronics, it has attracted a large interest. During the last decade, a large number of materials showing large spin Hall effect including heavy metals,[70] alloys,[71] and semiconductors[41] were discovered.

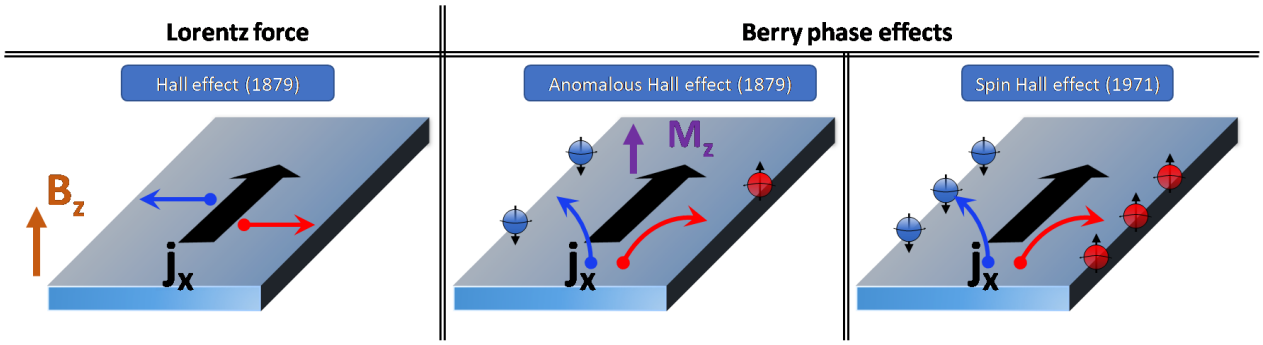

Figure 1.15 – a) Schematic representation of the different Hall effects: a) Ordinary Hall Effect, b) Anomalous Hall Effect and c) Spin Hall Effect.

While in the ordinary Hall effect, an accumulation of charge is obtained transverse to the electric and the magnetic field, that breaks the time reversal symmetry. In the spin Hall effect, an accumulation of spins is obtained in a non-magnetic material in absence of magnetic field, preserving the time reversal symmetry. The ordinary Hall effect is due to the deflection of carriers moving along an electric field by an external magnetic field (Fig. 1.15 a)). This effect is well known to be caused by the Lorentz force, and leads to a charge accumulation resulting in a Hall voltage. But there is no net spin accumulation because the number of spin up and down is the same. The anomalous Hall effect is the result of spin-dependent deflection of carriers in a ferromagnetic material, which produces both a spin accumulation at the edges and a Hall voltage[72] (Fig. 1.15 b)). The spin Hall effect is also caused by the spin-dependent deflection of carriers. As the number of deflected spin up and down is the same, it produces no Hall voltage but gives rise to a spin accumulation (Fig. 1.15 a)).[73] In two dimensions, the Ohm's law can be given as:

$$\mathbf{E} = \begin{bmatrix} \rho_{xx} & \rho_{xy} \\ \rho_{yx} & \rho_{yy} \end{bmatrix} \mathbf{J} \tag{1.55}$$

All these mechanisms are associated with a non zero off-diagonal term of the resistivity tensor: ρ_{xy}. The spin-to-charge conversion efficiency, i.e. the figure of merit of a (I)SHE material is dimensionless and called the spin Hall Angle θ_{SHE}. It can be interpreted as the angle of deflection of the electrons with respect to the applied current direction. The charge and spin currents are connected by the following vectorial expression:

$$\mathbf{J_c} = \theta_{\mathrm{SHE}} \mathbf{J_s} \times \hat{\sigma} \tag{1.56}$$

where $\hat{\sigma}$ is the spin polarization unit vector. The spin Hall angle can thus be defined as the off-diagonal term of the resistivity tensor, the spin Hall resistivity, $\rho_{xy} = \rho_{\mathrm{SHE}}$, divided by the diagonal one ρ_{xx}:

$$\theta_{\mathrm{SHE}} = \frac{\rho_{\mathrm{SHE}}}{\rho_{xx}} \tag{1.57}$$

As this value is intimately related to the spin orbit interaction, high charge-to-spin conversion efficiency is expected to occur in heavy metal such as Pt,[69] Ta[63] or W,[74] and alloys containing heavy metals impurities such as CuBi[71] or AuW.[75] Similarly to the case of AHE, the SHE has two different contributions, an intrinsic and an extrinsic one. The intrinsic contribution is related to the anomalous velocity of the carriers (Berry phase), and the extrinsic contribution is related to skew or side-jump scattering on impurities in presence of spin orbit coupling. I will not give additional details on these three mechanisms but one can refer to this exhaustive review paper: [73].

1.3.2.2 Observation by magneto-optical Kerr microscopy

The first direct observation of the spin Hall effect was reported in 2004 by Kato *et al.* in Ref. [67]. A DC current is applied in a GaAs channel along the x direction, the spins $\uparrow$ ($\downarrow$) are deflected in opposite directions ($\pm y$), resulting in an accumulation of spins oriented perpendicularly to the sample plane ($\pm z$). The spin diffusion length in GaAs is large enough so the accumulation can be spatially resolved using a visible light wavelength.
The Fig. 1.16 a) shows the GaAs channel reflectivity and the corresponding polar Kerr rotation is shown in Fig. 1.16 b). In this configuration, the light polarization is sensitive to the out-of-plane component of the spins. Indeed, we can see that opposite Kerr rotations hence local magnetic moments are found at opposite channel edges, as predicted for the spin Hall effect.
Although the observation is direct, quantifying the spin Hall angle from Kerr measurements is not straightforward. In any case, this pioneer work paved the way for future spin Hall effect detection and quantification methods.

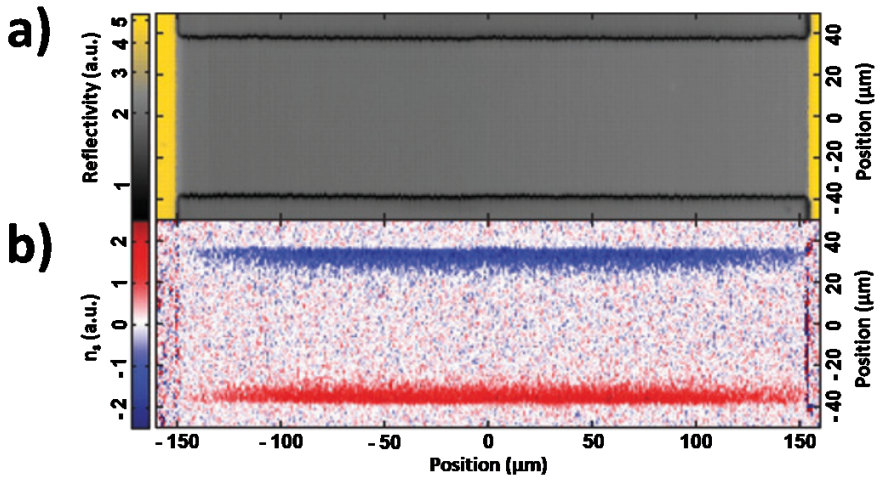

Figure 1.16 – Two-dimensional maps of the GaAs channel a) reflectivity and b) Polar Kerr signal. Adapted from Ref. [67]

1.3.2.3 All electrical detection in lateral spin valves

In 2006, S. Valenzuela reported a second technique based on a metallic lateral spin valve to quantify the direct and inverse spin Hall effect in Al.[68] Here, we present a similar work developed soon after by Y. Otani's group to investigate the (I)SHE in Pt.[76] As shown in Fig. 1.17 a), a ferromagnetic electrode (Py) is used to generate a pure spin current in a non-magnetic channel (Cu). The channel length being shorter than the spin diffusion length in Cu, the spin current reaches the SHE electrode (Pt). The Py magnetization is first set along the y direction by shape anisotropy, then, an external magnetic field along x is applied to progressively align the magnetization along x. In this geometry the inverse spin Hall effect gives rise to a charge current along the y direction, which is detected as a voltage. The spin signal saturates when the Py magnetization is saturated, as indicated by the anisotropic magnetoresistance measurement in Fig. 1.17 b).
Further measurements with these devices were performed with or without Pt, allowing for a precise quantification of the spin diffusion length, spin mixing conductance and the spin Hall angle.

1.3.2.4 Dynamical spin generation: ferromagnetic resonance-spin pumping

A third technique that is widely used to detect and estimate the spin-to-charge conversion efficiency is the ferromagnetic resonance-spin pumping (FMR-SP). This technique is popular because it is simple to implement and does not require nanofabrication. A thin ferromagnetic layer is deposited on the material of interest. Typical systems are ferromagnetic metal/heavy metal bilayers (FM/HM) such as NiFe/Pt or NiFe/W. The bilayer is placed in a microwave cavity immersed in a static magnetic field. At a specific applied magnetic field, the absorption of a radiofrequency wave results in the resonant precession of the FM layer magnetization,

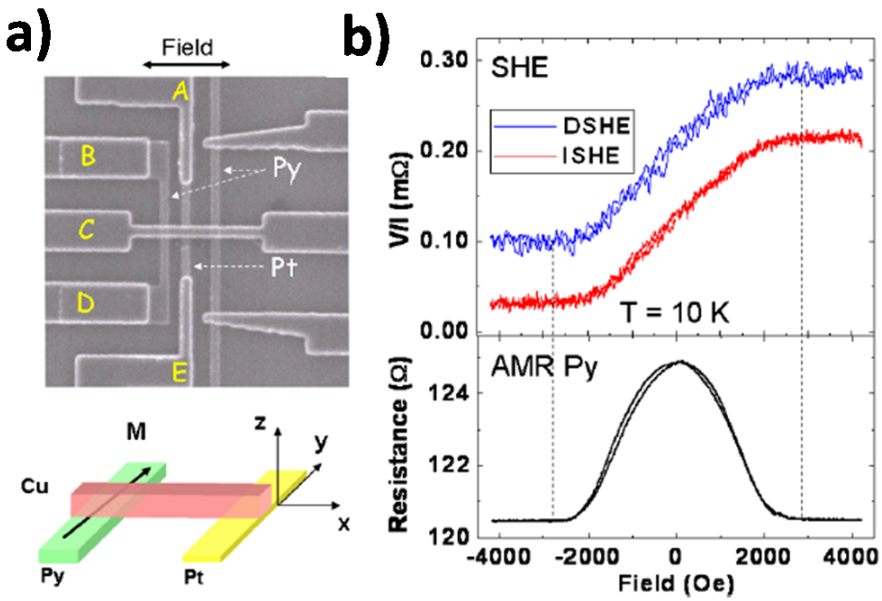

Figure 1.17 – a) SEM image of the typical device for SHE measurements and an illustration of the device. (b) Direct and inverse SHE (SHE and ISHE) recorded at $T = 10$ K using a device with a Pt thickness of 20 nm, altogether with the AMR from the Py wire measured in the same conditions. The SHE measurement corresponds to V_{BC}/I_{AE} and ISHE to V_{EA}/I_{BC}; A, B, C, and E are the contact leads as denoted in the SEM image. Extracted from Ref. [76]

leading to the release of angular momentum towards the HM: equivalent to a spin current from the FM to the HM. Based on spin-dependent diffusive transport, Tserkovniak *et al.* predicted theoretically the spin pumping effect and,[77] it was later observed experimentally by Saitoh *et al.*[69]

Fig. 1.18 a) shows the spin pumping measurement geometry: the sample is centered in a TE_{011} microwave cavity so that the radiofrequency (RF) magnetic field is maximum while the electric field is minimum. During the experiment, the sample is illuminated with microwaves at $f = 9.45$ GHz in the cavity and an external in-plane magnetic field H_{DC} is swept in order to reach the FMR of the FM film. H_{DC} is applied along y and at the resonance, a net angular momentum (i.e. a spin current) is transferred along the z direction to Ge. This three-dimensional spin current $\mathbf{J}_{\mathrm{s}}$ along z is then converted into a DC charge current $\mathbf{J}_{\mathrm{c}}$, recorded as a voltage in open circuit conditions using a nanovoltmeter. The charge current intensity is obtained by dividing this spin pumping voltage by the sample resistance between the two-probe contacts, it is further normalized by the RF field amplitude squared so to be expressed in $m\mathrm{A.G}^2$.

As shown in Fig. 1.18 b), the FMR linewidth broadening of the NiFe/Pt sample as compared to the reference NiFe film demonstrates the presence of the SP effect (i.e. spin diffusion and absorption by the HM layer). Indeed, the absorption of angular momentum by the HM layer increases the magnetic damping of the FM precession. The induced SP voltage measured simultaneously across the sample is shown in Fig. 1.18 c), it demonstrates that the signal is

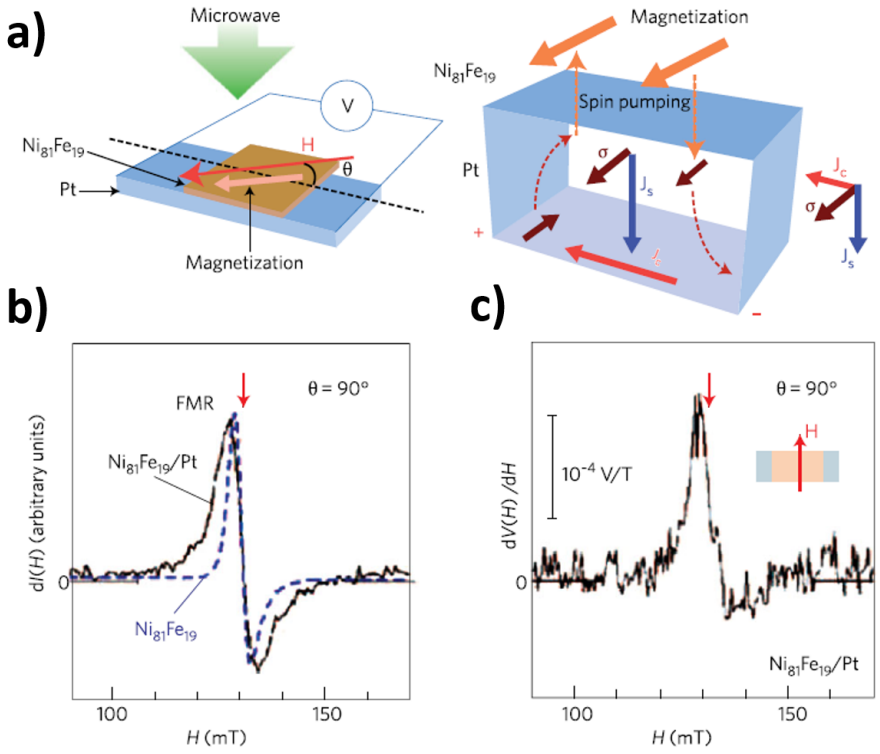

Figure 1.18 – Example of FMR-spin pumping measurements. Extracted from Ref. [69]

present only when the spin-polarization vector of the injected spin current has a component perpendicular to the measured electric field across the sample, which is consistent with the ISHE picture.

The spin current intensity J_s can be determined using a complementary technique: called broadband FMR. Here, the microwave excitation frequency is varied in order to measure the magnetization damping factor in both the FM/HM bilayer and a reference sample without the HM.[78] The measured extra damping allows to extract the value of J_s. By normalizing J_c by J_s, we can extract the conversion efficiency i.e. the spin Hall angle.

This type of experiment is not free from spurious effects such as thermal effects and rectification effects can be measured. However, advanced modeling and the analysis of symmetries allow to identify and remove these effects.

1.3.2.5 Spin Hall magnetoresistances

Magnetotransport experiments in similar heavy metal/ferromagnetic metal bilayers (HM/FM) have shown that the spin Hall effect also gives rise to novel magnetoresistance (MR) effects. The so-called spin Hall MR arises from the interplay between the SHE in the HM and the spin absorption/reflection at the HM/FM interface. It can be understood as the combined action of the direct and inverse SHE in the HM. The spin current generated by the direct SHE is partially reflected at the HM/FM interface when the magnetization is parallel to

the spin direction and converted into a charge current by the inverse SHE, resulting in a resistance term proportional to the square of the spin Hall angle (θ^2_{SHE}). This effect was first found in insulating FM/HM bilayers[79–84] and the first theoretical development was reported by Chen, Matsukura, and Ohno (2013). The theoretical approach still relies on the the spin drift-diffusion and the Boltzmann scattering formalism.

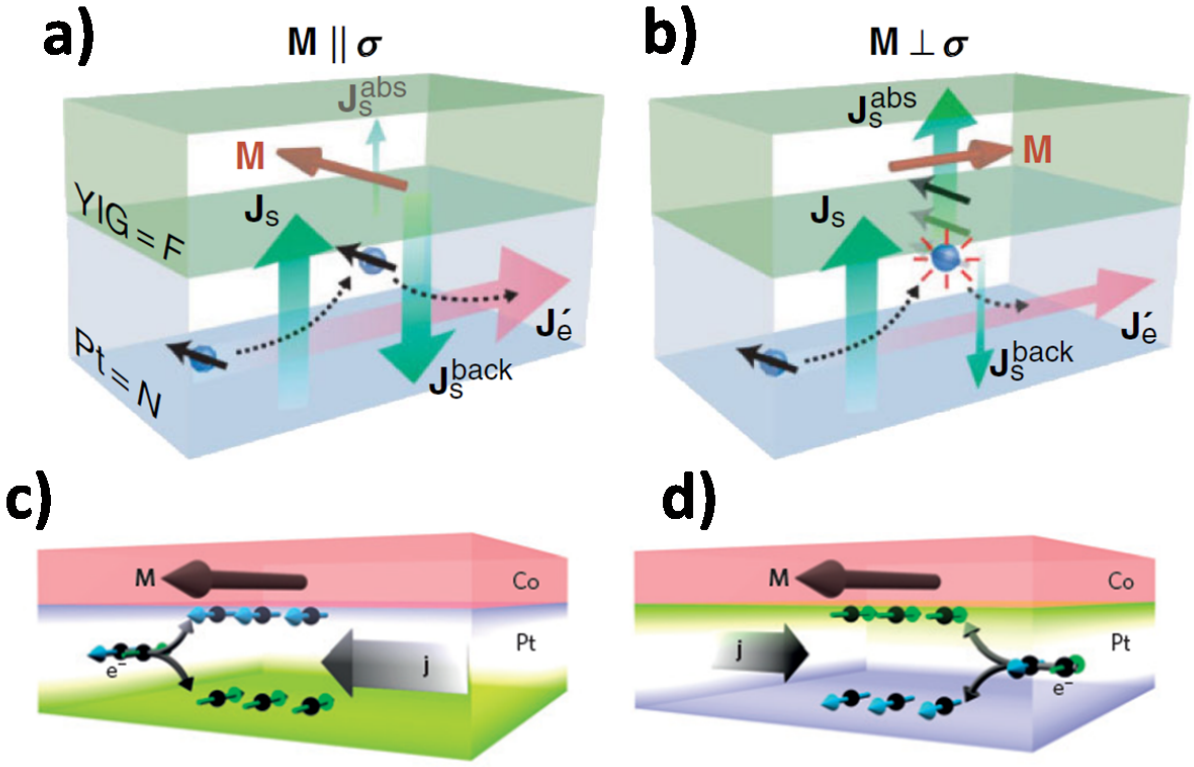

Figure 1.19 – a-b) Illustration of the spin hall magnetoresistance in YIG/Pt. c-d) Illustration of the spin hall magnetoresistance in Co/Pt.

More recently, in HM/FM metallic bilayers, a current-dependent magnetoresistance term was reported and identified as a consequence of the SHE. In systems like Pt/Co or W/Co, a spin accumulation is induced by the SHE in the HM and the spin-dependent scattering process occuring at the HM/FM interface results in a magnetoresistance effect called the unidirectional spin Hall magnetoresistance (USMR). The resistance of the system depends on the relative orientation and magnitude of the spin accumulation and the magnetization, so that the resistance term linearly scales with the applied current, magnetization and the HM spin Hall angle θ_{SHE}.[85–88] This type of unidirectional MRs will be the focus of chapter 4.

1.3.2.6 Spin-orbit torque magnetization switching

Together, these experiments led to a global understanding of the effects induced by the spin-orbit coupling. In 2011, it was shown that the spin current generated by the spin Hall effect could be exploited to manipulate the magnetization orientation of thin ferromagnetic films.[62] This effect was called the spin-orbit torque by analogy with the spin transfer torque (STT) discovered fifteen years before. In STT devices, the exchange interaction was the mechanism at the origin of the spin polarization of the electrons, here it has been replaced by the spin-orbit interaction. One of the main advantages is that the current is no longer applied through the tunnel junction to reverse the magnetization, but in the film plane, simplifying the device fabrication and increasing the magnetic tunnel junction cyclability.

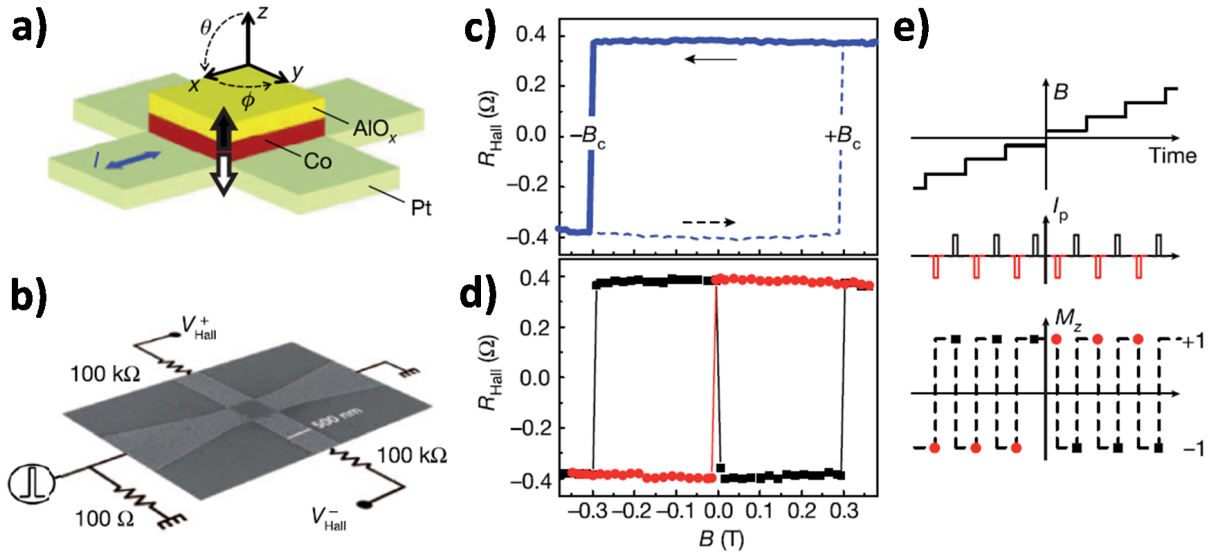

Figure 1.20 – a) Schematics of the device and current-induced switching in a Hall-cross geometry. Black and white arrows indicate the up and down equilibrium magnetization states of the Co layer, respectively. b) Scanning electron micrograph of the sample and electrical circuit used in the measurements. c) Low-current reference hysteresis loop of the Co magnetization given by the anomalous Hall resistance. The magnetic field is applied mostly in-plane ($\theta = 88°$), this controlled tilt of the magnetic field allows for deterministic switching thanks to the small out-of-plane component. d) Anomalous Hall resistance recorded after injection of positive (black squares) and negative (red circles) current pulses. The data are reported during a single sweep of B. e) Summary of the measurement procedure and pulse sequence.

The pioneer work by Miron *et al.* in Ref. [62] is summarized in Fig. 1.20. The use of ultra-thin Co films in contact with Pt leads to a strong perpendicular magnetic anisotropy. In this experiment, a current pulse is applied in the Pt layer and the transverse voltage resulting from the anomalous Hall effect is measured. The magnetic field is parallel to the current direction ($\phi = 0°$) and is tilted at a polar angle $\theta = 92°$. The 2° offset with respect to the in-plane direction is used to define the residual component B_z unambiguously. The magnetization of

the Co layer is first measured using a low current to record the anomalous Hall resistance as a function of the magnetic field (Fig. 1.20 c)). Then a single magnetic field sweep is performed, at each value of B, a large positive current pulse is injected in the Pt film followed by a large negative current pulse, the magnetization M_z is measured after each pulses. A deterministic switching of the Co magnetization is observed (Fig. 1.20 d)).

This short review introduced the spin-charge interconversion by means of the direct and inverse spin Hall effects. Here, a three-dimensional charge current is converted into a transverse three-dimensional spin current and vice-versa. As these effects are connected to the presence of high spin-orbit coupling, it was predicted that surfaces and interfaces, where the crystal or structural inversion symmetry is broken and the spin-orbit interaction is large, could lead to an increase in conversion efficiency. I now focus on this class of materials owning two-dimensional spin-polarized states.

1.3.3 Rashba interfaces and topological insulators

In this section, I will introduce an emerging approach to manipulate the spins by harnessing the spin-orbit interaction using two-dimensional spin textures.

1.3.3.1 Rashba interfaces

In 1984, Bychkov and Rashba introduced a simple form of spin–orbit coupling to explain the electron spin resonance in two-dimensional semiconductors.[89]
In the bulk of a crystal with bulk inversion symmetry, free electrons are moving in a periodic lattice with both inversion symmetry $E(\uparrow, \mathbf{k}) = E(\uparrow, -\mathbf{k})$ and time reversal symmetry $E(\uparrow, \mathbf{k}) = E(\downarrow, -\mathbf{k})$. This thus leads to the spin degeneracy $E(\uparrow, \mathbf{k}) = E(\downarrow, \mathbf{k})$, where $\uparrow$ ($\downarrow$) are the spin up (down) and $\mathbf{k}$ is the electron Bloch-wavevector. In that case, the dispersion curve of free electrons is degenerate in spin. However, when the inversion symmetry is broken either at a surface or an interface, the electrons experience an electric field $\mathbf{E}$ perpendicular to the surface that creates an effective in-plane magnetic field $\mathbf{B}_{\text{eff}}$, lifting the spin degeneracy. The so-called Rashba effect can be modeled by the following Hamiltonian:

$$\mathscr{H}_{\text{Rashba}} = \alpha_{\text{R}} \left(\sigma \times \mathbf{p}\right) \cdot \mathbf{z} \tag{1.58}$$

where α_{R} is the Rashba coefficient, $\mathbf{p}$ is the electron momentum and σ is the Pauli matrix. For a given momentum $\mathbf{p}$, the Rashba effect lifts the spin degeneracy.
From the eigenvalues of this Hamiltonian, we obtain the energy dispersion for spin up and down:

$$E_{\uparrow(\downarrow)} = \frac{\hbar^2 k^2}{2m^*} + (-)\alpha_{\text{R}} k \tag{1.59}$$

The resulting typical spin-splitted parabolic band structure is schematically shown in Fig. 1.21 a) and was experimentally observed using angle resolved photoemission spectroscopy at the Au (111) surface[90] and Bi/Ag (111) interface[91] (see Fig. 1.21 b)). A rather large splitting of the bands is obtained ($\sim$ 250 meV) as a consequence of the large spin-orbit coupling of Bi atoms and the enhanced electric field at the interface. More importantly, one can note that the Rashba Hamiltonian is maximum when the spin orientation, the Bloch wavector and the surface normal are perpendicular. This leads the spin to lie in the plane perpendicular to $\mathbf{k}$; an effect known as the spin-momentum locking.

1.3.3.2 Topological insulators

Introduction

In this section, I give a short introduction of the physics of topological insulators. In particular, specific broken symmetries give rise to different states of matter characterized by new physical effects that can be experimentally measured. Since 1980 and the discovery of

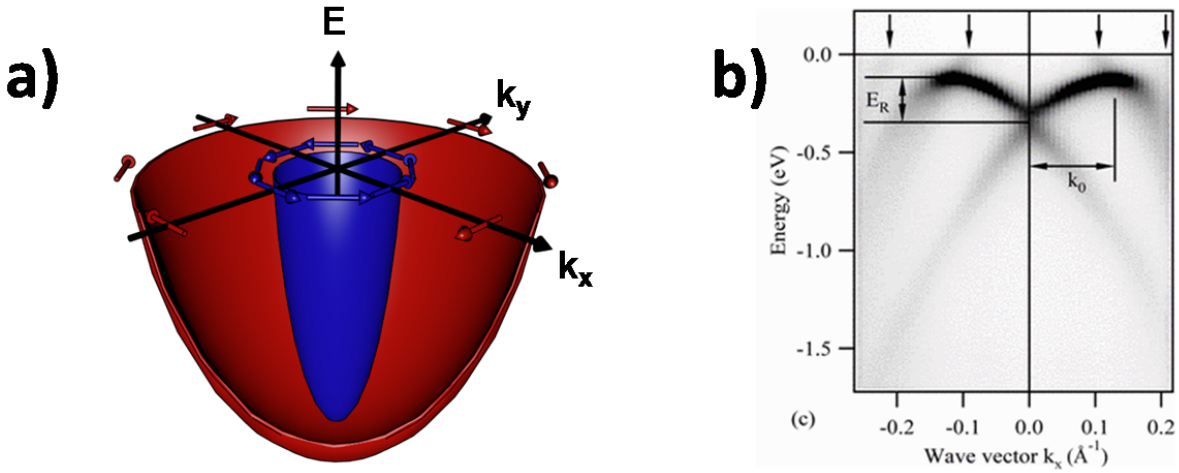

Figure 1.21 – a) Schematic band structure of a Rashba system, the spin degeneracy is lifted by the strong Rashba spin-orbit interaction. b) Band structure of the Bi/Ag interface measured by angle resolved photoemission spectroscopy.

the quantum Hall effects,[92,93] it was shown that this vision is insufficient and that topology is the essential ingredient to understand this new physics. Through the discoveries of the ordinary, anomalous and spin quantum Hall effect[94] (QHE, AQHE, QSHE, respectively), we will see how the topology allows to further understand and predict new properties that hold many promises for efficient spin manipulation. Topological insulators correspond to a condensed matter phase characterized by a new kind of order, which does not fit to the standard symmetry breaking paradigm. Instead, these new phases are described by a global quantity which does not depend on the details of the system - the so-called topological order.

Intuitive picture

The existence of topological order in an insulator induces unique characteristic experimental signatures. The most universal and remarkable consequence of a nontrivial bulk topology is the existence of gapless edge or surface states; in other words, the surface of the topological insulator is necessarily metallic. An informal argument explaining the existence of those surface states is as follows. The vacuum as well as most conventional insulating crystals are topologically trivial. At the interface between such a standard insulator and a topological insulator, it is not possible for the « band structure » to interpolate continuously between a topological insulator and the vacuum without closing the gap. This forces the gap to close at this interface leading to metallic states of topological origin.

Trivial to non-trivial band insulator

A band insulator is a material which has a well-defined set of valence bands separated by an energy gap from a well-defined set of conduction bands. The object of interest in the study of topological order in insulators is the ensemble of valence bands, which is unambiguously well

defined for an insulator. The question underlying the topological classification of insulators is whether all insulating phases are equivalent to each other, i.e. whether their ensemble of valence bands can be continuously transformed into each other without closing the gap. Mathematicians usually group geometric objects into broad topological classes. Objects with different shapes, such as a donut and a coffee cup, can be smoothly deformed into each other and can therefore be grouped into the same topological class. Mathematicians also developed the concept of a topological invariant that uniquely defines the topological class and can most of the time be experimentally measured in a real system. Topological insulators correspond to insulating materials whose valence bands possess non-standard topological properties. Related to their classification is the determination of topological indices which will differentiate standard insulators from the different types of topological insulators.[95] In a non-trivial or twisted insulator, one faces an impossibility or obstruction to define electronic Bloch states over the whole band using a single phase convention: at least two different phase conventions are required, as opposed to the usual case. This obstruction is a direct manifestation of the non-trivial topology or twist of the corresponding band.

The quantum Hall trio

The quantum Hall effect occurs when a two-dimensional electron gas is dipped into a large magnetic field applied perpendicularly to its plane.[92,93] In a classical picture, the electrons describe a cyclotron orbital motion due to the Lorentz force. In the film, this results in the localization of the carriers, making it insulating. On the edges of the sample however, the electrons are reflected, creating a unique chiral conduction channel as shown in Fig. 1.22 a). Alternatively, the system can be described using quantum mechanics: without external magnetic field, the free electron-like energy band is spin-degenerated. Applying a magnetic field breaks time reversal symmetry and lifts the spin-degeneracy, resulting in an energy spectra composed of Landau levels (LLs) ($E_c = \hbar\omega_c\left(n+\frac{1}{2}\right)$) where ω_c is the cyclotron frequency and n an integer called the LL index. If the Fermi level lies within the energy gap between two LLs, this is an insulating state, whereas a Fermi level coinciding with a LL results in a quantized transverse conduction $\sigma_{xy} = ne^2/h$.

Alternatively, the quantization of the Hall conductivity can be attributed within the standard linear response theory to a topological property of these bulk Landau levels, the so-called first Chern number of the bands located below the chemical potential.[96]

Up to now, only the momentum degree of freedom was treated: an electron can propagate either forward or backward. In the QHE picture, electrons travel only along the edges of the 2DEG, and the two counterflows of electrons are spatially separated into different channels located at opposite edges. When an edge-state electron encounters an impurity, it simply makes a detour and still keeps going in the same direction, as there is no way for it to scatter back. Such a dissipationless transport mechanism could be extremely useful for semiconductor devices with low power consumption. Unfortunately, the requirement of a

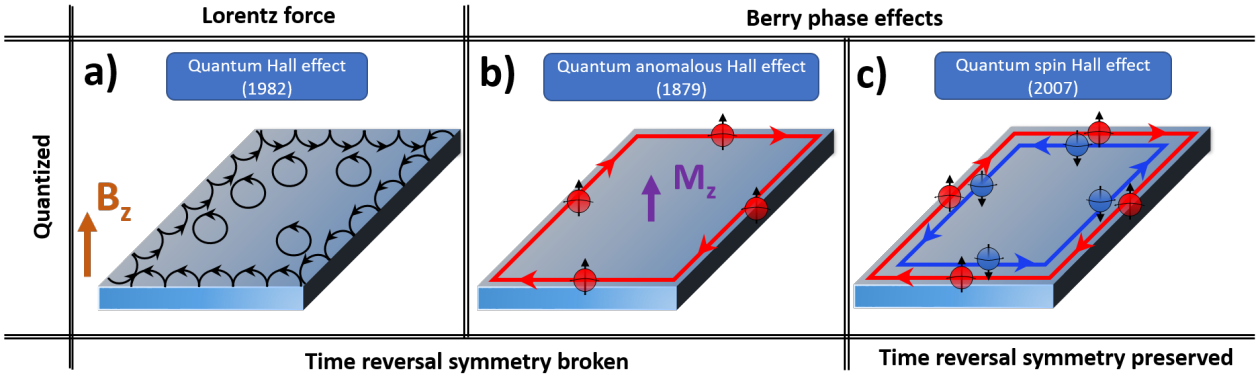

Figure 1.22 – The quantum Hall trio. a) Quantum Hall effect. An external perpendicular magnetic field is required to localize dissipative channels and obtain quantized LLs. Due to the TRS breaking, chiral edge conduction is dominant. b) Quantum Anomalous Hall effect. The TRS is broken by the presence of a magnetization. When the film is magnetized along z, only spin-up electrons flow clockwise along the edge. c) Quantum spin Hall effect. Due to the TRS and the spin-momentum locking mechanism, spin up (down) electrons flow clockwise (counterclockwise) along the edges in the quantum spin Hall system.

large magnetic field severely limits the potential application of the QH effect.

In 1988, Haldane showed that this type of order, while remaining specific of two-dimensional systems, did not necessarily require a strong magnetic field, but only time reversal symmetry breaking.[97] This is practically achieved using two-dimensional systems with non-zero magnetization, the corresponding phase of matter is now denoted as Chern topological insulator and exhibits the quantum anomalous Hall effect (see Fig. 1.22 b)).

If we now consider the spin degree of freedom (up or down), in addition to the forward and backward motions, it gives four conduction channels.[98,99] Spin up electrons are moving forward (backward) on the top (bottom) edge and the opposite takes place for spin down electrons. A system with such edge states is said to be in a quantum spin hall (QSH) state, because it has a net transport of spin forward along the top edge and backward along the bottom edge, just like the edge transport of charge in the QHE state (see Fig. 1.22 c)).

Two-dimensional topological insulators

The observation of the quantum spin Hall effect requires the counterpropagation of opposite spin states. Such a coupling between the spin and the orbital motion is a relativistic effect most pronounced in heavy elements. Although all materials have spin-orbit coupling, only a few of them turn out to be topological insulators. In 2006, Bernevig, Hughes, and Zhang predicted that mercury telluride quantum wells should be a topological insulator beyond a critical thickness d_c.[100] The general mechanism responsible for this is band inversion, in which the usual ordering of the conduction band and valence band is inverted by spin-orbit coupling. In most semiconductors, the conduction band is formed from electrons in s orbitals and the valence band is formed from electrons in p orbitals.

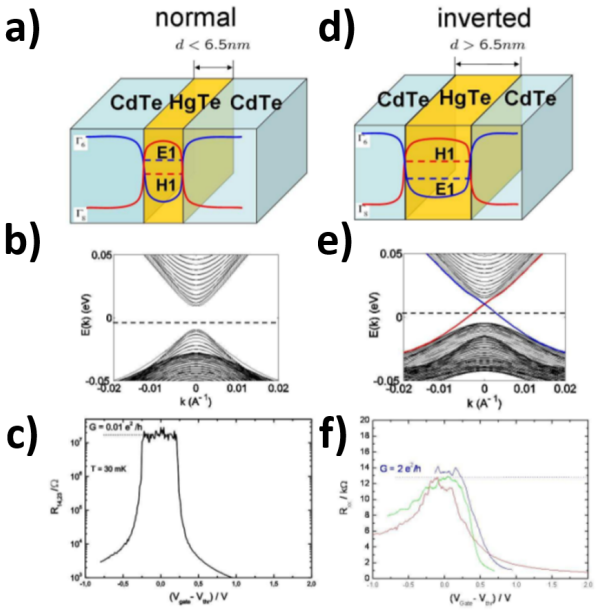

Figure 1.23 – a) CdTe/HgTe/CdTe heterostructure, in this thickness regime ($d < d_c$), the valence band is below the conduction band. b) Corresponding calculated band structure: a trivial band insulator. c) Measurement of the film resistance, the very large resistance at zero gate voltage emphasizes the insulating behavior. d) Same heterostructure for $d > d_c$), here the valence band shifts above the conduction band: this band structure is inverted. e) Corresponding calculated band structure: a 2D topological insulator. f) Measurement of the film resistance, the quantized resistance is the fingerprint of the quantum spin Hall effect.

However, in HgTe, the spin-orbit interaction is so large that the p-orbital band is pushed above the s-orbital band: the bands are inverted. A short time after the theoretical prediction, Molenkamp *et al.* could observe experimentally the QSH state.[101] HgTe quantum wells can be prepared by sandwiching the material between CdTe layers, which are lattice-matched but own a weaker spin-orbit coupling. It was predicted that for a thin quantum well ($d < d_c$), the quantum well behaves like a normal band insulator: the s conduction band is located above the p valence band as shown in Fig. 1.23 a) and b). In such trivial insulator phase, the resistance is almost infinite at zero gate voltage as shown in Fig. 1.23 c). In a thick quantum well however, where $d > d_c$, the increased thickness of the HgTe layer results in the predicted band inversion shown in Fig. 1.23 d) and e). Here, the two edge channels of the QSH insulator act as two conducting 1D channels, which each contributing to one quantum of conductance e^2/h, leading to the ~ 12.7 kΩ resistance state observed in Fig. 1.23 f).
While the quantum Hall effect arises in electronic systems with low symmetry and is characterized by a non-zero Chern number, this new topological phase does require time-reversal symmetry: it disappears when an external magnetic field is applied. The QSH state is also often called the two-dimensional topological insulator state, it belongs to a different topological class called $\mathbb{Z}^2$.[102,103]

Three-dimensional topological insulators

In 2007, three-theoretical groups derived the expression of the $\mathbb{Z}^2$ topological index in three dimensions: it was then demonstrated that three dimensional insulating materials could also exhibit a topological order. The most famous three-dimensional topological insulator materials are bismuth-based compounds like BiSb, Bi_2Se_3 or Bi_2Te_3[102] The fingerprint of the $\mathbb{Z}^2$ topological order in three dimensions is the existence of surface states with a linear dispersion i.e. a Dirac cone shape (see Fig. 1.24 a)). The first experimental observation of a three-dimensional topological insulator state was achieved a short time after the theoretical predictions by Hsieh *et al.*[104] in Bi_1Sb_{1-x} grown by molecular beam epitaxy by using angle resolved photoemission spectroscopy. Several reports followed investigating the Dirac cone dispersion and spin-polarization in the surface states of Bi_2Se_3 and Bi_2Te_3.[104,105]

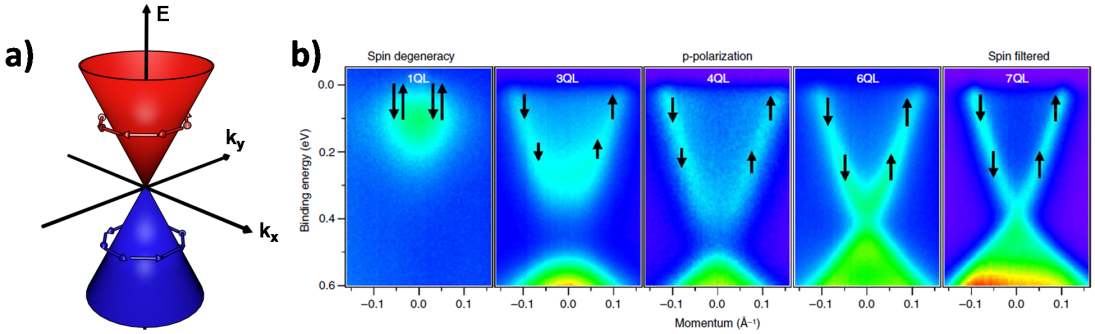

Figure 1.24 – a) Characteristic Dirac cone dispersion of the surface states of a topological insulator exhibiting spin-momentum locking. b) Thickness evolution of the Bi_2Se_3 spin-resolved band structure measured by spin and angle resolved photoemission spectroscopy. Extracted from Ref [106].

Fig. 1.24 b) shows the band structure of Bi_2Se_3 grown on sapphire by MBE as a function of the deposited thickness.[106] Interestingly, we can observe that the Dirac dispersion of the surface states is not present for the thinner films. When increasing the film thickness, the Dirac cone starts to appear and becomes gapless above 6 quintuple layers. The fact that the Dirac states are vanishing is due to the hybridization of the top and bottom surface states wave functions in the ultra-thin film regime.

Soon after the early spectroscopic results, numerous experiments were carried out to characterize the electrical transport,[107–110] optical[111,112] and spin properties[106] of these materials. Clear signatures were obtained, their interpretation based on the existence of surface states is usually oversimplified because bismuth-based topological insulators are known to be intrinsically n-doped due to the systematic presence of Se vacancies in the lattice.[113] As a consequence, a large density of bulk states often hides the effects of the Dirac surface states. The linear dispersion of the Dirac states (also called topological surface states or TSS) can be modeled by the following Hamiltonian:

$$\mathscr{H}_{\mathrm{TI}} = v_{\mathrm{F}} \left(\mathbf{z} \times \mathbf{p} \right) \cdot \sigma \tag{1.60}$$

where v_{F} is the Fermi velocity. Similarly to the case of the Rashba spin-splitted two-dimensional states, this Hamiltonian shows that the spin is locked perpendicularly to the particle momentum in the TSS as shown in Fig. 1.24 b). Contrary to the Rashba states, there is a single spin contour at the Fermi level, promising unprecedented spin-charge interconversion efficiencies.

1.3.3.3 Spin-charge interconversion at surfaces and interfaces

We have shown previously that the spin textures at surfaces or interfaces resulting from spin-momentum locking are promising for strong spin-charge interconversion. The underlying mechanism was identified by V. Edelstein in 1990[61] and called the Rashba-Edelstein effect. This spin-charge interconversion is a consequence of a rigid shift of the spin-momentum locked Fermi surface of TIs and Rashba interfaces when applying an electrical current or setting a spin accumulation. As the band structures of the two latter are very similar, we will present both of them simultaneously in the following.

Direct Rashba-Edelstein effect

Fig. 1.25 a) shows the Fermi contour of a topological insulator at equilibrium (the Fermi level lies in the surface states and no current is applied), with a clockwise spin chirality. Fig. 1.25 c) presents the Rashba case where there is now two Fermi contours of opposite spin chiralities: one clockwise (CL) in red and the other one counterclockwise (CCL) in blue. When a current density $\mathbf{j}$ is injected in the plane of the sample along $-x$, the electric field $\mathbf{E}$ is defined by: $\mathbf{j_c} = \sigma \mathbf{E}$ where σ is the electrical conductivity. Therefore, a Coulomb force $\mathbf{F}_{\mathrm{Coul}} = q\mathbf{E}$ acts on the electrons of the material (q is the carrier electrical charge). From the Newton's principle of dynamics we also have: $\mathbf{F}_{\mathrm{Coul}} = \frac{\mathrm{d}\mathbf{p}}{\mathrm{d}t}$, where $\mathbf{p}$ is the carrier momentum. As $\mathbf{p} = \hbar\mathbf{k}$, injecting a charge current during a time δt induces a rigid shift of the Fermi surface $\mathbf{\Delta k}$ that can be obtained by combining the previous equations:

$$\mathbf{\Delta k} = \frac{q \Delta t \mathbf{j}}{\hbar \sigma} = \frac{q \tau \mathbf{j}}{\hbar \sigma} \tag{1.61}$$

where τ is the momentum scattering time, typically of tens of fs in a metal and of few ps in semiconductors.

This rigid shift is shown in Fig. 1.25 d) for the case of a TI and d) for a Rashba interface. For the sake of simplicity, only the case of a single contour (TI) will be treated in the following. The more complex case of two contours (case of a Rashba interface) was fully treated in Ref [230]. In the following, we only consider electrons ($q = -e$). It leads to a shift of the Fermi contour opposite to the current direction as shown in Fig. 1.25. As a result of this $\mathbf{\Delta k}$ shift, a spin accumulation takes place at the surface of the TI. In the case of a Rashba interface

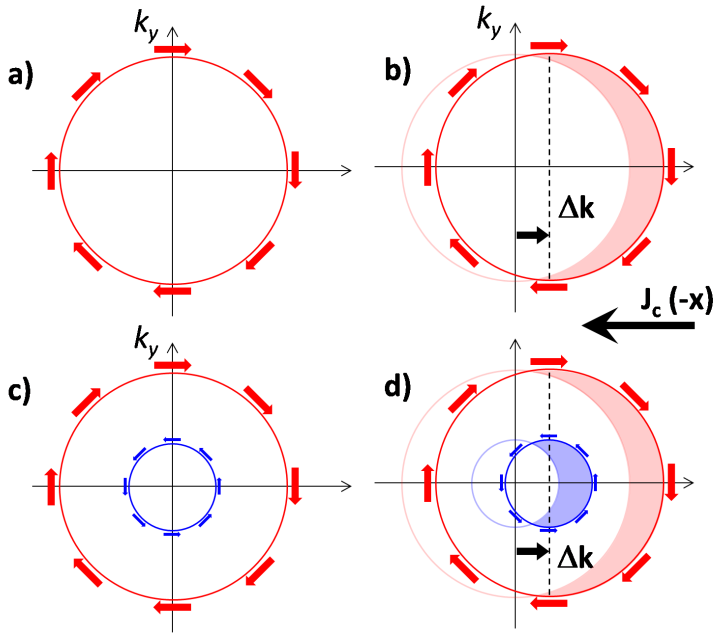

Figure 1.25 – Schematic representation of the direct Edelstein effect: a) Fermi contour of the topological surface state at the equilibrium. b) When a charge current is injected along $-x$ the contour is shifted which leads to a spin accumulation. c-d) The same phenomenons arises in a Rashba interface, although the two contours of opposite helicities partially compensating each others.

however, the total spin accumulation is reduced as the two contours of opposite helicities partially cancel each other. As a consequence, a spin accumulation has been generated from the application of a charge current (like in the spin Hall effect mechanism) thanks to the specific spin texture. This spin accumulation can diffuse into an adjacent material as a spin current. This effect is known as the direct Rashba-Edelstein effect, that was first predicted by V. Edelstein in 1990.[61] Here, the conversion from a 2D charge current to a 3D spin current is defined a the inverse of a length:

$$q_{\mathrm{REE}} = \frac{J_s^{3D}}{J_c^{2D}} \tag{1.62}$$

In chapter 4, we will see that the spin-polarization of electrons in a Rashba system resulting from the Rashba-Edelstein effect can lead to a novel magnetoresistance effect that is promising for efficient spin manipulation in a semiconductor.

Inverse Rashba-Edelstein effect

Similarly to the case of the three-dimensional spin-charge conversion by the spin Hall effect, the inverse mechanism also exists, it was naturally called the inverse Rashba-Edelstein effect. We start again from the equilibrium Fermi contour of a TI and a Rashba interface (Fig. 1.26 a) and c)). When a spin current with an orientation along the $+y$ direction is injected perpendicularly to the surface, the electrons fill the available states for this spin direction:

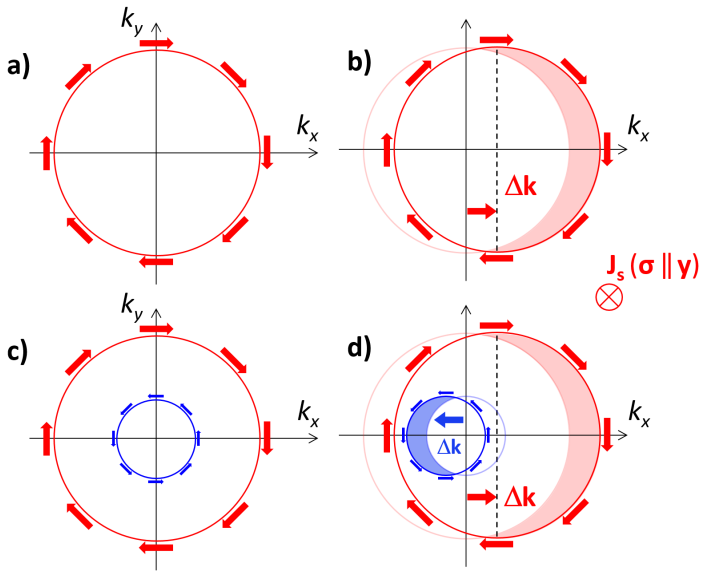

Figure 1.26 – Schematic representation of the inverse Edelstein effect: a) Fermi contour in a topological surface state at equilibrium. b) Fermi contour in a topological surface state when a spin current is injected along z with the spin along y. The Fermi contour is shifted, giving rise to a non-zero $\mathbf{\Delta k}$, and thus to a charge current. c-d) The same effect takes place in a Rashba interface, although the two contours of opposite helicities are partially compensating each others.

in the $k < 0$ region of the Fermi contour. This results in an accumulation of electrons with a positive momentum, hence, a charge current, which is given by the resulting Fermi contour shift $\mathbf{\Delta k}$. In this case, a three-dimensional spin current injected perpendicularly to the surface is converted into a two-dimensional charge current. The efficiency of the so-called spin-to-charge conversion is given by the inverse Rashba-Edelstein length λ_{IREE} defined as:

$$\lambda_{\mathrm{IREE}} = \frac{J_c^{2D}}{J_s^{3D}} \tag{1.63}$$

Conversion efficiency

Unlike the spin Hall angle θ_{SHE}, which is dimensionless, q_{REE} and λ_{IREE} have a dimension (a length or the inverse of a length, respectively). In order to compare the three-dimensional spin-charge interconversion in (I)SHE materials with the two-dimensional one in Rashba interfaces and TIs, we further define an equivalent figure of merit λ^* for (I)SHE systems as:[114–116]

$$\lambda^* = \theta_{\mathrm{SHE}} \lambda_{\mathrm{SF}} \tag{1.64}$$

This expression accounts for the fact that in a (I)SHE material the spin-charge interconversion occurs on a typical thickness of the order of the spin diffusion length λ_{SF}.

Numerous groups reported strong spin-charge interconversion by the (I)REE mechanisms.

The same experimental techniques employed for the characterization of the (I)SHE were used in Rashba interfaces and topological insulators. For instance, spin pumping experiments were conducted in Bi_2Se_3 or Bi_2Te_3, yielding a conversion efficiency of about $\lambda_{\mathrm{IREE}} \sim 30$ pm.[117–119] It is comparable to the equivalent figure of merit of Pt, the most common I(SHE) material: $\lambda^*_{\mathrm{Pt}} \sim 30$ pm.[120] The rather low conversion efficiency of those TIs is still controversial nowadays for two main reasons.

First, in the binary bismuth-based TIs grown by MBE like Bi_2Se_3, the high concentration of Se vacancies results in a high n-type doping, shifting the Fermi level to the bottom of the bulk conduction band.[113] These bulk states, still characterized by a strong spin-orbit coupling, can give rise to the spin Hall effect-based spin-charge interconversion, overhidding the possible strong conversion in the TSS. More recently, ternary compounds like $BiSb_xTe_{1-x}$ were developed to adjust the Fermi level position within the surface states,[121] but still, rather low conversion efficiencies were reported.[122]
This leads to the second issue. Most of the spin-to-charge conversion experiments were done by spin pumping using an adjacent ferromagnetic film. However, it was shown that the chalcogenide species (Se or Te) can chemically react with the ferromagnetic film,[123] damaging or even destroying the surface states.[124] This discrepancy between the theoretical expectation of large spin-charge interconversion efficiencies in three-dimensional TIs and the current experimental observations calls for alternative techniques to probe the spin-to-charge conversion in pristine TIs. This will be the topic of chapter 3 where we develop an original technique to circumvent these issues. Other studies reported larger conversion efficiencies in the elemental TIs α-Sn[125] and HgTe,[126] the Rashba interfaces Ag/Bi (111),[127] Al/$SrTiO_3$[128] and Fe/Ge (111)[78] also using spin pumping.
In 2020, topological insulators and Rashba interfaces are well established in the landscape of spin-orbitronics. This new class of materials characterized by the spin-momentum locking induced spin texture are very promising for future applications.

1.4 Thesis objectives: towards hybrid systems

The aim of my PhD work is to develop the generation, transport, detection and manipulation of the spin information in a semiconductor-based spintronics platform. While the three first points were well addressed by the community, the manipulation of spins with an electric field still remains a challenge as the intrinsic spin-orbit interaction is rather weak in conventional group IV-semiconductors. Our approach was to induce or enhance this interaction by growing thin films with strong SOI on a semiconductor: Ge.

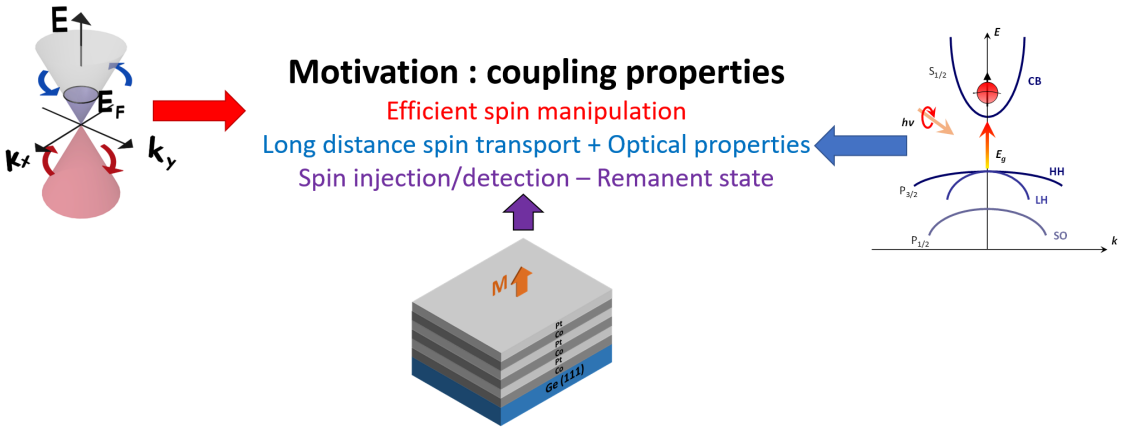

Figure 1.27 – Summary of the experimental development of a semiconductor-based spin-orbitronics platform: we combine the properties of topological insulators, semiconductors and perpendicularly magnetized ferromagnetic thin films.

Fig. 1.27 summarizes our approach: we aim at combining the properties of three types of materials into a single platform able to perform logic and memory tasks. In the following, I focus on two approaches in order to tune the spin-orbit interaction (SOI) in the Ge-based platform. Both rely on the structural inversion asymmetry and the spin-orbit coupling at surfaces and interfaces with germanium (111).

In chapter 3, I present the epitaxial growth of the topological insulator (TI) Bi_2Se_3 on Ge (111). After characterizing the structural and electrical properties of the Bi_2Se_3/Ge heterostructure, we developed an original method to probe the spin-to-charge conversion at the interface between Bi_2Se_3 and Ge by taking advantage of the Ge optical properties. The results showed that the hybridization between the Ge and TI surface states could pave the way for implementing an efficient spin manipulation architecture.

Chapter 4 summarizes the results from the second approach. Here we try to exploit the intrinsic SOI of Ge (111). The generation of spin accumulation in Ge has been long studied in our group, and the results showed that the SOI of Ge (100) was not strong enough to generate large spin currents. Here, we show that using the spin-splitted Rashba states at the interface between Ge (111) and a metal could lead to an efficient manipulation of the spins. By investigating the electrical properties of a thin Ge (111) film epitaxially grown

on Si (111), we found a large unidirectional Rashba magnetoresistance, which we ascribe to the interplay between the externally applied magnetic field and the current-induced pseudo-magnetic field applied in the spin-splitted subsurface states of Ge (111). The unusual strength and tunability of this UMR effect opens the door towards spin manipulation with electric fields in an all-semiconductor technology platform.

Chapter 5 focuses on integrating perpendicularly magnetized magnetic tunnel junctions on the Ge (111) platform. I first investigated the magnetic properties of Co/Pt multilayers grown by sputtering on Ge (111) by using three magnetometry techniques simultaneously: the anomalous Hall effect, the Kerr microscopy technique and a new original technique based on the thermo-electrical detection of the magnetic circular dichroism in (Co/Pt). These MTJs were then used to perform spin generation and detection in a lateral spin valve. The perpendicular magnetic anisotropy (PMA) allows to generate spin currents with a spin orientation being also perpendicular to the sample plane. Finally, we gathered all the building blocks that were studied during my PhD work to build a prototypical spin transistor shown in Fig. 1.28. Its principle relies on a gate voltage tunable Rashba spin-orbit field at the Bi_2Se_3/Ge (111) interface. Spin accumulations are generated either optically by the optical spin orientation or electrically using the MTJ with PMA as a spin injector. Using perpendicularly magnetized spin injectors is interesting for the development of the spinFET as the spin orientation is orthogonal to the film plane, allowing to make the spins to precess around the Rashba field.

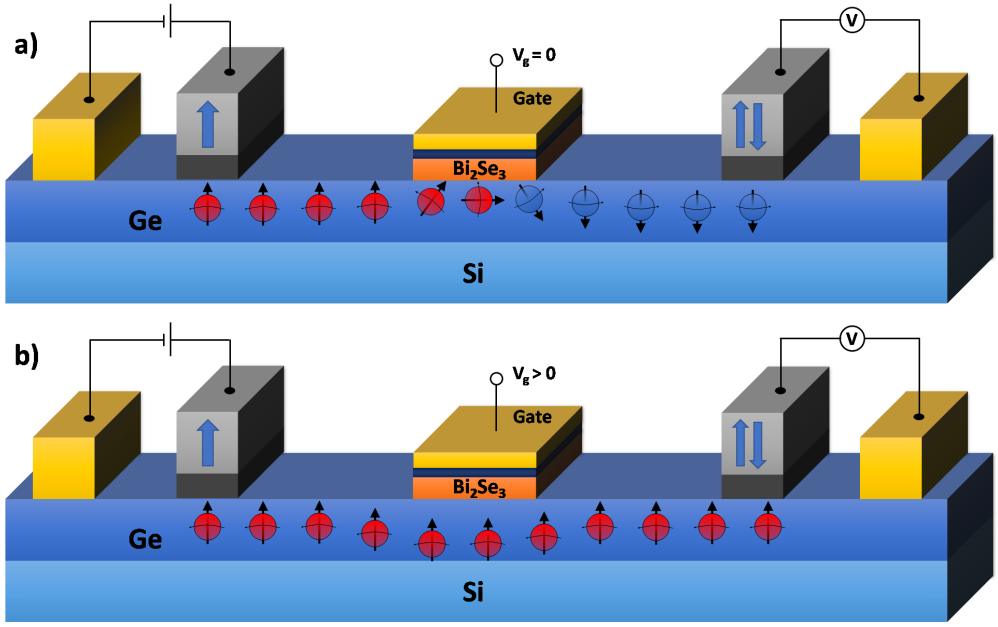

Figure 1.28 – Proposed spin transistor architecture on the Ge platform gathering all the building blocks individually studied in this thesis work.

CHAPTER 2

My daily life in experimental physics

The ultimate goal of my work is to inject, manipulate and detect the spin information in a Ge channel, keeping this in mind I daily used a wide variety of experimental techniques. The purpose of our research group is to control all the different experimental steps: I start by growing ultra-thin films by molecular beam epitaxy and/or magnetron sputtering and characterize their structural properties. Then I use micro and nano-fabrication techniques to pattern devices to ultimately, quantify electrical, optical, magnetic properties and eventually study spin-dependent phenomena. This part aims at explaining what a day in experimental spintronics looks like, following our experimental approach which resides between fundamental physics and nano-engineering.

2.1 Crystal growth

During my PhD, I focused on the introduction of spin-orbit interaction at the surface of Ge or at the interface between Ge and a material with large spin-orbit coupling (SOC). The materials of choice to do so are topological insulators (TIs) (see 1.3.3). In order to grow epitaxially the TIs, we chose to work with the (111) orientation of Ge that exhbits the same hexagonal symmetry as the bismuth-based TIs. In my PhD, I mostly used molecular beam epitaxy which is the best suited to grow such materials. I also employed magnetron sputtering to grow perpendicularly magnetized materials. Both in-situ and ex-situ characterization techniques were used systematically to investigate the films quality and to give constant feedback in order to improve the growth conditions.

2.1.1 Molecular beam epitaxy

Molecular beam epitaxy (MBE) is the most powerful technique to grow epitaxial thin films. The high crystalline quality is obtained using very low deposition rates (typically less than 1 nm/min). Lower deposition rate necessitates better vacuum conditions (typically in the 10^{-10} mbar pressure range) to maintain the impurities concentration as low as possible. The materials are usually sublimated from a high-purity target (typically 99.99999% or *5n* purity in a crucible), the ejected atoms form a molecular beam that can travel several tens of centimeters thanks to the long mean free path induced by the ultra-high vacuum (UHV). Eventually, they meet the surface of the substrate, condensate and react with the other species. Heating the substrate gives mobility to the incoming adatoms, allowing them to find the position on the surface that minimizes their energy. By carefully choosing the substrate properties: lattice parameter, surface symmetries and chemical reactivity, the process usually results in a the growth of a single crystalline epitaxial film with a very low density of defects. The UHV conditions also allow for in-situ characterizations by Reflection High Energy Electron Diffraction (RHEED), Low Energy Electron Diffraction (LEED), X-ray Photoemission spectroscopy (XPS) and Scanning Tunneling Microscopy (STM). All together, those techniques allow us to gain insight into the crystal structure, morphology and chemical composition of the epitaxial films in the MBE chamber. They provide information about the growth mechanisms which is necessary to adjust the growth parameters. I now focus on the different aspects that make MBE a unique and powerful technique to grow thin epitaxial films.

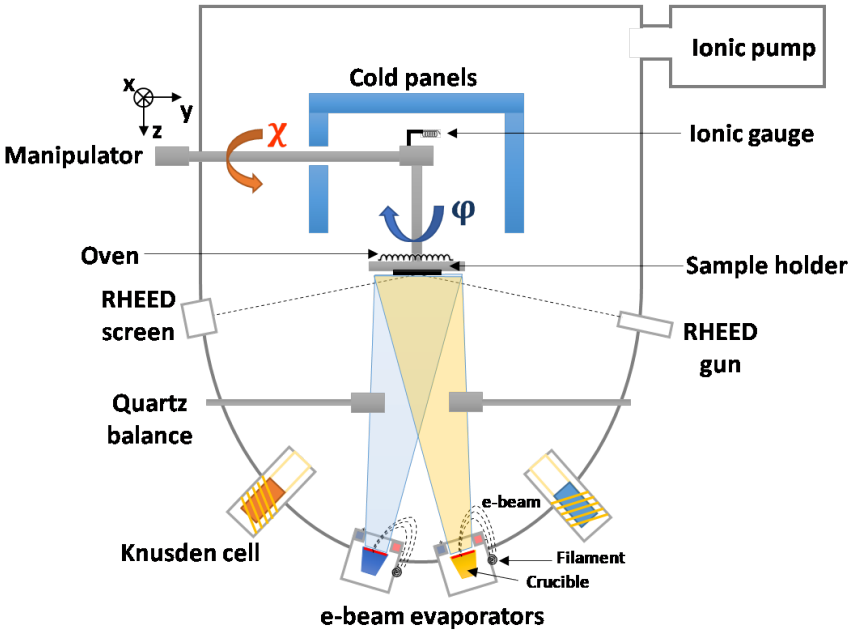

Figure 2.1 – Schematic drawing of the molecular beam epitaxy chamber and its key components.

Ultra-high vacuum and pumping systems

The most important aspect of MBE is the very low working pressure, UHV conditions ($P \leq 10^{-9}$ mbar) are obtained by combining several pumping technologies: a primary or membrane pump, a secondary or turbo-molecular pump, an ionic pump, cryopumping and Ti sublimator. The primary pump lowers the pressure in the chamber down to 10^{-3} mbar, then secondary pumping is turned on to reach pressures in the range of 10^{-8} mbar. Then, the ionic pump takes over to reach a pressure of 10^{-9} mbar in the chamber. A cold panel maintained at liquid nitrogen temperature (77 K) insures cryopumping in the MBE chamber by adsorbing the remaining species during the deposition and the different substrate preparation steps. It makes the pressure drop by one order of magnitude in the 10^{-10} mbar range.

In this range, we are able to measure the pressure in the chamber by a ionic gauge. Its principle relies on ionizing the ambient atoms and molecules by applying a strong electric field, the resulting measured current being proportional to the amount of atoms and molecules still present in the chamber and gives an indication of the pressure.

Sample holder and the heater

The substrate is mechanically fixed to a sample holder, which we call *molyblock* because made of molybdenum. The use of this refractory material allows a good temperature withstand. The molyblock is transferred from an introduction chamber in which the pressure is kept in the 10^{-10} mbar range to the manipulator arm which is facing the evaporators, it can be translated along x,y and z directions and rotated around two axis by the angles ϕ and θ as shown in Fig. 2.1.

To heat the sample, we apply a high current (up to 8.5 A) into a tungsten filament facing the backside of the molyblock. This filament can radiatively heat the molyblock up to a temperature of 950°C. Even higher temperatures (up to 1100°C) can be reached by applying a high voltage (up to 1 kV) between the filament and the molyblock to initiate electron bombardment. The temperature is measured using a thermocouple mounted on a spring to keep a point contact with the backside of the molyblock. This temperature is only an indication of the sample temperature and may vary from molyblock to molyblock and with the thermal contact between the substrate and the molyblock.

e-beam evaporators, Knusden cells and quartz balance

The MBE techniques relies on evaporating high quality materials at extremely low rate. Two main techniques are commonly used to sublimate/evaporate materials, the first one is the most versatile: electron-beam evaporation (e-beam). Again, a tungsten filament is heated to emit electrons that are accelerated by high electric fields, the electron beam is then deflected and focused on a target loaded in a crucible using permanent magnets and a set of scanning coils. This technique allows to evaporate any materials, although highly-conducting materials requires more power because most of the power is evacuated in the water-cooled e-gun evaporator.

The second technique is Joule heating in a Knudsen cell (or effusion cell). In this case, the material to evaporate lies in crucible that is heated by a tungsten filament. This allows to reach very low and stable flux, but is restricted to less refractory materials. During my PhD, I used a Knudsen cell to evaporate selenium which is a volatile material. In both cases, the deposition rate is monitored using a quartz microbalance. The resonance frequency of quartz crystal is disturbed by the amount of material deposition at its surface. The shift in resonance frequency is recorded and the deposited thickness can be calculated from the Sauerbrey equation. This sensor allows to reach high degrees of control on the deposition rate and ultimately, on the total film thickness.

Reflection High Energy Electron Diffraction: RHEED

The Reflection High Energy Electron Diffraction or RHEED is a commonly used in-situ technique to characterize thin films, it runs in UHV conditions and can be used during the thin film growth. Its principle relies on the diffraction of an electron beam by the crystal lattice.

An object can diffract a wave when its size is comparable to the wavelength. For instance, visible light can be diffracted by a grid with micrometer spacings. In this way, wave diffraction can be used to measure the object characteristic dimensions. Using shorter wavelength allows to probe smaller objects, ultimately, X-rays can be diffracted by the atomic planes of a crystal and are used to determine the crystal structure and lattice parameter.

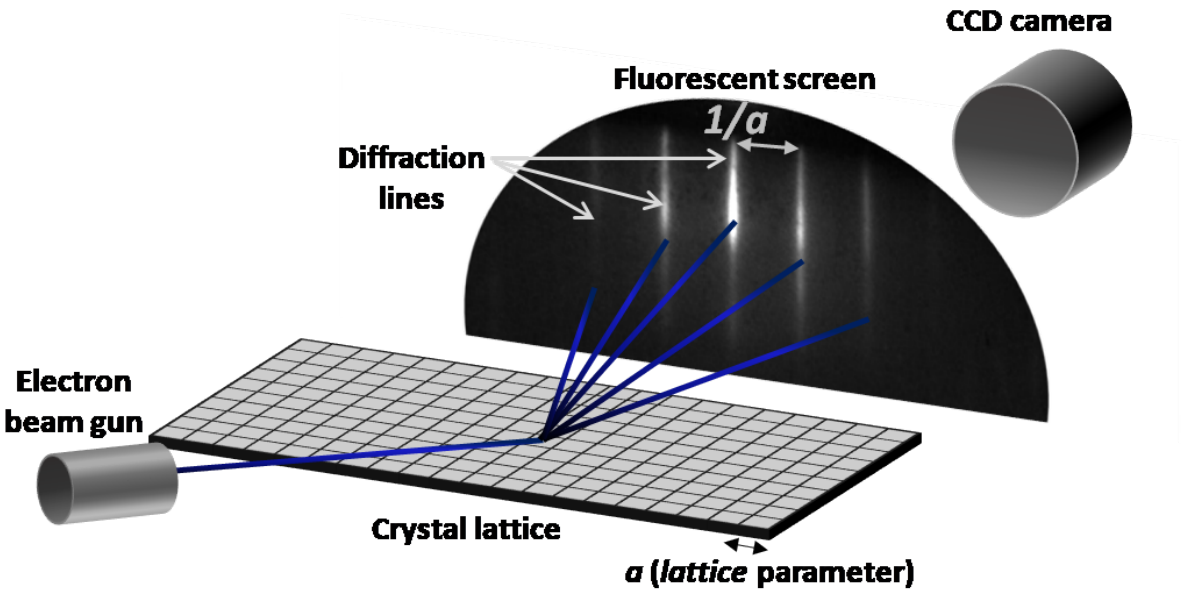

Figure 2.2 – Schematic drawing of a RHEED system, the coherent electron beam scatters on a periodic lattice, resulting in a peculiar diffraction pattern that is representative of the surface structure and quality. The electron pattern is projected on a fluorescent screen that convert the electron density into a visible pattern that is recorded using a CCD camera.

With a De Broglie wavelength in the sub-angström range, high energy electrons can also be

used to probe the crystalline lattice structure of solids and thin films. Here, the electrons are emitted from a hot tungsten filament, and accelerated at 20 keV before being reflected by the sample surface at grazing incidence. They interact with the lattice and form a diffraction pattern on a fluorescent screen, recorded with a CCD camera. In Fig. 2.2, we can see how the incident electrons scatters on the crystal surface. This streak pattern results from the intersection of the Ewald sphere with the reciprocal lattice made of a regular lattice of rods being the reciprocal lattice of a crystalline surface. A perfect surface will result in an array of dots regularly distributed on rings but usually, a set of lines or streaks is observed. The observation of broad lines comes from a distribution of lattice parameters due to defects, strain or from the small size of the diffracting grains that becomes lower than the electron beam coherence ($\sim$ 30 nm). When dots appear along the lines, it means that the surface is rough and that 3D diffraction takes place. Analogously to X-ray diffraction, a polycristalline film exhibits a diffraction pattern made of concentric rings and an amorphous film shows a diffuse pattern. To summarize: a good epitaxial film shows a RHEED pattern made of thin streaks which is anisotropic with respect to the electron beam azimuth angle (ϕ) on the sample demonstrating the single crystalline character of the film.

2.1.2 Magnetron sputtering

Thin films deposition by magnetron sputtering is commonly used in the industry because of the important depositing rates and the ability to sputter any material or alloy. Fig. 2.3 shows how an argon plasma is created in the reactor by applying an electric field between the cathode and the anode. The material to deposit is called the target and is fixed to the cathode. In the argon plasma, Ar^+ ions are accelerated toward the target and collide with the target atoms, communicating their momentum, triggering the sputtering mechanism. Free target atoms eventually reach the substrate and condensate on its surface. Similarly to the MBE technique, the sample can be heated to favor crystal ordering and the deposition rates are monitored using a quartz balance. The argon pressure is usually set in the 10^{-2} mbar range, increasing the pressure increases the plasma density and reduces the sputtering and deposition rate.

Despite of its several advantages, the sputtering technique often leads to a very poor control of the interfaces, indeed residual atomic bombardment can easily produce defects and interface atomic intermixing between the different layers, and the overall thin films crystalline quality is usually worse than the one of MBE films.

During my PhD, I used the MBE technique to grow high quality single crystals and I used the sputtering technique to grow perpendicularly magnetized materials. Typical systems are Ta/CoFeB/MgO trilayers (with post-annealing) or (Co/Pt) multilayers, I focused on the latter stack. Here, the material thicknesses are critical to obtain the targeted magnetic properties and rigorous procedures were used to reach sub-nanometer thickness precision.

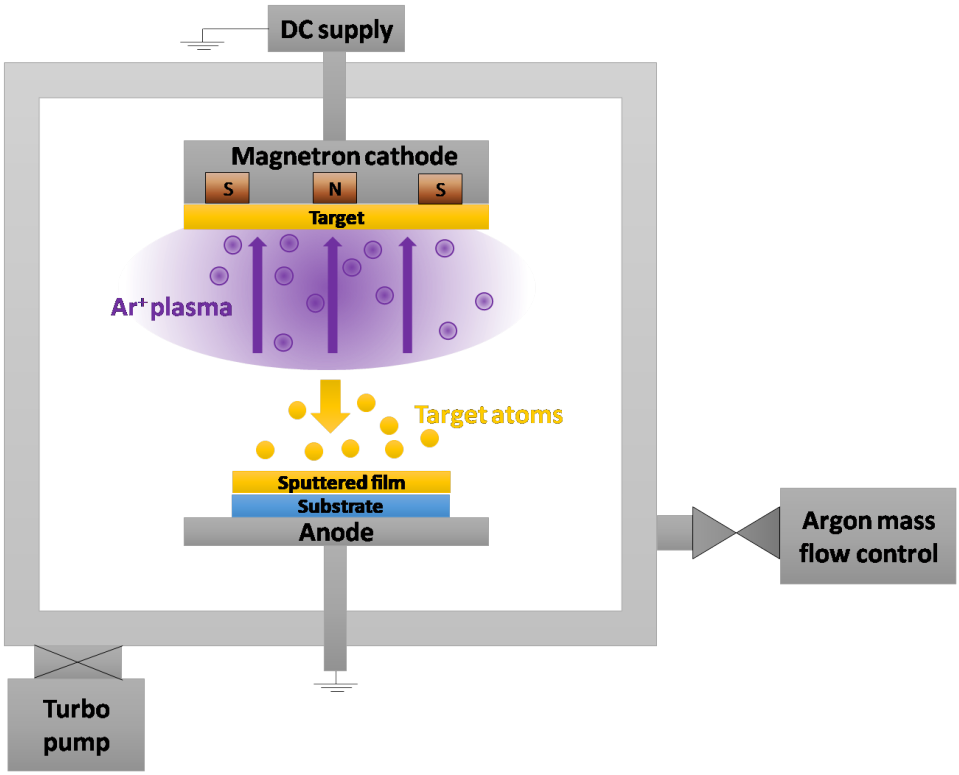

Figure 2.3 – Magnetron sputtering deposition principle. A voltage between the target material and the sample is applied, generating a plasma. The bombardment of Ar^+ results in the sputtering of the target, free target atoms reach the substrate and condensate on its surface, forming the thin film.

2.2 Structural characterization

In the process to develop functional materials and study their physical properties, structural characterizations constitute an essential step in order to control, understand and improve the process. In this part, I describe the two main ex-situ techniques that I used on a weekly basis to gain knowledge about the epitaxial thin films grown.

2.2.1 X-ray diffraction

When a coherent monochromatic X-ray beam interacts with a periodic structure (like a crystal), it undergoes constructive and destructive interference leading to a diffraction pattern. The X-ray diffraction (XRD) by a crystal is ruled by the Bragg's law:

$$n\lambda = 2d_{hkl}.sin(\theta) \tag{2.1}$$

Where n is a positive integer, λ is the X-ray wavelength, θ is the incidence angle and d_{hkl} is the interplanar distance. Technically, a collimated X-ray beam is obtained by bombarding a target (usually made out of Cu or Co) with high energy electrons (several keV). The high-

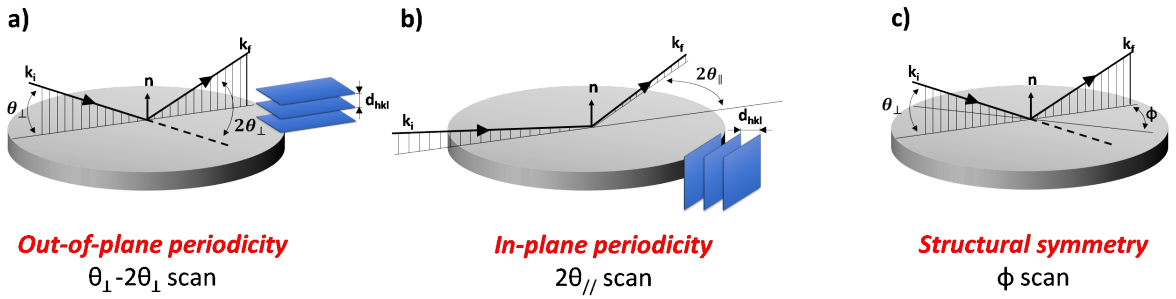

Figure 2.4 – a) Out-of-plane XRD b) In-plane XRD c) In-plane angular dependence: ϕ scans

energy electrons impinging the Cu or Co target excite core-electrons of the material which de-excitation produces the X-ray beam. The shape and energy spectrum of the beam is adjusted by using a monochromator and a set of slits. A precise control of the sample position is essential, the most versatile diffractometers usually use a six-axis positioning system to align the X-ray beam relative to the sample and perform angular scans. This very powerful technique allows an in-depth structural characterization of thin films. During my PhD, I investigated the crystal structure of the MBE-grown layers. This step is very important since the crystalline structure fully determines the electronic properties of the material, in particular, the spin-orbit interaction.

The Fig. 2.4 shows different XRD configurations. We usually start by looking at the film X-ray reflectivity (XRR) to gain information about its thickness and roughness. Then we perform out-of-plane $\theta - 2\theta$ scans: the beam and the detector angles are swept symmetrically, long penetration depth of X-rays allows to probe the out-of-plane crystal lattice.

By comparing the different diffraction peaks position and width with data from the literature, we can identify the material phase and assess its crystalline quality. For ultra-thin films and ultimately, 2D materials, the out-of-plane periodicity is vanishing, but we can still measure the in-plane periodicity. In this case, we use a grazing incidence X-ray beam (see Fig. 2.4 b)). Finally, one can also set the incidence and detector angles to a specific diffraction peak and then rotate the sample in its plane in order to study the in-plane mosaicity and symmetries. For instance, a hexagonal (resp. a cubic) lattice should exhibit a six-fold (resp. a four-fold) in-plane periodicity.

2.2.2 Atomic force microscopy

This technique is complementary to XRD, it allows to characterize the surface morphology by direct imaging at the nanometer-scale. The atomic force microscopy (AFM) exploits the near-field interactions (attractive/repulsive) between a nanometer-sized tip and the atoms of

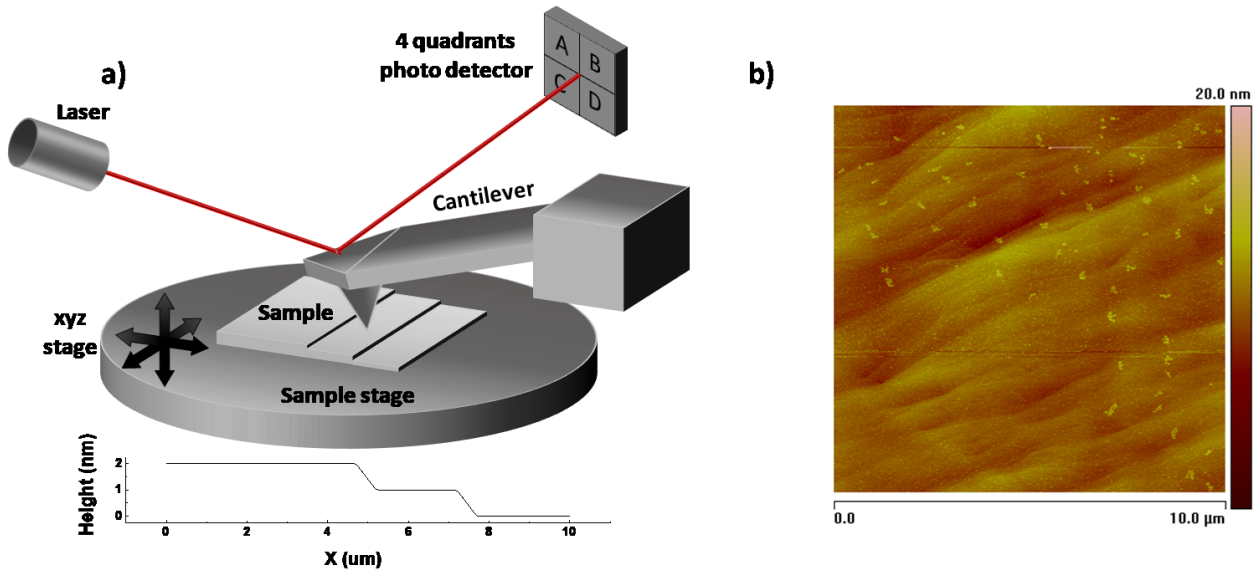

Figure 2.5 – a) Atomic force microscope principle, the laser beam reflection is analyzed, allowing to detect the cantilever deflection related to the sample topography. b) 10×10 µm^2 topographic image of the Ge/Si (111) substrate, atomic terraces are revealed.

the sample surface. The image size is typically tens of nanometers to tens of micrometers with a sub-nanometer height resolution. The sensing tip is located at the end of a silicon cantilever that is mounted on an x-y-z piezoelectric stage. Scanning the tip on the surface results in the cantilever deflection according to the Hooke's law of deformation. The deflection is recorded using the reflection of the laser beam by the cantilever surface on a four-quadrants photodiode detector as shown in Fig. 2.5 a).

The most straightforward mode is the contact mode: the tip follows the surface and its height is regulated to sense a constant force. For fragile Van der Waals materials, the tapping mode is preferably used to minimize the tip-surface interaction: the cantilever vibrates at its resonance frequency and the interactions with the surface modify the amplitude and phase of the oscillations. Here, the laser deflection is synchronously monitored using a lock-in detection. Fig. 2.5 b) shows an example of AFM measurement in the tapping mode on a Ge/Si (111) substrate, we can clearly see micrometer-sized atomic terraces.

2.3 Micro and nano-fabrication

One keystone of my PhD work was to design and fabricate microdevices in order to study the magnetotransport, magneto-optical and spin properties of our thin films. In that scope, I used a large panel of clean room techniques. In this part, I show the techniques I used the most for micro-fabrication through two examples of device.

2.3.1 The Ge/Si (111) substrates

The substrates used in this thesis work were made by using Low Energy Plasma Enhanced Chemical Vapor Deposition (LEPECVD) at the Politecnico di Milano, Como, Italy. 2- µm-thick germanium epilayers were deposited on a 3-inch high-resistivity Si (111) wafer at a rate of $\approx$ 4 nm/s and a substrate temperature of 500° C. Post-growth annealing cycles have been used to reduce the threading dislocation density down to $\approx 2\times10^7$ cm^{-2} and to improve the crystal quality.[129] Three types of substrate were grown:
- Non-intentionally doped (NID) Ge/Si (111), resulting in a residual doping $p \approx 2\times10^{16}$cm^{-3} as measured by the Hall effect at room temperature. Those substrates are the most resistive ones, they were used for most magnetotransport experiments.
- Low-n doped Ge/Si (111), where $n \approx 2 \times 10^{16}$cm^{-3}. Those substrate were mostly used for experiments with light: optical spin orientation, magnetic circular dichroism and magneto-optical Kerr effet.
- Strongly n-doped Ge(n++)/Ge/Si (111), those particular substrates were used specifically for lateral spin valve experiments, the 20 nm-thick n_{++} Ge layer on top reduces the Schottky barrier between the magnetic tunnel junction and the semiconductor, increasing the spin injection efficiency.

2.3.2 Hall bar process

The Hall bar is probably the mostly used device to study the electronic properties of a material by magnetotransport measurements in fundamental physics. It allows to measure simultaneously the four-probe longitudinal resistance of any conductor as well as its transverse resistance, more details will be given in the following part dealing with magnetotransport experiments. Fig. 2.6 represents the three steps of fabrication, we define the number of steps in a process to be equal to the number of lithography steps, regardless of the amount of deposition and etching steps.
In this first example; our objective is to pattern a 120×20µm^2 Hall bar out of an ultra-thin Fe film epitaxially grown on a Ge/Si (111). The studied Fe layer thickness is typically less than 3 nm, it is important to know that even if the Si substrate is almost insulating, the epitaxial 2- µm-thick Ge layer is not. This makes ultra-thin films transport study a challenge as any current passing through the bilayer will be mostly shunted into the substrate. For this purpose, both the Fe and the Ge layers are etched into Hall bar pattern in order to reduce and control the shunting process. I will skip the MBE growth part here as it is extensively described in the chapter 4 of the manuscript.

Pattern transfer using laser lithography
Each process step begin by laying down the photosensitive resist on the sample (AZ1512HS). This resist is spin coated at 4000 rpm with an acceleration of 2000 rpm/s, during 60 s,

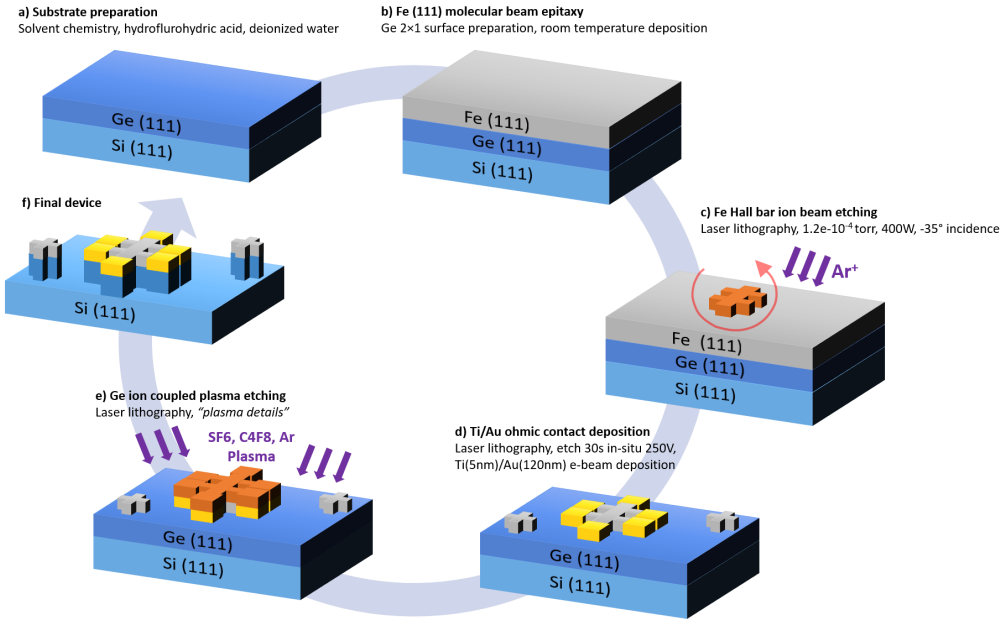

Figure 2.6 – Representation of the different micro-fabrication steps to obtain Fe/Ge/Si (111) Hall bars that were used for magnetotransport experiments.

resulting in a 1.2- μm-thick homogeneous resist. The sample is annealed for 90 s at 100° C in order to evaporate the resist solvents. Laser lithography is employed to expose the resist and draw the pattern, the machine consists in x-y-z stages moving below a focused UV laser spot ($\lambda = 380$ nm). I used and optimized this lithography technique during my three years of PhD, which presents many advantages as compared to standard photolithography using solid masks and e-beam lithography. Exposure times are short, typically less then 5 minutes, there is no need for mask manufacturing as the machine directly expose the layout, positively or negatively.

A positive resist becomes dissolvable when exposed to UV light: opening holes in the resist to deposit contacts correspond to a positive exposure (exposes the resist following the pattern drawn in the drawn layout). Inversely, a negative exposure will expose the resist on areas where there is no pattern in the layout, leaving the resist as a protective layer for an etching process. Once exposed, the sample is developed using a 50 % AZ developer solution during 7 to 10 s.

Step 1: Defining the Fe Hall bar

The first step is a negative exposure of the Hall bar pattern using the standard procedure described above. We obtain the pattern shown in Fig. 2.6 c), the Fe film is etched using an anisotropic etching method: the ion beam etching (IBE). In this technique, Ar^+ ions from an argon plasma are accelerated toward the sample to sputter the film. The chamber pressure is maintained at 1.2×10^{-4} torr and the supply power is 400 W, the ion beam bombards the sample with a 35° incidence angle in order to prevent redeposition and the sample is rotating

around its own axis to prevent shadow effects and increase etching homogeneity.
The etched thickness is measured using several quick methods: the change of reflectivity at the surface of the sample is a first indicator: Fe being a metal, it is more reflective than Ge and looks brighter. A second indication is the sample resistivity, which should change drastically with or without Fe. Scanning electron microscopy (SEM) can also be used thanks to its chemical sensitivity: Fe and Ge regions are well contrasted. Finally, after the resist removal, a profilometer or AFM can be used to measure the step height between Ge and Fe. IBE might burn the resist on the first tens of nanometers, making it difficult to remove simply using solvents. To solve this issue, the sample is exposed to a soft O_2 plasma during 30 s. The plasma etches the burned resist and allows to remove easily the remaining resist with acetone.

Step 2: Depositon of ohmic contacts

The second step is a positive exposure, here, we open holes in the resist to deposit thick metallic contacts inside. The sample is transferred to a chamber equipped with e-beam evaporator operating at a base pressure of 5×10^{-7} mbar. This machine is also equipped with IBE, allowing to improve the electrical contacts by removing native oxide layers. The sample is typically etched for 30s at 250 eV in normal incidence, then a Au(120 nm)/Ti(5 nm) stack is deposited. 5 nm-thick Ti layer is deposited at 0.1 nm/s in order to increase the Au adhesion, then, the 120 nm-thick Au layer is deposited at 0.5 nm/s.
The sample then undergoes a lift-off process: when immersed in acetone, the resist acts a sacrificial material that is washed away together with parts of the contacts covering it. Only the material that was in direct contact with the substrate remains on the sample. The result is shown in Fig. 2.6 d).

Step 3: Etching the Ge layer

The Ge layer is also etched following the Hall bar pattern in order to control the current lines during transport experiments. After the laser lithography step, the sample is transferred into an ion-coupled plasma etching chamber. This type of technique differs from purely mechanical etching like IBE, it relies both on mechanical milling and the chemical reactions between the plasma species and the material to etch. To this purpose, reactive gases are employed such as SF_6 or C_4F_8. This particular recipe is developed to etch Si anisotropically and works well for Ge etching. The etching rates are considerably larger than IBE (500 nm/min versus 10 nm/min). The Ge layer being 2 µm-thick, the etching process can be monitored in real time using a laser interference pattern. A laser beam is focused on the Ge surface; as the film thickness decreases during etching, the light paths of the beam reflected on the top and bottom Ge interface change. Constructive and destructive interferences are observed, giving rise to light intensity oscillations as a function of time, the layer is completely etched when the oscillations vanish. Again, a soft 30s O_2 plasma is used to help removing the resist with solvents. Fig. 2.6 f) shows what the final devices look like.

2.3.3 Optical spin orientation devices

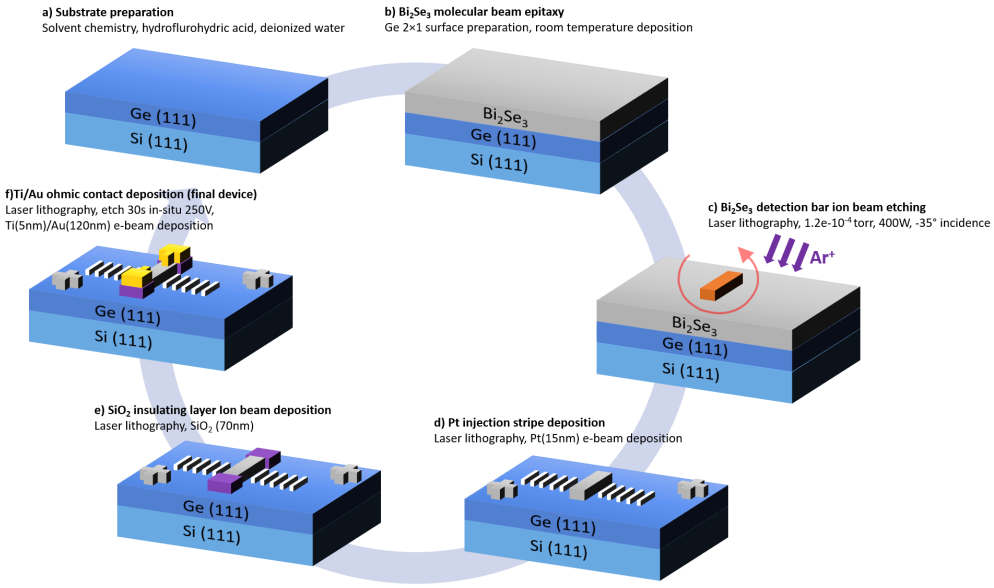

Figure 2.7 – The different steps to pattern the devices for optical spin orientation magneto-optical experiments.

The same set of techniques was employed to process the samples with Bi_2Se_3. The growth procedure will be described in detail in the following chapter, here we only focus on the microfabrication. The four-step process is sketched in Fig. 2.7. The main difference with the previous process is that the size of the device is much smaller and careful precaution has to be taken to align the different lithography levels.

The Bi_2Se_3 layer is first etched using IBE and cleaned using soft O_2 plasma. After a re-alignment procedure, a 15 nm-thick Pt layer is deposited by e-beam evaporation using the lift-off technique. The third step is crucial: an insulating 70 nm-thick SiO_2 layer is deposited by ion beam sputtering between the Ge and the metallic contacts to insulate them from the substrate. Finally, Au(120)/Ti(5) pads are deposited by e-beam evaporation to contact the Bi_2Se_3 central bar. This type of device will be extensively studied in chapter 3.

2.4 Magnetotransport

The electronic properties of a material including spin-orbit effects can be investigated in detail by electrical measurements. For this, we use Hall bars, as the ones described in the previous paragraph, to measure the longitudinal and transverse resistances as a function of temperature, current and magnetic field intensity and direction. This is why an important part of my work as an experimental physicist was to install and automate a helium-free superconducting magnet cryostat: the SpectromagPT from Oxford Instruments. Helium-free cryostats rely on a closed-cycle refrigerator based on successive helium gas compression and expansion. This technique allows a cooling plate to reach about 3 K. The cooling plate is then used to cool both the superconducting magnet and the variable temperature insert (VTI) as shown in Fig. 2.8. This system does not require liquid helium supply and can run during long periods (typically several months) without warming up the system.

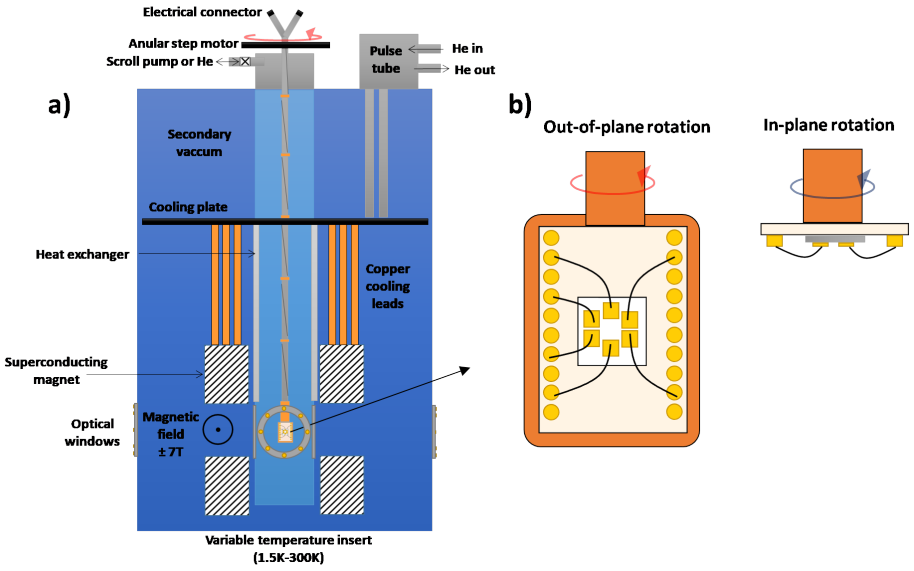

Figure 2.8 – a) Cryostat schematic cross-view b) Sample holder used for transport experiments, the sample is glued to the holder with a General Electrics (GE) varnish that resists to the cryogenic environment and bonded to the copper electrical contacts using 25 µm diameter-Al wire.

Numerous technical tasks were accomplished to shape this cryostat into an autonomous and versatile experiment. To cite only few of them:

- The wiring of the measurement probe and associated connectors.
- The motorization of the probe rotation, allowing to automate angular dependent measurements.
- The development of a versatile control software that can be used to run and queue measurement sequences: the interface is called Measurement Sequence Builder (MSB). It has been a key tool in the success of our experimental work in the laboratory during the past three years, the appendix C of the manuscript is dedicated to its design and capabilities.

The SpectromagPT is schemed in Fig. 2.8 a), it can be used to apply an intense magnetic field up to 7 T and to control the sample temperature from 1.5 K to room temperature within a mK temperature stability. It is different from other superconducting magnet cryostats for the presence of four windows to access optically to the sample: the sample can be illuminated by a laser beam which adds several degrees of freedom to our measurements like the laser power, wavelength and polarization. The sample is glued to a PCB sample holder using a General Electrics varnish that can hold the cryogenic strain without cracking and damage. The sample holder is then plugged at the end of the measurement probe in either an out-of-plane or in-plane configuration with respect to the magnetic field (Fig. 2.8 b)).

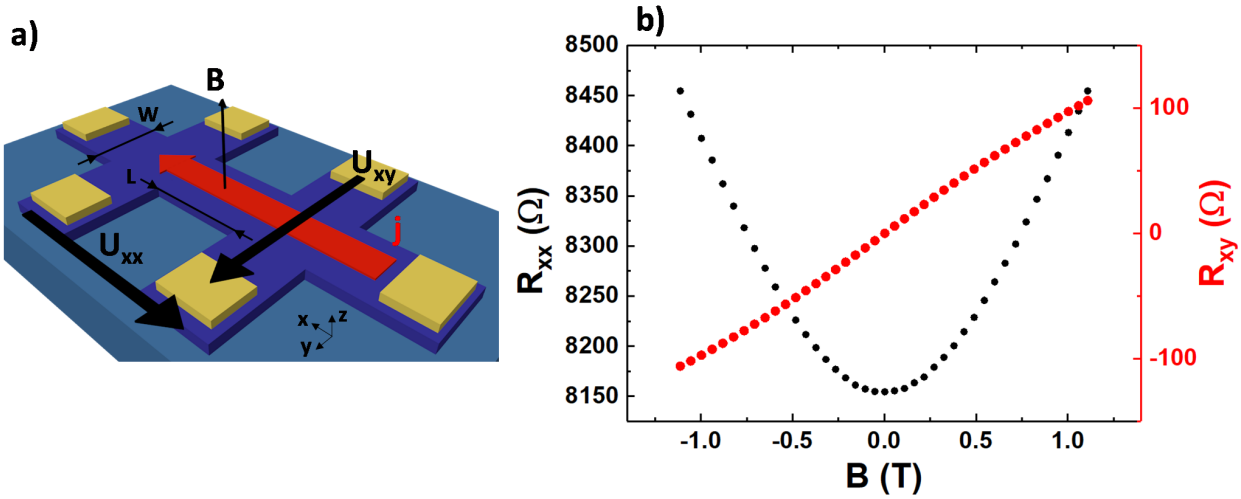

Figure 2.9 – a) Hall measurement geometry: the magnetic field is applied perpendicularly to the current and the sample plane, inducing a transverse voltage. b) Longitudinal and transverse resistance of a p-type Ge/Si (111) Hall bar at room temperature.

Fig. 2.9 a) presents the Hall measurement geometry: a current is passed through the channel, allowing the simultaneous measurement of the four-probe longitudinal voltage drop as well as the transverse voltage. When a conductor is dipped into a magnetic field, the Lorentz force acts on the electrical carriers:

$$F_L = q\vec{E} + q\vec{v} \wedge \vec{B} \tag{2.2}$$

Where q is the carrier charge (negative for electron, positive for hole), v is its velocity and E and B are the electric and magnetic field, respectively. This magnetic component of the Lorentz force deflects the carriers from their trajectory, resulting into a transverse voltage known as the Hall effect:

$$R_{xy} = \frac{U_{xy}}{I} = \frac{B}{\rho te} \tag{2.3}$$

Where I and B are the applied current and magnetic field, t is the conductor thickness, e is the electron elementary charge, and ρ is the carrier density. In this measurement geometry, electron transport (n-type) results in a negative $U_{xy} = f(B)$ slope where p-type transport (holes) results in a positive slope.

As an example, Fig. 2.9 b) shows a measurement realized on a 2 µm-thick Ge/Si (111) Hall bar at room temperature. The longitudinal resistance $R_{xx}= U_{xx}/I$ shows a quadratic magnetoresistance, typical of a three-dimensional conduction. The transverse resistance $R_{xy}= U_{xy}/I$ shows the Hall measurement. The positive slope indicates a hole conduction and linear fit using eq. 2.3 is used to extract the carrier density $p = 2 \times 10^{16}$ cm^{-3}.

This short study intention was to briefly show how helpful magnetotransport can be in this quest for fundamental understanding of material properties.

2.5 Magneto-optical microscopy

During my thesis, I also developed a very powerful and versatile magneto-optical setup allowing to spatially resolve the physical effects of light on different types of materials and microstructures by playing with several degrees of freedom (DOF): temperature, magnetic field, electrical current, light wavelength, power, polarization and angle of incidence. This setup led us to develop new original experiments and ultimately, toward the discovery of unprecedented physical effects.

2.5.1 LUMOS: Low temperature Universal Magneto-Optical Setup

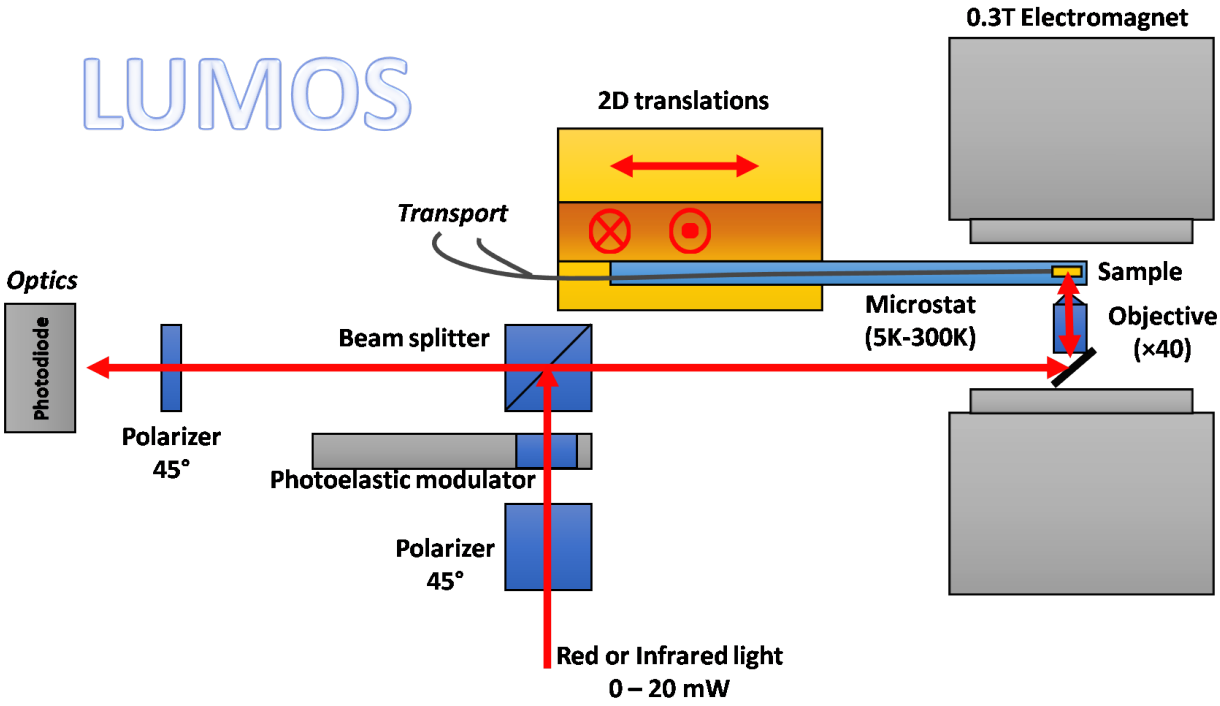

Figure 2.10 – Schematic top view of the LUMOS system showing its main components: cryostat, electromagnet, the scanning x-y stage and the polarized light path.

LUMOS is a homemade confocal microscope that can operate at variable temperatures (5 K-300 K), its strength resides in the amount of DOF that can be controlled to perform original experiments. Fig. 2.10 shows a schematic top view of the optical bench, the light source is coming from a laser diode out of an optical fiber, the wavelength can be changed easily by changing the diode without moving any part of the setup. The beam emerging from the fiber is strongly divergent so it first passes through a convergent $f = 5$ cm lens that shapes it into a 1 cm-diameter collimated beam. Dynamic circular polarization is obtained by combining a Wollaston biprism with a photoelastic modulator (PEM). This circularly polarized light beam is reflected on a beam splitter (BS) to enter the microscope objective (×40). This

objective is unique, it is completely amagnetic and thanks to its a long focal length (2 mm), it allows to focus the beam on the sample through the cryostat quartz optical windows. The cryostat can be cooled down to liquid nitrogen or liquid helium temperature (77 K and 4.2 K respectively) in a continuous nitrogen or helium gas flow. Like in the SpectromagPT setup, the sample is glued on a sample holder mounted on a measurement probe that allows to perform electrical measurements using 10 electrical contacts. The sample lies at the center of a 0.3 T electromagnet with a 10^{-4} T resolution. The whole cryostat is mounted on a x-y translation stage that bring the additional spatial DOF, this stage can adjust the sample position within a 250 nm resolution, allowing to perform optical microscopy and detect in the meantime any physical signal at each laser spot position.

2.5.2 Magneto-optical Kerr effect microscopy

In magnetic materials, light-matter interaction can be used to probe the magnetic state. Indeed, the reflection of linearly polarized light on a magnetized sample modifies its intensity and polarization. This effect is known as the magneto-optical Kerr effect (MOKE), different geometries can be used to obtain vectorial information about the sample magnetization. The incidence angle of light is the key ingredient:
- Illuminating the sample at normal incidence with a linearly polarized light induces a polarization rotation and ellipticity if the sample is perpendicularly magnetized: it is known as the polar Kerr effect.
- Illuminating the sample with oblique incidence results in a polarization rotation and ellipticity if the sample magnetization is in-plane: this is the longitudinal Kerr effect.
To detect the polarization rotation and ellipticity, we use a lock-in technique. For this purpose, the light polarization is modulated by a PEM at $f = 42$ kHz. The PEM is composed of a piezoelectric transducer in contact with a transparent bar. The transducer imposes a periodic deformation to the bar. Under the stress the material becomes birefringent, implying that different linearly polarized lights have different speeds when passing through the material. The stress and birefringence can be adjusted with the applied voltage to the transducer to induce particular retardation values such as $\lambda/2$ or $\lambda/4$. A light source linearly polarized at 45° from the optical axis of the PEM with a $\lambda/4$ retardation becomes circularly polarized. We take advantages of this optical effects to generate a light source with an oscillating circular polarization at 42 kHz. As shown in Fig. 2.11, the linear polarization can be decomposed into two equal components E_x and E_y. At τ_1, E_x is ahead of E_y, resulting in a clockwise circular polarization whereas at τ_2, E_y is ahead of E_x, resulting in a counterclockwise circular polarization.
After the reflection on the magnetic material, the light circular polarization transforms into an elliptical polarization, two quantities can be considered:
- The Kerr ellipticity ϵ_k, results from the helicity-dependent light absorption by the magnetic material. Experimentally it can be detected synchronously with the PEM modulation using

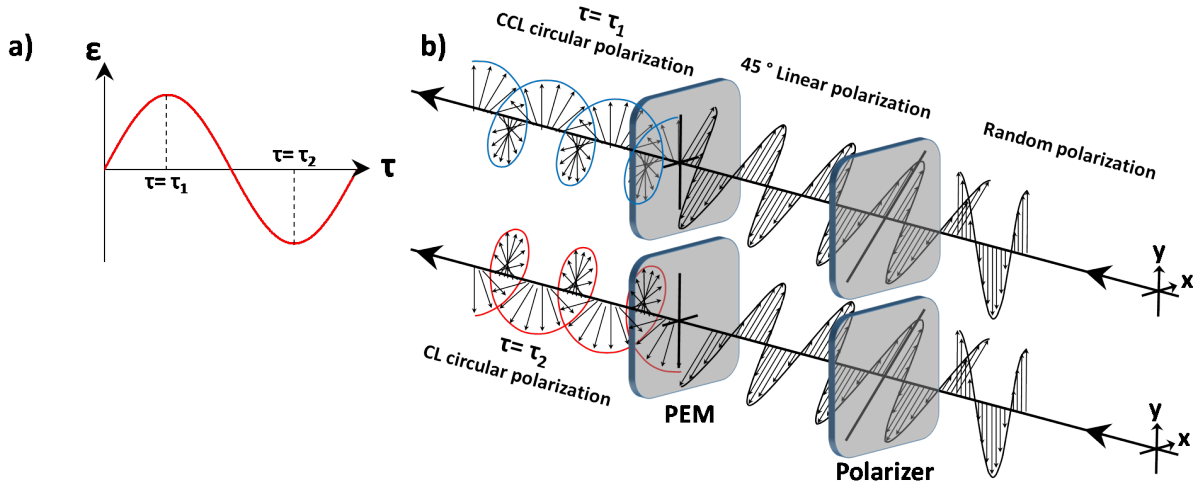

Figure 2.11 – a) Oscillating deformation of the PEM window, at τ_1, the retardation is $\lambda/4$, at τ_2, it becomes $3\lambda/4$. b) Schematic representation of the light polarization state.

a lock-in detection. The light source first crosses a polarizer aligned with one of the PEM optical axis and the light signal is converted into a voltage by a photodiode. The photovoltage is demodulated at the PEM modulation frequency ω. The ellipticity is given by the following expression:

$$\epsilon_k = \frac{\sqrt{2}}{4J_2}\frac{I_\omega}{I_{DC}} \tag{2.4}$$

Where J_2 is the second order Bessel function, I_{DC} the average light intensity and I_ω the first harmonic light intensity.

- The Kerr angle θ_k, results from the light-matter interaction assisted by spin-orbit coupling, it is experimentally detected at the second harmonic of modulation. It is given by the following expression:

$$\theta_k = \frac{\sqrt{2}}{4J_1}\frac{I_{2\omega}}{I_{DC}} \tag{2.5}$$

Fig. 2.12 a) schematically shows a typical polar Kerr microscopy experiment, the studied material is a $(Co/Pt)_n$ multilayer grown on a Ge (111) substrate. The layer is patterned into a Hall bar and mounted in the LUMOS bench. In chapter 5, I will present an extensive study of this system, here I use real data to show an example of LUMOS application.

$(Co/Pt)_n$ multilayers are known to exhibit perpendicular magnetic anisotropy (PMA).[130,131] In usual thin ferromagnetic films the magnetization is always in-plane, as a result of strong shape anisotropy. However, motivated by memory applications, materials with perpendicular magnetization were developed by tuning the interface magnetic anisotropy. Ultra-thin Co film grown on a Pt substrate exhibits a weak PMA, an approach to increase the anisotropy was to switch to multilayers. Indeed, the PMA increases when increasing the number of interfaces,

so by repeating the (Co/Pt) bilayer deposition. Using this technique, we successfully grew perpendicularly magnetized thin films ($t \leq 10$ nm) on Ge (111).

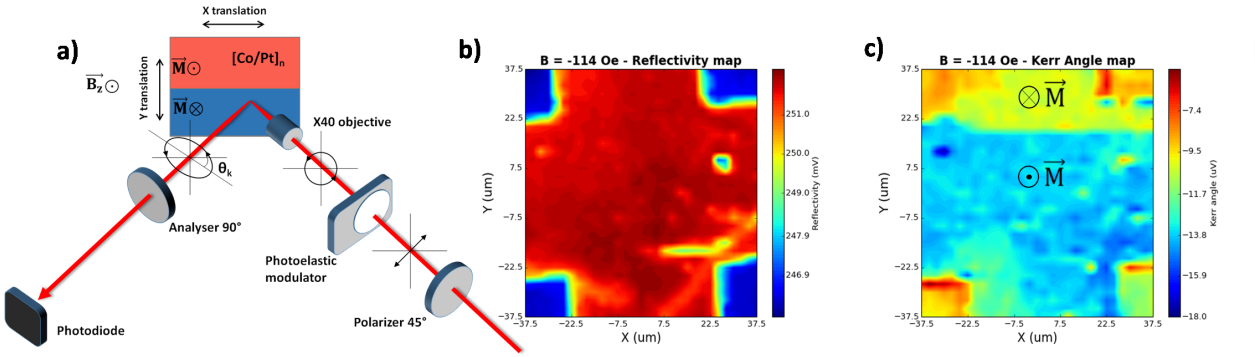

Figure 2.12 – a) Scheme of the optical setup used for Kerr microscopy b) Reflectivity map of the Hall bar. c) Corresponding Kerr microscopy map of the [Co/Pt] magnetization.

Fig. 2.12 b) shows an optical image of one of the Hall bar crosses. To obtain this image, the laser reflection is collected point-by-point by scanning a 1 µm-diameter laser spot on the sample. The light is illuminating the sample at normal incidence and is circularly polarized, therefore, we have access to the out-of-plane magnetization information by measuring the Kerr angle. Fig. 2.12 c) shows the magnetic image of the cross, the sample was intentionally prepared to have a multidomain configuration. This is done by first saturating the sample magnetization in one direction and subsequently applying an opposite magnetic field close to the coercive field.
Using this homemade setup, we can perform Kerr microscopy and image the opposite magnetic domains.

To conclude and summarize this second chapter, I presented the main techniques that I employed all along my PhD work. In the following, we will see how molecular beam epitaxy was used to grow epitaxial topological insulators on a Ge (111) substrate. The structural, electrical and optical techniques presented here will be systematically used to investigate the properties of the materials. Although some techniques are rather usual, I will show in the following chapters that original experiments can be designed by cleverly associating materials and taking advantages of homemade setups were all degrees of freedoms can be controlled as will.

CHAPTER 3

Topological insulator - Semicondutor heterostructures

Topological insulators (TIs) like Bi_2Se_3 are a class of materials with topologically protected surface states (TSS) in which spin-momentum locking may enable spin-polarized and defect-tolerant transport as well as large spin-charge interconversion.[102,114–116,132] The research community has shown an increasing interest for TIs since the first experimental observation of the predicted TSS by spin and angle resolved photoemission spectroscopy (SARPES) in Bi_2Se_3.[105,133] Numerous reports followed this discovery to investigate promising properties: as the charge carriers in the surface states are supposed to be 100 % spin-polarized, one expect a dramatic increase in the spin-charge interconversion efficiency compared to heavy metals like Pt, W or Ta.[69] Using ferromagnetic resonance-based technique (FMR), spin-pumping FMR and spin-torque FMR, large conversion parameters were indeed measured although the two techniques did not converge quantitatively.[117–119] More recently, the high charge-to-spin efficiency was used to manipulate the magnetization state of a large variety of materials with rather low currents and power consumption.[134–138] These experiments are at the heart of modern spin-orbitronics.

Germanium also exhibits interesting properties with respect to the electron spin: in particular, Ge-based spintronic devices offer many advantages such as high carrier mobility, very long electronic spin lifetime[139] and the tunability of the electrical and optical properties.[50,140] All-electrical spin injection and detection have been demonstrated in both n-doped and p-doped Ge films using lateral spin valves,[41,42] three terminal devices[40,43] and spin pumping.[141] Alternatively, spin currents can be optically generated in Ge, with a spin polarization up to 50% thanks to the symmetry of the Ge bandstructure around the Γ point of the Brillouin zone.[53] My PhD work lies in between the well established semiconductor spintronics and the more emerging spin-orbitronics field. We aim at combining the long spin diffusion length of Ge with the spin-momentum locking property at the surface of Bi_2Se_3.

3.1 Growth of Bi_2Se_3 on Ge (111) by MBE and charaterizations

In a first part, I will focus on the epitaxial growth of Bi_2Se_3 on Ge (111). A thorough structural study of Bi_2Se_3 films using electron and X-ray diffraction as well as transmission electron and atomic force microscopy is presented in the following.

3.1.1 MBE growth

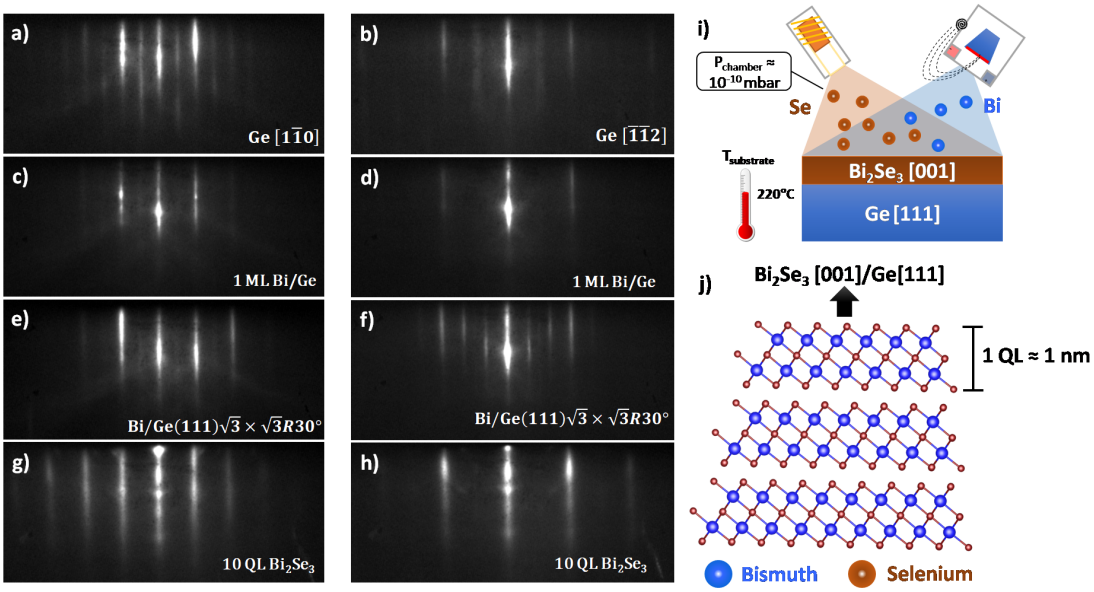

Figure 3.1 – RHEED patterns recorded during the growth of Bi_2Se_3 on Ge (111). a), b) Bare Ge (2×8) reconstructed surface after ion bombardment and annealing up to 850° C. c), d) After deposition of one monolayer of Bi at room temperature. e), f) Bi/Ge (111)-$(\sqrt{3}\times\sqrt{3})R30°$ surface reconstruction after annealing at 500° C during 10 minutes. g), h) 10 QL of Bi_2Se_3 grown at 220° C. i) Sketch of the MBE growth of Bi_2Se_3/Ge (111). j) Quintuple layer structure of Bi_2Se_3, Bi and Se atoms are represented in blue and brown color, respectively.

Ultrathin films of Bi_2Se_3 were grown on Ge (111) by MBE, the surface quality and structure were followed by reflection high-energy electron diffraction (RHEED) all along the growth. Before the growth of Bi_2Se_3, the Ge (111) surface was first annealed up to 850° C under ultrahigh vacuum (UHV) ($p \approx 5\times10^{-10}$ mbar) in order the remove the native germanium oxide. Then, we used soft argon etching and performed a subsequent annealing to obtain the Ge (2×8) surface reconstruction as shown in Fig. 3.1 a) and b). In order to initiate the epitaxial growth of Bi_2Se_3, we first deposited one monolayer (ML) of Bi at room temperature (see Fig. 3.1 c) and d)) and annealed the substrate until the Bi/Ge (111)-$(\sqrt{3}\times\sqrt{3})R30°$ surface reconstruction appeared as shown in Fig. 3.1 e) and f). This Bi layer prevents the reaction of Ge with Se to form GeSe alloys.[142] Bi_2Se_3 was then grown by co-depositing Bi and Se at a substrate temperature of 220°C as illustrated in Fig. 3.1 i). Bi and Se

were evaporated using an e-beam evaporator and a Knudsen cell operating at ≈200° C, respectively. Bi and Se evaporation rates were adjusted in order to reach a high Se:Bi ratio of about 15:1 and limit the presence of Se vacancies in the film. Fig. 3.1 g) and h) show characteristic RHEED patterns along two different azimuths of the as-grown 10 quintuple layers (QL) of Bi_2Se_3 (1 QL corresponds to 1 nm). The lamellar crystal structure is schematically shown in Fig. 3.1 j). We selected this Bi_2Se_3 film thickness because thicknesses above 6 QL are required to obtain a 3D topological insulator behavior with gapless surface states. As demonstrated experimentally by of ARPES in Ref. [106], for thicknesses $>$ 6 QL, the Dirac-cone-like band structure of surface states starts to form with an increased spin polarization of surface electrons. Furthermore, for thicknesses $>$ 6 QL, an increased contribution of the surface states to electrical transport is obtained as shown in Refs. [143, 144]. In particular, the main feature that can be captured in magnetotransport measurements is a crossover from a unitary behavior or weak localization to weak anti-localization when the thickness of the film increases, this is due to a gap opening in the TSS for thicknesses $<$ 6 QL. For thicker films ($>$ 20 QL), an increased bulk contribution is expected to reduce the TSS contribution to electrical conduction. Hence, for a 10 QL-thick Bi_2Se_3 film, the TSS are expected to be gapless and the bulk contribution to magnetotransport to be limited.

3.1.2 Atomic force microscopy and surface morphology

A characteristic AFM image in Fig. 3.2 a) shows the film surface morphology. Typical steps of 1-2 QL height can be seen on the profile shown in Fig. 3.2 b). The root-mean-square roughness is of the order of 0.51 nm. The film is capped with 2 nm of aluminum to prevent from oxidation and pollution. The aluminum layer is grown in two steps: 1 nm was deposited by e-beam evaporation and 1 nm by magnetron sputtering in the same UHV setup in order to gain uniformity. The final RHEED pattern exhibits rings characteristic of a polycrystalline Al layer.

3.1.3 X-Ray diffraction structural analysis

In-plane and out-of-plane X-ray diffraction (XRD) measurements were performed with two different diffractometers. The grazing incidence X-ray diffraction (GIXD) was done with a SmartLab Rigaku diffractometer equipped with a rotating copper anode beam tube (K_α=1.54 Å) operating at 45 kV and 200 mA. Parallel in-plane collimators of 0.5° of resolution were used both on the source and detector sides. The out-of-plane diffraction was performed using a Panalytical Empyrean diffractometer equipped with a cobalt source, (K_α=1.79 Å) operated at 35 kV and 50 mA. The incident beam divergence slit was set to 0.125° and the diffracted beam was measured using a camera PIXcel-3D detector allowing a resolution of 0.02° per pixel. Both diffractometers are equipped with multilayer mirrors on the incident beam and K_β filter on the diffracted beam.

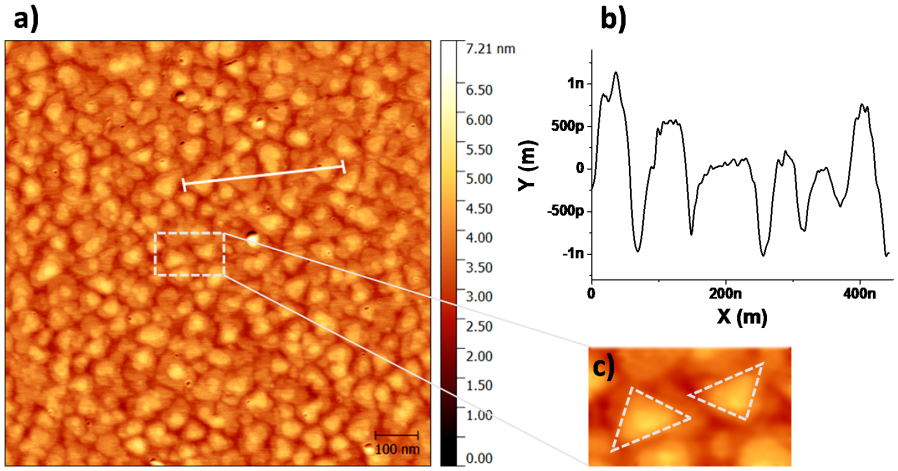

Figure 3.2 – a) Atomic force microscopy image of the 10 QL-thick Bi_2Se_3 film. b) Height profile along the light grey solid line shown in (a). c) Zoom-in of the AFM image showing two triangular grains pointing at opposite directions.

Fig. 3.3 a) shows the symmetric out-of-plane $\theta/2\theta$ diffraction spectrum along the Ge $(h\,h\,h)$ reciprocal space direction. In addition to the substrate Ge (111) peak, the 5 other peaks can be attributed to the rhombohedral structure $R\bar{3}m$ of Bi_2Se_3.[145] They are indexed in the hexagonal unit cell ($a = b = 0.4143$ nm and c =2.8636 nm) which consists of three Se-Bi-Se-Bi-Se quintuple layers separated from each other by a van der Waals gap (see Fig. 3.1 j)). The relative intensities of the peaks are consistent with the calculated structure factors. It can be noticed that the 2 most intense peaks in this reciprocal direction can be easily understood: the (0015) reflection corresponds to the average lattice spacing c/15 of the 15 atomic planes regardless the nature of the atoms, whereas the (006) reflection is attributed to the average lattice spacing separating the 6 Bi atomic layers, Bi having the larger diffusion factor.

Fig. 3.3 b) and c) show GIXD measured with an optimized incidence angle of 0.32°. Radial scans [Fig. 3.3 b)] along the two 30° apart in-plane directions Ge $(2h\,\bar{h}\,\bar{h})$ and Ge $(h\,\bar{h}\,0)$ give the epitaxial relationship between Bi_2Se_3 and the Ge substrate: Bi_2Se_3 (110)‖Ge $(1\bar{1}0)$. The peak positions corresponding to the bulk Bi_2Se_3 ones show that there is no substrate induced in-plane strain. Azimuthal scans around the Bi_2Se_3 (hk0) Bragg peaks [Fig. 3.3 c)] show the in-plane alignment of Bi_2Se_3 and Ge crystals: 30° rotational domains are completely absent. However, pure in-plane measurements cannot exclude twinning which generally occurs due to the simultaneous nucleation of twinned domains on lattice mismatched substrates but with the same in-plane symmetries.[146] Indeed, the ABCAB and ACBAC stackings of the quintuple layer structure give in-plane diffraction peaks {hk0} at the same positions. Nevertheless, the 3-fold symmetry of the out-of-plane {015} reflections allows to quantify the degree of twinning.[147] The measurement shows that the film is composed of both twins in equal proportions which leads to the presence of triangular grains pointing at opposite directions

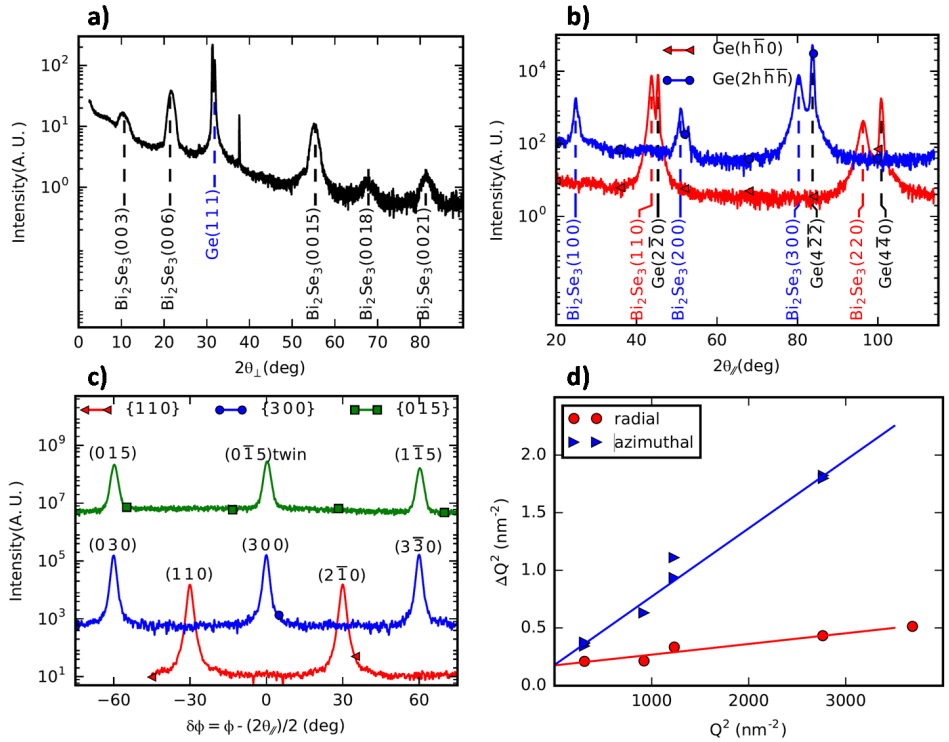

Figure 3.3 – a) Out-of-plane symmetric $\theta/2\theta$ spectrum close to the substrate reciprocal direction Ge $(h\,h\,h)$ substrate. A small offset $\delta\omega = \omega - \theta = 0.25°$ was used to attenuate the substrate peaks. b) In-plane GIXD radial scans along the two reciprocal directions separated from each other by 30°. c) In-plane GIXD azimuthal scans for two peaks families {300} and {110}. The azimuthal scan of the {015} reflection shows the presence of twin domains. This measurement was performed using the same grazing incidence, 0.32°, but with suitable exit angles. d) Square of the FWHM of Bragg peaks (in Q units) as a function of the square of the momentum transfer Q for both in-plane radial and azimuthal scans. The two linear fits show equal intercepts at the origin giving an estimation of the domains size: $D \approx$15 nm.

as shown in Fig. 3.2 c).

From the Bragg peaks width in radial and azimuthal scans as a function of the momentum transfer: $Q = \frac{4\pi}{\lambda} sin(\theta)$, we can estimate the in-plane domain size D, the in-plane mosaicity $\Delta\xi$ and the lattice parameter distribution, $\Delta a/a$ according to the quadratic relations[148]:

$$\Delta Q_{rad}^2 = \left(\frac{2\pi}{D}\right)^2 + Q^2 \left(\frac{\Delta a}{a}\right)^2 \tag{3.1}$$

$$\Delta Q_{azi}^2 = \left(\frac{2\pi}{D}\right)^2 + Q^2 \Delta\xi^2 \tag{3.2}$$

where the radial and azimuthal full width at half maximum (FWHM) in Q units are related to the diffraction peaks widths through the relations: $\Delta Q_{rad} = \frac{4\pi}{\lambda} cos(\theta) \frac{\Delta(2\theta)}{2}$ and $\Delta Q_{azi} = Q\Delta\Phi$. Both least-squares fits in Fig. 3.3 d) give similar domain sizes close to $D = 15$ nm which is a lower bound since we did not consider here the setup resolution. The slopes of

the fits give a lattice parameter dispersion less than 1% (radial) and an in-plane mosaicity of $\Delta\xi = 1.4°$ (azimuthal) which are rather low values considering the presence of twinned domains.[147] Despite their weak intensity, the presence of forbidden peaks like (100) and (200) of Bi_2Se_3 in the radial scan of Fig. 3.3 b) comes from the non-integer number of unit cells in crystal grains. This can be due to a non-uniform layer thickness (10 ± 1 QL), and a substantial twin boundaries density. The absence of thickness fringes around Bragg peaks in the out-of-plane measurements [Fig. 3.3 a)] can also be explained by the film roughness shown in the AFM image of Fig. 3.2 a).

3.1.4 Cross-sectional transmission electron microscopy

We obtain a very sharp Bi_2Se_3/Ge interface with the Bi_2Se_3 (110)||Ge ($1\bar{1}0$) epitaxial relationship as illustrated in Fig. 3.4 a) and b) by cross-sectional transmission electron microscopy. The energy dispersive X-ray spectroscopy maps shown in Fig. 3.4 c) confirm the elemental sharpness of the interface with only little selenium diffusion in the first atomic planes of germanium.

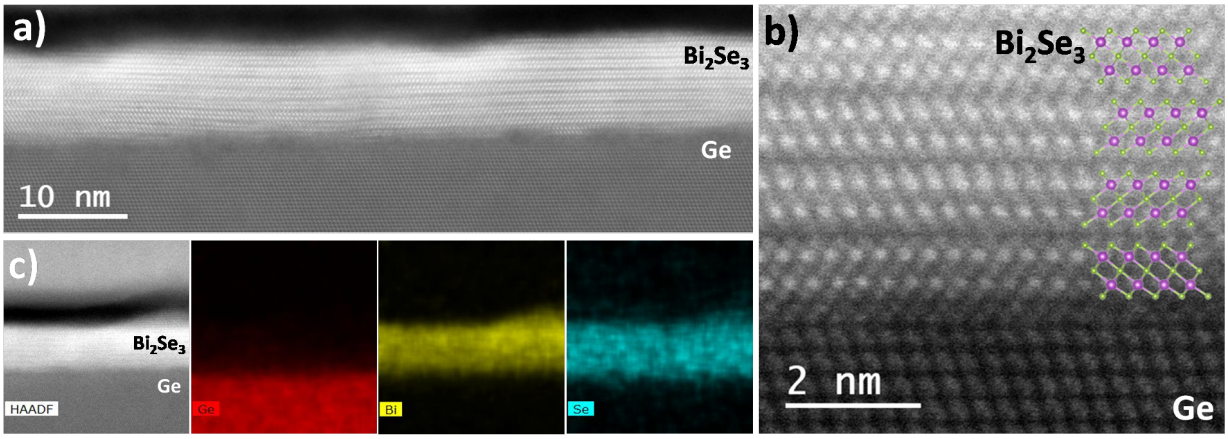

Figure 3.4 – a) Low and b) High magnification transmission electron microscopy cross-section images of the Bi_2Se_3/Ge interface showing the atomic sharpness and epitaxial relationship. c) Energy-dispersive X-ray spectroscopy of the Bi_2Se_3/Ge stack. From the high-angle annular dark-field (HAADF) image, we extracted the elemental maps of Ge, Bi and Se.

3.2 Magnetotransport study

After this careful structural analysis of the heterostructure, I investigated the electrical properties of the bilayer. In a first paper, I could figure out the electrical current distribution in the different parallel conduction channels (surface and bulk Bi_2Se_3 and Ge).[149] Then, at low temperature, I could measure the weak antilocalization effect as a result of two-dimensional transport in the presence of spin-orbit coupling. We could interpret our results as the signature of magnetotransport in a single strongly coupled coherent channel in the presence of surface to bulk scattering.

3.2.1 Two conduction channels in the heterostructure

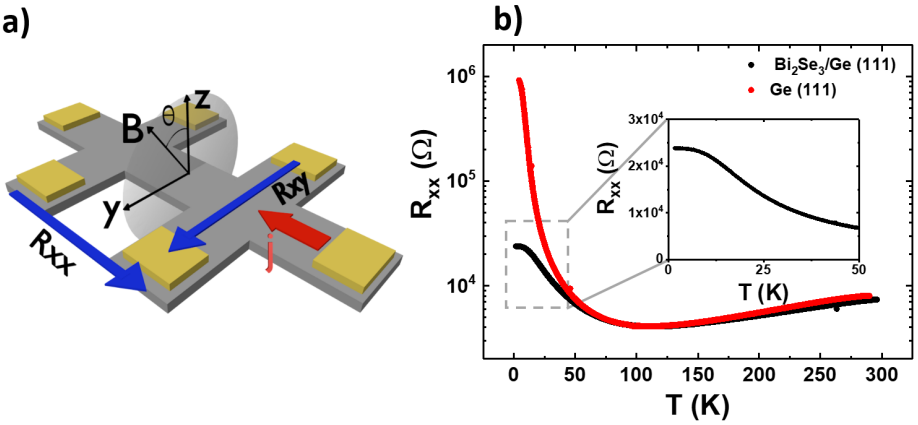

Figure 3.5 – a) Sketch of the Hall bar microstructure and description of the four-probe measurements geometry. b) Log-scale representation of the longitudinal resistance R_{xx} as a function of temperature, the red curve is for Bi_2Se_3/Ge (111) and the black curve for the substrate. Inset: zoom-in at low temperature showing the resistance saturation.

As-grown Bi_2Se_3 films were patterned into micron-sized Hall bars (length $L = 130$ μm and width $W = 10$ μm) as shown in Fig. 3.5 a) to perform magnetoresistance (MR) and Hall measurements. The microfabrication of Hall bars required three successive steps: laser lithography to define the pattern, e-beam evaporation of Au(90 nm)/Ti(5 nm) ohmic contacts and ion beam etching. MR and Hall measurements were performed in a helium closed cycle cryostat working in the 1.6-295 K temperature range and equipped with a superconducting magnet delivering up to 7 Tesla. The red curve in Fig. 3.5 b) shows the temperature dependence of the DC 4-probe longitudinal resistance $R_{xx} = U_{xx}/I$ for an applied current of 10 μA. We find an overall semiconducting character due to the current shunting into the Ge substrate. However, the resistance saturation at low temperature shown in the inset of Fig. 3.5 b) corresponds to electrical transport into the Bi_2Se_3 film due to the increasingly high resistance of the Ge substrate. As a comparison, we show in Fig. 3.5 b) (red curve) the temperature dependence of the Ge substrate resistance.

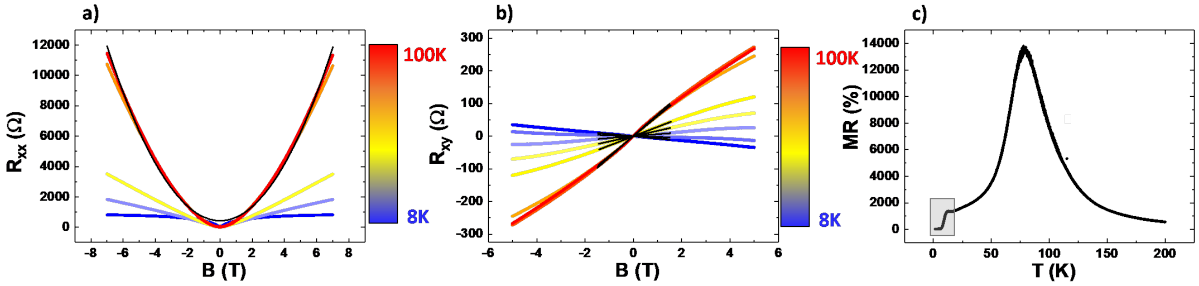

Figure 3.6 – a) Longitudinal magnetoresistance measured at different temperatures with B being perpendicular to the film. b) Transverse resistance R_{xy} in the same geometry as a function of the temperature, the sign of the Hall effect changes as the Ge channel is being activated. c) Continuous MR(T) curve. The grey box shows the transition to magnetotransport in the Bi_2Se_3 film at low temperature.

Fig. 3.6 a) shows MR measurements at high temperatures, where the germanium conducting channel is thermally activated. In this case, we find a conventional Lorentz MR behavior where $\frac{\Delta R}{R_0} \propto (\mu B)^2$ characteristic of a 3D bulk transport. The magnitude of this MR is the one expected from the high carrier mobility in germanium. Fig. 3.6 b) shows R_{xy} as a function of temperature in Hall configuration. When the temperature increases, the sign of the Hall effect changes from negative for n-type doping (Bi_2Se_3 carriers) to positive for p-type doping (Ge carriers). By measuring continuously the longitudinal resistance R_{xx} as a function of the temperature for 0 Tesla and 7 Tesla, we could extract a continuous MR curve given by: $\frac{R_{7T}-R_{0T}}{R_{0T}}$ and shown in Fig. 3.6 c). It shows a maximum at 78 K corresponding to the temperature at which all the dopants in Ge are thermally activated and the electron-phonon scattering is minimum. For $T \leq 10$ K, we observe a sharp drop of the MR when the charge current is no more shunted into the Ge substrate but only flows into the Bi_2Se_3 film where the MR is limited to some percents (see Fig. 3.7 a)).

3.2.2 Weak anti-localization measurements

The weak anti-localization effect (WAL) acts as a quantum correction of the conductance. It finds its source in the theory of quantum electronic transport in disordered systems.[150] The resistivity of a material is related to the probability for a carrier to be transported from point A to point B. Classically, this probability is the sum of the probabilities of each path taken to go from A to B. In quantum mechanics, these paths can interfere with each other constructively if the phase coherence length of the carriers is greater than the mean free path (see Fig. 3.7 c)). When the quantum interference is constructive, the carriers will tend to locate around a scattering impurity, increasing the resistance. By applying a magnetic field, a different phase is added for each path of the carrier, which breaks the phase coherence and thus the constructive interference. This is called negative magnetoresistance since the application of a magnetic field makes the material less resistive by eliminating the weak

localization effect. In materials where the spin-orbit coupling (SOC) is strong, (i.e. the spin of a carrier is strongly connected to its momentum), each diffusion modifies the spin state of the carrier. This has the effect of adding a random phase term to the wave functions and thereby eliminating constructive interference. Here, when applying the magnetic field, we force the spins of the carriers to align along the field and thus re-phase the wave functions, allowing the interferences to set in again. This gives rise to a positive magnetoresistance, i.e. the increase of the material rsistance when applying a magnetic field.

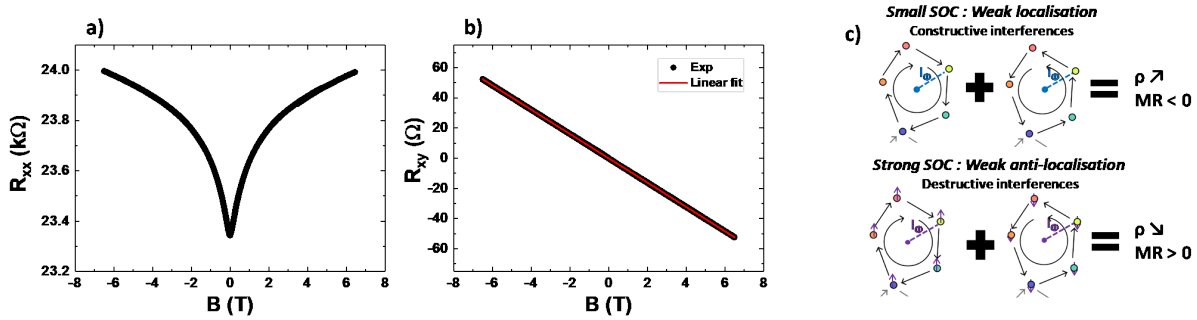

Figure 3.7 – a) R_{xx} as a function of the applied magnetic field at 1.6 K. The field is perpendicular to the film. b) Corresponding transverse Hall resistance R_{xy} at 1.6 K. c) Closed-loop scattering processes inducing quantum interferences between clockwise and counterclockwise carrier diffusion paths.

Fig. 3.7 a) and b) show longitudinal and transverse resistance measurements recorded at 1.6 K with an applied current of 1 μA. R_{xx} clearly exhibits a MR dip at low magnetic field corresponding to the weak anti-localization effect. The linear dependence of R_{xy} on the magnetic field is interpreted in terms of a single-carrier electrical transport. From the slope, we obtain a n-type doping as expected for MBE-grown Bi_2Se_3 films where Se vacancies act as donors. We find a carrier concentration of 4.6×10^{19} cm^{-3} assuming 3D transport (both into surface states and the bulk) and 5.4×10^{13} cm^{-2} if we consider 2D transport into the surface states. We further find a low mobility of 37 cm^2/(V.s) which might be explained by the high concentration of twin defects as unveiled by XRD and AFM measurements.
The observation of WAL strongly suggests a 2D electrical transport in the presence of spin-orbit coupling.[150,151] This is supported by the temperature and angular dependences of the magnetoresistance. Fig. 3.8 a) presents MR measurements as a function of the projected magnetic field $B_\perp = B \times \cos(\theta)$. All the curves perfectly overlap at low fields which is the signature of WAL.[152] Fig. 3.8 b) shows the film magnetoconductance at temperatures varying from 2 K to 6 K. In Fig. 3.8 b), the data are fitted using the Hikami-Larkin-Nagaoka (HLN) two-dimensionnal quantum diffusion model:[107,108,150]

$$\Delta C = -\frac{\alpha e^2}{2\pi^2\hbar}\left[\psi\left(\frac{\hbar}{4eBL_\phi^2}+\frac{1}{2}\right) - ln\left(\frac{\hbar}{4eBL_\phi^2}\right)\right] \tag{3.3}$$

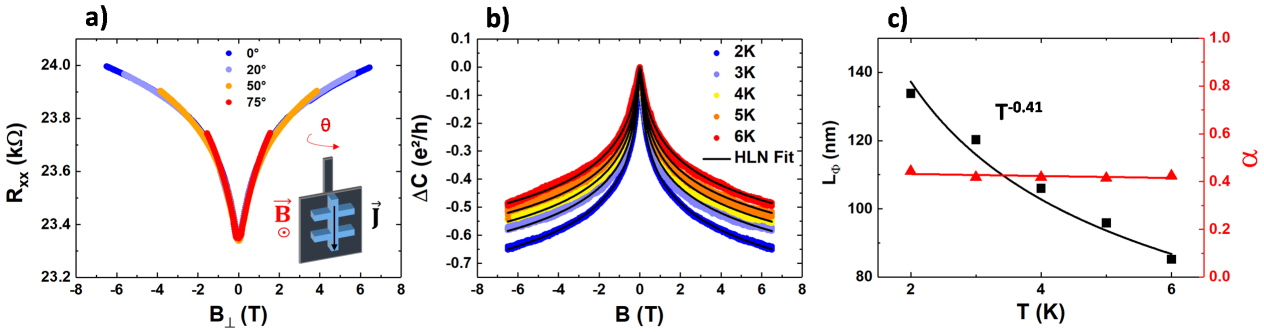

Figure 3.8 – a) R_{xx} as a function of $B_\perp = B \times \cos\theta$. The angle θ is shown in the inset and defined as the angle between the surface normal and the applied magnetic field. b) Magnetoconductance ΔC normalized to the quantum of conductance e^2/h as a function of temperature. Black solid lines are fits using the HLN model. (c) Parameters extracted from the HLN model: L_ϕ is the effective phase coherence length and α, the characteristic parameter related to the number of transport channels.

where ψ is the digamma function, B is the applied magnetic field perpendicular to the film, L_Φ is the effective phase coherence length and α a parameter related to the number of channels contributing to the transport.[153,154] $\alpha = 0.5$ is for one channel contributing to the transport and $\alpha = 1$ for two channels contributing. In the literature, α varies from 0.25 to 1 depending on the thickness,[109,110] or the film fabrication technique.[155] Using the HLN model, we can extract a temperature independent α value of 0.42. This value is close to 0.5 which corresponds to a single conducting channel. For a 10 QL-thick Bi_2Se_3 film, bulk states are quantized and we can exclude pure magnetotransport into those 2D bulk states since they should give rise to a weak localization (WL) signal as predicted by Shen *et al.*[151] Considering the high electron density extracted from Hall measurements, the Fermi energy is larger than the energy spacing between the quantized bulk states of the 10 QL-thick Bi_2Se_3 film. Hence, those bulk states are energetically accessible for electron transport and scattering (non-TI regime). As a consequence, magnetotransport and the WAL take place in a single coherent channel corresponding to strongly coupled surfaces and bulk states.[156]

We find an effective phase coherence length L_ϕ of 110 nm at 1.6 K which corresponds to a lower bound as compared to the values already published: 106-237 nm[153]; 100-600 nm[143]; 75-200 nm[157]; 100-1000 nm[109] or 15-300 nm.[158] L_ϕ decreases with increasing the temperature as $T^{-0.41}$, which is in good agreement with the theory predicting $L_\phi \propto T^{-0.5}$.

3.2.3 Semiconductor-Topological insulator *pn* junction diode effect

Fig. 3.9 a) shows MR measurements at 1.6 K for bias currents varying from 1 μA to 50 μA. To eliminate the offset voltage due to thermal effects, the current sign is changed from $+I$ to $-I$ and the longitudinal resistance is calculated using: $R_{xx} = \frac{R_{+I}+R_{-I}}{2}$. Two different transport regimes can be observed depending on the applied magnetic field. The critical field separating those two regimes (indicated by arrows in Fig. 3.9 a) increases with the bias current. By measuring $I(V)$ curves at different magnetic fields in Fig. 3.9 b), we find the characteristic magnetic field dependence of a *pn*-junction $I(V)$ curve[159,160] in parallel with a resistor. The *n*-doped (resp. *p*-doped) layer can be associated to the Bi_2Se_3 film (resp. the germanium substrate). When the current is kept low enough ($\approx$ 8 μA), the $I(V)$ curve keeps a ohmic character and the magnetotransport takes place in the Bi_2Se_3 film only. For a current higher than 8 μA, the current source generates a high enough bias voltage to make the *pn*-junction conducting and the current mostly flows into germanium. Despite its high resistivity (1 kΩ.cm at 2 K), the germanium substrate is thick enough so that its resistance is much lower than the one of the Bi_2Se_3 film. This regime corresponds to the steeper slope in the $I(V)$ curve. The diode threshold voltage V_d increases with the applied magnetic field. Hence, for a given bias voltage, the magnetic field allows to select the conducting channel and magnetotransport properties.

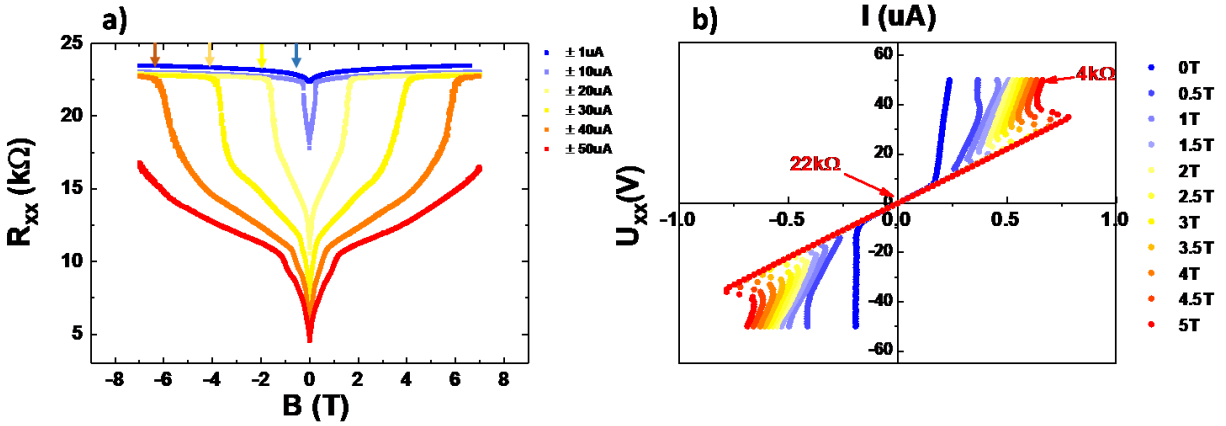

Figure 3.9 – a) Field MR curves measured at 1.6 K for different applied currents with the field perpendicular to the film. Two magnetotransport regimes can be clearly identified. The transition magnetic field is indicated by arrows. (b) $I(V)$ curves at different magnetic fields exhibiting a *pn*-junction behavior.

In regime 1, when the applied magnetic field is lower than a critical field (marked by a vertical arrow in Fig. 3.9 a)), the current flows in the germanium substrate and the resistance (resp. MR) is low (resp. high). In regime 2, when the applied magnetic field is higher than the critical field, the current flows in the Bi_2Se_3 film and the resistance (resp. MR) is high (resp. low). At the transition between the two regimes, we observe very sharp steps in MR curves

in Fig. 3.9 a) with slopes up to 20 Ω/mT and negative differential resistances in $I(V)$ curves (Fig. 3.9 b)).
This *pn*-junction effect at a semiconductor/topological insulator could be of great interest to tune spin transport since one can control whether the charge current is spin-polarized (regime 2) or not (regime 1). It also paves the way to develop spin-FET structures where the spin information can be transmitted by the application of an electric field.

To conclude this study, we have successfully grown by epitaxy a 10 QL-thick Bi_2Se_3 film on germanium. Despite the presence of twin boundaries, we obtained a high-crystalline quality material with a surface roughness of ±1 QL. Low temperature magnetotransport measurements showed the signature of two-dimensional weak antilocalization in a single coherent channel corresponding to strongly coupled surface and bulk states with a phase coherence length of the order of 110 nm at 2 K. By studying the temperature dependence of the MR and Hall effect, we found that the electrical current flows into the Bi_2Se_3 film at low temperature. In this case, we measured a low MR and *n*-type doping. When the temperature increases, the electrical current is progressively shunted into the Ge layer and we measured a high MR and *p*-type doping. Finally, at 1.6 K, we could tune the conduction channel between Bi_2Se_3 and Ge by adjusting the bias voltage or the applied magnetic field. Hence, it could be possible to select electrically or magnetically the Bi_2Se_3 conduction channel with spin-momentum locking or the Ge conduction channel with a long spin diffusion length. These findings pave the way to design innovative spintronic devices by combining semiconductors and topological insulators for which the energy barrier between the two materials acts as a controllable switch between two spin transport regimes.

3.3 Optical spin orientation and spin-to-charge conversion

In the past decade, the discovery of topological insulators (TIs) has promised a breakthrough in the efficiency of the spin-charge interconversion phenomena, since TIs are known to host topologically-protected surface states (TSS) with spin-momentum locking,[102] this has been experimentally verified by means of photoemission measurements,[105,133] scanning tunneling microscopy and magnetotransport experiments.[109,161,162] In particular, the conversion of a charge current, flowing into the TSS, into a spin current is called the Rashba-Edelstein effect (REE), whereas the reverse process is referred to as the inverse Rashba-Edelstein effect (IREE).[18,61] In these systems, the most important parameter to address is the spin-charge interconversion efficiency $\lambda_{\mathrm{REE(IREE)}}$. However, an experimental estimation based on spin pumping-ferromagnetic resonance (FMR) or spin torque-FMR is questionable,[117–119] since TIs are known to chemically react, when they are in contact with a ferromagnetic metallic film.[163] Therefore, a non-local architecture where spins are optically generated in Ge and electrically detected in a thin TI film, deposited on top of Ge, would represent a convenient route to avoid the aforementioned issue. The following results are published in Ref. [164].

3.3.1 In-plane optical spin orientation using scanning confocal microscopy

When circularly polarized light is absorbed by a semiconductor, the optical spin orientation process occurs, generating spin-polarized electron-hole pairs at the Γ point of the Brillouin zone. The photogenerated electrons spin polarization is defined as:

$$P = \frac{n_\uparrow - n_\downarrow}{n_\uparrow + n_\downarrow} \tag{3.4}$$

Where $n \uparrow (\downarrow)$ is the spin-up (down) density referred to the quantization axis given by the direction of the light wave vector in the material. Photogenerated holes are rapidly depolarized due to their very short spin lifetime.[41] Resonant absorption can be achieved by setting the wavelength at the Ge direct gap (λ = 1550 nm), where P reaches 50 %.[53] Right after the photogeneration, spin-oriented electrons thermalize from the Γ to the L valleys within approximately 300 fs, maintaining most of their spin polarization.[50] In the microscope, the laser beam impinges the sample at normal incidence and only an out-of-plane spin polarization is generated by optical spin orientation in Ge, preventing any electrical spin detection by the Bi_2Se_3 or Pt bars. The Pt micro-stripes allow to overcome this issue, when the sample is illuminated with circularly polarized light focused at the edge of a Pt stripe, the x component of the field induces oscillating charges in the Ge substrate, inducing a near-field with a large out-of-plane component (z) direction. The latter is in antiphase with respect to E_x, it combines with the incoming E_y and results in an elliptic field polarization in the yz plane that can generate electrons with spin polarization along the x axis.[139] As a consequence of the field symmetries, opposite spin polarization is attained at opposite edges

of the Pt stripes.

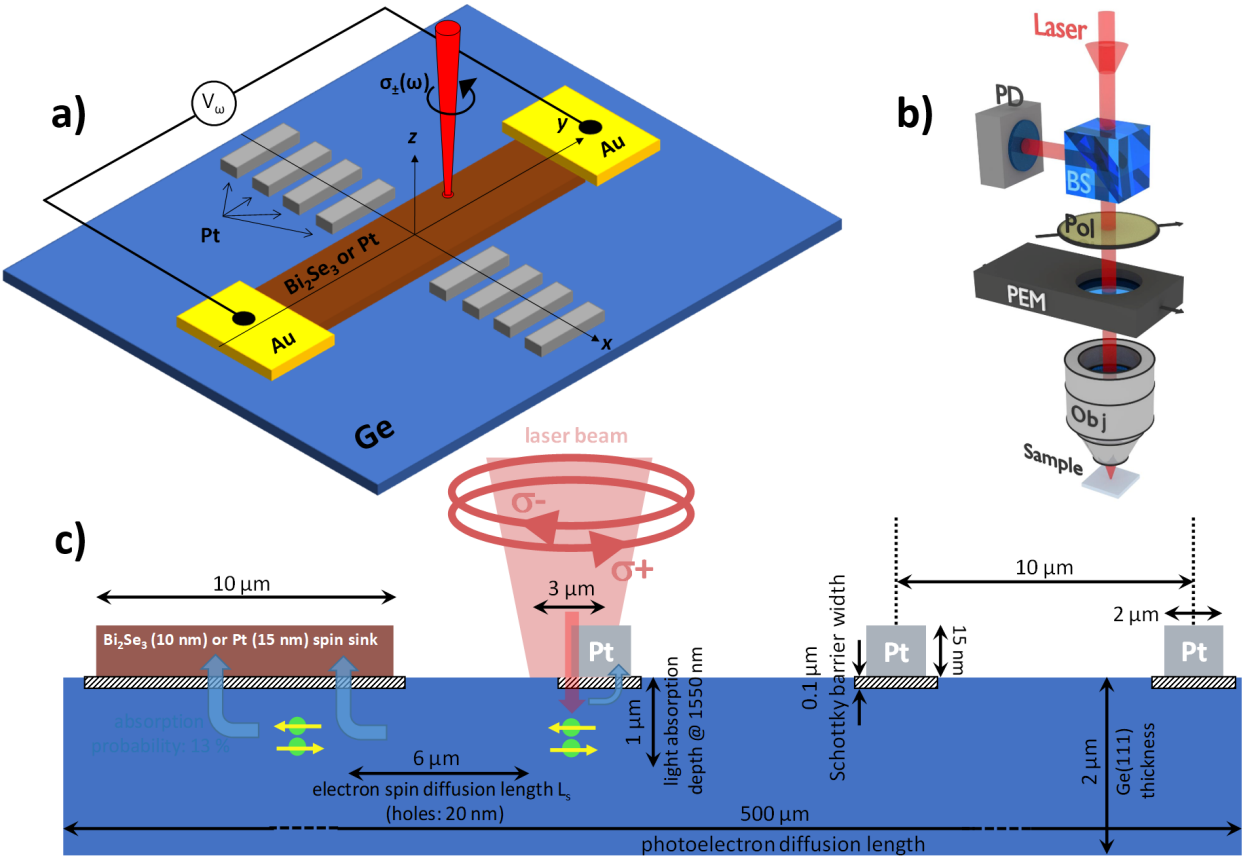

Figure 3.10 – a) Sample layout. The vertical brown bar represents the spin-detector and is made either of Bi_2Se_3 or platinum. The bar is electrically contacted by two Ti/Au pads. b) Confocal microscopy setup. PD, BS, Pol and PEM represent the photodetector, beam splitter, polarizer and photo-elastic modulator respectively. c) Schematics of the device in cross-section summarizing all the dimensions and relevant characteristic lengths.

Here, we probe the spin-to-charge conversion in a Bi_2Se_3/Ge (111) heterostructure at room temperature. The investigated sample is sketched in Fig. 3.10 a), it is composed of a 2 µm-thick n-doped Ge (111) film (doping concentration $N_d = 9 \times 10^{16}$ cm^{-3}), epitaxially grown on a Si substrate of 800-1200 Ω·cm resistivity. A 10 QL-thick Bi_2Se_3 single crystalline film is grown by the MBE process detailed in sect. [3.1.1]. The film is then patterned into a $75 \times 20 \mu m^2$ bar using the process given in sect. [2.3.3]. Briefly, we use laser lithography and Ar ion-beam etching to define the pattern and two Au(120)/Ti(5) electrical contacts are deposited by e-beam evaporation. A 80 nm-thick SiO_2 layer is inserted between the Au/Ti pads and germanium to prevent direct spin absorption by the contacts. Multiple $20 \times 2 \mu m^2$ Pt microstructures of 15 nm-height are finally evaporated on the Ge film by e-beam evaporation beside the Bi_2Se_3 bar.

As shown in Fig. 3.10 b), when the circularly-polarized light beam impinges on the edge of a Pt stripe, a highly-localized spin population polarized along the x-axis is generated, through

the optical spin orientation technique,[55] in the Ge layer underneath the Pt edge.[165] If the light impinges on the opposite edge of the Pt stripe, the direction of the spin-polarization parallel to the x-axis is reversed, as previously demonstrated in Ref. [165]. After generation, the spin-polarized electrons diffuse in the Ge substrate toward the detection bar, where spin-to-charge conversion occurs and the spin current is converted into an equivalent charge current directed along y. Since we are in open circuit detection conditions, this equivalent charge current is actually detected as a voltage drop ΔV between the electrodes.

To estimate the fraction of photons with in-plane angular momentum when light impinges the edge of a platinum stripe, three-dimensional numerical simulations have been performed by applying finite-difference time-domain simulations.[165,166]

We reproduce the experimental illumination conditions, with complex dielectric constants $\epsilon_{\mathrm{Ge}} = 19 + i\,0.087$ and $\epsilon_{\mathrm{Pt}} = -21.36 + i\,74.8$ for Ge and Pt, respectively.[167] The Stokes parameter $c_x = 2\,\mathrm{Im}\{E_z E_y^*\}$ is calculated inside the Ge substrate when the focus of the light beam is centered on the edge of a Pt microstructure. In this geometry, the fraction of photons with a projection of the angular momentum along the x-axis of the sample is estimated as the ratio between the integral of c_x and the integral of the total electric field intensity $I = E_x^2 + E_y^2 + E_z^2$ over the volume of the Ge film. The result is further normalized to the fraction of impinging photons that are absorbed in Ge, yielding to a final value of $\eta_{\mathrm{g}} = 2.2\,\%$.

3.3.2 Quantification of the spin-to-charge conversion

Experimental results

The reflectivity and IREE maps of the sample are shown in Fig. 3.11 a) and b), respectively. At variance with the optical signal, the IREE signal is reversed when the opposite Pt edges are illuminated. This is a fingerprint of the spin-related nature of the detected voltage ΔV_{IREE}, since electrons, photogenerated at opposite edges of each Pt stripe, have opposite in-plane spin polarization along the x-axis.[165,168] Moreover, due to spin relaxation, ΔV_{IREE} clearly decreases when illuminating Pt microstructures far from the Bi_2Se_3 detection bar.

This can be highlighted by the profile of both the reflectivity and IREE signals, integrated over the whole length of the Pt stripes along the y-axis, as shown in Fig. 3.11 c) and d). Indeed, by varying the distance between the injection and detection points, it is possible to estimate the electron spin diffusion length L_{sf} in the Ge (111) film. To this aim, we report in Fig. 3.11 e) the amplitude of the $|\,\Delta V_{\mathrm{IREE}}\,|$ signal at correspondence with the edges of each Pt microsctructure. Then, we consider a simple unidimensional spin diffusion model, so that $|\,\Delta V_{\mathrm{IREE}}\,| \propto e^{-x/L_{\mathrm{sf}}}$.[168] This expression is then used to fit the ΔV_{IREE} dependence upon x of Fig. 3.11 e), by assuming L_{sf} as the only free parameter. We finally estimate $L_{\mathrm{sf}} = 5.8 \pm 0.7$ μm, slightly lower than the value reported for the Ge (001) substrates with similar doping (note that we neglect the spin absorption by the Pt stripes).[168]

The same analysis, summarized in Fig. 3.12, has been performed for a second sample where the detection bar is now made of Pt. Panels a) and b) show the reflectivity and the normalized

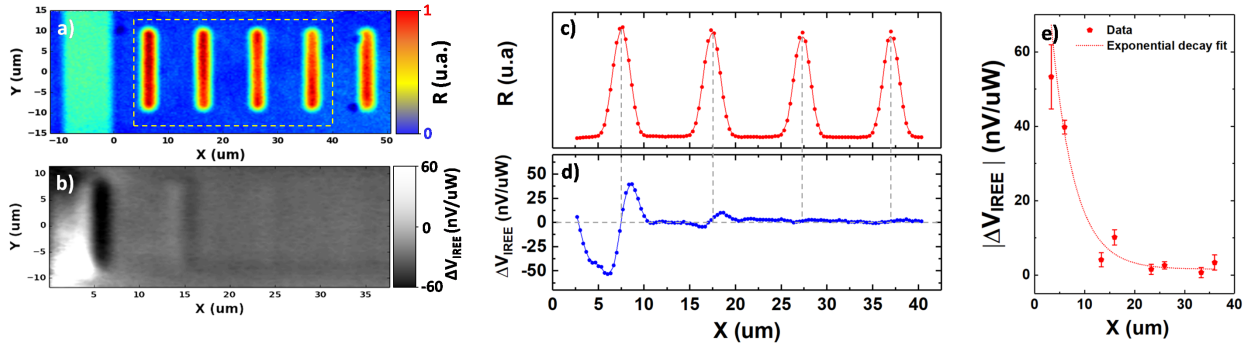

Figure 3.11 – Optical (reflectivity) a) and electrical (IREE) map b) of the Bi_2Se_3/Ge (111) sample. Profiles of the c) reflectivity and d) IREE signal along the x-axis of the sample integrated along y. (e) Absolute value of the IREE signal at correspondence with the right edge of each Pt microstructure.

ISHE voltage map of the sample, respectively, while in panels c) and d) we report the profiles along the x axis of the two maps. In panel e), we plot the dependence of the absolute value of the ISHE signal acquired at correspondence with the Pt edges as a function of the distance from the spin detector. We find $L_{sf} = 6.0 \pm 1.1$ μm, which perfectly matches the value obtained with the Bi_2Se_3 sample.

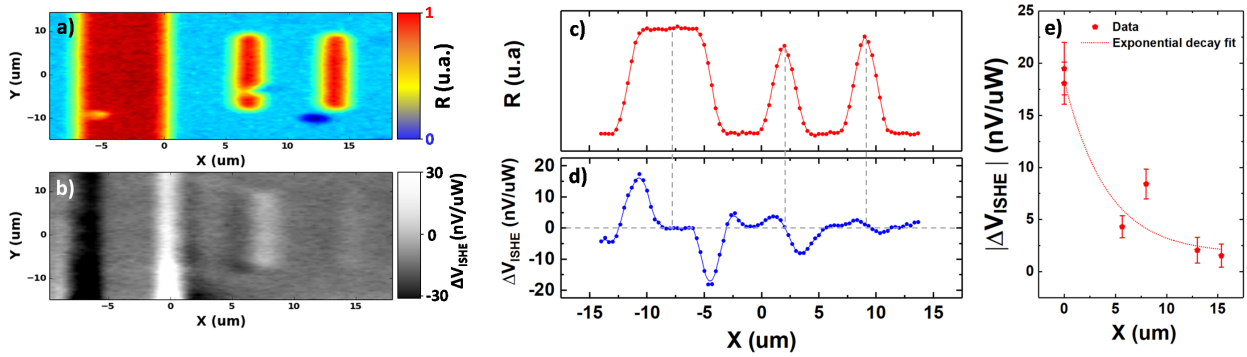

Figure 3.12 – Reflectivity (a) and ISHE map (b) of the Pt/Ge (111) sample. Profiles of the (c) reflectivity and (d) ISHE signal along the x-axis of the sample. (e) Absolute value of the ISHE voltage $|\Delta V_{\mathrm{ISHE}}|$ at correspondence with the edges of each Pt microstructure.

Since the spin injection and transport mechanisms are the same for the two samples, it is possible to quantitatively compare the results obtained with the Bi_2Se_3 and Pt detectors. First, from Fig. 3.12 a) and b), we observe that the Bi_2Se_3 detection provides a negative (positive) voltage drop when the focused light beam illuminates the left (right) edge of the Pt injection stripes. Conversely, when SCC is performed via the ISHE in Pt, the signal is positive (negative) at the left (right) edge of the injection microstructures (see Fig. 3.12 c) and d)). Hence, the sign of the spin-to-charge conversion in Bi_2Se_3/Ge is found to be opposite to that in Pt. Previous experiments were performed to characterize the spin-to-charge conversion in Bi_2Se_3 thin films[117–119] and, at variance with our result, the conversion parameter

was always measured with the same sign as the ISHE in Pt, which we arbitrarily define as "positive". Although the SCC measurements in Refs. [117–119] were carried out with the TI in direct contact with a ferromagnet, this positive sign is also expected from photoemission spectroscopy[105,106] and electrical spin detection.[169,170] Hence, as further discussed in the following, our experimental results suggest that the spin-split states at the Bi_2Se_3/Ge (111) interface display a substantially different SCC behavior compared to the ones of a freestanding Bi_2Se_3 surface.

Beyond this sign reversal, the comparison of Fig. 3.11 and Fig. 3.12 allows one to estimate the relative spin detection efficiency of Bi_2Se_3/Ge and Pt. With the light beam focused on the first Pt stripe ($x = x_0 \approx 6$ µm), we measure $\Delta V_{\mathrm{IREE}}/W \approx 40$ nV/µW for Bi_2Se_3/Ge and $\Delta V_{\mathrm{ISHE}}/W \approx 7$ nV/µW for Pt. Since the two samples only differ by the spin detector, we conclude that the overall efficiency for spin detection with Bi_2Se_3/Ge is a factor 5 larger than with Pt. The insulating character of bulk TIs indeed produces higher voltage drops compared to a metal like Pt for the same charge current.

Modeling the spin-to-charge conversion

The macroscopic spin-to-charge conversion parameter is given by:

$$\gamma = i_c/i_s \tag{3.5}$$

i_s being the spin current entering the detector and i_c the equivalent charge current across the detection bar, defined as the ratio between the open circuit ISHE or IREE signal ΔV and the detector resistance R:

$$i_c = \Delta V/R \tag{3.6}$$

If we assume the same value of i_s for the two samples (due to equal spin injection and transport mechanisms), the relative spin-to-charge conversion efficiency of the materials is

$$\gamma_{BiSe}/\gamma_{Pt} = i_{c,BiSe}/i_{c,Pt} \tag{3.7}$$

Considering the ΔV values for $x = x_0 \approx 6$ μm and being $R_{BiSe} \approx 10$ kΩ and $R_{Pt} \approx 500$ Ω the detector resistance (that includes possible shunting in Ge), as measured by a four-probe technique, we obtain $\gamma_{Pt} \approx -3.5\,\gamma_{BiSe}$. The absolute determination of γ requires the knowledge of i_s.

To estimate its value, we start from the spin current excited at the generation time:

$$i_{s,0} = (TW/\hbar\omega)\,P\,\eta_g \tag{3.8}$$

$T\,W/\hbar\omega$ is the photon absorption rate ($T \approx 0.6$ is the transmittance of Ge at $\hbar\omega = 0.8$ eV and W the impinging light power), η_g the fraction of absorbed photons with a projection of the angular momentum along the x-axis and $P = 50\,\%$[55] is the ratio between spin-polarized photogenerated electrons and absorbed photons. Exploiting numerical simulations, we obtain the value $\eta_g \approx 2.2\,\%$ when the light beam is focused on the edge of a Pt stripe. The spin current reaching the position of the detector is $i_{s,0}\,e^{-x_0/L_s}$, the exponential term accounting for the spin depolarization along the distance x_0 from the generation point to the detector. Because of the built-in electric field of the junction, only a fraction η_t of the spin-polarized electrons reaching the detector position effectively enters the detector and thus contributes to the measured signal. We calculate η_t by applying the same numerical simulations detailed in Ref. [171], which account for the Schottky barrier height (SBH) Φ_{bar} between the detector and the Ge substrate and the barrier reduction Φ_{ph} produced by the photovoltaic effect.

We experimentally measure the SBH by performing three-probe transport measurements. A DC current is circulating from the Schottky contact (Bi_2Se_3/Ge or Pt/Ge) to an ohmic Au/Ti contact in the substrate. The interfacial voltage drop is recorded using a third contact which acts as potential reference (see Fig. 3.13). Several $I(V)$ curves were recorded as a function of temperature and fitted with the following equation:

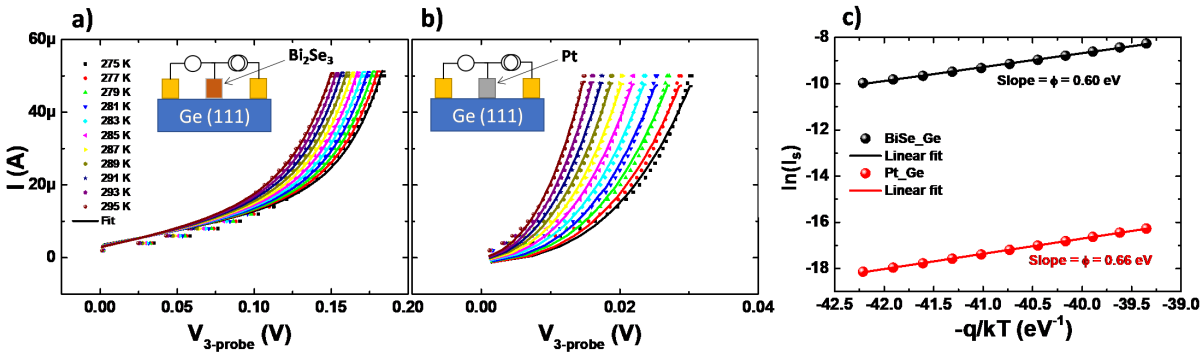

Figure 3.13 – Temperature dependent three-probe I(V) curves for a) Bi_2Se_3/Ge (111) b) Pt/Ge (111) interfaces. Data are fitted according to the Eq. [3.9]. c) Extraction of the Schottky barrier height using the Eq. [3.11].

$$I = I_S \left[\exp\left(\exp \frac{qV}{k_B T} \right) - 1 \right] \tag{3.9}$$

where the extraction saturation current I_S can be expressed as:

$$I_S = A_{eff} A^{\star} T^2 \exp\left(\frac{q\phi_{\mathrm{SBH}}}{k_B T} \right) \tag{3.10}$$

or:

$$\ln\left(I_S\right) = cnst + \phi_{\mathrm{SBH}} \times \frac{q}{k_B T} \tag{3.11}$$

This method simplify the fitting procedure as the material constant and geometry are not necessary. Finally we extract $\Phi_{\mathrm{SBH,BiSe}} \approx 0.60$ eV and $\Phi_{\mathrm{SBH,Pt}} \approx 0.66$ eV, as expected from the Fermi level pinning at the surface of Ge due to the presence of surface/interface states.[172] We also calculate the value $\Phi_{\mathrm{ph}} = 0.29$ eV for both samples using the Nextnano software.[173] With these parameters, we obtain $\eta_{\mathrm{t,BiSe}} = \eta_{\mathrm{t,Pt}} = 13\,\%$.

Numerical estimation of the conversion parameter

We validate the numerical model with Pt, for which the spin Hall angle has been addressed by several works in the literature. In this case, we have measured $\Delta V_{\mathrm{ISHE}}/W = 7$ nV/μW (obtained for an incident optical power $W = 15$ μW) at $x = x_0 \approx 6$ μm, corresponding to $i_{\mathrm{c}} = 210$ pA. Our numerical estimation of i_{s} yields $i_{\mathrm{s}} = 6$ nA, giving $\gamma_{\mathrm{Pt}} \approx 3.5\,\%$. This value is comparable to previously reported ones for evaporated Pt films,[174,175] therefore we apply the same model to the sample with a Bi_2Se_3 detector. At $x = x_0 \approx 6$ μm, we obtain $\Delta V_{\mathrm{IREE}}/W = -40$ nV/μW (measured with $W = 18$ μW). Hence $i_{\mathrm{c}} = -72$ pA and $i_{\mathrm{s}} = 7.2$ nA, yielding $\gamma_{\mathrm{BiSe}} \approx -1\,\%$.

Since the spin-to-charge conversion by the IREE occurs in surface states, the relevant parameter describing the SCC efficiency is the inverse Rashba-Edelstein length λ_{IREE}, which

can be obtained as the product between the macroscopic efficiency parameter γ_{BiSe} and the spatial extension d of the surface or interface states in which the conversion takes place. In bulk-terminated Bi_2Se_3, the extension of the TSS is $d = 3$ nm from Ref. [106]. In our case, the extension of Bi_2Se_3/Ge interface states is given by first principles calculations in the next section. Note that, to derive λ_{IREE} from BiSe, we only need to consider SCC occurring in the Bi_2Se_3/Ge interface states and neglect SCC at the opposite Bi_2Se_3 free surface, since the film is thicker than the spin diffusion length.[176]

3.3.3 Understanding the spin-to-charge conversion origin: ab-initio calculations

In order to understand the opposite SCC signs for the two samples, we have performed first principle relativistic calculations to unveil the spin-resolved band structure at the Bi_2Se_3/Ge interface. We first consider eight quintuple layers (8 QL) of Bi_2Se_3. In Fig. 3.14 a), the band structure is plotted along the K-Γ-M direction as shown in the inset. In this particular direction along which K-Γ (Γ-M) is parallel to the x (y) direction, we plot the band structure weighted by the y (x) spin component S_y (S_x) of the topmost QL, as highlighted by the thick red and blue lines. The red (blue) color indicates an in-plane spin pointing in the positive (negative) direction of the axis. We clearly observe the presence of surface states belonging to Dirac cones. Due to spin-momentum locking characteristic of TIs, the in-plane spin helicity of the surface states above the Dirac point (characterized by a positive dispersion) displays a clockwise (CW) chirality, while the helicity of states below the Dirac point (with a negative dispersion) is counterclockwise (CCW). Because of the opposite dispersion relation, both types of chiral states (either above or below the Dirac point) thus lead to a *positive* λ_{IREE} value and to the same sign of the SCC coefficient as the one observed in platinum.[125]

Fig. 3.14 b) displays the band structure of 8 QL of Bi_2Se_3 in contact with 3.2 nm of Ge. Compared with pure Bi_2Se_3, many additional electronic states appear due to the strong hybridization with Ge. The same color code are used to highlight the spin texture at the Bi_2Se_3/Ge interface. Interestingly, due to the strong hybridization between Bi_2Se_3 and Ge orbitals, the bottom Dirac cone is inverted. This cone inversion gives rise to a Rashba-like helical spin texture exhibiting a counter-clockwise (CCW) chirality of the outer contour for -0.05 eV $< E - E_{\mathrm{DP}} <$ 0.15 eV, E_{DP} being the energy of the Dirac point. Therefore, in this energy range, the CCW spin chirality of the outer contour leads to a *negative* λ_{IREE} value. First principles calculations thus qualitatively support our experimental observations concerning the sign of the spin-charge conversion.

We can conclude that SCC does not take place in the TSS of Bi_2Se_3 but rather in hybridized Rashba states at the Bi_2Se_3/Ge interface. Moreover, from the calculations, we find that those states extend over 2 QL of Bi_2Se_3 and 3 monolayers of Ge giving a spatial extension d = 2:6 nm. We then deduce: $\lambda_{\mathrm{IREE}} = \gamma_{\mathrm{IREE}} \times d \approx 26$ pm. It should also be noticed

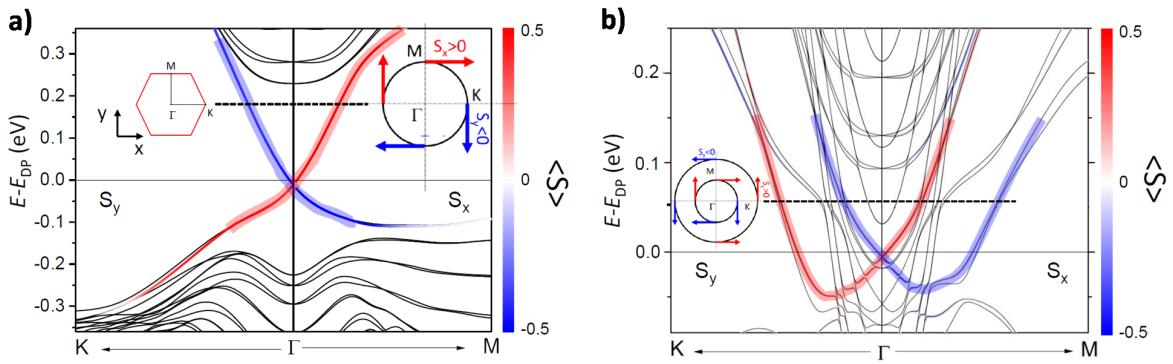

Figure 3.14 – a) Electronic band structure with spin-orbit coupling for 8 QL of Bi_2Se_3. The red and blue colors indicate the spin texture of the topmost QL projected along the y and x direction for the K-Γ and Γ-M high symmetry axes, respectively. The corresponding Brillouin zone as well as a specific spin-resolved Fermi contour are reported in the insets. b) Electronic band structure for the Bi_2Se_3 (8 QL)/Ge (3.2 nm) stack. The same color codes as in a) is used for the interface spin texture. The inset shows a specific spin-resolved Fermi contour. E_{DP} corresponds to the energy position of the Dirac point of Bi_2Se_3 surface states in a) and Bi_2Se_3/Ge interface states in b).

that, by adjusting the position of the Fermi level in Fig. 3.14 b) with a gate voltage to the Bi_2Se_3/Ge heterostructure, it could be possible to control both the magnitude and the sign of the spin-to-charge conversion.

To summarize, we have probed the spin-to-charge conversion at the Bi_2Se_3/Ge interface by using a non-local spin injection/detection scheme. Notably, we measure larger voltage drops with Bi_2Se_3 than with the Pt reference, which makes the former an excellent spin detector for future spin-based technologies. We have numerically modeled the spin injection and transport in Ge to the Bi_2Se_3 detector and found an equivalent spin-Hall angle close to the one derived for Pt. It corresponds to an inverse Rashba-Edelstein length $\lambda_{IREE} \approx -30$ pm. The sign of the spin-to-charge conversion is found to be opposite for Bi_2Se_3/Ge and Pt. By employing first principles calculations, we ascribe this behavior to the interfacial hybridization between the topologically protected surface states of Bi_2Se_3 and Ge leading to the formation of Rashba interface states with a spin chirality opposite to the one of states at the free Bi_2Se_3 surface. Our results demonstrate that semiconductors constitute a very promising platform for the exploitation of topological insulators in spintronics, where, by gating the heterostructure, spin-to-charge conversion could in principle be tuned in magnitude and sign.

3.4 Helicity-dependent photovoltage: two interacting spin accumulations

It was recently shown that a similar type of electro-optical scanning technique could be used to directly image the spin accumulation in Bi_2Se_3 when a DC current is passed through the material.[177] In this thesis, I used the Bi_2Se_3/Ge (111) microstructures patterned for optical spin orientation experiments to try to investigate this effect. By using a similar experimental procedure to measure the helicity-dependent photovoltage, I could demonstrate a new effect related to the interaction between two spin accumulations. The first spin population is generated by the optical spin orientation in Ge, and the second by the direct charge-to-spin conversion in Bi_2Se_3: the Spin Hall effect (SHE) and/or the Rashba-Edelstein effect (REE).

3.4.1 Principle of the experiment

The technique proposed in Ref. [177] relies on the out-of-equilibrium magnetic circular dichroism at the Bi_2Se_3 channel edges due to the the spin accumulation by spin Hall effect. Indeed, when a DC charge current flows through a 10 nm-thick Bi_2Se_3 layer, it induces an out-of-plane spin accumulations at the opposite edges of the conduction bar due to the SHE/REE. Then, as shown by Fig. 3.15 a), the circularly-polarized (CP) red laser beam is scanning the Hall bar and the different absorption of the right CP (σ_+) and left CP (σ_-) light occurs at opposite edges due to the local spin accumulation generates a differential photovoltage: an *helicity-dependent photovoltage* (HDP) given by:

$$\mathrm{HDP} = V_{\sigma_+} - V_{\sigma_-} \tag{3.12}$$

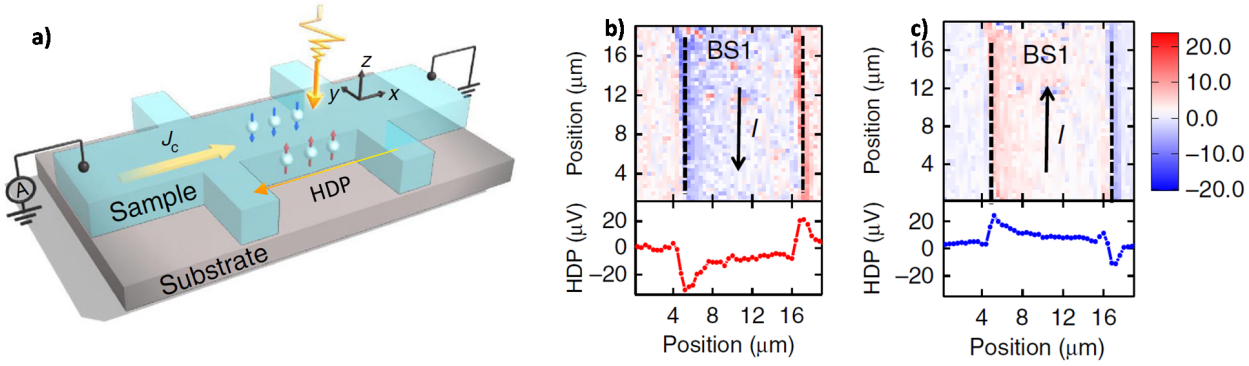

Figure 3.15 – Extracted from Ref. [177]. a) Schematic representation of the spin-dependent photovoltage measurements. b) and c) HDP two-dimensional maps of the Bi_2Se_3 Hall bar with opposite bias currents.

The sample is made of a 10 nm-thick Bi_2Se_3 film grown on sapphire by MBE and patterned into a 100×10 µm^2 Hall bar sketched in Fig. 3.15 a). A DC 10^6 A.cm^{-2} current density

is applied in the Hall bar and the CP laser spot (λ = 650 nm, P = 4.62 mW, spot size $d \approx 1$ µm) is scanning the Hall bar at normal incidence. The demodulated HDP is plotted as a function of the beam position in Fig. 3.15 b) and c) for positive and negative DC bias currents, respectively. The HDP at the two channel edges have opposite signs, and the signs are reversed when the bias current direction is reversed. Their interpretation relies on the different absorption of light at the edge of the Bi_2Se_3 bar due to spin accumulation, implying that the effect is purely *local*: a HDP signal can only be detected only when the beam is focused on the Bi_2Se_3 Hall bar edges.

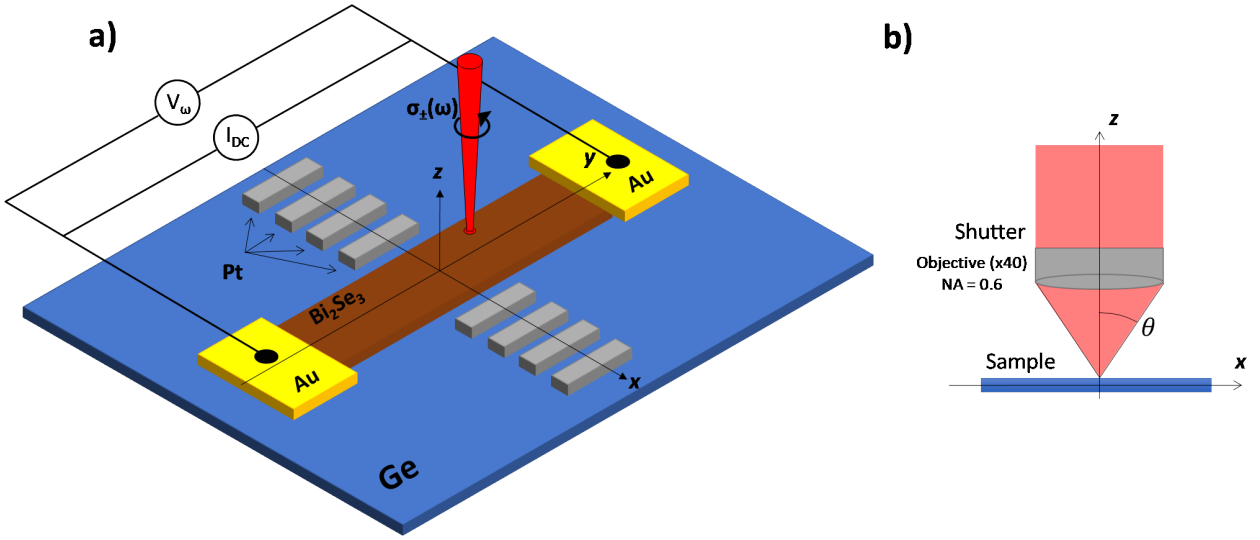

Figure 3.16 – a) Sketch of the Bi_2Se_3/Ge (111) sample layout used for helicity-dependent photovoltage experiments. A DC bias current I_{DC} is applied in the Bi_2Se_3 bar contacted by two Au/Ti pads, the light circular polarization ($\sigma_\pm$) is modulated at ω = 42 kHz (the PEM frequency), the demodulated voltage V_ω is recorded with a lock-in amplifier while the focused laser beam raster scans the microstructures at normal incidence. b) Schematics of the the beam focusing on the sample surface, θ denote the maximum angle of incidence of the light cone while the average incidence is zero.

In my work, I first tried to reproduce those published results using the Bi_2Se_3/Ge (111) microstructures sketched in Fig. 3.16 a). The fabrication process has already been described in sect. [3.3.1]. Several effects should be observable when scanning the sample with the laser beam at normal incidence:

- At zero bias current: we should retrieve the same open-circuit electrical map resulting from the spin-to-charge conversion when the beam impinges the Pt pads edges (See sect. [3.3.2] of the manuscript).
- At non-zero bias current: we expect to measure HDPs of opposite signs at opposite channel edges, adding up to the zero-bias non-local signal previously mentioned.

3.4.2 Helicity-dependent photovoltage results

For the light in normal incidence

We perform two-dimensional maps at normal incidence. A DC bias current is applied in the Bi_2Se_3 bar, the light circular polarization is modulated at ω, the demodulated voltage V_ω is recorded with a lock-in amplifier while the focused laser beam is scanning the microsctuctures. Since V_ω results from the difference of photovoltage generated with σ_+ and σ_- light, it is by definition an helicity-dependent photovoltage (HDP). The reflectivity and HDP maps are shown in Fig. 3.17 a) and b), for a negative bias current I_{DC}. Fig. 3.17 c) and d) show the reflectivity and HDP profiles integrated along y. We observe a clear non-local HDP, its sign is opposite when the laser beam is illuminating opposite Pt edges, and when the bias current is reversed: it corresponds to a unidirectional effect.

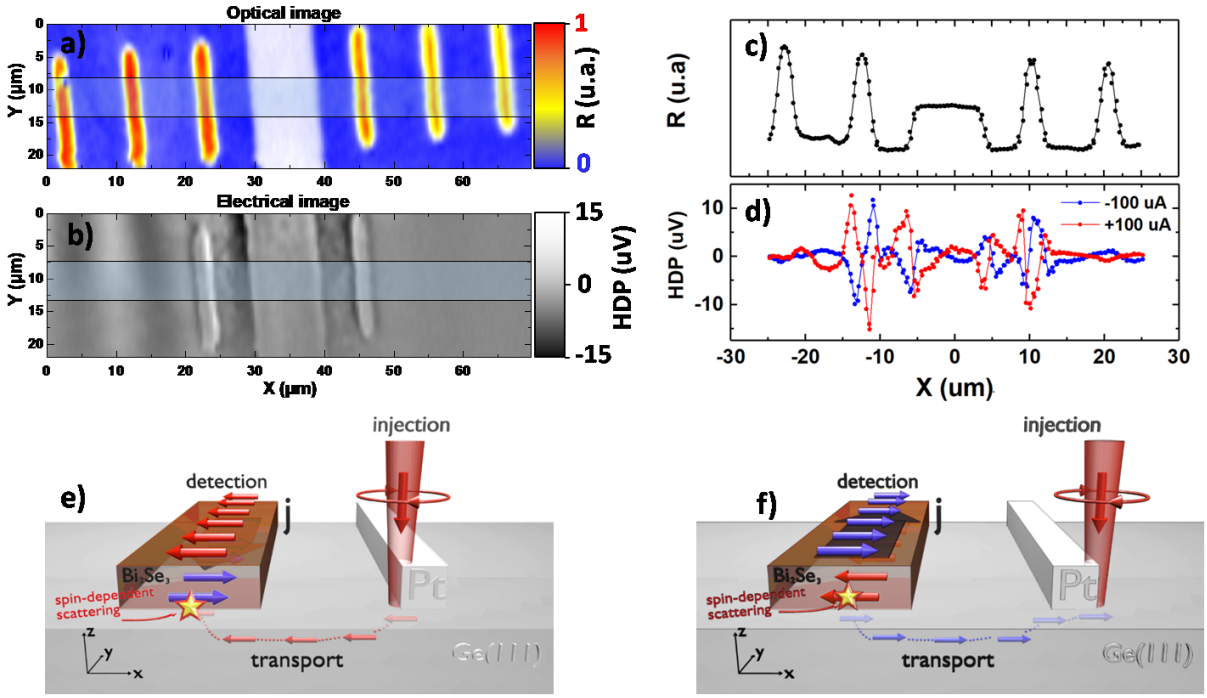

Figure 3.17 – a) Optical (reflectivity) and b) electrical (HDP) two-dimensional maps taken with an applied bias current I_{DC} =-100 µA. c-d) Corresponding line profiles integrated along y, a clear non-local signal that changes sign with the direction of the bias current can be observed. e-f) Schematic representation of the two spin populations in Ge and Bi_2Se_3.

We explore the HDP dependencies with respect to the applied current and the degree of circular polarization (DCP) of the light. Line scans along x were performed at room temperature, the HDP signal of the first left Pt bar is reported in Fig. 3.18, the left and right edges correspond to $x \approx -14$ µm and $x \approx -11$ µm, respectively. The HDP scales almost linearly with the applied current and the DCP, hence, we observe a bilinear effect.

The fact that the current-dependent signal that we observe can be non-local contradicts the interpretation given in Ref. [177], i.e. the absorption of light by Bi_2Se_3 as the origin of HDP.

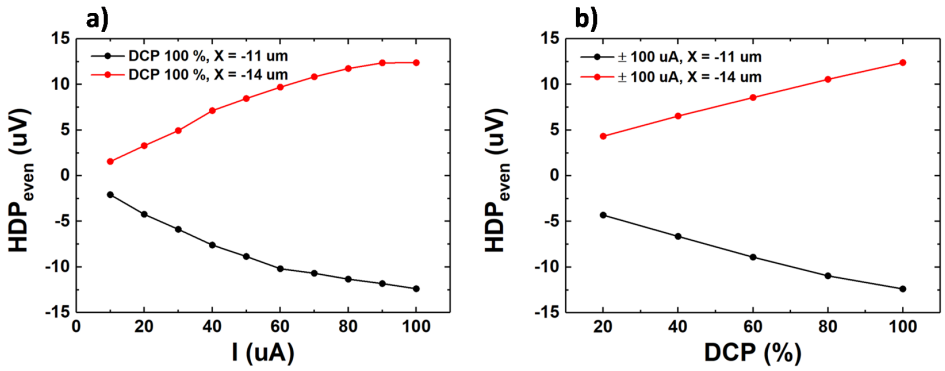

Figure 3.18 – HDP dependencies with respect with to the a) current (for DCP = 100 %) b) degree of circular polarization (for I_{DC} =-100 μA). Line scans were carried out at room temperature and the HDP data of the first left Pt injector are plotted (The left and right edges correspond to $x \approx -14$ μm and $x \approx -11$ μm, respectively).

We further show in Fig. 3.22 a) a reference measurement, where no HDP can be measured in Bi_2Se_3 grown on sapphire.
This normal incidence study demonstrates that the HDP is bilinear with the applied current, and the in-plane spin orientation. An alternative method to probe this effect is to illuminate the sample at oblique incidence.

For the light in oblique incidence

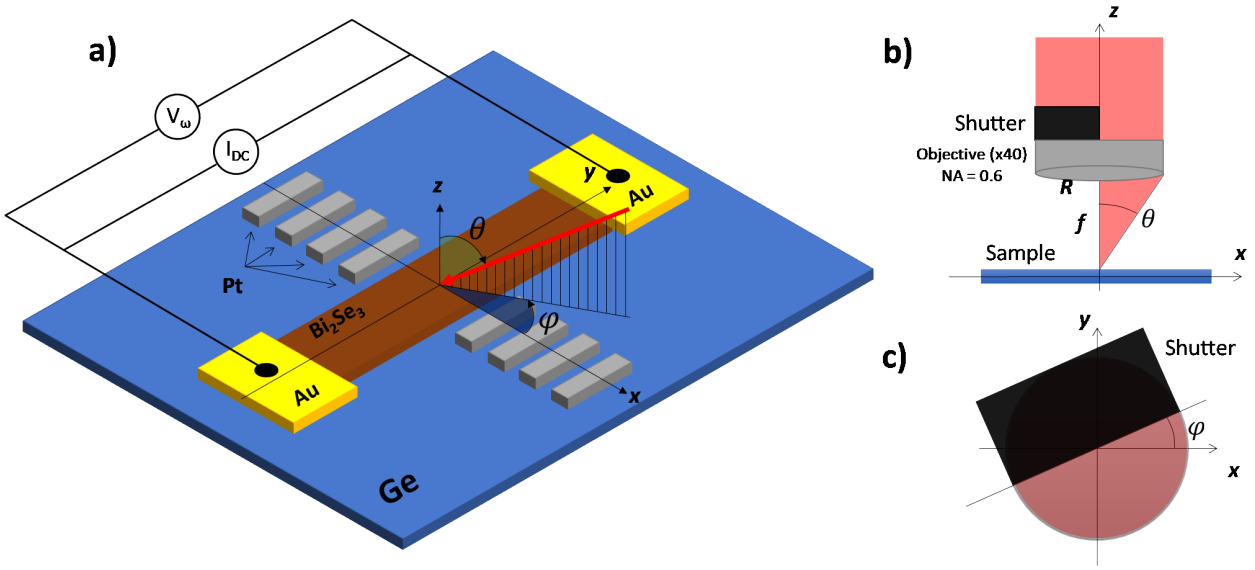

Figure 3.19 – a) Oblique incidence HDP measurements. The laser direction is given by θ and φ in spherical coordinates. b) Schematics of the shutter covering half of the beam, the non-zero average incidence is $\theta \approx 17°$. c) Control of the beam azimuth by setting the shutter angle φ.

Fig. 3.19 a) illustrates the oblique incidence measurement geometry. We use a shutter that

covers half the *cm*-sized laser beam and placed between the beam splitter and the microscope objective, inducing a non-zero average oblique incidence on the sample as shown in Fig. 3.19 b). We note θ the average angle of incidence of the light with respect to the sample normal (in spherical coordinate), by hiding half of the beam, we get the following expression:

$$\tan(\theta) = \frac{1}{\pi} \frac{\frac{R}{fH}\sqrt{1+\left(\frac{R}{f}\right)^2} - \ln\left(\frac{R}{f} + \sqrt{1+\left(\frac{R}{f}\right)^2}\right)}{\sqrt{1+\left(\frac{R}{f}\right)^2} - 1} \tag{3.13}$$

where R is the objective radius and f is the focal length. These quantities are related by the numerical aperture (NA):

$$\frac{R}{f} = \frac{NA}{\sqrt{1-NA^2}} \tag{3.14}$$

In our case, the objective numerical aperture is 0.6, yielding an average incidence of $\theta \approx 17°$. The optically generated spins being oriented along the incoming wavevector of light, this allows us to reach an in-plane spin polarization up to $P = \sin(\theta) = 29.7$ %. The in-plane orientation is controlled by setting the beam azimuth, denoted by the angle φ. This is done by rotating the shutter on its axis as shown in Fig. 3.19 c). This technique allows us to perform the full angular dependence of HDP with spatial resolution.
Fig. 3.20 a) and c) illustrate how setting the shutter at 0° results in an oblique beam incidence.

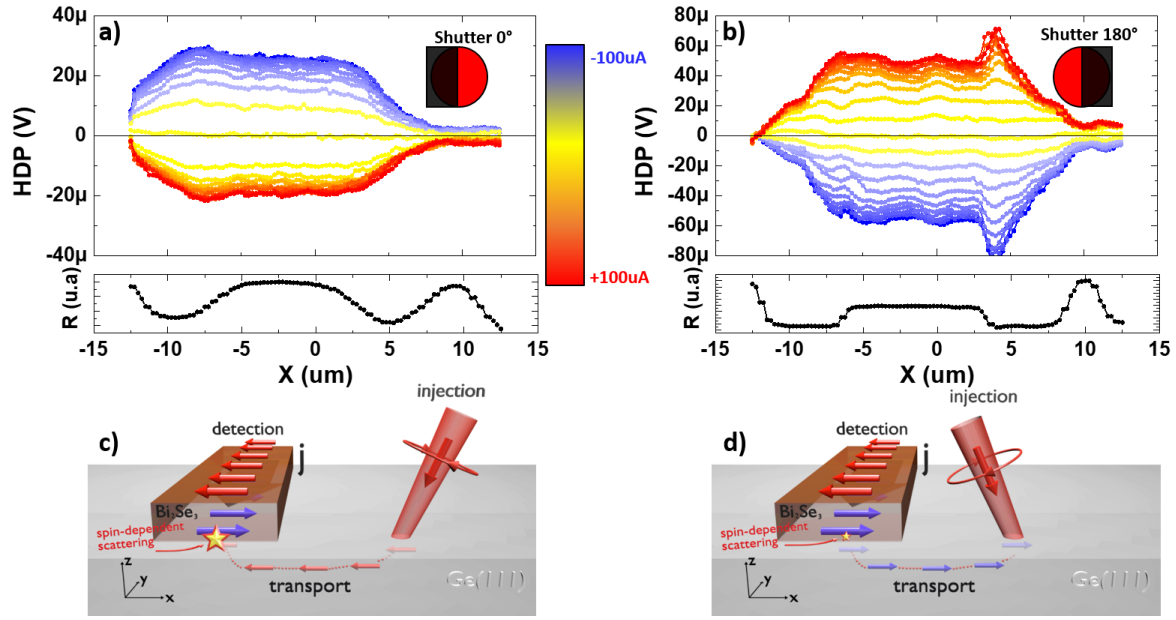

Figure 3.20 – Line scans recorded along the x axis for a set of currents ranging from -100 µA to +100 µA for $\varphi = 0°$ in a) and $\varphi = 180°$ in b). c-d) Schematic representation of the two spin populations coexisting.

In this shutter position, the average light wavevector exhibits an in-plane component along $-x$ generating a spin accumulation with a spin polarization along $-x$. The HDP and reflectivity line scans are recorded along the x axis, for currents ranging from -100 µA to +100 µA (blue to red color). The same experiment is performed positioning the shutter at 180°, resulting in an average x incidence (see Fig. 3.20 b) and d)). We find the same bilinear behavior as the one previously observed in normal incidence measurements: reversing the current or the angle of incidence (i.e. the optically generated spin direction) results in an opposite HDP.
The spatial resolution also gives important information: it first confirms the non-local nature of the signal since the HDP exponentially decreases when the beam is scanned outside the detector. Also, the fact that the HDP is maximum when shining Ge through the Bi_2Se_3 detection pad show that very small amount of light is absorbed by Bi_2Se_3 and that most of the light power is transmitted.
Fig. 3.21 a) describes the oblique incidence geometry, the in-plane spin polarization is given by the angle φ. For each azimuth φ, a two-dimensional map is recorded and the HDP is average over the detector area at a given current and degree of circular polarization of the light (DCP). For each data point, the HDP is measured for both current direction ($+I$ along $+y$, $-I$ along $-y$) and HDP_{even} is calculated as:

$$\mathrm{HDP}_{even} = \frac{1}{2}\left[HDP_{+I} - HDP_{-I}\right] \tag{3.15}$$

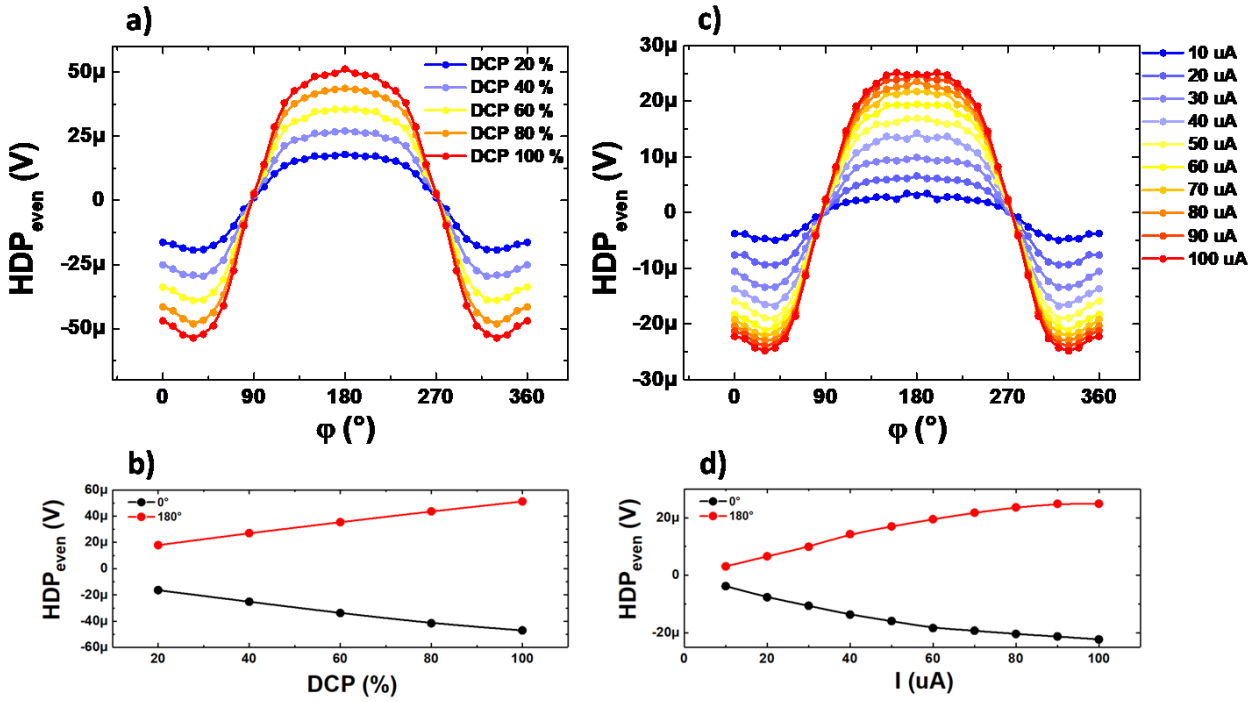

Figure 3.21 – Full angular dependence of the HDP a) for different DCP ($I_{\mathrm{DC}} = 100$ µA) and c) for different currents (DCP = 100 %). Dependence of the HDP b) on the applied current (DCP = 100 %) and d) on the DCP ($I_{\mathrm{DC}} = 100$ µA) for $\varphi = 0°$ and $\varphi = 180°$.

The results are shown in Fig. 3.21, the panel a) shows the averaged-HDP angular dependence for different values of DCP. The angular dependence follows a cosine function: the HDP is maximum when the spins generated in Ge are along x, perpendicular to the Bi_2Se_3 detection bar. The spin accumulation is proportional to the light degree of circular polarization: increasing the DCP increases the spin polarization of photogenerated electron-hole pairs, resulting in a larger spin accumulation. Indeed, Fig. 3.21 b) clearly shows that the HDP scales almost linearly with the DCP for $\varphi = 0°$ and $\varphi = 180°$. Fig. 3.21 c) shows the angular dependence at maximum DCP (100 %), for different currents, and again, we see that the HDP is proportional to the current. As a consequence, we can write this phenomenological equation to account for the observed HDP behavior:

$$HDP_{even} = A.\theta_{CTS}.I_{\mathrm{DC}}.\rho_{\mathrm{opt}}.\cos\varphi \tag{3.16}$$

Where θ_{CTS} is the direct charge-to-spin conversion parameter in the Bi_2Se_3 detector, I_{DC} is the applied bias current, ρ_{opt} is the spin accumulation resulting from the optical spin orientation mechanism and φ is the light beam azimuth. This set of observations allowed us to define the HDP symmetries with respect to the two sources of spin accumulations (electrical in Bi_2Se_3 and optical in Ge). We conclude that the HDP behaves like the current-in-plane giant magnetoresistance (CIP-GMR). We look deeper into this analogy in sect. [3.4.3].

Control experiments

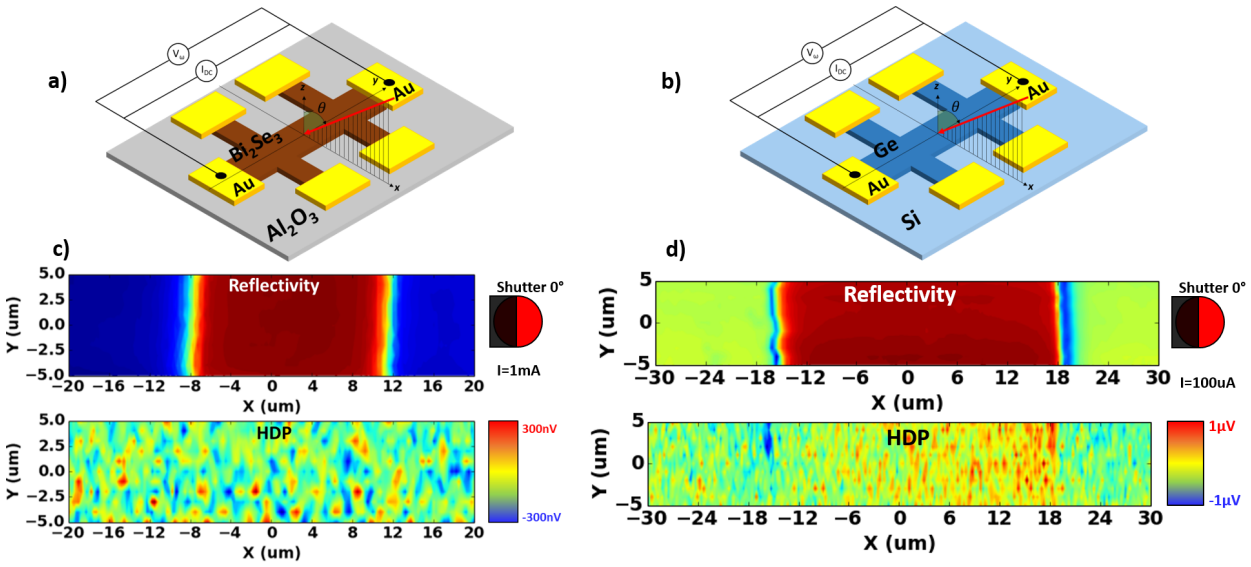

Figure 3.22 – a) Bi_2Se_3 grown on Al_2O_3 and b) Ge/Si (111) Hall bars. c) and d) Control experiments on the two reference samples. The azimuth angle is $\varphi = 0°$ (a fraction of photogenerated electrons are spin polarized in-plane along $-x$). The applied bias current is 1 mA for both measurements.

Oblique incidence HDP maps were recorded on two reference samples in order to demonstrate that Bi_2Se_3 nor Ge (111) can generate such effect. The first sample consists in a 10 nm-

thick Bi_2Se_3 grown on sapphire by MBE, the growth and transport characterizations are presented in the appendix. [A]. The Bi_2Se_3 film is then patterned into a 200×20 μm^2 Hall bar microstructure. Fig. 3.22 a) shows the reflectivity and HDP maps measured using the same experimental conditions as that for Bi_2Se_3/Ge (111). We do not detect any HDP signal neither locally (on the Bi_2Se_3 film) nor non-locally. The second sample is a 130×35 μm^2 Hall bar directly patterned into the n-type Ge/Si (111) substrate used to grow Bi_2Se_3 films. Again, we do not measure a detectable HDP signal (see Fig. 3.22 b)).
These two control measurements strengthen our interpretation that the HDP only takes place when two sources of spin accumulation interacts at the topological insulator/semiconductor interface.

3.4.3 Origin of the effect

Spin-dependent scattering interpretation

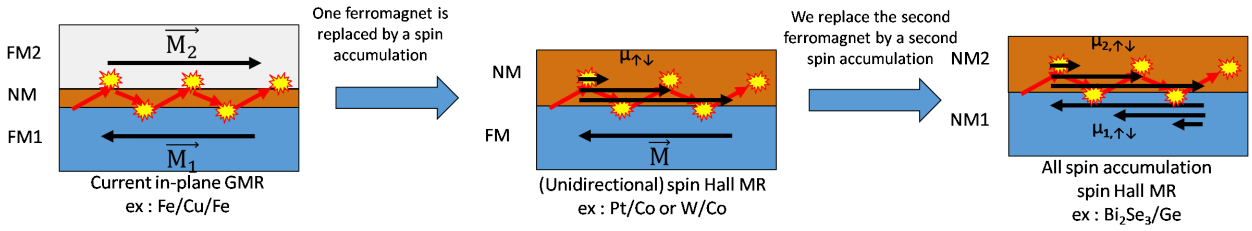

Figure 3.23 – a) CIP-GMR: Subsequent spin-dependent scattering processes when a current flows in the FM/NM/FM trilayers. b) USMR: Spin-dependent scattering at a heavy metal/ferromagnet interface due to the spin accumulation induced by the SHE in the heavy metal layer. c) Ferromagnet-free USMR due to spin accumulations at the topological insulator/semiconductor interface.

Let's first consider the ferromagnet/normal metal/ferromagnet (FM/NM/FM) trilayer shown in Fig. 3.23 a). When flowing a current through such structure, the electrons become spin-polarized because of the exchange interaction with the FM layers. The two possible orientations of spins give rise to two current channels $J_\uparrow$ and $J_\downarrow$ experiencing different electrical resistances due to spin-dependent scattering events during the transport. When the two FM magnetizations are parallel, the spin-dependent scattering rate is minimum in the system, resulting in a lower total resistance state. If now the two magnetizations are anti-parallel, the scattering rate increases so does the trilayer resistance. This is the giant magnetoresistance (GMR) effect, in the current in-plane (CIP) geometry that was discovered in the late 80's and extensively studied experimentally and theoretically.
In the field of spin-orbitronics, the scientific community attempted to remove one of the two ferromagnets used in CIP-GMR devices and replace it by a heavy metal where spin accumulation can be induced by the spin Hall effect (see Fig. 3.23 b). Typical systems are Pt/Co

or W/Co metallic bilayers, the current flowing in the Pt film induces a spin accumulation at the Pt/Co interface. Here, the relative orientation between the Co magnetization and the current-induced spin accumulation gives rise to spin-dependent scattering that resembles the GMR mechanism. This effect is known as the unidirectional spin Hall magnetoresistance (USMR).[85] Again, two resistance states are obtained by reversing the FM magnetization or the current direction.

Fig. 3.23 c) schematically represents the Bi_2Se_3/Ge (111) heterostructure with the two sources of spin accumulation: in the NM1 region (Ge in our case), the spin accumulation is generated by optical spin orientation. In NM2 region (Bi_2Se_3), it is generated by charge-to-spin conversion (SHE and/or REE). In this work, we removed the second ferromagnet from the original CIP-GMR device geometry and showed that two resistance states could be obtained through the HDP bilinearity.

Discussion

This picture however, does not give information about the microscopic mechanisms behind the interaction between the two interface spin accumulations. In principle, in a linear system (for instance, a good metallic spin conductor like Cu or Al), two spin accumulations should add up or cancel out depending uniquely on their relative orientation, corresponding to a linear effect. Our observation highlighted a non-linear effect, where the two spin accumulations do not add up. The topological insulator/semiconductor interface could bring the non-linearity but the underlying physics is yet to be fully understood and theoretical work is needed to model and understand the microscopic mechanisms.

To conclude, when looking for a direct technique to image the spin accumulation in a TI, we discovered a new interesting effect that occurs when a current flows at the interface between two spin accumulations. The direct application of this discovery is the tunability of a TI-based spin detector by applying a charge current: the detected voltage that was in the nanovolt range when using pure spin-to-charge conversion in open-circuit detection is now in the microvolt range by biasing the Bi_2Se_3 detector.

CHAPTER 4

The unidirectional Rashba magnetoresistance in germanium

In the field of spintronics, the generation and detection of spin-polarized currents has long relied on the exchange interaction in ferromagnetic materials. However, the spin–orbit coupling (SOC) appears now as a very efficient mechanism to complete both operations.[24,132,178] Magnetotransport experiments are used to relate the magnetization of a conductor to its electrical resistance.[179,180] The anomalous Hall effect, discovered in the 19th century, owes its strength to the intensity of the spin-orbit coupling acting on electron scattering.[72] A few decades later, the anisotropic magnetoresistance, corresponding to the change of resistance with the relative orientation of the magnetization and the electrical current, is also due to the SOC and was exploited to manufacture the first magnetic sensors.[181,182]

The progress in thin film growth techniques allowed to engineer magnetic stacks where the magnetizations of two ferromagnetic layers (FM) separated by a non-magnetic metal (NM) can be either parallel or antiparallel to each other, leading to the discovery of the giant magnetoresistance (GMR).[6,183] The microscopic origin of the GMR resides in the electron scattering at the NM/FM interfaces that depends on the relative orientation of the electron spin and the FM magnetization. The GMR could give very contrasted resistance levels later used in magnetic sensors like the read heads of magnetic hard disks.

More recently, heavy metal/ferromagnetic metal (HM/FM) bilayers like Pt/Co or W/Co were studied in magnetotransport experiments. Here, a spin accumulation is induced by the spin Hall effect in the HM and the spin-dependent scattering process occuring at the HM/FM interface results in a novel magnetoresistance effect. The resistance of the system depends on the relative orientation of the spin accumulation and the magnetization. It was called the unidirectional spin Hall magnetoresistance (USMR).[85] An another kind of mag-

netoresistance was observed in the topological insulator Bi_2Se_3,[184] and the two-dimensional electron gas at the $SrTiO_3$ (111) surface.[185] In both cases, there is no ferromagnetic order and the effect has been related to the characteristic spin-momentum locking present at the surface of the topological insulator or in the 2D electron gas due to the Rashba SOC.[184–186] The detected magnetoresistance exhibits two characteristic features: it is unidirectional (i.e. odd with respect to the electrical current and magnetic field directions) and linear with the applied magnetic field and electrical current intensities; therefore it has been classified as a unidirectional magnetoresistance (UMR).[184–186] Even though they share the same angular dependences, the microscopic origin of this UMR is different from that of the USMR that involves a ferromagnetic layer.[85–88]
In the first part of this chapter, I explain how harmonics separation in AC electrical measurements and magnetic field angular dependences can be used to sort and understand the different magnetoresistance contributions we observe.

In the second part, I report the observation of the UMR in Ge (111) at low temperature (15 K). We ascribe its origin to the Rashba SOC, which generates spin-momentum locking in the subsurface states of Ge (111). Their presence and spin texture have already been demonstrated exploiting angle and spin-resolved photoemission spectroscopy.[187–190] The origin of this magnetoresistance comes from the interplay between the externally applied magnetic field and the pseudomagnetic field generated by the current applied in the spin-splitted subsurface states of Ge (111).[191] Experimentally, we find that the UMR in the Ge (111) subsurface states is drastically larger compared to previous reports[184,185] although the effect progressively vanishes when increasing the temperature due to carrier activation in the bulk valence bands of Ge and to the low value of the Rashba spin-orbit coupling ($\sim 58\, k_B$).[187]

Finally, the intrinsic Rashba spin splitting being too small to be used at room temperature in applications, we attempted to enhance it by interfacing the Ge with another material to engineer the interface band structure. I present the case of Fe/Ge where the Rashba spin splitting could be indeed enhanced. Moreover, in this system, the combination of the ferromagnetic properties of Fe and the strong UMR could be used in device applications.

4.1 Symmetries and harmonics analysis in magnetotransport

In a linear conductor the longitudinal (R_{xx}) and transverse (R_{xy}) resistances are independent of the applied current given by the Ohm's law. If we now consider a non-linear conductor where the resistance can be current-dependent, by assuming that the current-dependent resistance $R(I)$ is small compared to the conductor linear resistance $R(0)$, R can be expressed using the Taylor expansion:

$$R(I) = R(0) + \frac{dR}{dI}(0)I + \frac{\frac{d^2R}{dI^2}(0)}{2!}I^2 + O(I^2) \tag{4.1}$$

Where I is a sinusoidal AC current $I = I_0 \sin(\omega t)$, $R(0)$ is the current-independent resistance, $\frac{dR}{dI}(0)$ and $\frac{d^2R}{dI^2}(0)$ are the first and second derivative of R with respective to I at zero current, respectively. At the first order, only the first two terms of $R(I)$ remains. The corresponding longitudinal voltage can be expressed as:

$$V(I) = IR(I) = I_0 R(0)\sin(\omega t) + I_0^2 \frac{dR}{dI}(0)\sin^2(\omega t) \tag{4.2}$$

The expression can be linearized and expanded in the harmonic contributions:

$$V(I) = IR(I) = \frac{1}{2}I_0^2\frac{dR}{dI}(0) + I_0 R(0)\sin(\omega t) + \frac{1}{2}I_0^2\frac{dR}{dI}(0)\sin(2\omega t - \pi/2) \tag{4.3}$$

This longitudinal voltage consists of a DC, an in-phase first harmonic, and an out-of-phase second harmonic terms. It is measured using lock-in amplifiers where the phase is set to 0° for the first harmonic signal and -90° for the second harmonic signal. We can then define the first harmonic resistance term $R^{\omega} = R(0)$, that is current-independent and the second harmonic resistance term $R^{2\omega} = \frac{1}{2}I_0\frac{dR}{dI}$ that scales linearly with I_0.
In this chapter, we study the magnetotransport properties of a system made of magnetic metals and semiconductors where the spin-orbit interaction leads to original effects. As a

Effects	Full names	Typical systems	References
AMR	Anisotropic magnetoresistance	Fe, Co, NiFe	[181, 182]
SMR	Spin Hall magnetoresistance	YIG/Pt	[79–84]
USMR	Unidirectional Spin Hall magnetoresistance	Pt/Co, W/Co	[85–88]
UMR	Unidirectional magnetoresistance	Bi_2Se_3, $SrTiO_3$	[184, 185, 191, 192]
HE	Hall effect	Si,Ge, GaAs	[149, 180]
AHE	Anomalous Hall effect	Fe, Co, NiFe	[72, 193]
PHE	Planar Hall effect	NiFe, Bi_2Se_3	[194]
NE	Nernst effet	BiSb	[195]
ANE	Anomalous Nernst effet	Fe, Co, NiFe	[72]

Table 4.1 – Summary of the main magnetoresistance effects we expect in the study of Ge (111) and Fe/Ge (111) systems.

consequence, several effects are expected to contribute to the longitudinal (R_{xx}) and transverse (R_{xy}) resistances with various dependences on the applied current (I), magnetization ($\mathbf{M}$) and magnetic field ($\mathbf{B}$). All these effects are listed in Table 4.1 and the contributions to the longitudinal resistance (resp. transverse resistance) as well as their dependences on I, ($\mathbf{M}$) and ($\mathbf{B}$) are summarized in Fig. 4.1.

All these effects take place in different materials, in a semiconductor, a perpendicular magnetic field $\mathbf{B} = B_z\hat{\mathbf{z}}$ deflects charge carriers by the Lorentz force and generates a voltage (U_{xy}) transverse to the current I applied along $+\hat{\mathbf{x}}$.[149,180] The corresponding magnetic field angular dependences are shown in Fig. 4.1 d), the magnetoresistance term $\Delta R^{1\omega}_{xy,HE} = R_H.B.\cos\theta$

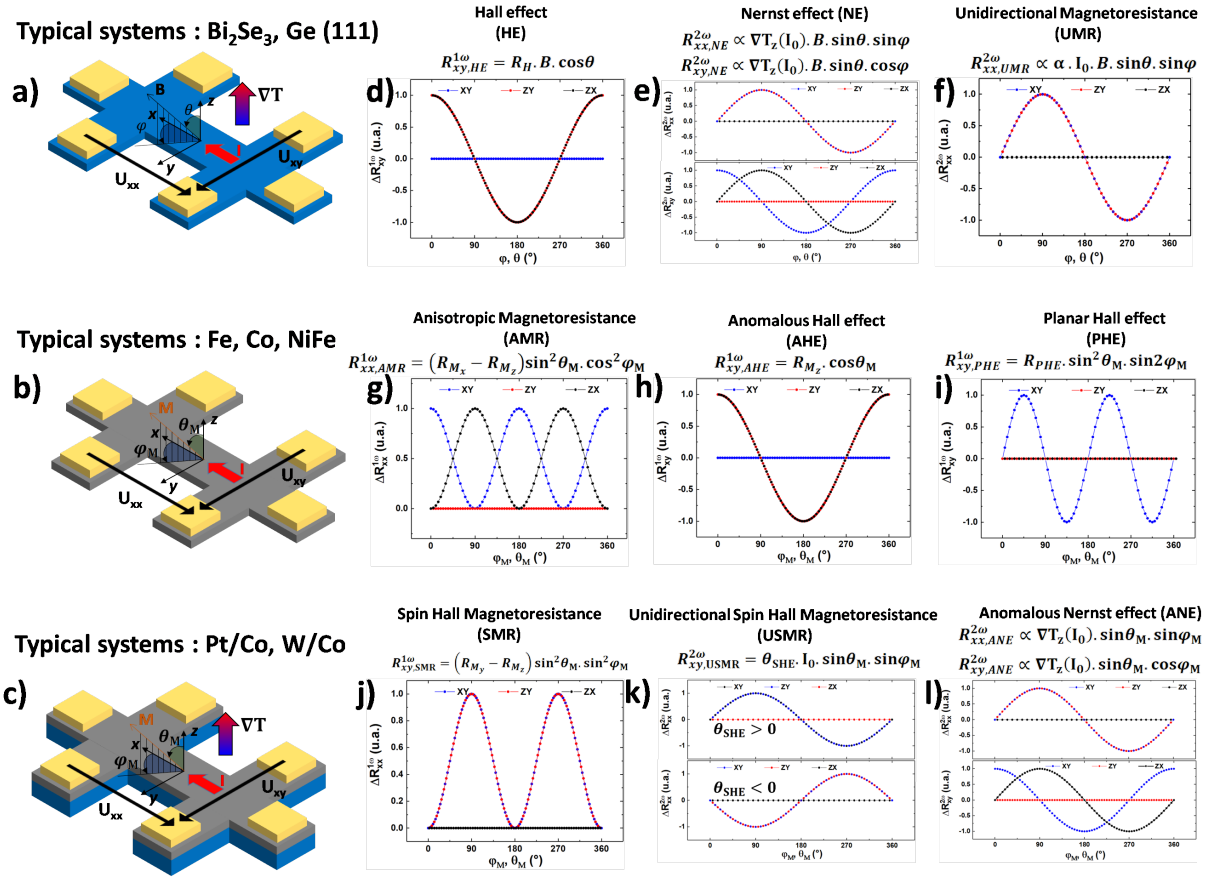

Figure 4.1 – Hall bar measurement geometry for three typical systems: a) non-magnetic semiconductor, b) a ferromagnetic metal and a c) heavy metal/ferromagnetic metal bilayer. The current is applied along $+\hat{\mathbf{x}}$ and the external magnetic field (magnetization) is set along the θ, φ, (θ_M, φ_M) direction, θ (θ_M) and φ (φ_M) being the polar and azimuth angles. We define the resistance contributions as $\Delta R^{1\omega(2\omega)}_{xx(xy)} = U^{1\omega(2\omega)}_{xx(xy)}/I_0$. Angular dependences of the d) Ordinary Hall effect. e) Longitudinal and transverse terms of the Nernst effect resulting from $\nabla T z$, a perpendicular to the plane temperature gradient. f) The unidirectional magnetoresistance. g) The anisotropic magnetoresistance. h) The anomalous Hall effect. i) The planar Hall effect. j) The spin Hall magnetoresistance. k) Unidirectional spin Hall magnetoresistance for positive and negative spin Hall angle θ_{SHE}. l) Longitudinal and transverse terms of Anomalous Nernst effect resulting from $\nabla T z$.

is current-independent and hence, measured in the first harmonic signal. The external magnetic field is set along the θ, φ direction, θ and φ being the polar and azimuth angles.

A similar effect occurs when a temperature gradient sets in the conduction channel: it is called the Nernst effect. The applied current leads to a vertical temperature gradient $\nabla \mathbf{T} = \nabla T_z \hat{\mathbf{z}}$ due to Joule heating. This temperature gradient along $\hat{\mathbf{z}}$ here gives rise to the Seebeck effect. By applying an external magnetic field (along $\hat{\mathbf{x}}$ or $\hat{\mathbf{y}}$), the carrier deflection due to the Lorentz force results in a transverse voltage (U_{xy} or U_{xx}, respectively).[195] Since the temperature gradient is induced by the Joule heating dissipating a power: $P = RI^2 = I_0^2.\sin^2(\omega T) = \frac{I_0^2}{2}\left[1 - \cos(2\omega t)\right]$, this term is current-dependent and measured in the second harmonic signal. As discussed in the following, the electrical conduction takes place at the surface of Ge (111) which results in a temperature gradient oriented along $\hat{\mathbf{z}}$. The corresponding angular dependences of $\Delta R^{2\omega}_{xx,NE} \propto \nabla T_z\left(I_0\right).B.\sin\theta\sin\varphi$ and $\Delta R^{2\omega}_{xy,NE} \propto \nabla T_z\left(I_0\right).B.\sin\theta\cos\varphi$ are shown in Fig. 4.1 e).

In Bi_2Se_3, $SrTiO_3$ or in Ge (111), the spin-orbit interaction can lead to an additional term: the unidirectional magnetoresistance. It exhibits two characteristic features: it is unidirectional (i.e. odd with respect to the electrical current and magnetic field directions) and linear with the applied magnetic field and electrical current intensities.[184,185,191,192] Therefore, this effect is detected in the second harmonic signal. As discussed in the following, we explain this mechanism as the result of the interplay between the externally applied magnetic field and the pseudomagnetic field generated by the current applied in the spin-splitted subsurface states of Ge (111). The corresponding angular dependences of $\Delta R^{2\omega}_{xx,UMR} \propto \alpha.I_0.B.\sin\theta\sin\varphi$ are shown in Fig. 4.1 f), α being the Rashba energy splitting.

In a ferromagnetic metal (FM), the different resistance contributions depend on the magnetization $\mathbf{M}$. The anisotropic magnetoresistance (AMR) corresponds to the dependence of the longitudinal resistance on the relative orientation of the current and the magnetization in a ferromagnetic film. It is current-independent and can be detected in the first harmonic signal. It originates from the interplay between the spin-orbit interaction and the d states that are spin-splitted by the exchange interaction and resulting in spin-dependent scattering.[181,182] The resistance is usually minimum when the current and the magnetization are perpendicular, the corresponding angular dependences of $\Delta R^{1\omega}_{xx,AMR} = \left(R_{M_x} - R_{M_z}\right).\sin^2\theta_{\mathrm{M}}\cos^2\varphi_{\mathrm{M}}$ are shown in Fig. 4.1 g). The current is applied along $+\hat{\mathbf{x}}$ and the magnetization is set along the $\theta_{\mathrm{M}}, \varphi_{\mathrm{M}}$ direction where θ_{M} and φ_{M} are the polar and azimuth angles, in spherical coordinates. Note that if the external magnetic field is strong enough to saturate the magnetization, we obtain: $\theta_{\mathrm{M}} = \theta$ and $\varphi_{\mathrm{M}} = \varphi$ where the external magnetic field is applied along θ,φ.

When a current I is applied in a FM along $+\hat{\mathbf{x}}$ with the magnetization oriented perpen-

dicular to the film $\mathbf{M} = M_z\hat{\mathbf{z}}$, a transverse voltage ($U_{xy}$) is generated as a consequence of spin-dependent scattering due to the spin-orbit coupling: this is the anomalous Hall effect (AHE).[72] Similarly to the Hall effect, the AHE is current-independent and measured in the first harmonic signal. This effect can be used to study the magnetic properties of a ferromagnetic film by measuring the saturation, coercive or anisotropy fields. The corresponding angular dependences of $\Delta R^{1\omega}_{xy,AHE} = R_{M_z}.\cos\theta_{\mathrm{M}}$ are reported in Fig. 4.1 h).

The AMR also gives rise to in a transverse MR term called the planar Hall effect. In most cases, the resistance of a FM is maximum when the current flows along the direction of magnetization and minimum when it flows perpendicular to the magnetization. This creates an asymmetric electric field perpendicular to the current, which depends on the magnetization direction of the film.[194,196] Like the AMR, this is a first harmonic effect, its angular dependences $\Delta R^{1\omega}_{xy,PHE} = R_{PHE}.\sin^2\theta_{\mathrm{M}}\sin 2\varphi_{\mathrm{M}}$ are plotted in Fig. 4.1 i).

In heavy metal/ferromagnetic metal bilayers (HM/FM), a novel magnetoresistance effect called the spin Hall MR arises from the interplay between the Spin Hall effect (SHE) in the HM and the spin absorption/reflection at the HM/FM interface. This effect was first found in insulating FM/HM bilayers.[79–84] It can be understood as the combined action of the direct and inverse SHE in the HM. The spin current generated by the direct SHE is partially reflected at the HM/FM interface when the magnetization is parallel to the spin direction and converted into a charge current by the inverse SHE, resulting in a resistance term proportional to the square of the spin Hall angle θ^2_{SHE}. It is also current-independent, so it can be detected in the first harmonic signal, the corresponding angular dependences of $\Delta R^{1\omega}_{xx,SMR} = \left(R_{M_y} - R_{M_z}\right).\sin^2\theta_{\mathrm{M}}\sin^2\varphi_{\mathrm{M}}$ are reported in Fig. 4.1 j).

In HM/FM metallic bilayers, a current-dependent magnetoresistance term can also be detected. In systems like Pt/Co or W/Co, a spin accumulation is induced by the SHE in the HM and the spin-dependent scattering process occuring at the HM/FM interface results in a magnetoresistance effect called the unidirectional spin Hall magnetoresistance (USMR). The resistance of the system depends on the relative orientation of the spin accumulation and the magnetization, so that the resistance term linearly scales with the applied current, magnetization and the HM spin Hall angle θ_{SHE}.[85–88]The unidirectional character of $\Delta R^{2\omega}_{xx,USMR} \propto \theta_{\mathrm{SHE}}.I_0.B.\sin\theta_{\mathrm{M}}\sin\varphi_{\mathrm{M}}$is highlighted by the angular dependences shown in Fig. 4.1 k).

Finally, in HM/FM metallic bilayers, a magnetoresistance term can arise from the interplay between a vertical thermal gradient and the FM magnetization. Analogously to its field-dependent counterpart (the Nernst effect), the anomalous Nernst effect occurs when a thermal gradient ($\nabla\mathbf{T} = \nabla T_z\hat{\mathbf{z}}$) is orthogonal to the FM magnetization ($\mathbf{M} = M_z\hat{\mathbf{z}}$) giving rise to

a transverse voltage (U_xy). The thermal gradient results from the Joule heating so this term is detected in the second harmonic signal. In most cases, it is oriented along the $\hat{\mathbf{z}}$ direction as because the different resistivies of the HM and FM films.[85] The corresponding angular dependences of $\Delta R^{2\omega}_{xx,ANE} \propto \nabla T_z\,(I_0)\,.B.\sin\theta_{\mathrm{M}}\sin\varphi_{\mathrm{M}}$ and $\Delta R^{2\omega}_{xy,ANE} \propto \nabla T_z\,(I_0)\,.B.\theta_{\mathrm{M}}\cos\varphi_{\mathrm{M}}$ are shown in Fig. 4.1 l).

This review is non exhaustive, additional effects like the field-like and damping-like spin-orbit torques can lead to additional current-dependent magnetoresistance contributions. Since we could not detect any of these effects, we do not comment their different dependences here. The different contributions to the longitudinal and transverse resistances listed above can be studied individually by using symmetry arguments, by selecting one specific signal harmonics in AC measurements or by performing magnetic field angular dependences. In the following sections, I will use these methods to explore and understand magnetotransport in Ge (111) Rashba states.

4.2 Large Rashba unidirectional magnetoresistance in Ge (111)

In this section, I report the observation of the unidirectional magnetoresistance (UMR) in Ge (111). I will show that this particular MR is related to the spin-orbit coupling acting on charge carriers. I first present a short review about the subsurface states in Ge (111). Then, I demonstrate experimentally that the electrical conduction in such subsurface states gives rise to the UMR due to the Rashba spin-orbit coupling. In order to understand the origin of this UMR, we first show that the available theories cannot fully explain our results and develop a new model based on the interplay between the externally applied magnetic field and the pseudomagnetic field induced by the current flowing in the Rashba gas.[191]

4.2.1 Existence of spin-polarized subsurface states in Ge (111) demonstrated by photoemission spectroscopy and ab initio calculations

The space inversion symmetry breaking at surfaces and interfaces lifts the spin degeneracy of surface states due to the Rashba spin-orbit interaction (SOI) giving rise to spin polarized states. Such exotic spin textures were first observed on the metallic Au (111) surface[90,197] or in Bi/Ag bilayers.[91,198] Motivated by the success of semiconducting spintronics, the community looked for Rashba spin splitting on semiconductor surfaces. Si (111) and Ge (111) were the most promising candidates, the inversion symmetry breaking was obtained by depositing a heavy metal monolayer (Bi for example), which also benefits from strong atomic SOI.
T. Aruga's group extensively explored Ge (111) surface spin properties by studying different heavy metal monolayer grown on Ge (111) by molecular beam epitaxy.[189] This group reported the observation of two-dimensional surface states localized in a couple of atomic

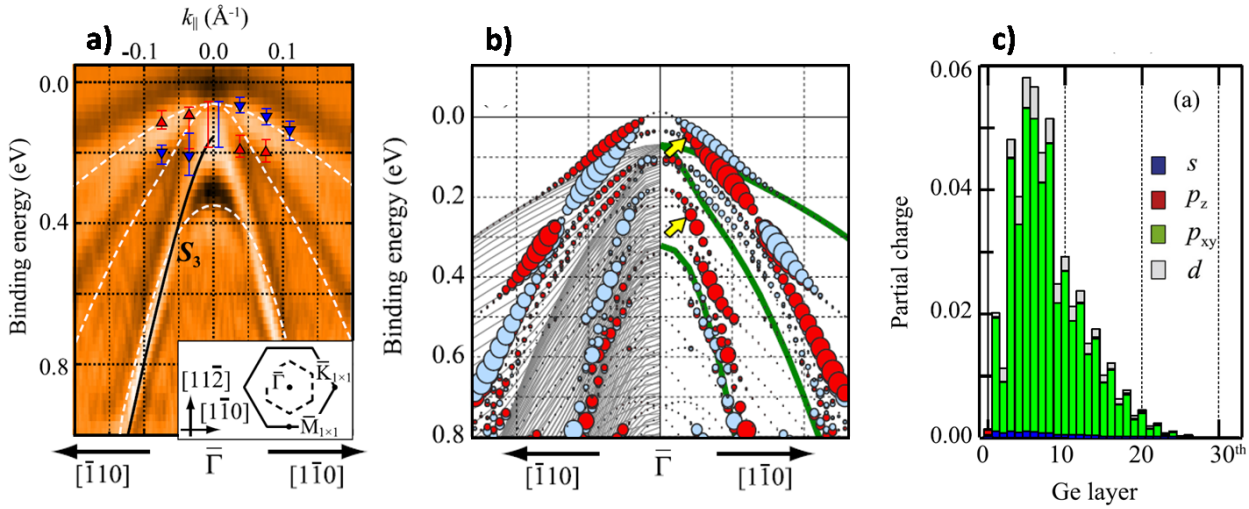

Figure 4.2 – Extracted from Ref. [188]. a) Second derivative ARPES image of Bi/Ge (111) b) Spin-resolved band structure obtained by ab initio calculations c) Layer-resolved partial charge distribution for the different orbitals, the dominant character is p_{xy}, in green.

planes below the Ge (111) surface using a combination of spin and angle resolved photoemission spectroscopy (SARPES) experiments and computational methods like the density functional theory (DFT).[187,188,190] Fig. 4.2 a) shows the second derivative ARPES images of the Bi-covered Ge (111) surface. In addition to the well known bulk valence bands of Ge (light hole, heavy hole and split-off bands), a surface band is identified, indicated by the white dashed lines in Fig. 4.2 a). The triangular markers represent the spin polarization of each band as measured by spin-resolved ARPES. To further investigate the properties of this surface band, ab-initio calculations were performed, Fig. 4.2 b) reports the calculated band structure. The blue and red circles are representative of the spin polarization pointing along the $[1\bar{1}\bar{2}]$ and $[11\bar{2}]$ directions, respectively. This type of helical spin texture is ascribed to the combined Rashba and atomic spin-orbit interactions.[187]

Fig. 4.2 c) shows the layer-resolved partial charge distribution for the different orbitals. The wave functions of the surface states vanishes at the Bi/Ge interface and extends over more than 10 subsurface layers, hence, those states are called subsurface states. At odd with previously reported Rashba systems, the spin polarization is induced by the SOI of a light element (Ge) with negligible contribution of the heavier one (Bi). It is important to note that only one monolayer of the heavy atom was deposited by MBE to allow the band structure mapping by SARPES, which is a surface sensitive technique. Thicker films could be grown in order to protect the surface states from the atmospheric conditions.

The same group investigated different metallic monolayers deposited on Ge (111) and showed that the Rashba states are very robust and that the spin splitting can reach 200 meV with Pb atoms.[190] Ultimately, this type of spin-splitted surface states are believed to be ubiquitous at any interface between Ge (111) and a metal.[78] Our aim is to find the signature of the Rashba states in magnetotransport measurements. In this work, the Ge (111) surface is covered by a 2 nm-thick Al film, which is oxidized naturally in air. This procedure ensures the protection of the Ge (111) subsurface states against oxidation.

4.2.2 Magnetotransport measurements

Sample preparation

In this study, we use a 2- μm-thick Ge/Si (111) film deposited by low-energy plasma-enhanced chemical vapor deposition (LEPECVD), as described in sect. [2.3.1]. The deposition rate was ≈4 nm s^{-1} and the substrate temperature was fixed at 500°C. Post-growth annealing cycles have been used to improve the crystal quality. The Ge layer is non intentionally doped with a residual hole carrier concentration $p \approx 2 \times 10^{16} cm^{-3}$ as measured by Hall effect at room temperature. The Ge-on-Si wafer is then transferred into our ultra high vacuum (UHV) molecular beam epitaxy (MBE) chamber. Cycles of annealing and ion beam etching are performed in UHV to remove the native Ge oxide layer, smooth the surface and obtain the Ge (2×8) surface reconstruction. On the clean surface, a 2 nm-thick aluminum layer is deposited in two steps: 1 nm by electron beam evaporation and 1 nm by sputtering, all in the same UHV system. This aluminum layer transforms into an alumina film that prevents the Ge (111) surface to be oxidized in air.

A two-step microfabrication process is used to define the Hall bars in the 2- μm-thick Ge epilayer. We first use laser lithography to define the conduction channel and we etch the Ge using ion-coupled plasma etching (ICP), the etching profile is made highly anisotropic using a plasma of SF_6, C_4F_8 and Ar gases. Then, electrical contacts are lithographically defined and the Au(120 nm)/Ti(5 nm) stack is deposited after etching the alumina layer beneath to perform electrical measurements. We stress the fact that the etching process does not change the carrier concentration of Ge ($p \approx 2 \times 10^{16} cm^{-3}$). In order to apply a gate voltage to the Ge (111) channel, we grow an Al_2O_3(5nm)/HfO_2(90nm) dielectric layer by atomic layer deposition on top of the device (Coll. L. Cagnon, NEEL Institute, Grenoble), followed by the deposition of a metallic Au(200 nm)/Ti(10 nm) counter electrode on top of the Hall crosses. The final devices are then contacted using microwire bonding and inserted into a 7 T-1.5 K cryostat where the different magnetoresistance (MR) effects and angular dependences are simultaneously recorded with a Keithley 6221 as a current source and two Keithley 2182 as nanovoltmeters. The gate voltage is applied using a Keithley 2400 as the voltage source.

Hall effect measurements

The Hall bar dimensions are $L = 120$ μm and $w = 30$ μm as shown in the inset of Fig. 4.3 a). We define the Hall bar aspect ratio as: $Z = L/w = 4$. We apply a DC charge current and measure the longitudinal and transverse resistances under the application of an external magnetic field $\mathbf{B}$. The direction of $\mathbf{B}$ is along the $\hat{\mathbf{z}}$ direction as shown in the inset of Fig. 4.3 a).

We report in Fig. 4.3 a) the temperature dependence of the zero magnetic field four-probe longitudinal resistance $R_{xx,0} = \frac{U_{xx,0}}{I}$. The resistance plateau below 10 K differs from the purely thermally activated transport behavior one would expect for bulk Ge, therefore we

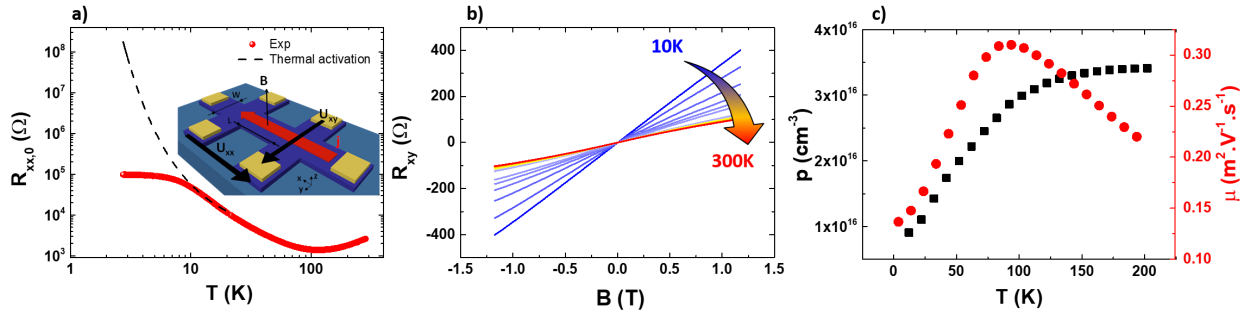

Figure 4.3 – a) Temperature dependence of the four-probe longitudinal resistance measured with an applied current of 10 μA. The red curve corresponds to experimental data exhibiting a resistance saturation; the dashed black line shows the expected semiconducting behavior considering a thermal activation of 2.6 meV. b) Hall effect measurements carried out at different temperature ranging from 10 K to 300 K using a DC excitation current of 10 μA, the external magnetic field is applied perpendicularly to the film plane. c) Extracted carrier density (black squares) and mobility (red dots) as a function of the temperature.

interpret this observation as a fingerprint of a conduction channel in parallel with the bulk conduction (black dashed line). This situation is very similar to the conduction by the surface states of 3D topological insulators.[126,149,199,200] Hall effect measurements were carried out as a function of the sample temperature. Fig. 4.3 b) shows the linear dependence of the transverse resistance $R_{xy} = \frac{U_{xy}}{I}$ with respect to the magnetic field, indicating that only one type of carriers contributes to the electrical conduction. The positive slope confirms the hole nature of the carriers. The conductivity is related to the carrier density and mobility by the following expressions:

$$R_{xy} = \frac{U_{xy}}{I} = \frac{B}{pte} \tag{4.4}$$

$$\sigma_{xx} = ep\mu_h \tag{4.5}$$

Where t is the Ge thickness, e is the hole elementary charge, p is the carrier density, σ_{xx} is the channel longitudinal conductivity and μ_h is the hole mobility.
Eq. 4.4 and Eq. 4.5 can be combined to extract the carrier density and mobility as a function of the temperature [Fig. 4.3 c)]. p decreases monotonously as the temperature decreases as a consequence of thermal activation. The mobility is maximum at $T_M = 85$ K when the electron-phonon scattering is minimum.

Angular dependences

We investigate the different magnetoresistance (MR) contributions in Ge (111) at low temperature. In DC measurements, the usual current-independent resistance is even with respect to the applied current direction, whereas a current-dependent ($R(I) \propto I$) resistance is odd. For each data point, the current direction is dynamically switched from positive to negative (along $+x$ and $-x$) and the even and odd components of the longitudinal and transverse resistances are calculated using the following definitions:

$$\begin{aligned} R_{xx}^{\text{even}} &= [R_{xx}(+I) + R_{xx}(-I)]/2 \\ R_{xx}^{\text{odd}} &= [R_{xx}(+I) - R_{xx}(-I)]/2 \\ R_{xy}^{\text{even}} &= [R_{xy}(+I) + R_{xy}(-I)]/2 \\ R_{xy}^{\text{odd}} &= [R_{xy}(+I) - R_{xy}(-I)]/2 \end{aligned} \tag{4.6}$$

Even if we use a DC current, we call our method pseudo-AC because the even and odd components correspond to the $1st$ and $2nd$ harmonic signals in AC measurements. First, we focus on the longitudinal magnetoresistance R_{xx}^{even}. Fig. 4.4 a-c) shows the different measurement geometries. The current is applied along $+x$ and the external magnetic field is applied along the (θ, φ) direction, θ and φ being the polar and azimuth angles. The magnetic field dependence up to 5 T and for 3 different orthogonal orientations is reported in Fig. 4.4 d).

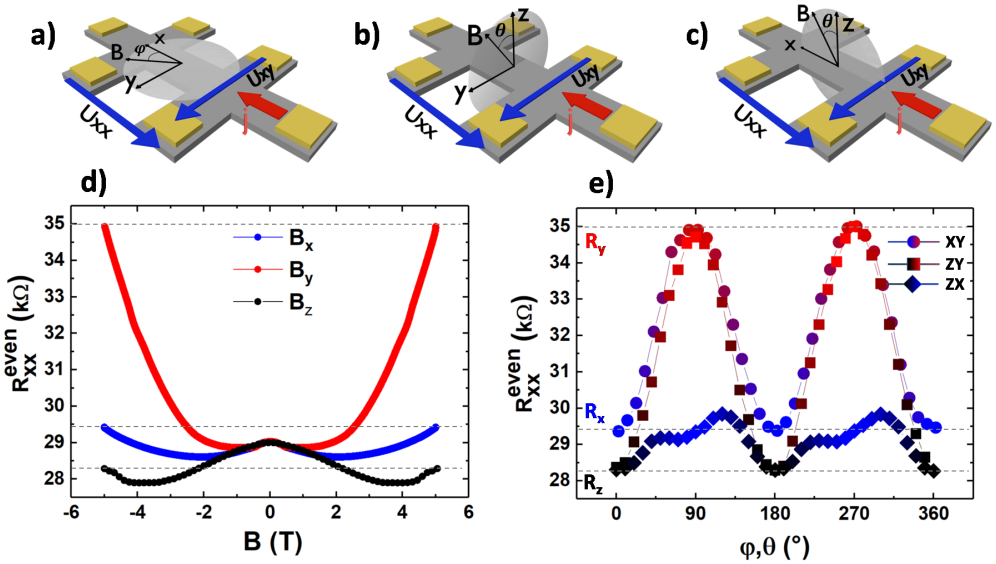

Figure 4.4 – a-c) Schematic of the angular dependent magnetotransport experiments where the magnetic field is applied within the 3 planes: xy, zy and zx. d) Magnetic field dependence of the current-independent longitudinal magnetoresistance R_{xx}^{even} for the three field directions. e) R_{xx}^{even} angular dependences recorded at $T = 15$ K using an applied current of $I = 10$ μA and an external field of $B = 5$ T. In d) and e), the color code indicates the magnetic field projection along: x (blue), y (red), x (black).

We observe an unusual behavior, indeed the magnetoresistance (MR) in a conventional three-dimensional semiconductor exhibits a parabolic MR ($\propto B^2$) as a consequence of the Lorentz force acting on the electrical carriers.[149] However, at low temperature (15 K), for a given field intensity: $R_{xx}^{even}|_{B_y} > R_{xx}^{even}|_{B_x} > R_{xx}^{even}|_{B_z}$. We also note that the MR is non-monotonous with respect to the field, regardless of the orientation. The MR is first negative until the field reaches a critical value B_c where the MR shows a minimum, and above which the MR becomes positive again and reaches up to 20 % at $B_y = 5$ T. Interestingly, the MR is almost constant and isotropic at low magnetic fields ($B < 1$ T).

Fig. 4.4 e) reports the angular dependence of R_{xx}^{even} at 15 K in the three orthogonal planes (xy, zy and zx) for $I = 10$ µA. This MR signal exhibits maxima for $\varphi = 90°$ and minima for $\varphi = 0°$ giving a periodicity of 180°. Since the sign is not reversed when reversing the magnetic field direction, we call this term anisotropic magnetoresistance (AMR) by analogy with ferromagnets. At 15 K, we find an AMR of 0.4 % under a magnetic field of 1 T. At this magnetic field, the out-of-plane angular dependences (in zy and zx planes) show similar behaviors. The same behavior has already been observed in InAs quantum wells as a consequence of the competition between the Zeeman and Rashba interactions in the conduction channels.[201] Therefore, this MR gives the first signature of the electrical transport in the Rashba states. We now extend our study to all the magnetoresistance contributions: longitudinal and transverse, even and odd with respect to the electrical current direction.

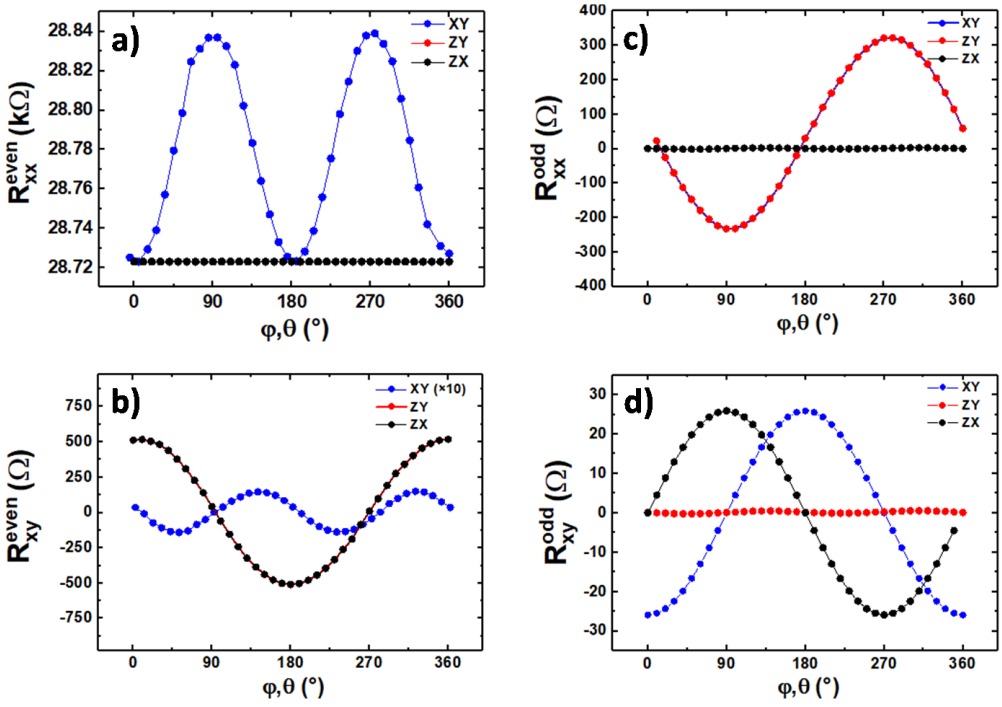

Figure 4.5 – a) R_{xx}^{even} b) R_{xy}^{even} c) R_{xx}^{odd} and d) R_{xx}^{odd} as a function of the magnetic field orientation. The measurements were carried out at 15 K, with a magnetic field of 1 T and a current of 10 µA.

We report in Fig. 4.5 the full angular dependences of the four MR components recorded at 15 K, with an applied magnetic field $B = 1$ T and a current $I = 10$ μA. At this magnetic field, R_{xx}^{even} exhibits an angular dependence only when the field is rotated in the xy plane, as suggested by the field dependence shown in Fig. 4.4 d). The in-plane angular dependence of R_{xy}^{even} follows a $\sin^2(\varphi)$ function (see Fig. 4.5 b)) which is characteristic of the planar Hall effect (PHE).[194] While this effect is usually restricted to magnetic materials, it was recently observed in high spin-orbit coupling systems like topological insulators.[194] The (zy) and (zx) scans show the expected Hall effect cosine dependence.

In Fig. 4.5 c) and d), we report the angular dependences of R_{xx}^{odd} and R_{xy}^{odd} in the (xy), (xz) and (yz) planes. We observe a unidirectional behavior for both the longitudinal and transverse resistances: R_{xx}^{odd} and R_{xy}^{odd}. Their maxima are respectively found where $\mathbf{B} \parallel \mp\hat{\mathbf{y}}$ and $\mathbf{B} \parallel \mp\hat{\mathbf{x}}$. Thus, we can write: $R_{xx}^{\text{odd}} = -R_{xx,\Delta}^{\text{odd}} \sin(\varphi)\sin(\theta)$ and $R_{xy}^{\text{odd}} = -R_{xy,\Delta}^{\text{odd}} \cos(\varphi)\sin(\theta)$ where $R_{xx(xy),\Delta}^{\text{odd}}$ is defined as the sine amplitude. These functions are shown as solid lines in Fig. 4.5. R_{xy}^{odd} angular dependence reveals the presence of the Nernst effect due to a current-induced vertical temperature gradient (along $\hat{\mathbf{z}}$) in the Ge (111) film (see Fig. 4.9). This effect generates a spurious thermal UMR signal in the longitudinal resistance.[195] The Nernst effect contribution to R_{xx}^{odd} can be written as: $R_{xx,\Delta}^{\text{odd,Nernst}} = Z\, R_{xy,\Delta}^{\text{odd}}$, with Z being the aspect ratio of the Hall bar channel ($Z = 4$ in our case).[85] Hence, to remove the Nernst effect contribution from the longitudinal signal, we study $R_{\text{UMR}}^{\Delta} = R_{xx,\Delta}^{\text{odd}} - Z\, R_{xy,\Delta}^{\text{odd}}$. This expression is derived in the next section dedicated to thermal effects.

In Fig. 4.6 we investigate the dependence of R_{UMR}^{Δ} on the applied current [Fig. 4.6 a)], magnetic field [Fig. 4.6 b)] and temperature [Fig. 4.6 c)]. The signal is normalized with respect to the zero field resistance $R_{xx,0}$ at the corresponding current.
In agreement with previous reports on the UMR as a consequence of the spin-momentum lock-

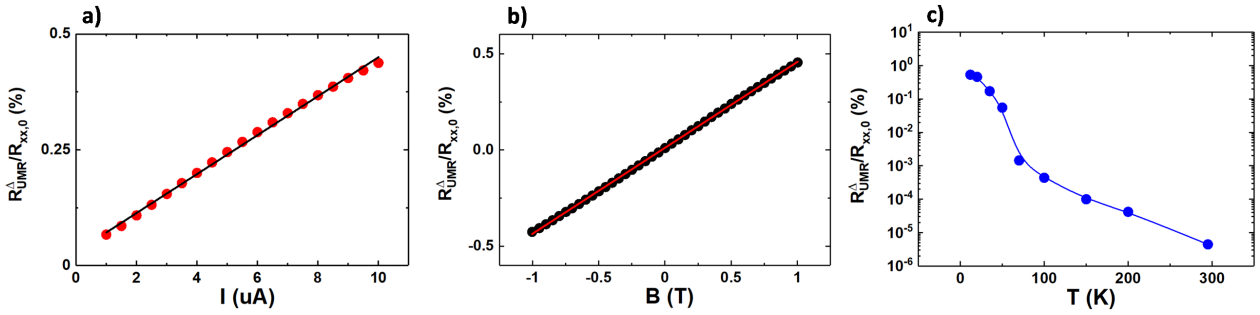

Figure 4.6 – R_{UMR}^{Δ} normalized to the zero magnetic field resistance $R_{xx,0}$ at $\varphi = 270°$ (in %) as a function of a) the applied current for $B = 1$ T and $T = 15$ K b) the magnetic field for $I = 10$ μA and $T = 15$ K, and c) the temperature for $B = 1$ T and $I = 10$ μA. The dots are the experimental data and the lines linear fits in a) and b).

ing,[85,86] we observe a signal proportional to the current and the magnetic field. $R^{\Delta}_{\mathrm{UMR}}/R_{xx,0}$ is maximum and almost constant at low temperature ($T < 20$ K) and sharply decreases when the temperature becomes comparable to the Rashba spin-splitting energy (≈ 60 K).
As shown in Fig. 4.7 a), the application of a top gate voltage modulates the channel resistance $R_{xx,0}$. In Fig. 4.7 b), we also plot both the longitudinal and transverse odd resistance components as a function of the gate voltage. The transverse component we attribute to the Nernst effect ($Z\,R^{\mathrm{odd}}_{xy,\Delta}$) stays constant with the gate voltage. This observation is consistent with the fact that this effect is due to a vertical temperature gradient in the Ge (111) film and is almost unaffected by the top gate voltage. By contrast, $R^{\mathrm{odd}}_{xx,\Delta}$ is much affected by the gate voltage: it increases from $V_g = -10$ V to $V_g = +10$ V by a factor ≈ 3. Therefore, after substracting the longitudinal magnetoresistance component due to the Nernst effect ($Z\,R^{\mathrm{odd}}_{xx,\Delta}$), we find that $R^{\Delta}_{\mathrm{UMR}}$ cancels out at $V_g = -10$ V and increases by about 50% from $V_g = 0$ V to $V_g = +10$ V [Fig. 4.7 c)].

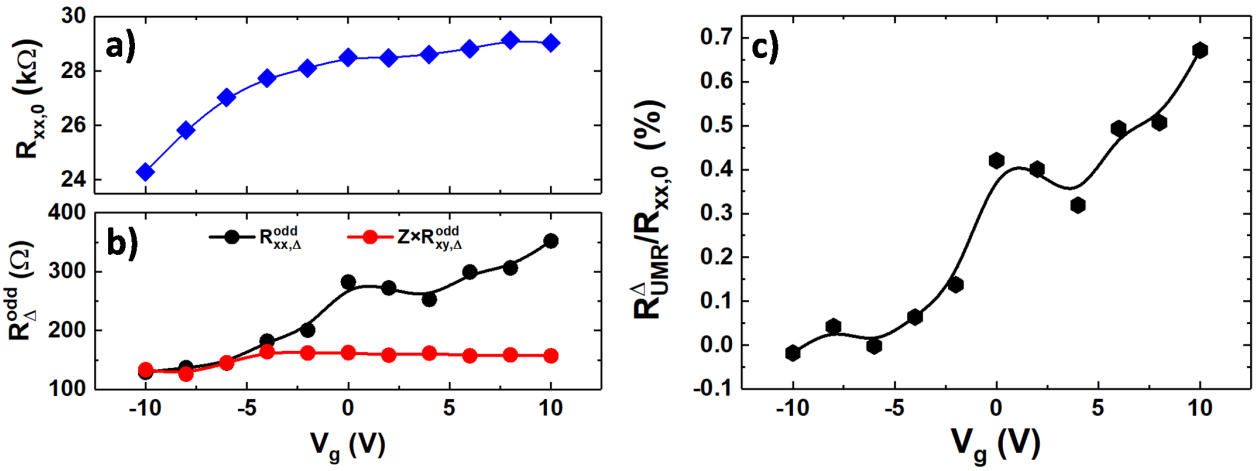

Figure 4.7 – a) Gate voltage dependence of the zero field resistance $R_{xx,0}$ b) UMR contribution $R^{\mathrm{odd}}_{xx,\Delta}$ and the Nernst contribution $Z\,R^{\mathrm{odd}}_{xy,\Delta}$ gate voltage dependence recorded at $\varphi = 270°$ using: $I = 10$ μA, $B = 1$ T and $T = 15$ K. c) Corresponding gate dependence of $R^{\Delta}_{\mathrm{UMR}} = R^{\mathrm{odd}}_{l,\Delta} - Z\,R^{\mathrm{odd}}_{t,\Delta}$, normalized by the zero field resistance $R_{xx,0}$.

To make a comparison with previous results on different systems, we can define a figure of merit η. Since the UMR signal is proportional to the current and magnetic field, a natural definition is: $\eta = R^{\Delta}_{\mathrm{UMR}}/(R_{xx,0}\,j\,B)$. At 15 K, in Ge (111), we obtain $\eta = 4.2 \times 10^{-7}$ cm^2/(A T) if we consider that the current completely flows within the spatial extension of the subsurface states (10 atomic layers from Ref. [189]). The value of η obtained in Ge (111) is orders of magnitude larger than the one of $SrTiO_3$ at 7 K [$\eta = 2 \times 10^{-9}$ cm^2/(A T)] from Ref. [184] and the one of Bi_2Se_3 at 60 K [$\eta = 2 \times 10^{-11}$ cm^2/(A T)] from Ref. [185]. Additionally, UMR the was observed in the recently discovered topological insulator $\alpha-$Sn where $\eta = 1.4 \times 10^{-9}$ cm^2/(A T).[202]

Thermal effect contributions

The Nernst effect is analogous to the Hall effect, where the driving force is no longer a voltage gradient but a thermal gradient:

$$\mathbf{E_{Nernst}} = N\nabla\mathbf{T} \times \mathbf{B} \tag{4.7}$$

Where N is the Nernst coefficient, by considering an arbitrary oriented temperature gradient $\nabla\mathbf{T} = (\nabla T_x, \nabla T_y, \nabla T_z)$ and an external magnetic field: $\mathbf{B} = ||\mathbf{B}||(\sin\theta\cos\varphi, \sin\theta\sin\varphi, \cos\theta)$, the resulting Nernst contributions give the following angular dependences to the second harmonic longitudinal ($R^{2\omega}_{xx,Nernst}$) and transverse ($R^{2\omega}_{xy,Nernst}$) resistances:

$$R^{2\omega}_{xx,Nernst} \propto N\left[\Delta T_y \cos\theta - \Delta T_z \sin\theta\sin\varphi\right] \tag{4.8}$$

$$R^{2\omega}_{xy,Nernst} \propto N\left[\Delta T_z \sin\theta\cos\varphi - \Delta T_x \cos\theta\right] \tag{4.9}$$

Our experimental results suggest that the temperature gradient in our system is mostly out-of-plane ($\nabla T_x \approx 0, \nabla T_y \approx 0, \nabla T_z > 0$) as a consequence of the current flowing simultaneously in the Ge bulk and subsurface states for temperatures close to room temperature or high current intensities. Eqs. [4.8] and [4.9] reduce to:

$$R^{2\omega}_{xx,Nernst} \propto R_{Nernst}\sin\theta\sin\varphi \tag{4.10}$$

$$R^{2\omega}_{xy,Nernst} \propto R_{Nernst}\sin\theta\cos\varphi \tag{4.11}$$

Where $R_{Nernst} = N||\mathbf{B}||\Delta T_z$, from the Fig. 4.5 d) and d), we identify that $R^{2\omega}_{xy,\Delta} = R_{Nernst}$. Therefore, by using the aspect ratio of the Hall bar, we can remove the Nernst effect contribution from the longitudinal signal to obtain the UMR term $R^{\Delta}_{\mathrm{UMR}}$:

$$R^{\Delta}_{\mathrm{UMR}} = R^{2\omega}_{xx,\Delta} - Z \times R^{2\omega}_{xy,\Delta} \tag{4.12}$$

Where Z is the Hall bar aspect ratio ($Z = 4$ here).

In order to distinguish between the UMR and Nernst effects, we plot in Fig. 4.8 $R^{\mathrm{odd}}_{xx,\Delta}/R_{xx,0}$ and $R^{\mathrm{odd}}_{xx,\Delta}/R^{\mathrm{odd}}_{xy,\Delta}$ as a function of the current intensity and temperature for two different aspect ratios Z. First, regardless the applied current, the UMR decreases sharply when increasing the temperature from 15 K to 60 K. Then we observe three different regimes for the current dependence. For low currents, we find the linear dependence on the current as expected for the bilinear character of the UMR. It reaches then a maximum value before decreasing down to a constant value. This current dependence can be interpreted from the electronic band structure shown in Fig. 4.2 as follows: (i) for low currents, the Fermi level lies in the subsurface states and we observe the UMR as a result of the spin-momentum locking; (ii) for intermediate currents, holes start to be thermally excited into the bulk valence bands

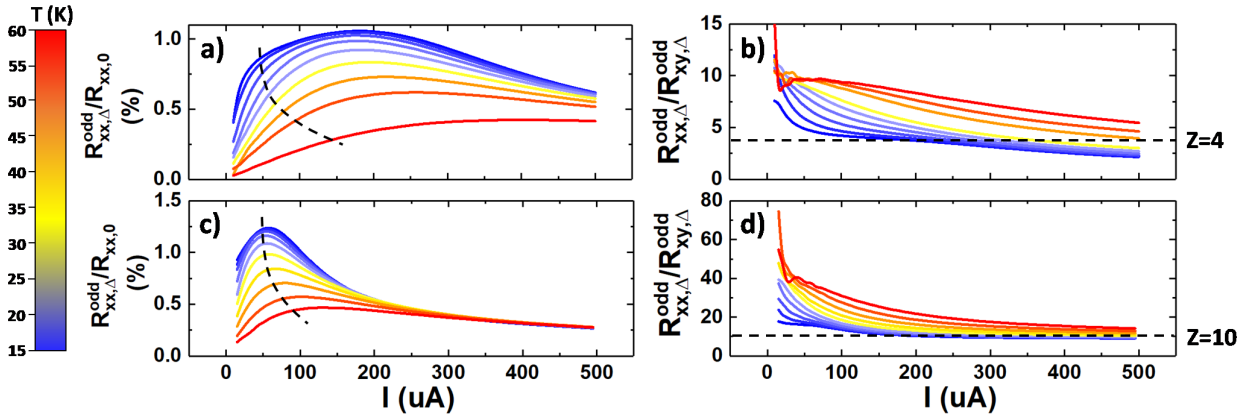

Figure 4.8 – Temperature and current dependences of $R^{\text{odd}}_{xx,\Delta}/R_{xx,0}$ for a Hall bar aspect ratio Z=L/w=4 (a) and Z=10 (c). Ratio $R^{\text{odd}}_{xx,\Delta}/R^{\text{odd}}_{xy,\Delta}$ for Z=4 (b) and Z=10 (d). In a) and c), the black dashed line separates two MR regimes and in b) and d), it indicates the Hall bar aspect ratio.

and the UMR decreases progressively because of the current short into bulk Ge, and (iii) for high currents, vertical thermal gradients set in the germanium film leading to the Nernst effect. The black dotted line in Fig. 4.8 a) and c) marks the transition from regime (i) to regime (ii). Then the Nernst effect can be detected in the MR signal by plotting the ratio $R^{\text{odd}}_{xx,\Delta}/R^{\text{odd}}_{xy,\Delta}$ as a function of the temperature and applied current (Fig. 4.8 b) and d)). This ratio should be equal to the Hall cross aspect ratio $Z = 4$ (Fig. 4.8 a) and b)) and $Z = 10$ (Fig. 4.8 c) and d)) when only the Nernst effect is measured. For high applied currents, we thus conclude that we only observe the Nernst effect in the Ge (111) film. In the $Z = 10$ Hall bar, the current density is larger as the conduction channel width is smaller, this results in a higher UMR but the Nernst effect appears at lower applied currents.

Control measurements on n-type Ge/Si (111) and Ge (100)

The UMR intensity depends on the Fermi level position in the band structure. Since the subsurface Rashba states are located below the mid gap and close to the top of the valence band, a similar 2- µm-thick Ge-on-Si (111) epilayer was grown using the same LEPECVD technique but with n-type doping. The carrier concentration at 15 K is comparable to the one of the p-type Ge layer previously studied ($n \approx 10^{16}$ cm^{-3}). The same Hall bars were patterned so that we can directly compare the different resistances.

The zero field resistance $R_{xx,0}$ is about 5.8 kΩ at 15 K. As shown in Fig. 4.9 b), in the same measurement conditions, we measure a very weak longitudinal signal R^{odd}_{xx} which corresponds to the longitudinal component of the Nernst effect: $R^{\text{odd}}_{xx} \approx Z \times R^{\text{odd}}_{xy}$ with $Z = 4$. Therefore the spin-dependent UMR is not measurable in n-type Ge (111).

As a control experiment, the same Hall bars with an aspect ratio $Z = 4$ were processed in a 120 nm-thick Ge (100) layer on insulator (GeOI). The presence of subsurface states is

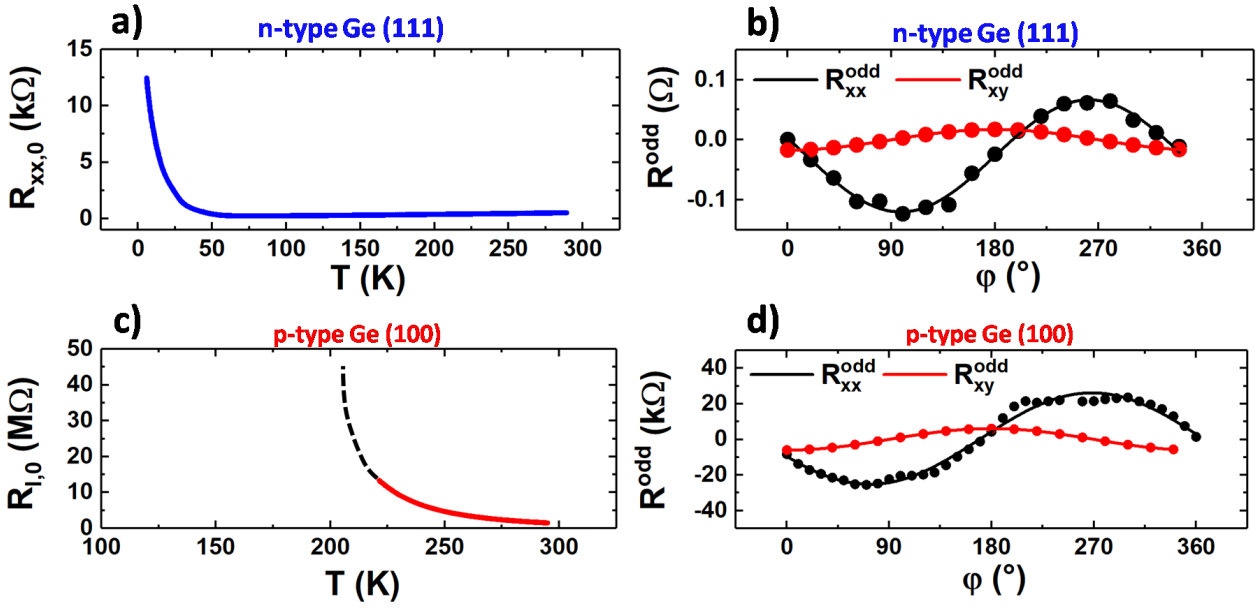

Figure 4.9 – a) Four-probe resistance of the n-type Ge (111) film as a function of temperature measured with an applied current of 10 μA. b) Angular dependence in the (xy) plane of R_{xx}^{odd} and R_{xy}^{odd} for the n-type Ge (111) film at 15 K. The applied field is 1 T and the current 10 μA. c) Temperature dependence of the Ge (100) film resistance. Due to high resistivity, the current is limited to 100 nA. d) Angular dependence in the (xy) plane of R_{xx}^{odd} and R_{xy}^{odd} for the p-type Ge (100) film at 200 K. The applied field is 1 T and the current 100 nA. The solid black and red lines are fitting curves of R_{xx}^{odd} and R_{xy}^{odd} respectively using sine and cosine functions.

specific to the (111) crystal orientation, therefore such states are not expected in the (100) orientation.[203] The doping level of the Ge (100) film is very close to that of the p-type Ge (111) sample ($p \approx 10^{16}$ cm^{-3}) at room temperature.

As shown in Fig. 4.9 c), the temperature dependence of the resistance is very different from that of the (111) orientation, the resistivity is orders of magnitude higher and eventually all carriers are frozen below 180 K. This behavior is in agreement with the absence of "metallic" subsurface states in Ge (100) as a parallel conduction channel to the bulk. At 200 K, the zero field resistance $R_{xx,0}$ is about 46 MΩ, we used reasonable current conditions $I = 100$ nA to detect UMR and again we could only measure the thermal contribution coming from the Nernst effect as: $R_{xx}^{\text{odd}} \approx Z \times R_{xy}^{\text{odd}}$ with $Z = 4$.

4.2.3 Origin of the Rashba unidirectional magnetoresistance

Literature review

In the literature, a few groups reported the observation of UMR in high spin-orbit coupling materials like topological insulator (TIs),[184] the two-dimensional electron gas (2DEG) at the $SrTiO_3(111)$ surface,[185] the polar semiconductor BiTeBr[204] and InAs quantum wells.[192] Different theoretical approaches were explored to explain the origin of UMR. The key point is to relate the material spin texture to the transport properties using a Boltzmann formalism.[186] In Refs. [184] and [185], the authors report that the essential ingredient to observe UMR is the hexagonal warping of the out-of-plane spin texture that adds to the usual in-plane spin-momentum locking in TIs and Rashba 2DEG. The system is described by the following Hamiltonian:

$$\mathscr{H}_{TI} = \sigma \cdot \left[\alpha\hbar\mathbf{k} \times \hat{\mathbf{z}} + \lambda\mathbf{k} \times \hat{\mathbf{y}}'(k_{x'}^2 - 3k_{y'}^2) + g\mu_B\mathbf{H}\right] \tag{4.13}$$

where $\hat{\mathbf{y}}'$ and $\hat{\mathbf{z}}$ are the unit vectors along $\overline{\Gamma M}$ and the normal to the surface respectively, σ are the Pauli spin matrices, α is the Fermi velocity and λ is an empirical parameter which is representative of the hexagonal warping strength. The authors used this model to derive the current-dependent part of the resistance, by expanding the solution of the Boltzmann equation to second order in the electric field and to first order in the magnetic field. The energy eigenvalues are obtained by solving the Eq. 4.13:

$$\varepsilon(\mathbf{k}) = |\alpha\hbar\mathbf{k} \times \hat{\mathbf{z}} + \lambda\mathbf{k} \times \hat{\mathbf{y}}'(k_{x'}^2 - 3k_{y'}^2) + g\mu_B\mathbf{H}| \tag{4.14}$$

The electron group velocity is given by:

$$\mathbf{v}(\mathbf{k}) = \frac{1}{\hbar}\frac{\partial\varepsilon(\mathbf{k})}{\partial\mathbf{k}} \tag{4.15}$$

Within the Boltzmann formalism, the current density can then be expressed as:

$$\mathbf{j} = -e\sum_k \mathbf{v}(\mathbf{k})f(\mathbf{k} - \mathbf{k_d}) \tag{4.16}$$

where the effect of the electric field $\mathbf{E}$ is to shift the Fermi contour by $\mathbf{k_d} = \dfrac{e\mathbf{E}\tau}{\hbar}$ where τ is the single-band relaxation time approximation. Note that this approximation is questionable as it implies a field independent relaxation time which is unrealistic.

This formalism leads to the following analytic expression for the second harmonic resistance $R_{xx}^{2\omega}$ (equivalent to R_{xx}^{odd} in our DC measurements):

$$R_{xx}^{2\omega} = E\frac{L}{W}\left[\frac{36\pi\lambda^2\varepsilon_F g\mu_B}{e\alpha^5\hbar^6}H_y + \frac{6\pi\lambda g\mu_B}{e\alpha^2\hbar^3\epsilon_F}H_z\cos 3\phi_{\Gamma K}\right] \tag{4.17}$$

where H_y and H_z are the y and z components of the magnetic field and $\phi_{\Gamma K}$ the angle between

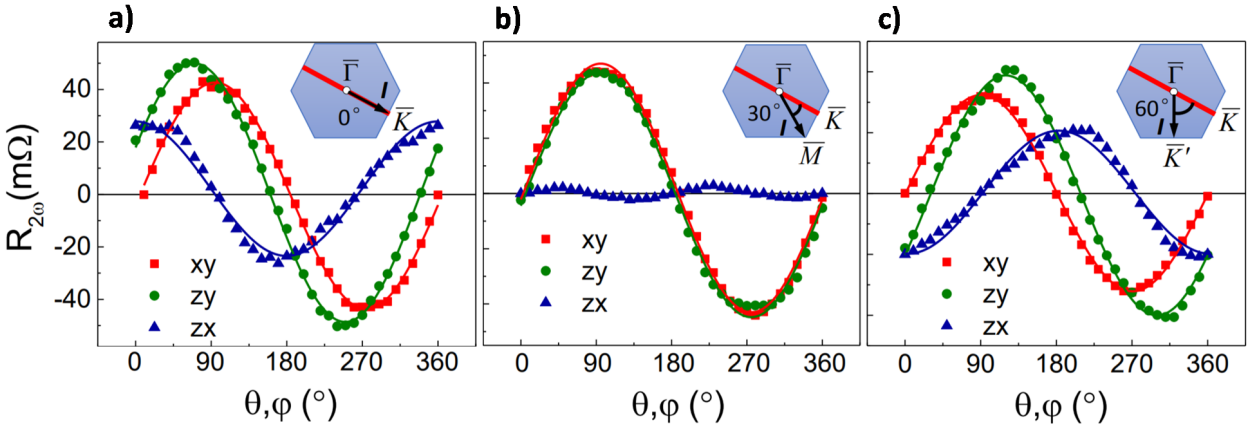

Figure 4.10 – Extracted from Ref. [184]. Second harmonic resistance recorded in the three orthogonal planes xy, zy and zx for three devices corresponding to the current applied at an angle of 0° a), 30° b) and 60° c) with respect to the $\overline{\Gamma K}$ direction, respectively. These scans were performed under $B = 9$ T, $T = 60$ K and $I = 0.55$ mA. Blue hexagons in a-c represent the Bi_2Se_3 surface Brillouin zone. The red lines indicates the $\overline{\Gamma K}$ direction and the black arrow denotes the current direction in the reciprocal space.

the $\overline{\Gamma K}$ direction of the reciprocal lattice and the current direction.

This theoretical approach is justified by the hexagonal warping of the Bi_2Se_3 spin texture. Fig. 4.10 (extracted from Ref. [184]) summarizes the second harmonic magnetotransport resistance measurements for different magnetic field orientations a 20 nm-thick Bi_2Se_3 film grown on Sapphire by MBE. The measurements were carried out at $T = 125$ K, using an AC excitation current $I = 0.55$ mA under an external magnetic field $B = 9$ T. The Hall bars were patterned in the Bi_2Se_3 film along different crystallographic axis to investigate the angular dependence of the second harmonic resistance predicted by Eq. [4.17].

Even though the UMR is extremely small, the experimental data show a very good agreement with the theory. However, the authors do not present any transverse resistance measurements, so that the thermal effects such as the Nernst effect are not properly accounted for. Ge (111) shares the same hexagonal symmetry and this theory could explain the observed UMR.

Origin of the UMR in Ge (111)

In order to understand the nature of the UMR effect, the crystal orientation dependence of the signals has been investigated. Hall bars of the same dimensions were patterned along $\overline{\Gamma K}$, $\overline{\Gamma K'}$ and $\overline{\Gamma M}$ using a similar process. The crystal orientation of the device is known from X-ray diffraction measurements.

In Fig. 4.11, we present the angular dependence of R_{xx}^{odd} at 15 K, 1 T and 10 μA in the (xy), (zy) and (zx) planes for the current flowing along 3 different directions in the surface Brillouin zone. Our experimental data clearly show that there is no quantitative difference in R_{xx}^{odd} between the 3 crystal orientations. At variance with the previously reported systems,[184,185] the UMR is isotropic with respect to the direction of the current in the surface Brillouin

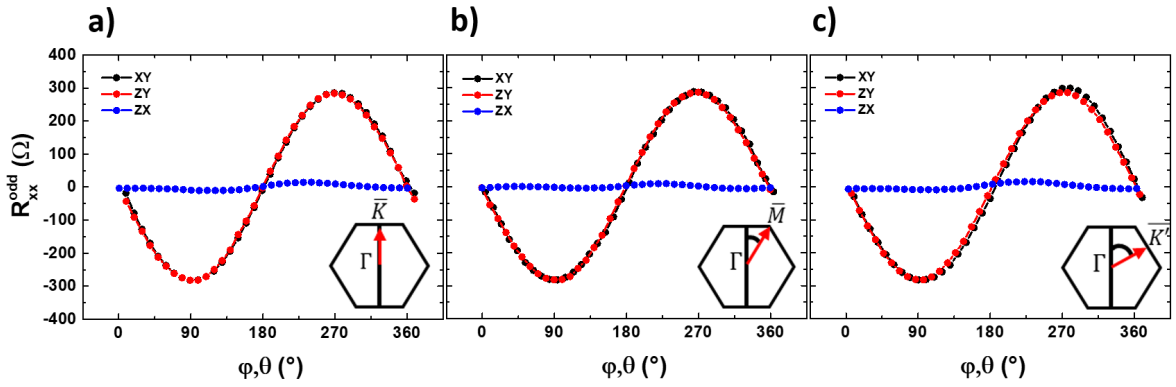

Figure 4.11 – Scans of R_{xx}^{odd} in the (xy), (zy) and (zx) planes for the conduction channel patterned with an angle of 0° a), 30° b) and 60° c) with respect to the $\overline{\Gamma K}$ direction of the surface Brillouin zone (SBZ) at 15 K. The applied magnetic field is 1 T and the current 10 μA. The insets show the SBZ and the red arrows indicate the current direction.

zone (SBZ). In the data of the previous section, the current is along the ΓM direction of the Ge (111) SBZ, but no difference is detected with the current flowing along other reciprocal lattice directions. In Refs. [184, 186], the magnetoresistance depends on the direction of the current flow in the SBZ, indicating that, in such a case, the UMR originates from the hexagonal warping[184] or strong crystal field effects.[185] In the case of Ge, this contribution appears to be negligible. We thus propose an alternative mechanism, in which the UMR in Ge (111), results from a combination of the applied magnetic field and the pseudomagnetic field generated by the current applied in the spin-splitted subsurface states of Ge (111) shown in Fig. 4.12 a). Ge (111) subsurface states are located close to the top of the valence bands and can only contribute to transport in p-type Ge (111).[188]

This interpretation is supported by the fact that we do not observe this effect for n-type Ge (111) nor for Ge (100) films.[203] It also explains the gate voltage dependence of R_{UMR}^{Δ} in Fig. 4.7 c). Applying negative gate voltage shifts the Fermi level down into the valence band which leads to the activation of bulk conduction and $R_{\text{UMR}}^{\Delta} \approx 0\ \Omega$ for $V_g = -10$ V. At variance, by sweeping the gate voltage from -10 V to $+10$ V, the Fermi level shifts into the subsurface states thus increasing R_{UMR}^{Δ}. Finally, this interpretation also explains the temperature dependence of the UMR. By increasing the temperature, bulk conduction in the valence band is activated and shorts the subsurface states. Moreover, the Rashba spin-orbit coupling of $\sim 58\, k_B$ in Ge subsurface states[188] becomes negligible with respect to $k_{\text{B}}T$ suppressing spin-momentum locking.

For the Fermi level crossing the subsurface states as shown in Fig. 4.12 a), the Fermi contour is made of two concentric rings [C and D in Fig. 4.12 b)] with opposite spin helicities. To describe the magnetotransport inside the subsurface states, we consider the following model Hamiltonian:

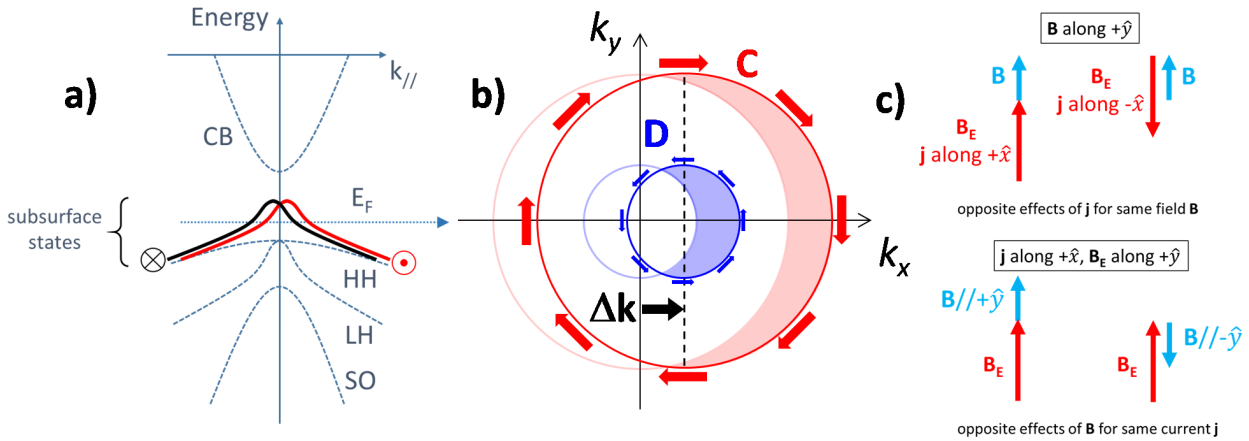

Figure 4.12 – a) Schematics of the Ge (111) electronic band structure (in agreement with Ref. [188]) showing the bulk conduction and valence bands. The Fermi level is at a position corresponding to a p-doped film. Subsurface states are located just above the maximum of the bulk valence band and are crossed by the Fermi level. They are spin-splitted by the Rashba and atomic spin-orbit interactions. b) Edelstein effect in a Rashba system: the outer (inner) contour is named C (D) with clockwise (counter-clockwise) spin helicity is shifted by $\pm\ \Delta\mathbf{k}$ due to the application of a current density $\mathbf{j}$ along $+\ \hat{\mathbf{x}}$. c) Illustration of the combined effects of the applied magnetic field $\mathbf{B}$ and the current dependent pseudo-magnetic field $\mathbf{B}_\mathrm{E}$ on the resistivity of subsurface states . The current direction and spin helicity set the pseudo-magnetic field direction.

$$\mathscr{H} = -\frac{\hbar^2 k^2}{2m^*} + \alpha\,(\mathbf{k}\times\boldsymbol{\sigma})\cdot\hat{\mathbf{z}} + g\mu_\mathrm{B}\boldsymbol{\sigma}\cdot\mathbf{B}, \tag{4.18}$$

with $\hbar$ being the reduced Planck constant, m^* the effective mass of holes in the subsurface states, α the Rashba spin-orbit interaction, $\boldsymbol{\sigma}$ the vector of Pauli matrices, g the Landé factor and μ_B the Bohr magneton. When a 2D charge current density $\mathbf{j}$ (in A/m) flows in the subsurface states, in the Boltzmann approach, the hole momentum acquires an extra component $\Delta\mathbf{k} = \beta\mathbf{j}$ with $\beta = 4\pi/(ev_\mathrm{F}k_\mathrm{F})$, where v_F and k_F are the Fermi velocity and wavevector and $e = |e|$. A well-known consequence of such a shift of the Rashba Fermi contours is the Rashba-Edelstein effect leading to a net carrier spin polarization[18,61] due to the unbalance between the opposite spin polarizations induced by the shift in the same direction of the Rashba Fermi contours of opposite helicity (see Fig. 4.13 b)).

In parallel with the Rashba-Edelstein effect, the shift $\Delta\mathbf{k}$ introduces a current-induced out-of-equilibrium energy term which, from Eq. 4.18, is equal to $\alpha(\Delta\mathbf{k}\times\boldsymbol{\sigma})\cdot\hat{\mathbf{z}} = \alpha\beta(\mathbf{z}\times\mathbf{j})\cdot\boldsymbol{\sigma}$ and acts on the spins as a pseudo-magnetic field $\mathbf{B}_\mathrm{E} = (\alpha\beta/g\mu_\mathrm{B})\,\hat{\mathbf{z}}\times\mathbf{j}$. As illustrated in Fig. 4.13 c), for a current along $\pm\ \hat{\mathbf{x}}$ with $\alpha > 0$, this field is directed along $\pm\ \hat{\mathbf{y}}$ and proportional to the current density. In the presence of an applied magnetic field $\mathbf{B}$, the spin of the subsurface states is submitted to $\mathbf{B} + \mathbf{B}_\mathrm{E}$, $\mathbf{B}_\mathrm{E}$ increasing or decreasing the effect of the y component of $\mathbf{B}$ for currents either along $+$ or - $\hat{\mathbf{x}}$. In the same way, still for $\alpha > 0$, for $\mathbf{j}$ along $+\hat{\mathbf{x}}$ and $\mathbf{B}_\mathrm{E}$

along $\hat{\mathbf{y}}$, there is addition or subtraction of the effects of $\mathbf{B}$ and $\mathbf{B}_{\mathrm{E}}$ for opposite orientations of $\mathbf{B}$ along $\hat{\mathbf{y}}$. The physics of the UMR thus comes from the pseudo-field $\mathbf{B}_{\mathrm{E}}$ induced by the out-of-equilibrium situation of a current that acts on the spins. We can go a little further by assuming that the AMR term shown in Fig. 4.5 d) (the only MR in the limit $j \to 0$) is also due to the effect of $\mathbf{B}$ on the spins. We thus follow Taskin *et al.*[194] who explain the AMR in systems with spin-momentum locking by the freezing of back scattering (partial freezing for Rashba 2DEG) at zero field (low resistance) and the anisotropic re-introduction of some back scattering and anisotropic re-introduction of resistance by the partial re-alignment of the locked spin by the magnetic field. We thus assume that the AMR comes only from the interaction of $\mathbf{B}$ with the spins and neglect other contributions such as the effect of the Lorentz force on the trajectories. Then, in the situation of finite j, we add $\mathbf{B}_{\mathrm{E}}$ to $\mathbf{B}$ in the B^2 term of the AMR to derive the expression of UMR. The AMR term can be written as:

$$(\Delta R/R)_{\mathrm{AMR}} = -A\,B^2\,\cos^2(\varphi) = AB_y^2 - A\,B^2 \tag{4.19}$$

Where $A \approx 0.004\ \mathrm{T}^{-2}$. Adding $B_{\mathrm{E}y} = \alpha\beta j/g\mu_{\mathrm{B}}$ to B_{y}, and keeping only the terms of first order in j gives:

$$\Delta R/R = -AB^2\cos^2(\varphi) + 2A(\alpha\beta/g\mu_{\mathrm{B}})\,j\,B\sin(\varphi) \tag{4.20}$$

Where the second term, proportional to $j\,B$, is the UMR. Our experimental results with a UMR proportional to $j\,B\sin(\varphi)$, see [Fig. 4.6], correspond to a negative value of the Rashba coefficient α, that is to the clockwise chirality of the spin orientation in the outer Fermi contour. This chirality is in agreement with the chirality derived from spin-resolved ARPES measurements for the subsurface states in Ge at the Ge/Bi interfaces, as shown in Fig. 3a of Ref. [187].

Quantitatively, we can estimate the UMR amplitude by taking reasonable values for the parameters. By setting $B = 1$ T, $j = 0.33\ \mathrm{A\,m^{-1}}$ in the subsurface states, $\alpha = -0.2\ \mathrm{eV}\cdot\mathrm{\AA}$ (in Ref. [187], this value corresponds to Bi covered subsurface states, in our case it is probably an upper bound), $k_{\mathrm{F}} = 0.025\ \mathrm{\AA}^{-1}$ (Rashba splitting $|\alpha k_{\mathrm{F}}| = 5$ meV$\sim 58\,k_B$), $m^* = 0.4\,m_e$,[205] m_e being the electron mass, $v_{\mathrm{F}} = \hbar k_{\mathrm{F}}/m^*$ and $g = 2$, we find a UMR amplitude of $\approx 0.2\%$. This value is in good agreement with our low temperature experimental data. We indeed find a maximum value of 0.5% at 15 K. Therefore, by using simple arguments, we capture the physics of the UMR in the Ge Rashba-splitted subsurface states.

In conclusion, we performed magnetoresistance measurements on Ge (111) and detected a unidirectional magnetoresistance (UMR) which scales linearly with both the current and the applied magnetic field. We ascribe the UMR to the spin-momentum locking generated by the Rashba effect in the subsurface states of Ge (111) and interpret our results in a simple model relating the UMR to the Rashba coefficient and the characteristic parameters of the

subsurface states. Such unidirectional effects can be expected in any Rashba 2DEG and can be used to obtain information about the electronic structure details. The amplitude of the detected UMR signal is much larger than the ones previously reported. We also showed that this UMR is tunable by turning on and off the Rashba coupling in the conduction channel by applying a gate voltage. Ultimately, these findings lead towards the development of a semiconductor-based spin transistor where the spin information can be manipulated by a gate-tunable Rashba field.

4.3 Study of magnetotransport in Fe/Ge (111)

Although the intrinsic Ge Rashba spin-splitting of the subsurface states is not strong enough to target room temperature applications, it can be greatly enhanced at the interface between Ge (111) and metals.[187–190] Hence, beyond providing a way to manipulate the electron spin state, these Rashba states could also be used to generate and detect spin currents in germanium at room temperature, which represents a very new paradigm in the field of semiconductor spintronics. Our group previously explored the influence of putting a metal, potentially heavy, in contact with germanium in order to induce and enhance the Rashba SOI.[78,206] In particular, Fe/Ge (111) and Bi/Ge (111) bilayers were extensively studied by a variety of experimental and theoretical techniques. In both systems we observed spin-charge interconversion at the interface between the two materials due to the presence of Rashba states. Our new motivation was to find the signature of such states by magnetotransport experiments.

Fe and Ge both being conducting materials, the electrical conduction will occurs in three parallel channels, exhibiting specific magnetoresistance effects. The Fe thickness was varied from 0 nm to 3 nm by depositing a wedge of Fe by MBE in order study the effect of the Fe/Ge interface. The magnitude of the UMR sharply decreases when increasing the Fe thickness as a consequence of the current shunting in the ferromagnetic film. Nonetheless, we managed to observe simultaneously the magnetotransport signatures of the ferromagnetic film and the UMR related to the presence of the Rashba states, which represents a promising observation for applications. Interestingly, the UMR decreases slightly slower when increasing the temperature, and the corresponding Rashba energy splitting can be extracted to be about $\sim 100\,k_B$, indicating that the SOC has been reinforced by the addition of Fe atoms at the Ge (111) surface.

4.3.1 Evidence of the Rashba states: spin pumping experiments in Fe/Ge (111)

Large spin-to-charge conversion was first discovered in heavy metals like Pt, W or Ta using the inverse spin Hall effect (ISHE). In this study, we demonstrated a strong spin-to-charge conversion at the Fe/Ge (111) interface by the spin-splitted Rashba states.[78]
Interestingly, the relative lightness of Fe and Ge atoms (Z_{Fe}=26 and Z_{Ge}=32) indicates that heavy metals are not necessary to obtain large conversion effects.
A 20 nm-thick Fe film was epitaxially grown by MBE (see sect. [4.3.3]) in order to characterize the spin-to-charge conversion using the ferromagnetic resonance spin pumping technique (FMRSP). Fig. 4.13 a) shows the spin pumping measurement geometry: the sample is centered in a TE_{011} microwave cavity so that the radiofrequence (RF) magnetic field is maximum while the electric field is minimum. During the experiment, the sample is submitted to microwaves at $f = 9.7$ GHz in the cavity and an external in-plane magnetic field H_{DC} is swept

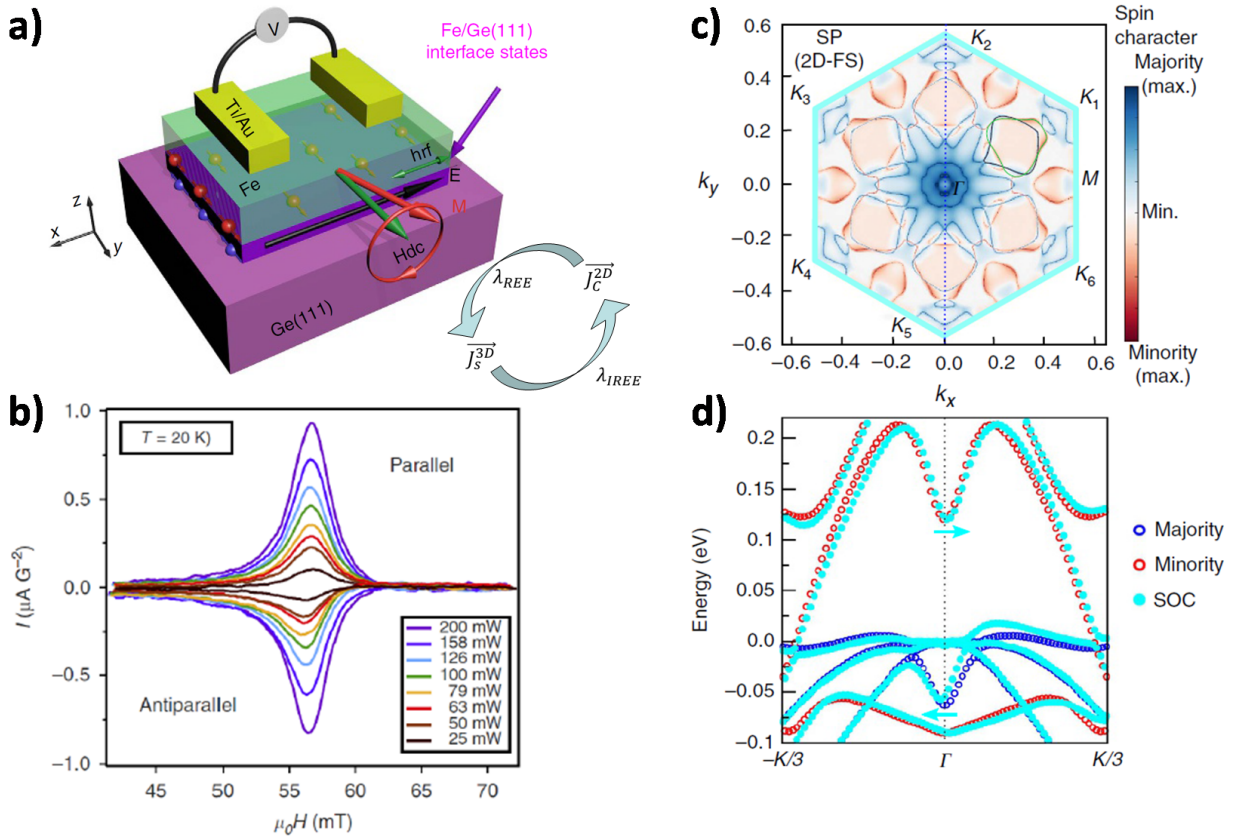

Figure 4.13 – a) Sketch of the experimental geometry for spin pumping and transverse voltage measurements. The top Fe layer is contacted using Au/Ti electrodes and the sample is inserted into an X-band cavity working at $f = 9.7$ GHz. The static magnetic field (H_{DC}) is applied in the film plane along y and the radiofrequency magnetic field (h_{rf}) along x. b) Spin pumping electrical signal recorded at 20 K as a function of the RF power and the static field direction. In the parallel (resp. antiparallel) configuration, H_{DC} is applied along $+y$ (resp. $-y$). c) Two-dimensional Fermi surface in the hexagonal Brillouin zone, the spin majority and spin minority character of the electrons are mapped in red and blue, respectively. d) Corresponding calculated band structure of the Fe/Ge (111) interface states along the ΓK direction with SOC (light blue). The bands experience are shifted in k under the action of the SOC, in the directions indicated by blue arrows, which are opposite for minority and majority bands. The initial majority and minority states are indicated by blue and red dots, respectively.

in order to reach the FMR conditions for the Fe film. H_{DC} is applied along y and at the resonance, angular momentum (i.e. a spin current) is transferred along the z direction to Ge. This three-dimensional spin current J_{s} along z is then converted into a two-dimensional DC charge current J_{c}, recorded as a voltage in open circuit conditions using a nanovoltmeter. The charge current intensity is obtained by dividing the spin pumping voltage by the sample two-probe resistance, it is further normalized by the RF field amplitude so that it is expressed in μA.G^2.

The Fe/Ge (111) spin pumping results are shown in Fig. 4.13 b), the normalized charge current is plotted for different microwave powers from 25 mW to 200 mW. We find that the current is proportional to the power and reverses sign between the parallel and antiparallel geometries, when H_{DC} is applied along $+y$ and $-y$ respectively. These observations are in good agreement with the inverse Rashba Edelstein effect (IREE).[125,127]
The spin current intensity can be determined using a complementary technique: broadband FMR. Here, the microwave excitation frequency is varied in order to measure the magnetization damping in both a reference sample Fe/SiO_2 and the Fe/Ge (111) sample. The extra damping measured in the Fe/Ge (111) sample allows to extract the value of J_s. By normalizing J_c by J_s we can extract the conversion parameter: the inverse Rashba-Edelstein length (λ_{IREE}). We obtain $\lambda_{\mathrm{IREE}} = J_c/J_s \approx 0.13$ nm at room temperature. It can be compared with other two-dimensional Rashba systems like Ag/Bi (0.3 nm)[127] or with three-dimensional ones using the following expression:

$$\lambda_{\mathrm{IREE}}^{\mathrm{eq}} = \theta_{\mathrm{SHE}} l_{\mathrm{sf}} \tag{4.21}$$

Where $\lambda_{\mathrm{IREE}}^{\mathrm{eq}}$ is the equivalent inverse Rashba Edelstein length, θ_{SHE} is the spin Hall angle and l_{sf} is the spin diffusion length of the considered material. In platinum, $\lambda_{\mathrm{IREE}}^{\mathrm{eq}} \approx 300$ pm.[69,120]

This large spin-to-charge conversion was explained by the presence of Rashba states at the Fe/Ge (111) interface. Ab-initio calculations were performed to examine the heterostructure band structure. Fig. 4.13 c) shows the calculated Fermi surface and demonstrates the existence of a large density of metallic states in which spin-to-charge conversion might occur. These states exhibit both p and d characters originating from hybridized Ge and Fe states, respectively. Without SOC, the FS is sixfold degenerate. The inner part of the FS shows a snowflake-like structure such as the pristine Ge (111) surface (not shown here) and thus corresponds mostly to Ge p states with a majority spin character due to the exchange coupling with Fe d states.
When including SOC, the snowflake-like structure at low k values remains but exhibits a strong left–right asymmetry giving rise to a lack of mirror symmetry with respect to the (yz) plane containing the Fe magnetization. Then, the SOC modifies the loops close to the K points by introducing a strong spin mixing between majority and minority spin subbands, as well as the same left–right asymmetry. Fig. 4.13 d) displays the calculated band structure at the interface along the ΓK direction. Only one-third of the first Brillouin zone corresponding to the snowflake-like structure is represented. At the Γ point, the exchange splitting is of the order of 180 meV. The Rashba coupling varies from 10 to 50 meV, from the Γ to the K point point.
Control measurements were performed on a Fe/Ge (100) sample also grown by MBE and showed no detectable spin spumping signal, re-enforcing the interpretation that the (111) orientation of Ge is the essential ingredient to obtain Rashba states.

In a second work, we studied the Bi/Ge (111) system,[206] by depositing an ultrathin Bi film epitaxially on a Ge (111) substrate. We found that quantum size effects in nanometric Bi islands drastically enhance the spin-to-charge conversion efficiency. Using X-ray diffraction, scanning tunneling microscopy, and spin and angle-resolved photoemission spectroscopy, we deduced the film morphology, crystal and electronic structures.
The spin-charge interconversion (SCI) was probed combining three different techniques: magneto-optical Kerr effect to detect the charge-to-spin conversion by the Rashba-Edelstein effect (REE), optical spin orientation, and spin pumping to generate spin currents and measure the spin-to-charge conversion generated by the inverse Rashba-Edelstein effect (IREE). The three techniques show a sizable SCI only for 1–3 nm-thick Bi films corresponding to the presence of bismuth nanocrystals at the surface of germanium. Due to three-dimensional quantum confinement, those nanocrystals exhibit a highly resistive volume separating metallic surfaces where SCI takes place by (I)REE. As the film thickness and islands size increase, the Bi film becomes continuous and semimetallic leading to the cancellation of SCIs occurring at opposite surfaces, resulting in an average SCI that progressively decreases and disappears.

The new motivation is to find the Rashba states signature in magnetotransport experiments, understand their nature and ultimately, try to tune the strength of the interfacial spin-orbit interaction.

4.3.2 Magnetoresistance in the ferromagnetic Fe film: Fe/MgO (100)

In order to understand all the magnetoresistance (MR) effects in the Fe/Ge (111) system, we first conducted magnetotransport experiments in Fe films epitaxially grown on an insulating substrate: MgO (100). Our aim is to study the different MR contributions in the ultrathin Fe films. This preliminary work allows us to identify which signatures are related to Fe in the more complex Fe/Ge (111) system presented in the following. In this study, the thickness dependence of Fe transport properties in the ultrathin regime is investigated.

The sample was prepared by MBE, the MgO (100) substrate was first chemically cleaned and annealed at 850° C in UHV. The Fe layer is then deposited at room temperature, on MgO in the form of a wedge: the MgO substrate is first covered by a mechanical mask that is progressively removed resulting in a Fe thickness gradient (see Fig. 4.14 a)). The total thickness of Fe t_F is 3.5 nm, deposited at the rate of r =0.05 nm/s on the 20×10 mm^2 MgO substrate. The linear speed of the mask, expressed in [mm/s], is given by: $v_{lin} = \frac{L_{subtrate} \times r}{t_F}$, where $L_{substrate}$ is the length of MgO (20 mm), the linear motion is controlled using a rotating step motor and one full turn corresponds to a 1 mm-translation. This finally gives $v_{rot} = \frac{L_{subtrate} \times r}{t_F}$, expressed in [rps].

The Fe film is single crystalline and slightly rough as shown by the RHEED pattern in Fig. 4.14 b) and c), it is finally capped with a 2 nm-thick Al layer protecting it from oxidation. Hall bars were patterned along the wedge direction in order to study the thickness dependence of the magnetotransport. Laser lithography and ion beam etching were first used to define the pattern, then Au(120 nm)/(Ti(5 nm) contacts were deposited by e-beam evaporation.

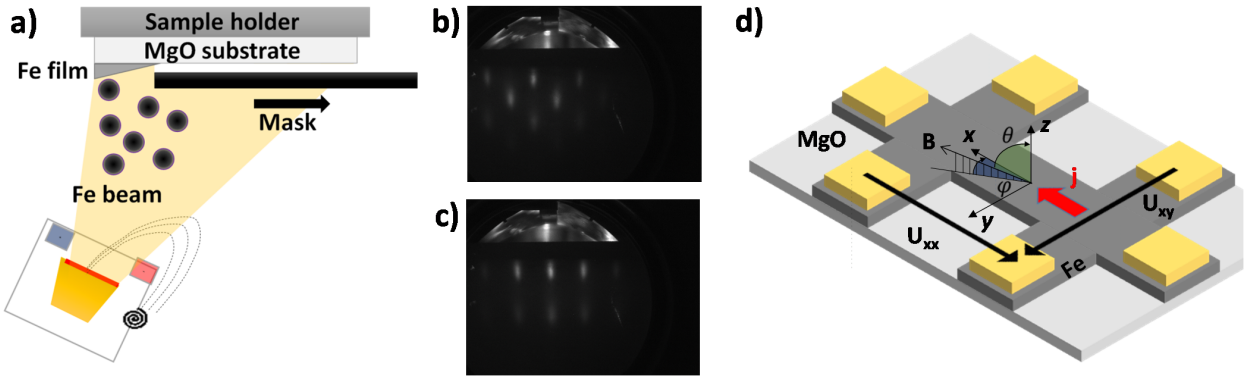

Figure 4.14 – a) Schematic side-view of Fe evaporation during the wedge deposition, the mask is being removed at constant speed, resulting in a Fe thickness gradient. b-c) RHEED patterns of the as-grown Fe epitaxial layer along two azimuths separated by 90°.

The Hall bar geometry allows to measure the four-probe longitudinal and transverse resistivities. They are defined as:

$$\rho_{xx} = R_{xx}\frac{W.t}{L} \tag{4.22}$$

and,

$$\rho_{xy} = R_{xy}.t \tag{4.23}$$

where W, L and t are the channel width, length and thickness. Fig. 4.15 a) shows the temperature dependence of the longitudinal resistivity for six different Fe thicknesses. The thicker layers ($t \geq 1.5$ nm) behave like metals: their resistivity decreases monotonously when decreasing temperature. Interestingly, the thinner layers have no longer a metallic behavior: ρ_{xx}(T) exhibits a minimum for the 1.4 nm-thick film and increases monotonously when lowering temperature for the 1.1 nm-thick film. This observation has already been reported in the literature as a consequence of the transport mechanism switching from the classical

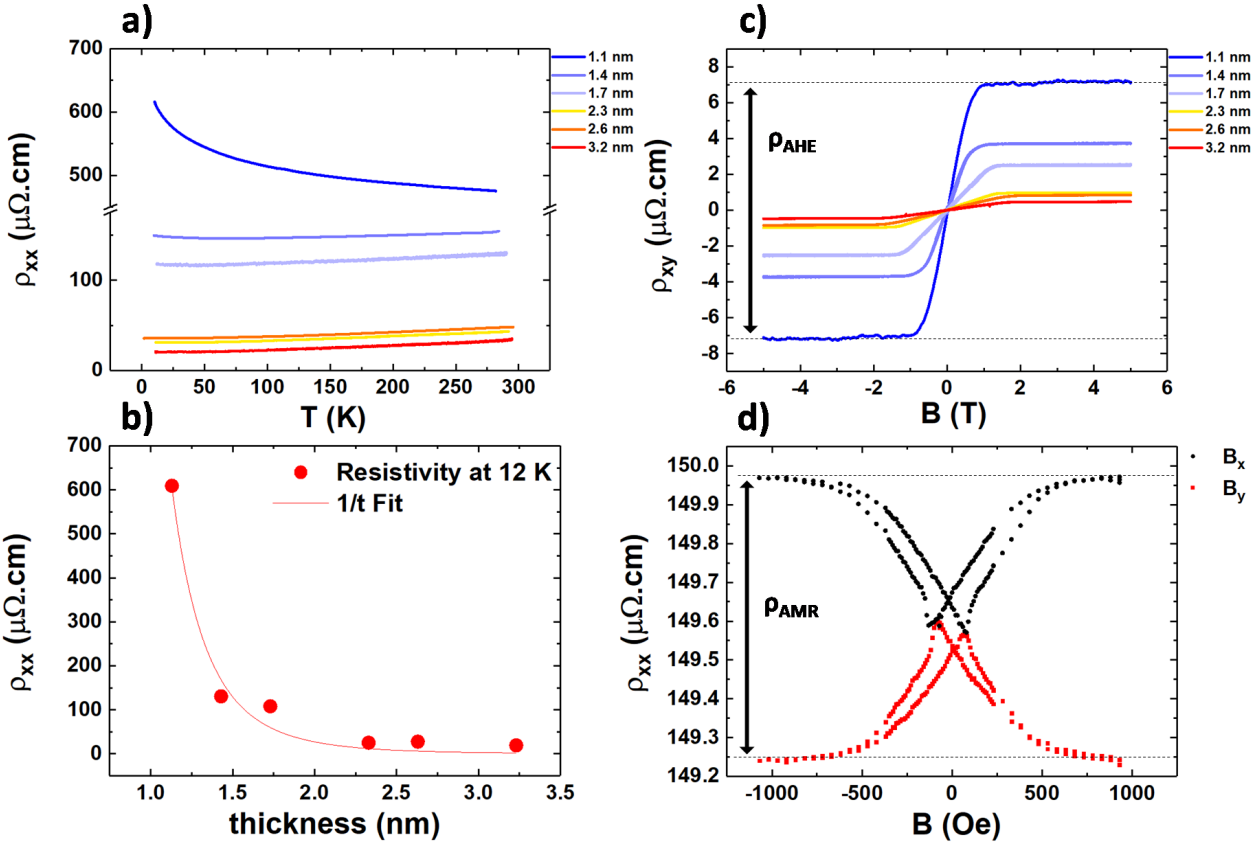

Figure 4.15 – Magnetotransport study performed on the Fe(1 nm - 3 nm)/MgO (100) sample. a) Fe resistivity as a function of temperature for film thicknesses starting from 1.1 nm to 3.2 nm. b) Thickness dependence of the Fe resistivity at 12 K, the continuous line is a $1/t$ fit. c) Anomalous Hall effect measurements at 12 K for the different Fe thicknesses. d) Example of Anisotropic Magnetoresistance measurements on a 1.4 nm-thick Fe film at 12 K.

three-dimensional Drude conduction to a two-dimensional transport in the presence of disorder.[193,207]

Fig. 4.15 b) shows the thickness dependence of the Fe longitudinal resistivity at 12 K, the curve shows a $1/t$ dependence, indicative of surface scattering in the ultrathin film regime.[208] Fig. 4.15 c) shows the transverse resistivity ρ_{xy} recorded at 12 K by applying a 10 µA DC current and a perpendicular to the film plane magnetic field. The anomalous Hall effect (AHE) is observed: the longitudinal current generates a transverse voltage U_{xy} when the material magnetization is perpendicular to the film plane. It can be described by the following phenomenological equation:

$$\rho_{xy} = R_0 B_z + R_s M_z \tag{4.24}$$

Where the ordinary (R_0) and anomalous (R_s) contributions add up. The curves confirm that the magnetic anisotropy of the Fe layer is in-plane: no hysteresis loop is observed. The AHE intensity increases when decreasing the Fe thickness, scaling with the increasing resistivity. This behavior is a consequence of the extrinsic anomalous Hall effect, and was extensively studied since the 70's.[72]
Additionally, we study the different magnetoresistance effects by applying an in-plane magnetic field. The dominant effect is called the anisotropic magnetoresistance (AMR): the resistance depends on the relative orientation of the current and the magnetization in a ferromagnetic film. The resistance is usually minimum when the current and the magnetization are perpendicular. It can be phenomenologically described by the following equation:

$$\rho_{xx}(\varphi) = \rho_{xx}^{\perp} + \left(\rho_{xx}^{\parallel} - \rho_{xx}^{\perp}\right) \cos^2 \varphi \tag{4.25}$$

Where $\rho_{xx}^{\parallel}$ and $\rho_{xx}^{\perp}$ are the longitudinal resistivities when the magnetic field is parallel ($\varphi = 0°$) and perpendicular to the current ($\varphi = 90°$), respectively. In a system without in-plane anisotropy, applying the magnetic field parallel to the current ($\varphi = 0°$ should result in a flat curve: the magnetization follows the field and stay parallel to the current, inducing no AMR contribution. In epitaxial Fe/MgO (100) though, the magnetization easy axis are along the [100] crystal axis of Fe, so at 45° of the current, the Hall bars being patterned parallel to the [110] crystal axis of Fe or along the [100] crystal axis of MgO.

This leads to the AMR curves shown in Fig. 4.15 d) for the 1.4 nm-thick Fe film: when B_x increases, there is a competition between the Zeeman energy and magnetic anisotropy energy because the field is applied along a hard axis. Ultimately, the magnetic field is strong enough to saturate the magnetization along x and $\rho_{xx}(\varphi = 0°) = \rho_{xx}^{\parallel}$. The same situation occurs when the magnetic field is applied along y when the magnetization is saturated along y, the resistance is minimum. The symmetric contributions of AMR for the magnetic field applied

along x and y shown in Fig. 4.15 d) are typical of single crystals when the field is applied along hard magnetization axis ($\varphi = 45°$ here). Similar curves could be observed for the other Fe thicknesses. The AMR in ultrathin Fe films is larger than bulk Fe, and shows a peak at 0.60 % for the 1.7 nm-thick film.

This study aimed at understanding the signatures of ultrathin crystalline Fe in magneto-transport measurements. We could show that the temperature dependence of the resistivity, corresponds to a metallic behavior (monotonous increase for increasing temperature) for thick films, whereas it exhibits a minimum or even a monotonous decrease when increasing the temperature for ultrathin films. The magnetic anisotropy was characterized through the AMR and AHE effects, these effects are characteristic signatures of the magnetotransport in a ferromagnetic material.

4.3.3 Signature of the Fe/Ge (111) Rashba states in magnetotransport measurements

Sample preparation

It starts with the substrate preparation: the low p-doped Ge/Si (111) substrate is subsequently cleaned in an acetone and isopropanol in ultrasonic bath for 5 minutes to remove organic species. Then the substrate is dipped during 30 secondes in a 50 % hydrofluoric acid solution to remove the oxide and is transferred to the MBE. The substrate is then annealed at 850°C during 30 minutes to evaporate the remaining Ge oxide and degas remaining adsorbents. The clean Ge surface is bombarded during 20 minutes using a soft argon etching, the argon pressure in the chamber is maintained at $P = 5.50\times10^{-5}$ mbar, the acceleration voltage is U = 450 V, creating a sample current of 4 µA). This procedure leading to strong surface disorder, it is followed by a second 850°C annealing in order to recrystallize the surface and obtain the Ge (2×8) surface reconstruction as shown in Fig. 4.16 b) and c).

A thickness gradient is obtained by depositing a wedge of Fe at room temperature as detailed in the previous section. The thickness continuously varies from 0 nm to 3 nm as illustrated in Fig. 4.16 a). The small lattice mismatch (≈ 1.3 %) between the Ge lattice and the one of bcc Fe allows the growth of a single crystalline film with the (111) orientation. The RHEED patterns in Fig. 4.16 d) and e) show that the film is single crystalline and the surface is rough.

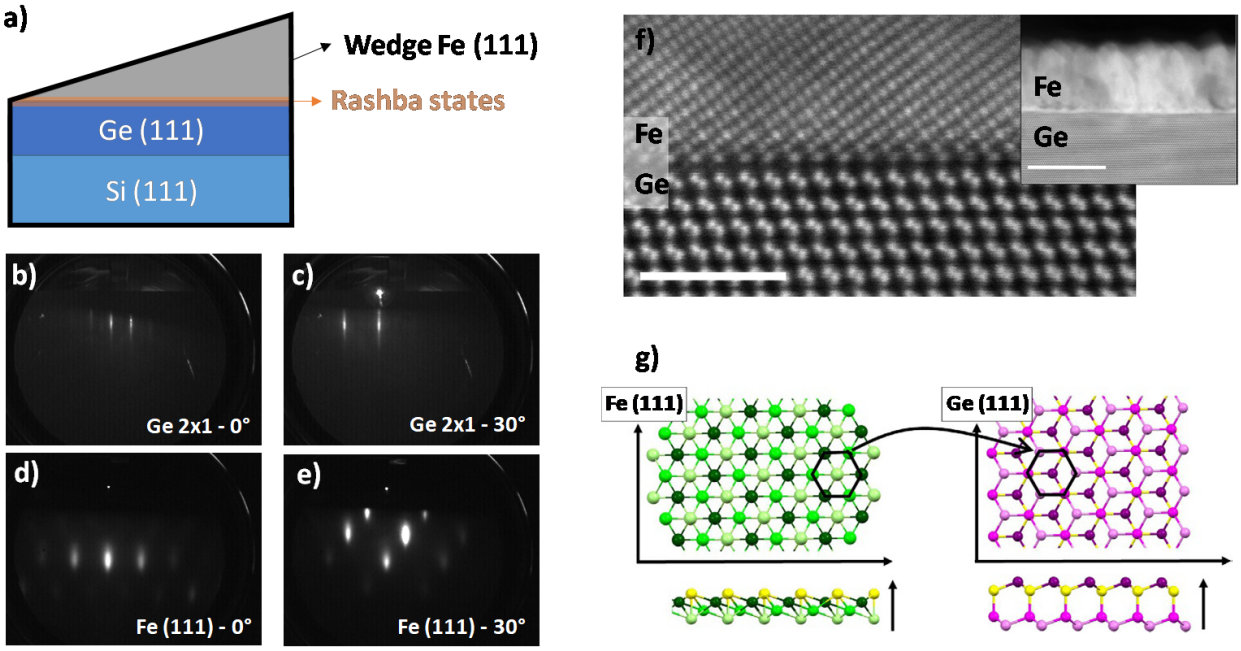

Figure 4.16 – a) Illustration of the wedge Fe/Ge/Si (111) sample. b-c) RHEED patterns of the pristine Ge (2×8) reconstructed surface after ion bombardment and annealing cycles. d-e) RHEED patterns of the as-grown Fe film. f) High-resolution scanning transmission electron microscopy in cross-section, extracted from Ref. [78]. g) Fe/Ge (111) atomic model, the green Fe atoms superimpose the purple Ge atoms.

The high-resolution scanning transmission electron microscopy image in Fig. 4.16 f) confirms the epitaxial growth of Fe on Ge (111) and the very sharp interface. Fig. 4.16 g) shows how the (111)-oriented Fe lattice is rotated by 60° with respect to the Ge crystal lattice.
The sample is then patterned into 130 × 35 μm^2 Hall bars using the process detailed in sect. [2.3.2]. In short, we use the laser lithography and ion beam etching to define the Fe channel and Au(120 nm)/Ti(5 nm) ohmic contacts are deposited by e-beam evaporation. Ion-coupled plasma is then employed to etch the 2 μm-thick Ge layer in order to limit the current shunting in Ge. The sample is then glued on a 20-contacts sample holder using a crystalbond resist, allowing to measure the full magnetotransport angular-dependences.

First harmonic measurements

Fig. 4.17 a) represents the three parallel conduction channels coexisting in the systems. We define the system equivalent parallel resistance such as:

$$R_{\parallel} = R_{Ge} \parallel R_{Fe} \parallel R_{Rashba2DEG} \tag{4.26}$$

The resistance temperature dependences of three devices with 1.1 nm, 1.7 nm and 2.3 nm of Fe are reported in Fig. 4.17 b). They were measured between 10 K and room temperature using a 10 μA AC current at $f = 13.3$ Hz and a lock-in detection. We obtain similar behaviors for the 2.0 nm and 2.3 nm-thick Fe films: a weak temperature dependence exhibiting a minimum value. This behavior was observed in the Fe/MgO (100) reference sample for thinner films, this discrepancy can be explained by the difference of substrate resulting in different film morphology. Interestingly, the 1.1 nm-thick Fe film resistance shows a different temperature dependence. The important increase at low temperature seems to indicate that the conduction mostly takes place in the thermally activated Ge channel but the resistance increases linearly when decreasing the temperature, suggesting that the transport might occur in a third channel: the Rashba gas.

We explore this interpretation using magnetoresistance (MR) and anomalous Hall effect (AHE) measurements as a function of the sample temperature. Fig. 4.17 d) to f) shows the longitudinal MR curves (MR $= \frac{R_{xx}(B)-R_{xx}(0)}{R_{xx}(0)}$) measured at different temperatures for the 1.1-nm thick Fe film. At low temperature (10 K), the MR is very weak and shows a saturation behavior, this is the manifestation of the anisotropic magnetoresistance (AMR) and indicates that the transport mostly occurs in the Fe film. In the intermediate temperature range, the fingerprint of the Rashba MR is observed (a W-shaped MR curve that is no longer linked to the saturation field of the Fe film). At high temperature ($T > 30$ K), the characteristic magnetoresistance of Ge is retrieved as the Ge conductivity increases by thermal activation of carriers.
The transverse resistance measurements show a similar behavior: at low temperature, the Fe AHE is dominant compared to the linear Ge ordinary Hall effect. At higher temperature,

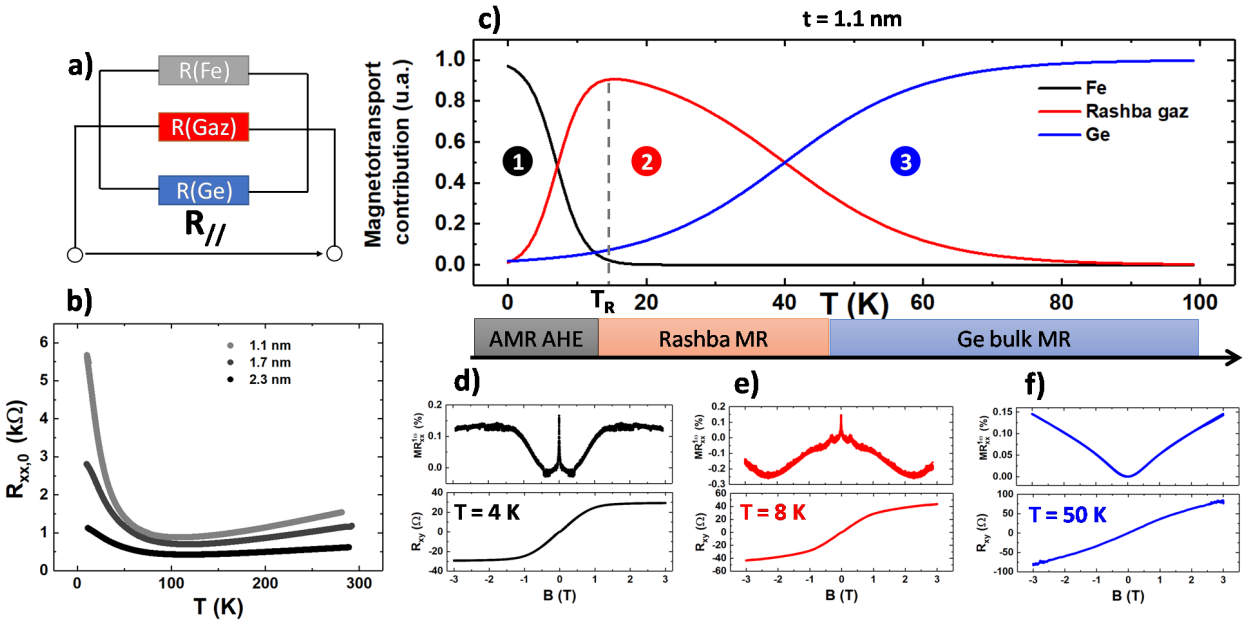

Figure 4.17 – a) Equivalent electrical resistance of the three-channels Fe/Ge (111) system. b) Resistance temperature dependence for different Fe thicknesses. c) Qualitative representation of the magnetotransport contributions between the three transport channels as a function of the temperature. d-f) Longitudinal and transverse magnetoresistance temperature dependence using a 10 μA ac current at $f = 13.3$ Hz and a lock-in detection.

the p-type conduction in Ge is indicated by the positive slope for magnetic fields higher than the saturation field of Fe ($\approx$ 2 T) as shown in Fig. 4.17 f) to h).

Those observations are summarized in Fig. 4.17 c), where the contributions to the magnetotransport are qualitatively represented. We also noted that the characteristic temperature where the maximum of conduction in the Rashba gaz is obtained increases as the Fe thickness increasing. These preliminary observations using first harmonic measurements support our assumption that in addition to the semiconducting (Ge) and ferromagnetic (Fe) conduction channels, a third channel is present in the system: the Rashba gas.

Angular dependent measurements

The spin-orbit interaction (SOI) is coupling the electron momentum with its spin, this results in specific broken symmetries in the system. In the Fe conduction channel, where the SOI is weak, we observe the anisotropic magnetoresistance reported in the previous section, it is current-independent, and quadratic with respect to the applied magnetic field: reversing the field direction does not change the resistance.

However, in the Rashba gas, the SOI results in a current-induced effective field that affects the magnetotransport properties. The resulting magnetoresistance is determined by the relative orientation between the applied field and the current-induced effective Rashba field: it is the unidirectional magnetoresistance (UMR).

The complete theoretical description was developed in sect. [4.2.3]. The corresponding symmetries can be easily found by noting that the total magnetic field acting on the carriers is the vector sum of the external field B and the current-induced Rashba field B_E. The magnitude of the magnetoresistance term is expected be proportional to both the applied magnetic field and to the applied current, as the Rashba field magnitude is proportional to the current.

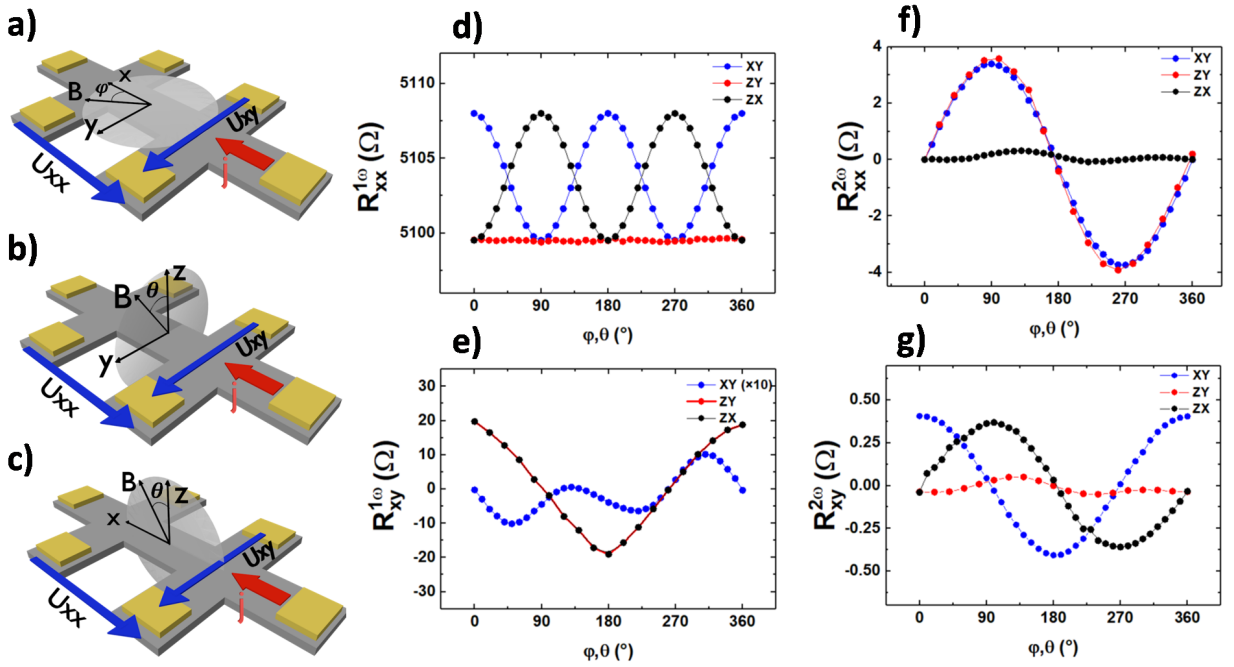

Figure 4.18 – Angular dependences of the longitudinal and transverse signals in the a) xy b) zy c) zx planes. Corresponding angular dependences of d) $R_{xx}^{1\omega}$, e) $R_{xy}^{1\omega}$, f) $R_{xx}^{2\omega}$ and g) $R_{xy}^{2\omega}$, measured at 12 K, with an applied magnetic field of 0.5 T and a current of 100 μA.

In this case, we obtain a resistance term which is linear in current, implying a quadratic dependence of the voltage drop on the applied current. Since the UMR signals are expected to be rather small due to the current shunting in the Fe layer, we use AC measurements to separate the different harmonics in order to distinguish current-dependent from current-independent resistance contributions. We apply an ac current $I_\omega = I_0 \sin(\omega t)$ and simultaneously record the first and second harmonic longitudinal and transverse resistances: $R_{xx}^{1\omega}$, $R_{xx}^{2\omega}$, $R_{xy}^{1\omega}$, $R_{xy}^{2\omega}$. In addition to this harmonic analysis, we use the magnetic field angular dependences to identify all the magnetoresistance contributions.

Fig. 4.18 a-c) illustrates the different measurement geometries. The applied current is along the x direction and the external magnetic field is applied along (θ, φ) directions, θ and φ being the polar and azimuth angles. The measurements were carried out at 12 K using a 100 μA AC current of frequency $f = 13.3$ Hz, while rotating the sample in the (xy), (zy) and (zx) planes in a uniform external field of 0.5 T. Fig. 4.18 d) shows the first harmonic

longitudinal resistance $R_{xx}^{1\omega}$ angular dependences measured for the 1.1 nm-thick Fe film. We identify the AMR angular dependence:

$$R_{xx}^{1\omega} = R_{xx}^{1\omega}|_{B_x} + \left(R_{xx}^{1\omega}|_{B_x} - R_{xx}^{1\omega}|_{B_y}\right)\cos^2\theta\sin^2\varphi \tag{4.27}$$

Where $R_{xx}^{1\omega}|_{B_x}$ ($R_{xx}^{1\omega}|_{B_y}$) is the longitudinal resistance for the field oriented along the x (y) axis. In the same way, Fig. 4.18 e) shows the first harmonic transverse resistance $R_{xy}^{1\omega}$ angular dependences measured for the 1.1 nm-thick Fe film. Out-of-plane (zy) and zx) scans well correspond to the anomalous Hall effect while the in-plane (xy) angular dependence indicates the presence of the planar Hall effect, the transverse counterpart of the AMR. The external field being only of 0.5 T, it is not strong enough to saturate the Fe magnetization, this results in the sawtooth-like out-of-plane angular dependence we observe. Overall, this contribution can be expressed as:

$$R_{xy}^{1\omega} = R_{AHE}\cos\theta + R_{PHE}\sin^2\theta\sin 2\varphi \tag{4.28}$$

Fig. 4.18 f) shows the second harmonic measurements corresponding to the contributions to the resistance that are current dependent. $R_{xx}^{2\omega}$ shows a sine angular dependence with respect to the external field: $R_{xx}^{2\omega}$ changes sign when the external magnetic field is reversed. As a consequence of these symmetries with respect to field and current, we call this term unidirectional magnetoresistance (UMR). A similar behavior is observed in the second harmonic transverse measurements $R_{xy}^{2\omega}$ as shown in Fig. 4.18 g). We fine the sine amplitude as $R_{xx,\Delta}^{2\omega}$ and $R_{xy,\Delta}^{2\omega}$ so that these contributions can be expressed as:

$$R_{xx}^{2\omega} = R_{xx,\Delta}^{2\omega}\sin\theta\sin\varphi \tag{4.29}$$

$$R_{xy}^{2\omega} = R_{xy,\Delta}^{2\omega}\sin\theta\cos\varphi \tag{4.30}$$

Similarly to the case of pure Ge (111), $R_{xy,\Delta}^{2\omega}$ shows the signature of the Nernst effect, we can remove this spurious contribution from $R_{xx,\Delta}^{2\omega}$ by using the following expression (see the derivation in sect. [4.2.2] through Eq. [4.8] to Eq. [4.12]).

$$R_{\mathrm{UMR}}^{\Delta} = R_{xx,\Delta}^{2\omega} - Z \times R_{xy,\Delta}^{2\omega} \tag{4.31}$$

Where Z is the Hall bar aspect ratio ($Z = 4$ here). In Fig. 4.19, we investigate the dependences of $R_{\mathrm{UMR}}^{\Delta}$ on the applied current [Fig. 4.19 a,d)], external magnetic field [Fig. 4.19 b,e)] and temperature [Fig. 4.19 c,f)]. The signal is normalized by the zero field longitudinal resistance $R_{xx,0}$ at the corresponding current. The UMR is proportional to the current and magnetic field and thus, follows the symmetries of the current-induced Rashba field. $R_{\mathrm{UMR}}^{\Delta}/R_{xx,0}$ is maximum at low temperature and sharply decreases with increasing temperature as the current starts to be shunted into the Ge substrate because of thermal activation.

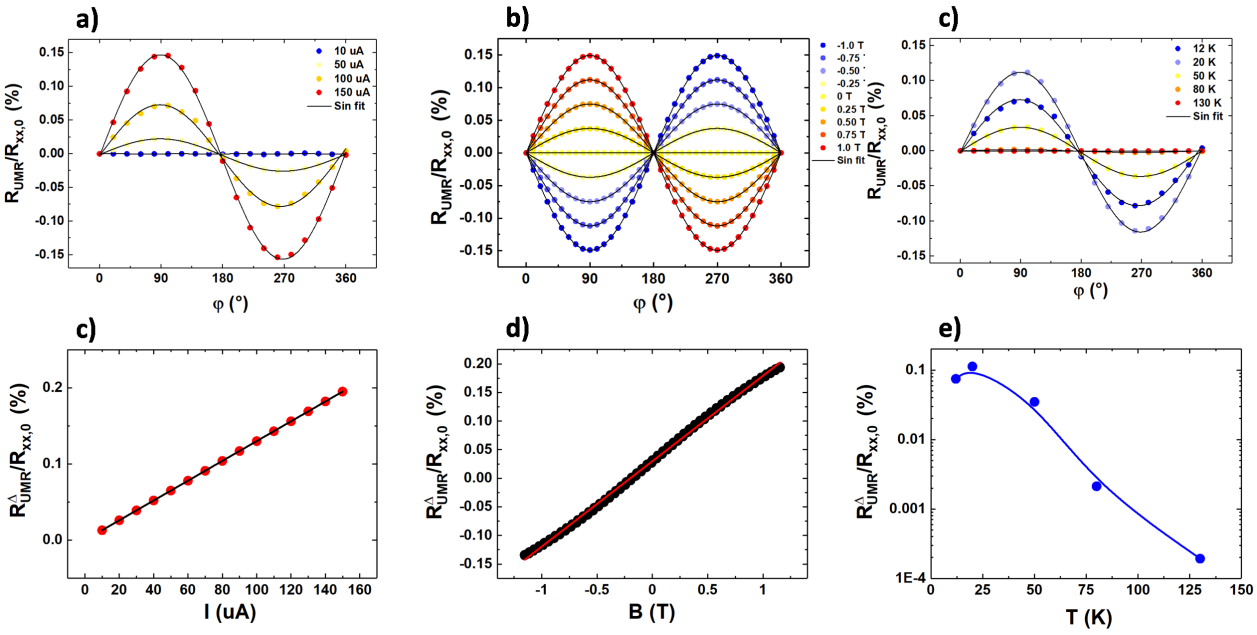

Figure 4.19 – Angular dependence of the second to first harmonic ratio in the (xy) plane for 1.1 nm of Fe applying different a) currents (0.5 T, 12 K), b) magnetic fields (100 µA, 12 K) and c) at different temperatures (0.5 T, 100 µA).d-f) Corresponding current, field and temperature profiles for $\varphi = 90°$.

At low temperature, our system is equivalent to a bilayer composed of the Rashba gas and a ferromagnet. Therefore, one would expect to detect the unidirectional spin Hall magnetoresistance effect (USMR),[85] the counterpart of the UMR effect with a ferromagnet ($R^{2\omega}_{xx,\mathrm{USMR}} \propto \mathbf{I} \times \mathbf{M}$), although this effect is supposed to be two to three orders of magnitude smaller. UMR and USMR effects share the same angular dependences, but USMR should follow the Fe magnetization, resulting in a hysteresis loop at low magnetic field. Fig. 4.19 e) shows that this contribution cannot be resolved in our system using these measurements conditions.

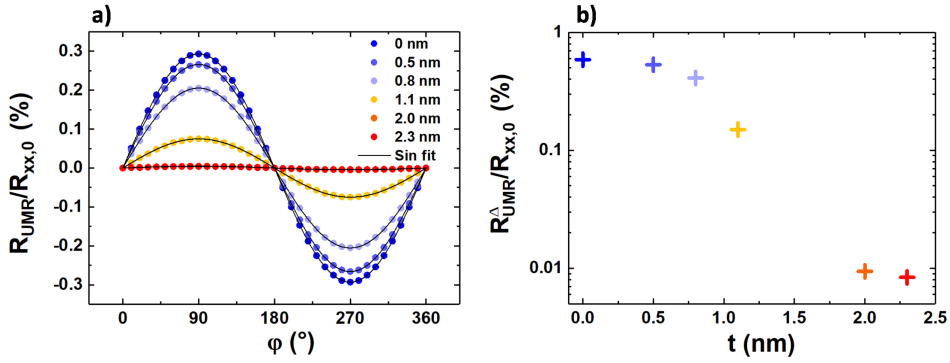

Figure 4.20 – a) Angular dependence of $R^{\Delta}_{\mathrm{UMR}}/R_{xx,0}$ in the (xy) plane for the different Fe thicknesses measured at 12 K, 0.5 T and 100 µA. b) Corresponding thickness dependence profile for $\varphi = 90°$.

Finally, we present the thickness dependence of $R^{\Delta}_{\mathrm{UMR}}/R_{xx,0}$ [Fig. 4.20]. The measurements were carried out at 12 K, applying an external magnetic field of $B = 0.5$ T and an AC excitation current of 100 µA. The UMR intensity decreases sharply as the Fe film becomes thicker, this can be understood as the proportion of the current shunted in the Fe layer becomes larger.
Interestingly, the UMR temperature decrease is slightly slower than in pure Ge (111), the corresponding Rashba energy splitting can be extracted to be about ($\sim 100\,k_B$), indicating that the SOC has been reinforced by the addition of Fe atoms at the Ge (111) surface.

In conclusion, we could measure simultaneously the MR contributions from the ferromagnetic Fe layer and the UMR from the Rashba gas at the Fe/Ge (111) interface. Although the magnitude of the UMR is smaller than for pure Ge (111), the temperature decay of the effect is less steep, which is a promising observation for future technological applications.

CHAPTER 5

Lateral structures with perpendicularly magnetized injectors

Spintronics aims at adding the spin degree of freedom to the well-established charge-based electronics, either by combining spin and charge or by using the spin only.[24,132] The latter promises a breakthrough in data processing speed, energy consumption, and integration densities with regards to current classical semiconductor-based transistors.[23] In 1990, Datta and Das proposed the very first spin transistor architecture, by analogy with the MOSFET, where the source and drain electrodes are ferromagnetic, and the control of the spin orientation in the conduction channel is achieved by precessing arong a gate-tunable spin-orbit magnetic field.[21,22] For a spin transistor to work, four elements are required: a channel with a long spin relaxation time, a high spin injection and detection efficiency and a gate voltage control of the spin-orbit coupling.

In the previous chapters, we demonstrated all these elements separately in a Ge (111)-based spin-orbitronics platform using optical spin generation. However, in order to implement a spin-based technology on large scale, the optical spin generation has to be replaced by the electrical spin generation. Although all-electrical spin injection and detection have been demonstrated in both n-doped and p-doped Ge (100) films using lateral spin valves,[41,42] it was not demonstrated yet in Ge (111).

In this chapter, we explore different solutions to electrically generate spin currents in Ge (111). This specific task is challenging as the electrical spin injection in semiconductor faces the impedance mismatch problem.[27] To overcome this issue, a thin tunnel barrier is introduced between the ferromagnetic (FM) contact and the semiconductor. The lateral spin valve architecture involves two magnetic tunnel junctions (MTJ) with different coercive fields, one is used to generate the spin accumulation and the second to detect it using a non-local mea-

surement. The magnetic anisotropy of the electrodes is in-plane and electron lithography is used to shape thin elongated ferromagnetic electrodes accordingly, a typical MTJ stack is Fe/MgO. Although single crystalline films could be obtained on Ge (100) by molecular beam epitaxy,[42] the growth on Ge (111) with six-fold surface symmetry does not result in good crystalline properties probably because the MgO (111) surface is the least stable. Tunnel barriers with an hexagonal crystal structure would be more adapted, the best candidate would be Al_2O_3. The spin diffusion length in Ge being in the micrometer range,[171] the gap between the two MTJs can be larger than in metallic LSVs. Therefore, we decided to make lateral spin valves without using e-beam lithography, which represents a novel approach in the field of LSVs.

In order to obtain a contrast between the magnetic electrodes coercive fields, we developed the growth of magnetic thin films with perpendicular magnetic anisotropy (PMA). The first section reports the development of cobalt/platinum multilayers deposited by sputtering. The magnetic properties of the $(Co/Pt)_n$ films were investigated using anomalous Hall effect and Kerr microscopy. The LUMOS optical bench was used to develop a new interesting magnetometry technique based on the electrical detection of magnetic circular dichroism (MCD). The latter is found to be very sensitive when the ferromagnetic film is ultrathin. We investigated the origin of the MCD detection and found out that the electrical detection is due to the Seebeck effect as a consequence of a difference of temperature between the two electrical contacts. As a thermoelectric-based detection is interesting but not always suitable, we also showed that this contribution can be eliminated by applying a bias current that acts as a source of drift for the photogenerated carriers. The study revealed that the $(Co/Pt)_n$ films are perpendicularly magnetized when $n > 1$ and that their coercive field could be tuned by increasing the number of repetitions n.

The second section reports the development of the nanofabrication process to pattern a lateral spin valve on Ge (111) as well as the observation of electrical spin generation and detection in Ge (111) using the developed PMA MTJs. Finally, a prototypical spinFET architecture is investigated in the last section. Its principle relies on a gate voltage tunable Rashba spin-orbit field at the Bi_2Se_3/Ge (111) interface. Spin accumulations are generated either optically by the optical spin orientation of electrically using the MTJ with PMA as a spin injector. Using perpendicularly magnetized spin injectors is interesting for the development of the spinFET as the spin orientation is orthogonal to the film plane, allowing to make the spins to precess around the Rashba field. I further describe the complex nanofabrication process and propose a set of future experiments to perform on the devices as the main perspective of my PhD thesis.

5.1 Development of a new magnetic microscopy based on the electrical detection of MCD

In this first section, I report the growth of perpendicularly magnetized electrodes on Ge (111). The thin films were deposited by magnetron sputtering. In order to obtain perpendicular magnetic anisotropy (PMA), we grow (Co/Pt) multilayers. The magnetic properties were characterized by different techniques based on magneto-optics (magneto-optical Kerr effect or MOKE) and magnetotransport (anomalous Hall effect). As these two techniques can be performed simultaneously using the LUMOS optical bench, I developed an original hybrid technique combining optical excitation and electrical detection of the magnetization. We study how the magnetic properties are affected by the number of repetitions of (Co/Pt). We further find that the $(Co/Pt)_n$ films are perpendicularly magnetized when $n > 1$ and that their coercive field can be adjusted with the number of repetitions n.

5.1.1 Perpendicular magnetic anisotropy

The properties of artificially layered materials have been investigated since the 50's leading to the discovery of a wide range of phenomena, interesting from both a fundamental and a technological point of view. Benefiting from the progress of thin film growth techniques, multiple applications emerged in the field of magnetic data storage (hard disk drives), solid-state magnetic memories (MRAM), magnetic logic and sensors.

Numerous effects were discovered in such magnetic multilayers like the giant and tunneling magnetoresistances,[6–8] the exchange bias at ferromagnetic/antiferromagnetic interfaces[209] and the observation of perpendicular magnetic anisotropy (PMA).[210–212] Since its early days, the hard drive disk industry has been a driving force in magnetism and spintronics.[213,214] The information is stored in small magnetic grains where two magnetization states (bits 0 and 1) are stabilized by the uniaxial magnetic anisotropy. The scalability of such technology imposes the anisotropy constant (K) to increase when decreasing the bit size (of volume V) keeping a large value of the KV product for thermal stability and long data retention time. The anisotropy times volume product has to be enhanced by switching from in-plane to out-of-plane anisotropy, reducing the demagnetization energy impact on the total anisotropy as the bit volume decreases.[215,216]

One important source of magnetic anisotropy is the magnetocrystalline anisotropy that arises from the crystal symmetries and the spin-orbit interaction. The orbital motion of the electrons is governed by the crystal electric field giving rise to preferential magnetization directions. Similarly, at interfaces, the reduced symmetry enhances and orients the electrons orbital moment, imposing preferential directions for the spin moment by spin-orbit cou-

pling.[216] In particular, the interfacial magnetic anisotropy often results in the magnetization being oriented perpendicularly to the film plane. This was thoroughly studied at the interface between a transition metal and an oxide (CoFeB/MgO for instance).[216–218] The origin of the perpendicular magnetic anisotropy in this system was elucidated from first principle calculations. Using the density functional theory as well as tight-binding simulations, it was shown that the PMA is due to the hybridization between the $s-p$ orbitals of the oxygen atoms of MgO and the Co and Fe d_z^2 orbitals. An analogous situation is expected in metallic multilayers like $(Co/Ni)_n$[211,212] or $(Co/Pt)_n$, the contribution to PMA of interface roughness and magnetoelastic coupling were highlighted, however, the exact microscopic origin of the PMA remains unclear.[219,220] Phenomenologically, it was shown that the PMA increases when increasing the number of (Co/Pt) repetitions (i.e. the number of interfaces).[221,222]

It was suggested that memory dots made of such perpendicularly magnetized thin films exhibit very fast switching dynamics.[223–226] As a consequence, intensive work is currently under way to design magnetic dots which magnetization on can be manipulated on a short timescale (sub nanosecond). Solid-state magnetic memories like spin-transfer-torque magnetic random access memories (STT-MRAM) employ the spin transfer torque generated by the passing of an electrical current through an adjacent pinned ferromagnetic layer to manipulate the free magnetic layer.[9,17,227,228] Lately, the generation of spin currents by the spin Hall effect in heavy metals to switch the magnetization of the free layer lead to a new generation of devices called spin-orbit-torque MRAM which are more energy-efficient.[62,229–233] Alternatively, the magnetization of perpendicularly magnetized multilayer films like $(Co/Pt)_n$ was manipulated on ultra-short timescales (sub picoseconds) using femtosecond laser pulses.[234–237] This field of research is called the all optical switching and is promising for future ultrafast applications.[238–240]

In the literature, different approaches were used to grow such multilayers. Films grown by molecular beam epitaxy showed really sharp interfaces with limited atomic intermixing,[241] and the use of lattice-matched substrates resulted in an epitaxial growth.[242] It was shown that the orientation of the crystal was a key aspect to obtain the PMA, indeed, the magnetic anisotropy of [100]-oriented films is in-plane whereas a strong PMA can be obtained for the [111] orientation.[243] Alternatively, films were grown using the sputtering technique, the overall quality of the thin films is not as good as the ones grown by MBE, but PMA can still be observed. The sputtering technique is more oriented toward the industry and allows to grow samples on a faster pace.[244]

The magnetic properties of the (Co/Pt) multilayers were characterized using a large panel of techniques: magneto-optical Kerr effect,[245–247] X-ray magnetic circular dichroism,[248,249] magnetic transmission electron microscopy,[250] magnetic Compton scattering,[220] SQUID and

torque magnetometry.[219,251]

The (Co/Pt) multilayers were also used in magnetic tunnel junctions in order to either pin the magnetization of a reference layer[227] or to inject spin currents. In this work, we probe the local magnetization orientation using simultaneously Kerr microscopy and a new original technique based on the modulation of the photocurrent in Ge by the magnetic circular dichroism in (Co/Pt).

5.1.2 (Co/Pt) multilayers growth by magnetron sputtering

The low n-doped 2- µm-thick Ge/Si (111) substrate is subsequently cleaned in acetone and isopropanol in an ultrasonic bath for 5 minutes to remove organic species. Then the substrate is dipped into a 50 % hydrofluoric acid solution to remove the native Ge oxide and is transferred to the sputtering chamber. We do not heat the substrate during the growth as it promotes the chemical reaction between Co and Ge atoms at the interface, which is detrimental for the magnetic properties.

The chamber base pressure is in the 10^{-8} mbar range. After introducing the sample, we set the Ar pressure in the chamber to $P_{Ar} \approx 1.2 \times 10^{-2}$ mbar using a flowmeter. A 5 W DC power is applied to generate the plasma, giving a deposition rate of 0.25 Å/s for Co and 0.79 Å/s for Pt as measured by a quartz microbalance. We begin with the deposition of a Co layer and end with a Pt layer which also acts as a capping layer preventing Co oxidation under atmospheric conditions (see Fig. 5.1 a)). In this work, we grew $(Co/Pt)_n$ samples where the (Co/Pt) bilayer is repeated from one to four times ($n = 1, 2, 3$ and 4).

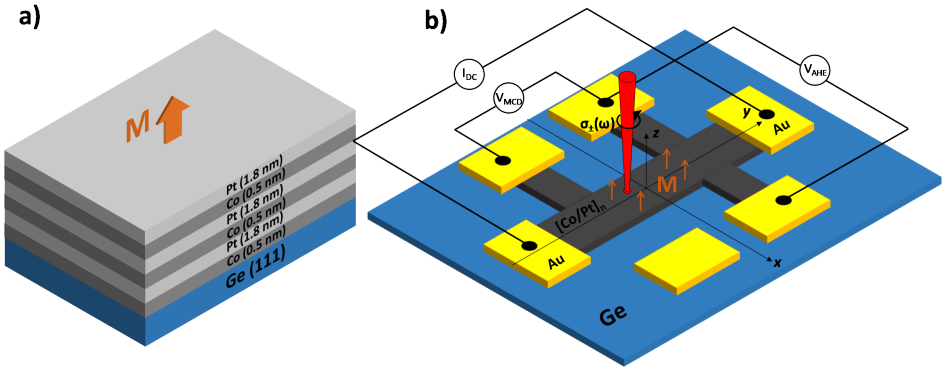

Figure 5.1 – a) $(Co/Pt)_3$/Ge (111) multilayer. b) Sketch of the $(Co/Pt)_n$/Ge (111) sample layout used for magnetic microscopy experiments.

Then, we proceed with the definition of 200×50 µm^2 Hall bars in the $(Co/Pt)_n$ film. We first use the laser lithography technique to define the conduction channel and we etch the $(Co/Pt)_n$ film using ion beam etching. Then electrical contacts are lithographically defined and Au(120 nm)/Ti(5 nm) contacts are deposited by e-beam evaporation. The final device is sketched in Fig. 5.1 b). The electrical contacts allow for magnetic characterizations by magnetotransport

measurements and the channel is large enough to perform Kerr microscopy. One contact is not connected to the Hall bar, in order to measure the voltage between the ferromagnetic film and the Ge substrate and to detect a possible non-local spin signal.

5.1.3 Three simultaneous magnetic measurements

We use the versatility of the LUMOS optical bench to perform simultaneously electrical, optical and hybrid electro-optical measurements of the magnetization orientation.

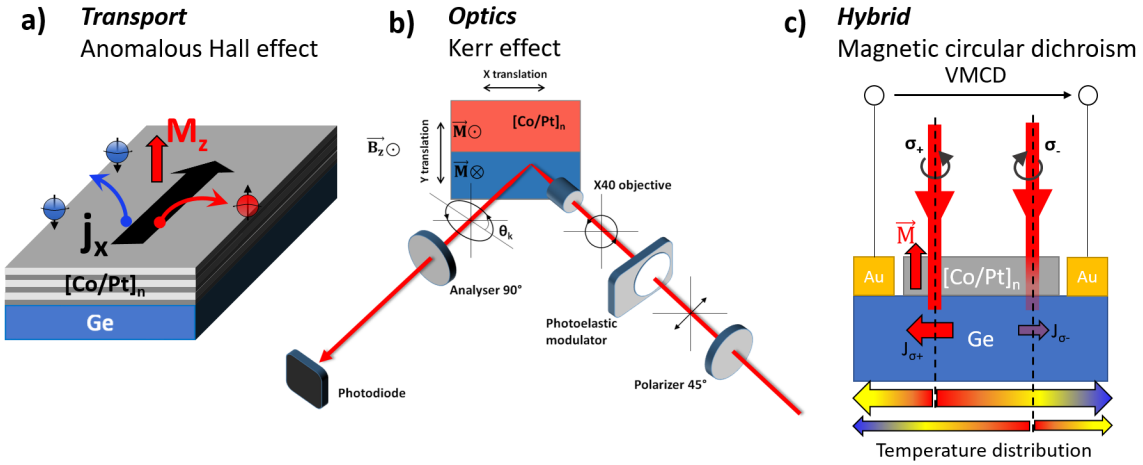

Figure 5.2 – a) Anomalous Hall effect b) Magneto-optical Kerr microscopy c) Helicity dependent photovoltage due to MCD, the color scale in the bottom part indicates the temperature distribution for two different laser beam position and helicity.

As shown in Fig. 5.2 a), a DC current I_{DC} is applied in the (Co/Pt) bar, the electrons are deflected transversely as a consequence of the anomalous Hall effect (AHE). The transverse resistance, defined by R_{AHE}, is proportional to M_z, the out-of-plane component of the magnetization. If the (Co/Pt) film is perpendicularly magnetized, an hysteresis loop should be observed when sweeping the external magnetic field above the coercive field.
In the same time, we perform magneto-optical Kerr effect (MOKE) imaging of the magnetization. The sample is illuminated with a circularly polarized laser beam, the circular polarization ($\sigma_{\pm}$) is modulated at $\omega = 42$ kHz by using a photoelastic modulator (PEM). The reflected light is then analyzed by a polarizer and the light intensity is recorded using a photodiode. The resulting photovoltage is demodulated at 2ω by a lockin amplifier, to give the Kerr rotation θ_k (see Fig. 5.2 b)).

The (Co/Pt) film being very thin, the circularly polarized light is partially transmitted through the film and electron-hole pairs are photogenerated in Ge. As the (Co/Pt) magnetization is perpendicular, the left and right circularly polarized photons are more or less transmitted depending on the magnetization orientation: this effect is called magnetic cir-

cular dichroism[248] (see Fig. 5.2 c)). Due to the absorption of light, the Ge layer is locally heated at the position of the laser spot and a Seebeck voltage $V_{DC}^{Seebeck}$ develops between the left (l) and right (r) Au electrodes (see Fig. 5.2 c)): $V_{\sigma_+} = S\Delta T_{\sigma_+}$ for the σ_+ polarized light and $V_{\sigma_-} = S\Delta T_{\sigma_-}$ for the σ_- polarized light, S being the Seebeck coefficient of Ge and ΔT_{σ_+} (resp. ΔT_{σ_-}) the temperature difference between the right and left electrodes for the σ_+ (resp. σ_-) polarized light. Note that if the laser spot is exactly located in the middle of the two Au electrodes, the Seebeck voltage is zero for both helicities. Since the σ_+ and σ_- polarized lights are differently absorbed in Ge due to the MCD in the (Co/Pt) layer, $V_{\sigma_+} \neq V_{\sigma_-}$ and we detect a voltage V_{MCD} at the PEM frequency as a combination of the Seebeck effect in Ge and the MCD in (Co/Pt).
The demodulated voltage V_{MCD} is recorded with a lock-in amplifier while the magnetic field is swept. Alternatively, we can fix the magnetic field and image the sample magnetic configuration by scanning the laser beam at normal incidence.

We first focus on the $(Co/Pt)_3$ sample, Fig. 5.3 a) shows the sample reflectivity recorded by scanning the laser beam on the microstructure, the (Co/Pt) Hall bar pattern is in green, the Au/Ti contacts in red and the Ge substrate in blue. The circularly polarized laser beam is first focused on the center of the Hall bar (at the position of the red spot). Fig. 5.3 a-c) show the magnetic signals for a ±500 Oe magnetic field sweep, applied perpendicularly to the film plane, recorded simultaneously using the three aforementioned techniques.

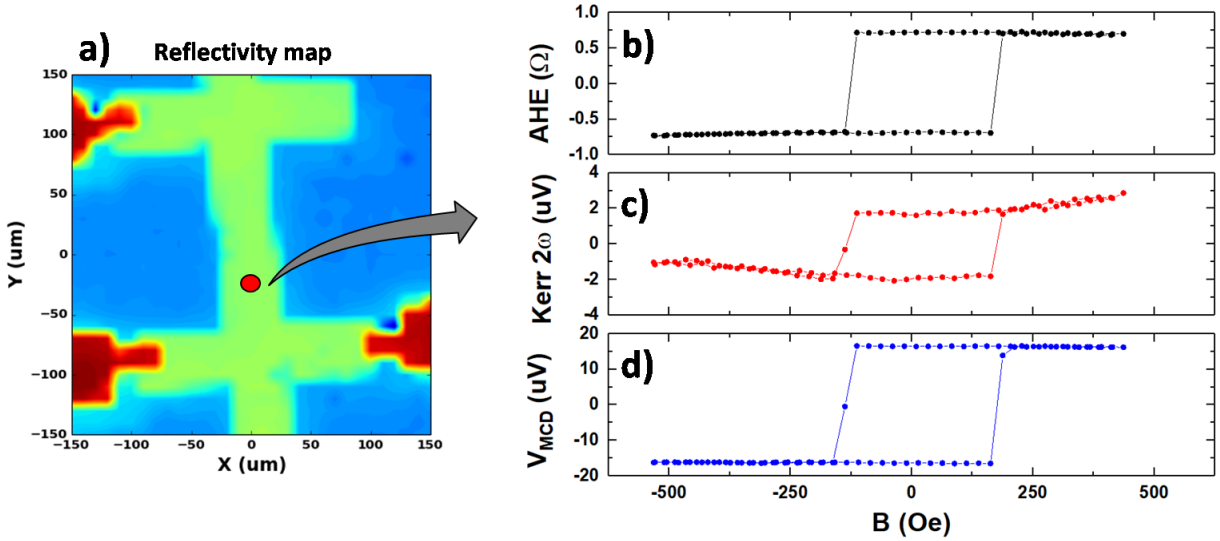

Figure 5.3 – a) Two-dimensional reflectivity map of the $(Co/Pt)_3$/Ge Hall bar, the red circle indicates the laser beam position during the magnetic field sweep (applied perpendicularly to the sample plane). b) AHE hysteresis loop recorded with a current $I_{DC} = 100$ µA. c) MOKE hysteresis loop using a 100 % circularly polarized red light ($\lambda = 661$ nm) focused on the Hall bar center, the spot size is about 1.5 µm. d) V_{MCD} hysteresis loop. The voltage is demodulated at the PEM frequency ω and is measured between a Hall bar contact and the substrate, a current $I_{DC} = 100$ µA is applied during the measurement.

In this geometry, the observation of a square hysteresis loop indicates that the $(Co/Pt)_3$ sample magnetization is out-of-plane. To our knowledge, this is the first time that such a perpendicularly magnetized material is grown on germanium, this milestone is very promising for future fundamental and technological explorations. For this $n = 3$ repetitions sample, the coercive field is $B_c \approx 160$ Oe. We also note that the MCD signal is one order of magnitude larger than the Kerr signal, so the technique looks interesting for ultrathin ferromagnetic films where the Kerr amplitude is very small.

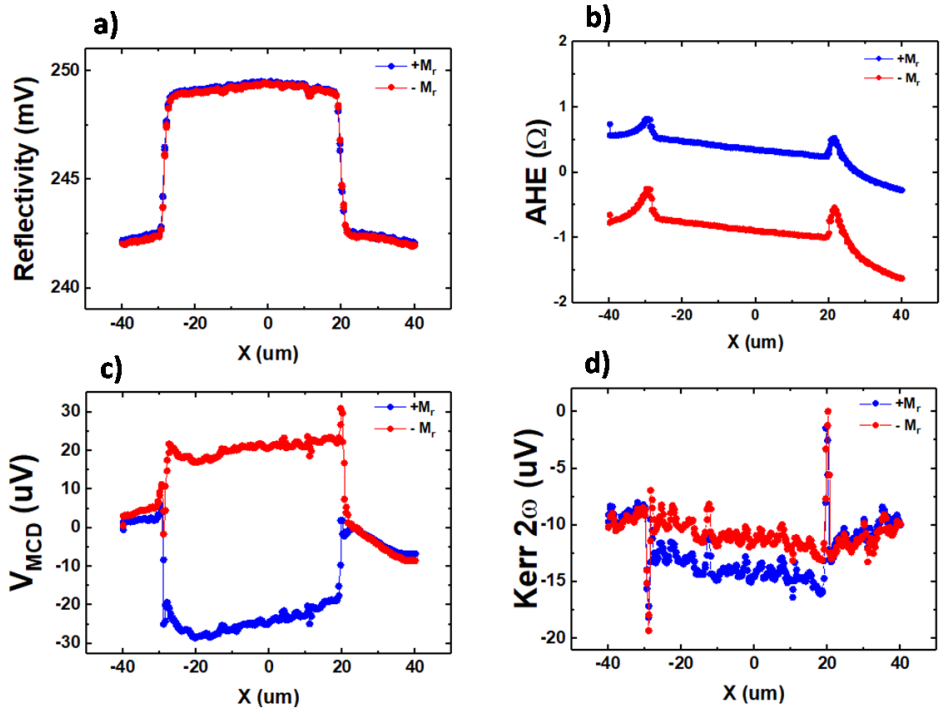

Figure 5.4 – Line scans along the x direction of the remanent magnetic states $+M_r$ along $+z$ in blue and $-M_r$ along $-z$ in red ($B = 0$ T). a) Sample reflectivity. b) Anomalous Hall effect c) V_{MCD} and d) Kerr angle.

The anomalous Hall effect gives a macroscopic picture of the magnetization, whereas the MOKE and MCD techniques can be spatially resolved by scanning the sample with the laser beam. We perform line scans along the x direction. We first apply +500 Oe or −500 Oe along z to saturate the film magnetization either up or down and then record the corresponding remanent state $+M_r$ or $-M_r$ at zero field. Fig. 5.4 a) shows the sample reflectivity, the (Co/Pt) film being more reflective than Ge, it corresponds to the central area where the photodiode signal is larger. Fig. 5.4 b) reports the AHE line scans, a weak spatial dependence of the signal is observed as a consequence of the Seebeck effect that takes place due to the scanning laser spot heating locally the Ge film (this contribution can be removed by using an AC current and a lock-in detection to measure the AHE). Fig. 5.4 c) and d) show the remanent magnetization measured by the V_{MCD} and the Kerr effect, respectively. A clear contrast can be observed in both cases and we confirm the local nature of the MCD signal:

when the laser beam directly illuminates the Ge film, the V_{MCD} signal vanishes. Again, we note that the V_{MCD} signal is more than one order of magnitude larger than the Kerr effect signal, which is promising for highly sensitive magnetic microscopy experiments. In order to better understand the nature of the V_{MCD} signals, we then performed large two-dimensional maps of the magnetic configuration.

The magnetization is first initialized in the $+M_r$ remanent state by applying a +500 Oe external magnetic field along $+z$. Fig. 5.5 a) shows the sample reflectivity, the Hall bar contours are highlighted by a black dashed line. Fig. 5.5 b) and d) shows the V_{MCD} signal and the DC photovoltage, respectively, using the contact configuration shown in Fig. 5.1. We observe that the DC photovoltage is positive when the laser beam scans the top area ($Y > 0$ μm) and negative in the bottom area ($Y < 0$ μm). This is a direct evidence of the Seebeck effect in Ge due to the temperature difference between the two electrical contacts. Interestingly, we observe the same behavior for the V_{MCD} signal (demodulated at the frequency of the PEM). By using both the DC and V_{MCD} photovoltages, I will show that we can obtain a position-independent map of the magnetic configuration, given by the Seebeck effect in Ge.

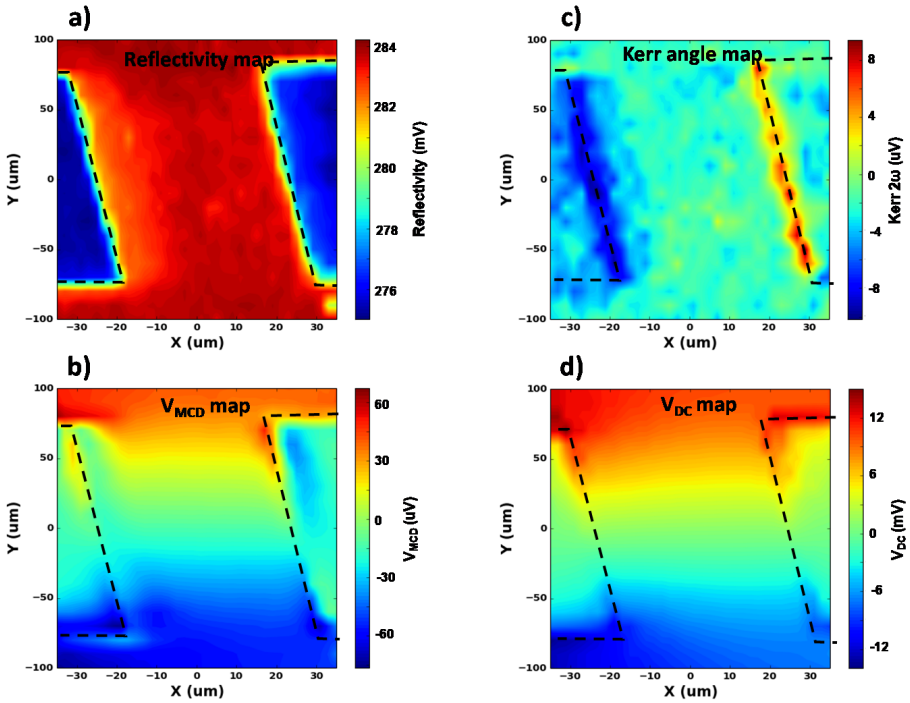

Figure 5.5 – Two-dimensional maps of the remanent magnetic states $+M_r$ along $+z (B = 0\ \mathrm{T})$. a) Sample reflectivity. b) V_{MCD} c) Kerr angle and d) DC photovoltage. Here, there is no applied current.

To further understand how the V_{MCD} signal is affected by the temperature distribution in Ge when scanning the laser beam, we record hysteresis loops for different vertical positions

(Y) of the laser beam on the Hall bar. Fig. 5.6 a) shows that the hysteresis loop signal is reversed between $Y > 0$ µm and $Y < 0$ µm while the Kerr effect is independent of the beam position (Fig. 5.6 b)). The difference of signal between the two remanent states is plotted as a function of Y in Fig. 5.6 c), we can see how the V_{MCD} signal is changing with the beam position.

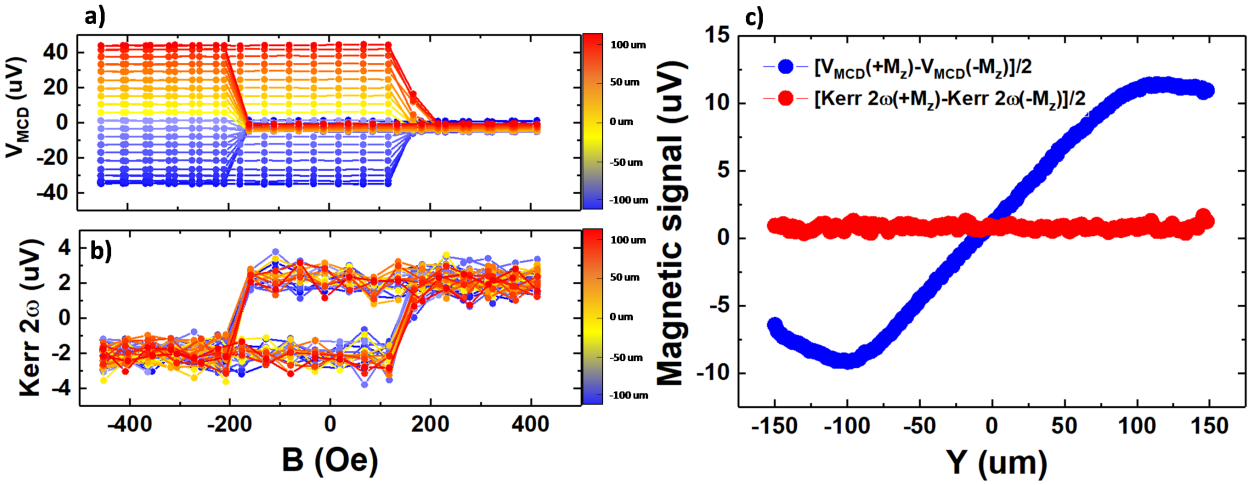

Figure 5.6 – a) V_{MCD} hysteresis loops recorded for different vertical positions of the laser beam on the Hall bar. b) Kerr angle hysteresis loops. c) V_{MCD} and Kerr angle remanent signals as a function of the position of the beam on the Hall bar.

The V_{MCD} signal being geometry-dependent, it is not suitable and reliable to perform magnetic imaging. Several approaches can be used to solve this problem. First, one can simply normalize the V_{MCD} signal by the DC photovoltage to obtain an almost position-independent measurement. Still, in the region located in the middle of the two electrical contacts, the sensitivity of this technique is negligible.

One can optimize the contacts geometry to have an almost uniform temperature in Ge at the level of the magnetic microstructure to image regardless of the laser beam position by patterning one contact close to the microstructure and a second one far away. This would optimize the Seebeck effect-based detection of the magnetic circular dichroism. Moreover, using a material with a large Seebeck coefficient like Ge ($S = 330$ µV/K) is necessary to obtain large signals.

An alternative technique consists in applying a bias current through the Hall bar, parallel to the MCD electrical detection axis (along y here). In this way, the difference of photogenerated charge carriers due to the difference of absorption of the σ_+ and σ_- polarized lights drifts along the bias electric field.

This type of measurement is reported in Fig. 5.7. A DC bias current is dynamically applied between the two detection contacts and the even and odd components of the V_{MCD} signal

with respect to the current are calculated and plotted as a function of the position of the laser spot. Fig. 5.7 a) shows two-dimensional maps of the current-dependent $V_{\mathrm{MCD}}^{\mathrm{odd}}$ for bias currents from 20 µA to 100 µA, the corresponding profiles for $X = 0$ µm are shown in Fig. 5.7 c). We observe a clear spatial-independent V_{MCD} signal, which is linear with the bias current. The current-independent component $V_{\mathrm{MCD}}^{\mathrm{even}}$ is reported in Fig. 5.7 b) and the corresponding profile in Fig. 5.7 d), we find again the fingerprint of the Seebeck effect-based MCD detection.

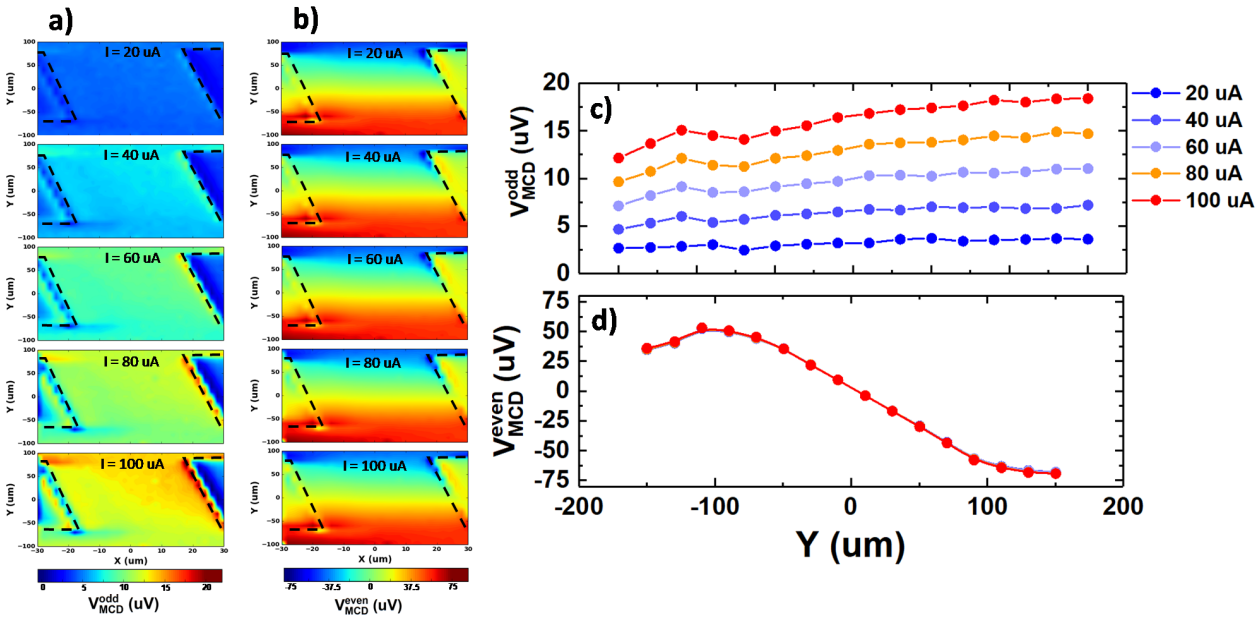

Figure 5.7 – a) Two-dimensional maps of the bias dependent (odd with I) component of the V_{MCD} signal for bias currents from 20 µA to 100 µA. b) Corresponding bias independent (even with I) component. c) $V_{\mathrm{MCD}}^{\mathrm{odd}}$ profiles at $X = 0$ µm. d) $V_{\mathrm{MCD}}^{\mathrm{even}}$ profiles at $X = 0$ µm.

In the following, we take advantages of the position of the disconnected contact far from the the Hall bar to maximize the Seebeck-based detection of MCD: by using this configuration, the scanning area is far from the middle of the two detection contacts and the Seebeck voltage (and then the V_{MCD} signal) is almost independent of the position of the laser beam on the scanned area. This is necessary to have a reliable magnetic image of the (Co/Pt) microstructure.

We now investigate the dependence of the magnetic properties as a function of the repetition number n of (Co/Pt) bilayers. Fig. 5.8 summarizes the results where the magnetization is measured simultaneously using the V_{MCD} and the Kerr effect.

The light beam is focused on the center of each Hall bars as illustrated in Fig. 1.3 a). When sweeping the magnetic field perpendicularly to the film plane, hysteresis loops are observed, indicating that all the films show PMA. We can also notice that the coercive field grows with the number of repetitions, as a consequence of a larger magnetic anisotropy due to the increase of the number of interfaces.[219,244]

V_{MCD} signal is approximately one order of magnitude larger than the Kerr signal, regardless the number of repetitions. We stress out that the signal to noise ratio is also significantly larger when using the V_{MCD} technique, the lock-in detection parameters (filtering and averaging) being the same for both techniques.
We also observe that V_{MCD} increases when decreasing the number of repetitions whereas the Kerr effect signal decreases as shown in Fig. 5.8 c) and d). So it confirms that this technique is very interesting to detect the magnetization of ultrathin ferromagnets where the Kerr effect signal is barely detectable.

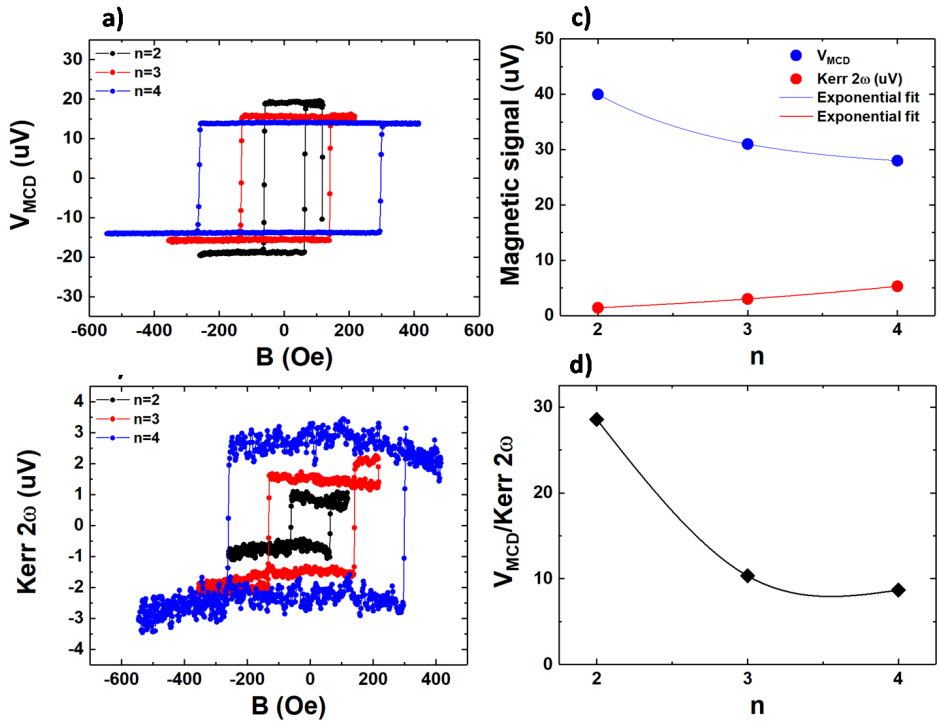

Figure 5.8 – Hysteresis loops for different (Co/Pt) repetitions ($n = 2, 3, 4$) simultaneously measured by a) the V_{MCD} technique and the b) the Kerr effect. The beam is focused on the center of the Hall bar for each $(Co/Pt)_n$ sample and the laser power is 650 μW. c) Summary of the two magnetic signal dependence with the Co/Pt repetition number. d) Ratio between the V_{MCD} and the Kerr effect signal as a function of the number of repetitions.

In order to further confirm the nature of the V_{MCD} signal, we vary the incident light polarization. The PEM is used to control the light helicity, the retardation is fixed at 0.3 λ. As shown in Fig. 5.9 a), we rotate the entrance polarizer with respect to the PEM axis. The angle of the rotation is defined as α (see Fig. 5.9 a) and b)). The light polarization is linear when the entrance polarizer and the PEM axis are aligned ($\alpha =$ 0°, 90 °, 180 ° and 270 °). The light polarization is circular for $\alpha =$ 45° and 225° (right handed), and for $\alpha =$ 135° and 315° (left handed).
Here, we focus on the $(Co/Pt)_4$. A 1000 Oe external field is first applied to saturate the magnetization along the $+z$ direction, it is then turn to zero to measure the remanent mag-

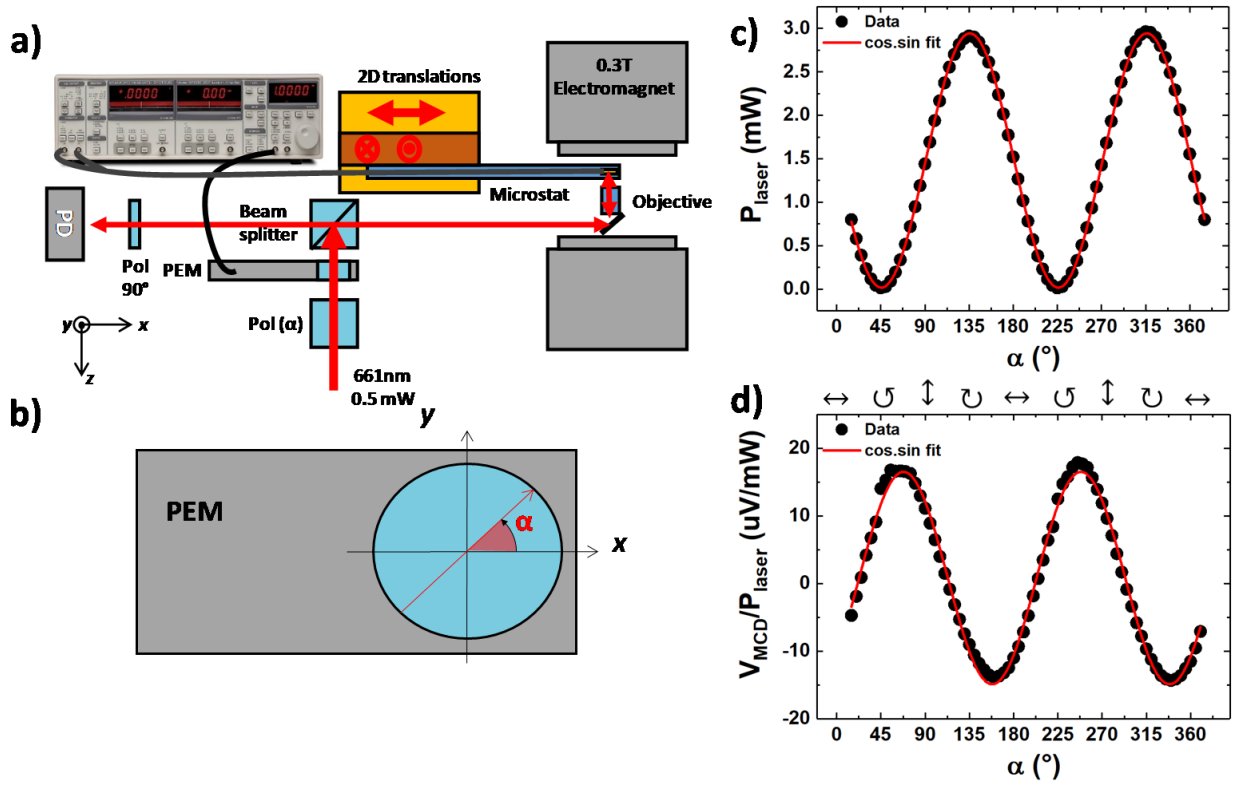

Figure 5.9 – a) Schematic top view of the LUMOS optical bench, the light polarization is obtained by associating a linear polarizer and a photoeleastic modulator. b) Definition of the angle α, x and y denotes the PEM optical axis. c) Laser power dependence with the polarizer angle α. d) V_{MCD} signal normalized by the laser power, the inset indicates the light polarization state.

netization state. The laser beam is focused on the Hall bar center and the dependence on the polarization angle is recorded, all the measurements are performed at room temperature. The laser beam is already polarized out of the optical fiber, so the transmitted laser power is also affected by the polarizer rotation. Therefore, the laser power is also recorded using a powermeter for each polarizer angle. As shown in Fig. 5.9 c), P_{laser} follows the Malus law:

$$P_{laser} = P_0 \cos^2(\alpha + \alpha_0) \tag{5.1}$$

Where P_0 is the nominal laser power, α is the angle between the polarizer and the PEM optical axis and α_0 is the angle between the initial laser polarization and the first polarizer (see Fig. 5.9 b)). The power dependence on the polarizer angle gives minima for $\alpha = 46°$ and 226°, indicating that $\alpha_0 = 136°$. In order to correctly measure the V_{MCD} signal, we have to normalize the recorded V_{MCD} by P_{laser}. The dependence of V_{MCD} on the polarizer angle is reported in the Fig. 5.9 d), the inset on top shows the incident light polarization state.
We observe a $\cos\alpha \sin\alpha$ angular dependence: V_{MCD} vanishes when $\alpha = 0°$, 90°, 180° and 270°, i.e. when the light polarization is linear. It shows minima (maxima) for $\alpha = 45°$ and 225° ($\alpha = 135°$ and 315°) for σ_+ and σ_- light polarization respectively. This result

emphasizes that the detected voltage is due to the different absorption of circularly polarized light by the ferromagnetic film, resulting in different photovoltages in Ge for clockwise and counterclockwise light helicities.

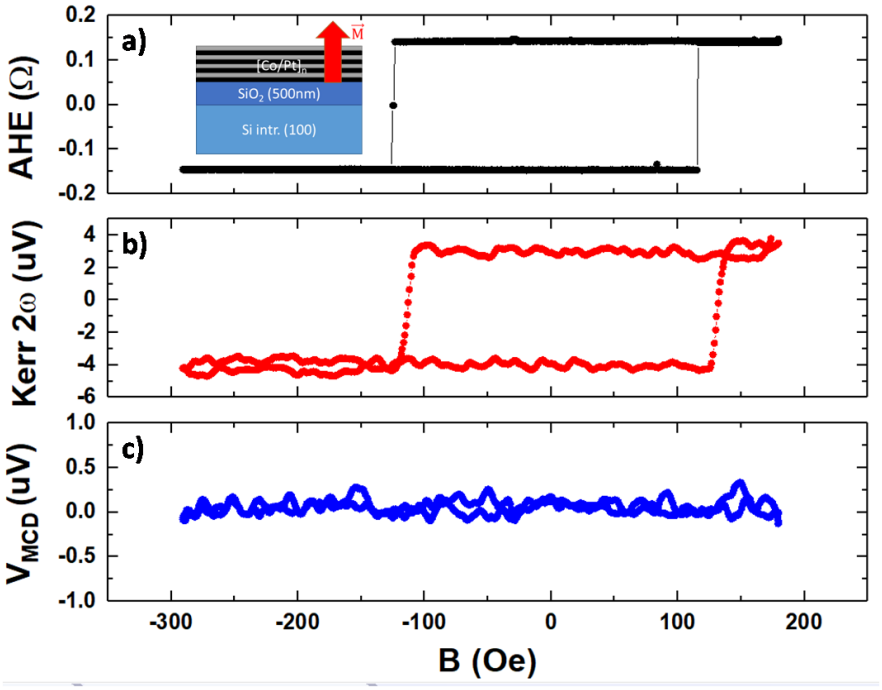

Figure 5.10 – a) AHE hysteresis loop recorded with a current $I_{DC} = 100$ μA. b) MOKE hysteresis loop using a 100 % circularly polarized red light ($\lambda = 661$ nm) focused on the Hall bar center, the spot size is about 1.5 μm. c) V_{MCD} hysteresis loop, the voltage is demodulated at the PEM frequency ω and measured between two Hall bar contacts.

Finally, to prove that the V_{MCD} signal is related to a photovoltage generated in Ge and not directly in the ferromagnetic film, we grew a $(Co/Pt)_2$ film on a SiO_2 substrate and used the same layout to pattern Hall bars. Again, the magnetic properties are measured using simultaneously the AHE, V_{MCD} and the Kerr effect. As shown in Fig. 5.10, the film magnetization anisotropy is also perpendicular, the hysteresis loop can be detected using the AHE or the Kerr effect but there is no V_{MCD} signal. This result confirms that the measured photovoltage comes from Ge due to MCD in the (Co/Pt) film.

5.1.4 Application to the study of magnetic domain wall motion

After characterizing the magnetic properties of the (Co/Pt) films we could demonstrate the detection of MCD by a photovoltage generated in the adjacent semiconducting film of Ge. We now exploit this technique to image multidomain magnetic configurations and the motion of domain walls.

Here, we focus on the $(Co/Pt)_3$ sample. Up to now, we have used the three magnetometry techniques to measure the hysteresis loops and image the sample remanent uniform magnetization. Here, we introduce a magnetic domain wall in the Hall bar by applying a specific magnetic field sequence. We further use the two magnetic microscopy techniques to image the domain wall propagation. We repeat following the field sequence: the magnetization is first saturated along $+z$, then a negative magnetic field B_{nucl} is applied to nucleate domains and we image the magnetic configurations. The sequence is iterated by increasing $|B_{\text{nucl}}|$.

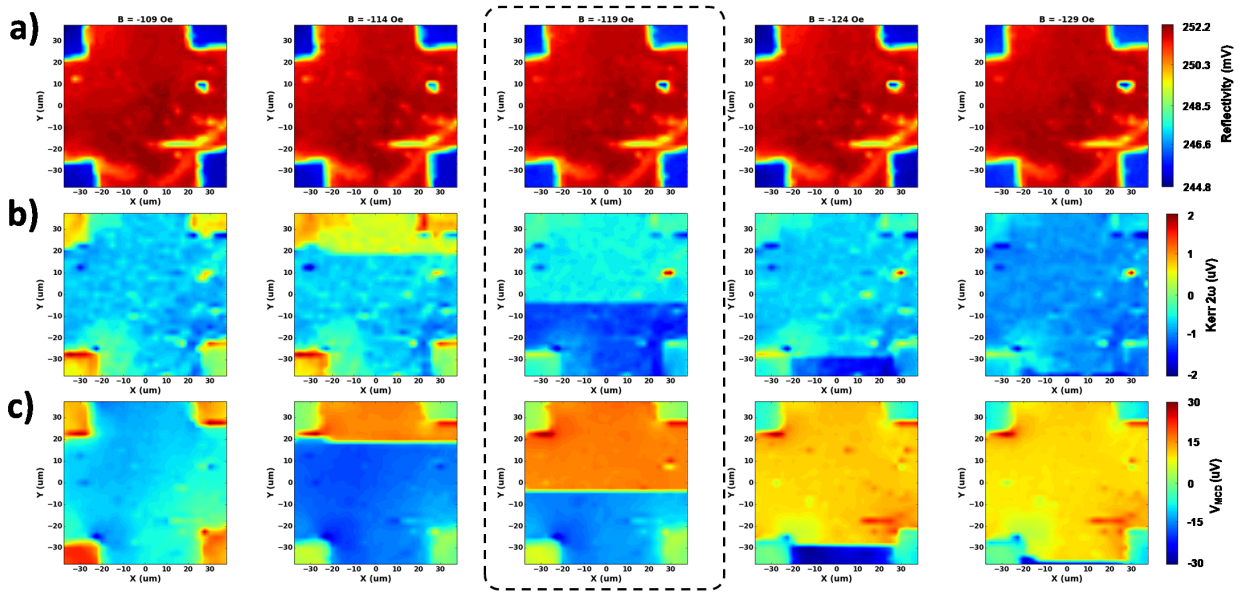

Figure 5.11 – a) Reflectivity maps. b) V_{MCD} maps. c) Kerr effect maps. Before each two-dimensional scans, a +500 Oe field is first applied to saturate the magnetization along the $+z$ direction, a precise negative magnetic field value is then applied to nucleate and propagate a domain wall. We can see the domain wall propagating when increasing the magnitude of the magnetic field.

This can be imaged simultaneously using the Kerr effect microscopy and our electrical detection of the local magnetization based on the magnetic circular dichroism in the (Co/Pt) film and the photogeneration in Ge. Fig. 5.11 a) shows the reflectivity of the sample for the different magnetic field intensities, the (Co/Pt) (Ge) film corresponds to the red (blue) color. Fig. 5.11 b) and c) show the Kerr effect and V_{MCD} maps recorded for the different applied magnetic fields. In the first panel set ($B = -109$ Oe), the magnetization is still saturated and homogeneous on the Hall bar scanned area. Then, by iterating the magnetic field se-

quence, we see a domain wall nucleating at $Y = 20$ µm, the magnetic domains are pointing toward $+z$ (in red) and $-z$ (in blue). By further increasing the negative magnetic field, we observe the propagation of the wall along the $-y$ direction. Interestingly, the domain wall (its propagation) is perpendicular (parallel) to the current line of the Hall bar.
Here, by imaging the two-dimensional magnetization maps simultaneously with the two techniques, we conclude that the V_{MCD} technique is very promising for future domain wall motion investigation in ultrathin ferromagnetic films like 2D materials.

To conclude, we have successfully grown perpendicularly magnetized thin films on a Ge (111) substrate. The magnetic properties of (Co/Pt) multilayers were investigated using the anomalous Hall effect, magneto-optical Kerr effect microscopy and a new hybrid electro-optical technique based on the magnetic circular dichroism in (Co/Pt), the thermoelectric and semiconducting properties of Ge. Our study reveals that this technique shows several advantages for ultrathin films magnetic characterization. First, the detection being electrical, the reflected light does not need to be analyzed, simplifying the experimental setup. Both the signal and the signal-to-noise ratio are larger using the V_{MCD} technique rather than the Kerr effect microscopy.
We showed that the electrical detection of the magnetic circular dichroism of the (Co/Pt) film originates from the Seebeck effect, as a result of a difference of thermal gradients between the two electrical contacts. We demonstrated that the measurement geometry can be optimized in order to maximize this thermal contribution and obtain a uniform measurement by using strongly asymmetric contacts. Alternatively, one can suppress or enhance the thermal contribution by applying a bias current parallel to the detection axis, in order to obtain a measurement completely independent of the geometry.

Finally, we point out the fact that it is not necessary to connect electrically the ferromagnetic film, the two contacts can simply be made on the semiconducting substrate close to the ferromagnet. This feature added to the high sensitivity of the technique in the ultrathin film regime make this technique an excellent alternative to traditional magnetometry for the investigation of ferromagnetism in two-dimensional materials grown (or transfered) on semiconductors[252] and will be the object of future experiments within our research group.

5.2 Electrical spin injection and detection in lateral spin valves

In the previous paragraph, I showed that we were able to grow perpendicularly magnetized (Co/Pt) multilayers on Ge (111) and to tune the magnetic properties by changing the repetition number. In this section, I take advantages of these developments to design lateral spin valves on Ge/Si (111). I first reports the fabrication of the lateral devices using only laser lithography, constraining the device dimensions above 1 µm. Although the electrical measurements were not conclusive and that no spin signal was observed in these structures, the nanofabrication process is worth reporting, as I pushed the laser lithography technique to its limits in resolution and re-alignment.
The second part reports devices made using both e-beam and laser lithography. By combining the two techniques, I could make devices with sub-micrometer critical dimensions at minimal fabrication time and cost. Lowering the dimensions of the injection electrode resulted in the observation of a non-local spin signal. To the best of our knowledge, it is the first time that a spin signal coming from a lateral spin valve with perpendicularly magnetized MTJs is reported in a semiconductor.
Still, there is room for the optimization of the tunnel barrier resistivity in order to enhance the spin signals.

5.2.1 Design and nanofabrication of the devices

A lateral spin valve (LSV) allows to perform all-electrical spin injection and detection measurements using magnetic tunnel junctions (MTJs). This type of devices were introduced in the first chapter of the manuscript. The generation of spin accumulation in a semiconductor using MTJs is very difficult and LSVs are costly devices that require five to six e-beam litography steps that usually results in several weeks of clean room works. Here, I report the development of two innovating techniques to pattern LSV reducing the time and cost of nanofabrication.

5.2.1.1 Patterning with laser lithography

The spin injection in low-doped semiconductors using MTJs is a difficult operation. One solution that was brought in the literature is to use a substrate that is highly n-doped at the surface. We use a 2 µm-thick Ge(n++)/Ge(low-n)/Si (111) substrate prepared by low energy plasma enhanced chemical vapor deposition. Phosphorus atoms are introduced in the chamber during the last 20 nm of the growth in order to reach a 10^{19} cm^{-3} n-type doping level as shown in Fig. 5.12 a).
We start the fabrication by cleaning the substrate using solvents and hydrofluoric acid to remove the organic contamination and the native oxide. The first lithography step is done in four substeps:

- First, a 1.2 µm-thick AZ1512HS resist film is spin-coated, we take a special care that there is no resist on the backside of the substrate so that the focal point of the laser lithography does not move when scanning the sample.
- Second, a first exposure is done to define for the alignment crosses.
- Then, without developing the resist, we define the first MTJ level using the alignment crosses (even without developing, the resist shows enough contrast to align).
- Finally, after those two exposures, the resist is finally developed in a AZ developer diluted 1:1 with deionized water for 7 s giving the result illustrated in Fig. 5.12 b).

Usually, the alignment level is done in the same exposure as the first MTJ level, so the two are virtually perfectly aligned. But the second level might suffer from the user-dependent natural misalignment. This two-exposure technique allows to include this natural misalignment in the first level, so that ultimately, all the levels are perfectly aligned. This technique gave me the best results and does not need for an additional deposition or etching as I exploit the natural contrast of the exposed resist.

The sample is then transferred inside our MBE system, where an 1 nm-thick MgO layer is deposited by e-beam evaporation. The sample is then transferred into the sputtering chamber (the two chambers are connected in a single UHV system), and $(Co/Pt)_2$ is deposited at room temperature. We then do a lift-off of the $(Co/Pt)_2$ in acetone for 4 h.

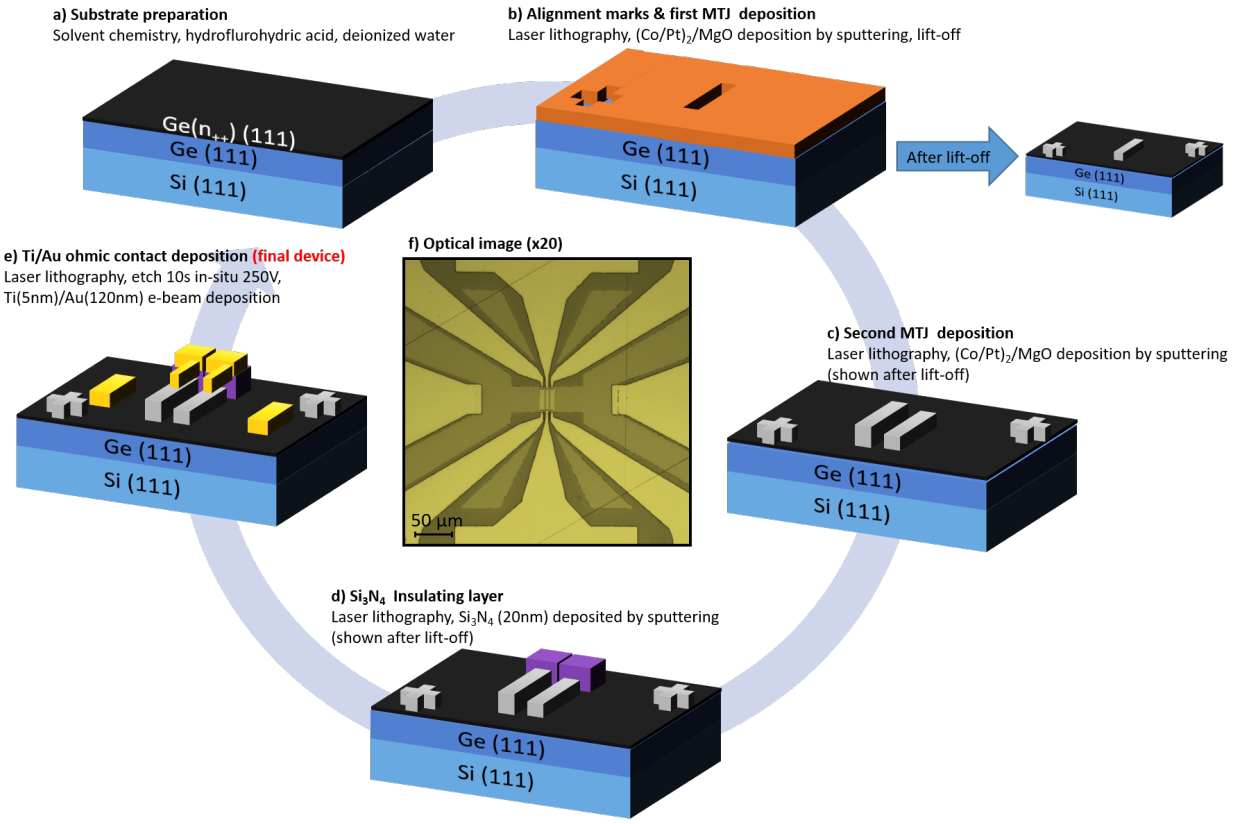

Figure 5.12 – Scheme of the different micro-fabrication steps to obtain the lateral spin valve device using a process entirely based on laser lithography.

In a second step, we use the same laser lithography process to pattern the second MTJ. Here, the optimization of the alignment procedure and of the exposure conditions allowed me to reach a sub-micrometer scale for the distance between the two electrodes which is in principle, smaller than the machine resolution. After the lithography, the sample is transferred again in the MBE chamber for the MgO deposition, and to the sputtering chamber for a $(Co/Pt)_3$ deposition this time. The increase in repetition number gives us different coercive fields for the two MTJs.
The first step consists in depositing an insulating layer that prevents the current shunting into Ge (see Fig. 5.12 d)) and the last one is the contact deposition itself (see Fig. 5.12 e)). An optical image of the final device is shown in Fig. 5.12 f).

I patterned several samples with different MgO thicknesses from 0.8 nm to 2 nm. Despite the microfabrication being as good as it can be, I was not able to detect a non-local spin voltage in such structures. Finally, we decided to move to an hybrid process combining the advantages of e-beam and laser lithography.

5.2.1.2 Patterning with electron-beam and laser lithography

We believe that the absence of spin signal in the previous devices is due to two main issues:
- First, even if single cristalline MgO thin films could be obtained when grown on Ge (100) by molecular beam epitaxy,[42] the six-fold symmetry of Ge (111) did not result in a well-oriented MgO film, leading to a low-quality tunnel barrier. After several attempts to improve the growth, we decided to switch to Al_2O_3 barriers.
- Then, to maximize our chance to have a uniform insulating tunnel barrier for the spin injection to occur, we chose to define MTJs by e-beam lithography, in order to reach typical electrode width of 150 nm, reducing the probability to have pin-holes.
Fig. 5.13 summarizes the complete nanofabrication process. After a standard cleaning procedure, we start by depositing a 1.4 nm-thick Al film by MBE. The sample is transferred into an oxidation chamber where it is exposed to a 300 mbar O_2 atmosphere for 45 min, transforming the Al film into Al_2O_3.
Afterward, the sample goes through a six-steps hybrid lithography process. The steps 1,3,4,5 are done using laser lithography (respectively shown in Fig. 5.13 c), e), f) and g)). The corresponding patterns being rather large (typically larger than 10 μm), this allows to speed up the process as an e-beam exposure on such scales can be several hours-long versus several minutes using laser lithography.
The steps 2 and 6 are done using e-beam lithography (respectively shown in Fig. 5.13 b) and h)). Here, we are exploiting the high-resolution of e-beam exposure to define the two MTJs (Fig. 5.13 b)) and contact them (Fig. 5.13 h)).
A scanning electron microscopy (SEM) image of the final device is shown in Fig. 5.13 i). The contrast of coercive fields between the two electrodes here is given by the difference in lateral

size (200 nm vs 2.5 um in width). For the large electrode, the presence of a nucleation center (on a defect for instance) is higher than for the small electrode. As a consequence, the large electrode is expected to have a lower coercive field.

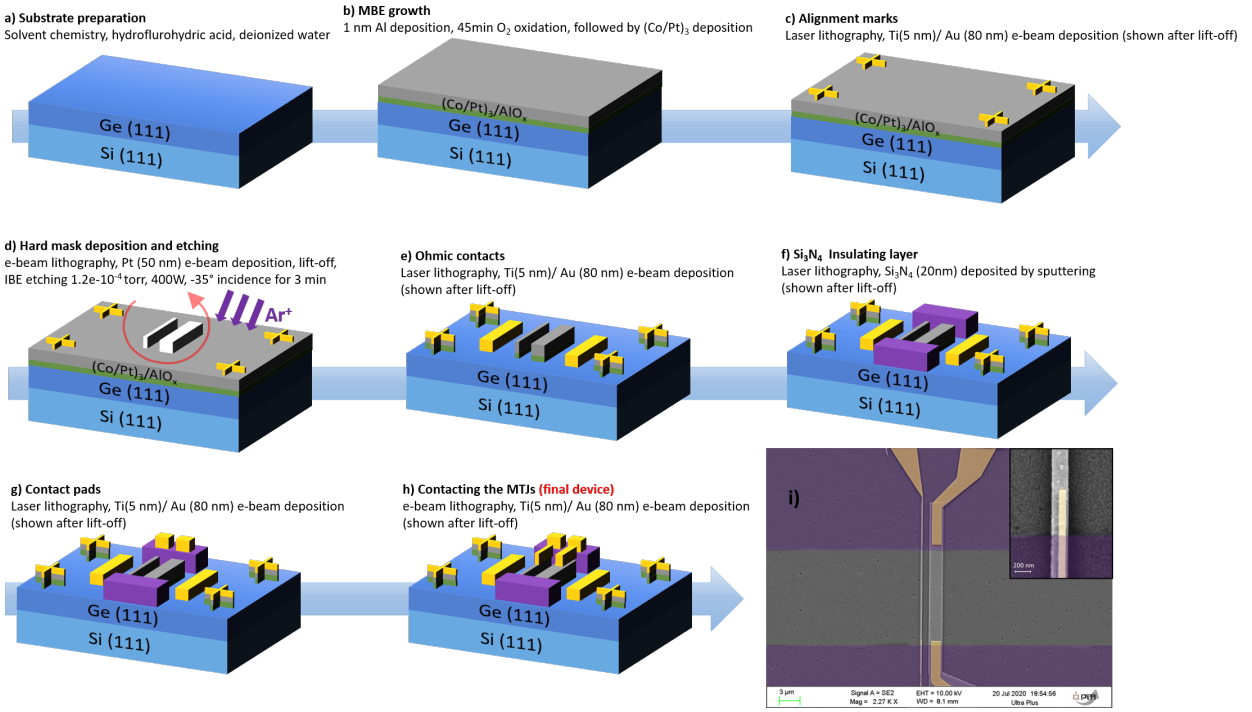

Figure 5.13 – Scheme of the different micro-fabrication steps to obtain the lateral spin valve device using the hybrid process based on e-beam and laser lithography.

5.2.2 Non-local spin detection and Hanle effect

The first important property to characterize is the contrast of coercive field between the two magnetic tunnel junctions in the lateral spin valve. For this purpose, two Hall bars sharing the same dimensions as the MTJs in the LSV were also patterned on the same sample in order to measure the coercive field using anomalous Hall effect (AHE) measurements.
Fig. 5.14 reports the evolution of the coercive fiels of the two MTJs extracted from the AHE measurements. For the thinnest MTJ, which we called the *hard* electrode, the coercive field decreases from 1000 Oe at 5 K to approximately 200 Oe at room temperature. The second MTJ, which we call the *soft* electrode, the coercive field decreases from 500 Oe at 5 K to 75 Oe at room temperature. This first study indicates that a clear contrast of coercive field is obtained between the two perpendicularly magnetized MTJs at any temperature.
Then, we proceed to characterize the tunnel properties of the Al_2O_3 tunnel barrier. We record the current-voltage characteristic of the interface using the three-terminal measurement geometry as depicted in Fig. 5.15 a). Most of the measured devices showed a Schottky-like current-voltage characteristic as shown in Fig. 5.15 b) (black curve). The non-local measurements on these devices presented no spin injection at any temperatures. Only one of

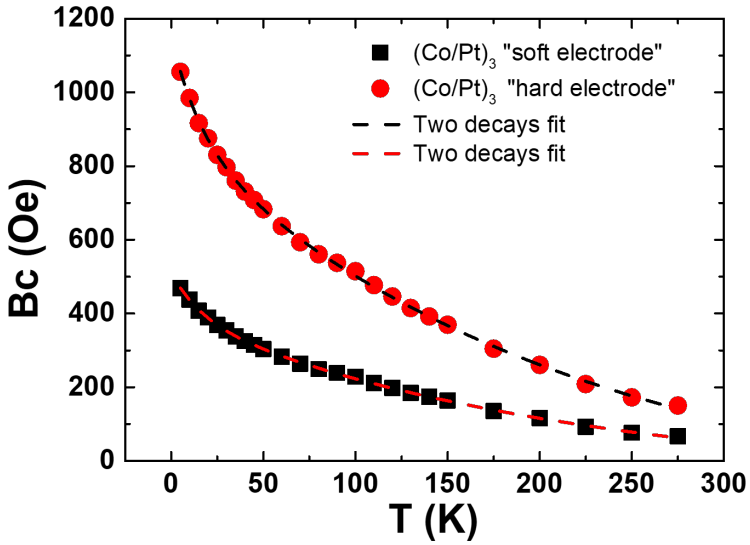

Figure 5.14 – Evolution of the coercive field of the two MTJs extracted using anomalous Hall effect measurements on a 200 nm-large Hall bar (red disks) and on a 2.5 µm-large Hall bar (black square). A clear contrast of coercive field is observed at any temperature.

the measured devices exhibited a cubic current-voltage characteristic which is reported in Fig. 5.15 b) (red curve).

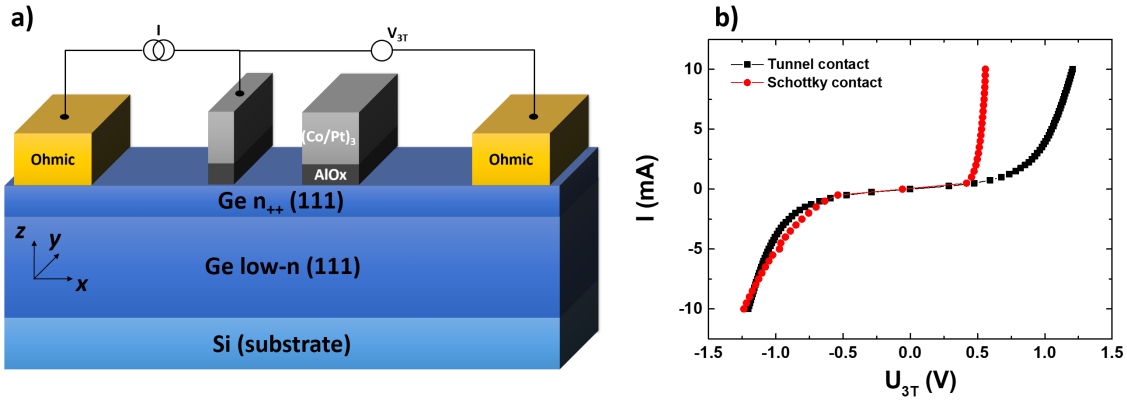

Figure 5.15 – a) 3 terminals geometry used to characterize the nature of the electrical contact between the MTJ and the Ge substrate. b) Asymmetric Schottky $I(V)$ curve recorded at 5 K (in red) and anti-symmetric $I(V)$ curve characteristic of the current injection through a tunnel barrier.

We focus on this device and move on to the spin generation and non-local detection experiment. Fig. 5.16 shows the measurement geometry. The MTJ stack is composed of a $(Co/Pt)_3$ perpendicularly magnetized layer deposited by sputtering on top of the 1.4 nm-thick Al_2O_3 layer. A 10 mA DC current is passed between the first MTJ/ohmic contact couple (on the

left) and we record the non-local voltage between the second MTJ/ohmic contact couple. As the magnetization of the MTJs is perpendicular to the sample plane, we sweep the magnetic field along z to manipulate their orientation and the sample temperature is set at 5 K.

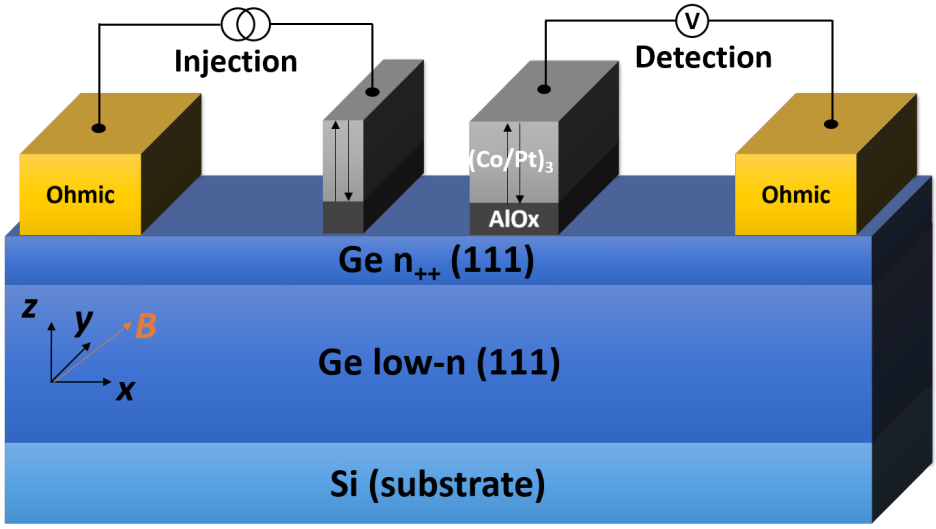

Figure 5.16 – Scheme of the lateral spin valve nanostructure. The thinnest MTJ (on the left here) is used as the spin injector: a current is passed between the MTJ and the ohmic contact. The largest MTJ (on the right here) is used as the non-local spin detector: the voltage between this MTJ and the second ohmic contact is recorded.

The magnetization of the two MTJs is first prepared in the parallel states by applying a +200 mT magnetic field along $+z$. The field is then sweep to -200 mT and the non-local voltage V_{NL} is recorded (blue curve in Fig. 5.17 a)). When $|B|> |B_c^{\mathrm{soft}}|$ ($|B_c^{\mathrm{soft}}|= 75$ mT), the soft MTJ magnetization reverses and the lateral spin valve is its antiparallel state. When $|B|> |B_c^{\mathrm{hard}}|$ ($|B_c^{\mathrm{hard}}|= 110$ mT), the hard MTJ magnetization also aligns with the magnetic field and the parallel configuration is retrieved. The same scenario occurs when sweeping the magnetic field from -200 mT to +200 mT (red curve in Fig. 5.17 a)).

The non-local signal is about 1.25 mΩ, which is rather small compared to the signal obtained on Ge (100) using Fe/Mgo-based MTJs.[42] Even if the measured voltages are in the microvolt range, the noise on the device is quite important. This is usually due to the ohmic contact being non perfectly ohmic at low temperature, inducing a detrimental high contact resistance that results in noisy measurements.

In order to further confirm that the non-local signal originates from the diffusion of the spin accumulation in the Ge channel, we attempt to measure the Hanle effect. For this purpose, we first prepare the LSV in the antiparallel state by applying a magnetic field sequence along z, then we turn the magnetic field off and rotate the sample so we can sweep the magnetic field along the x direction. In this way, the injected spins that are aligned along z are precessing along x during the diffusion, affecting the non-local detection.

The result of this experiment is shown in Fig. 5.17 b), we observe the non-local voltage drops

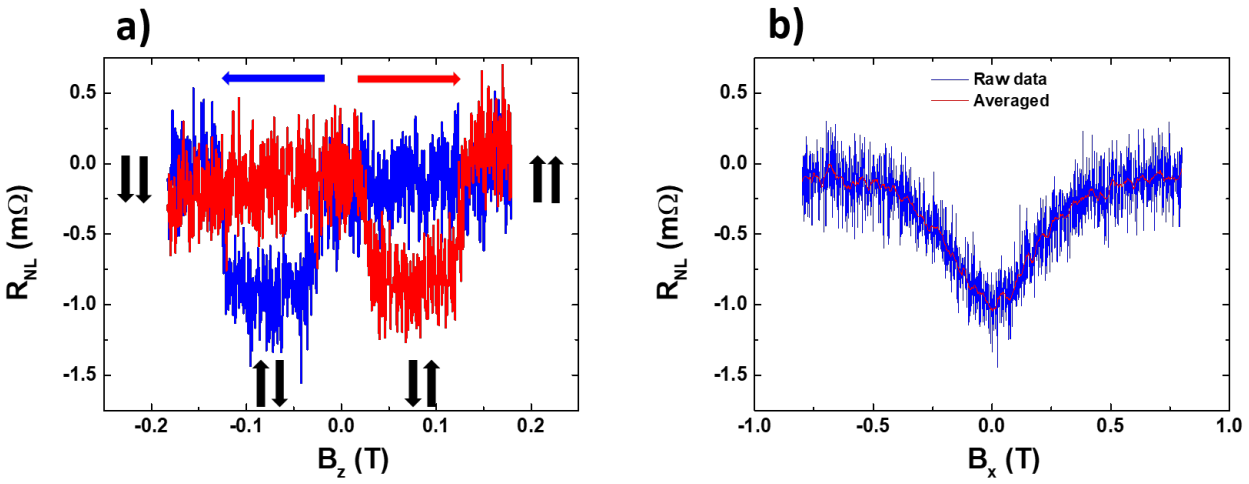

Figure 5.17 – a) Non-local measurement recorded at 5 K using a 10 mA DC current. b) Non-local Hanle effect.

to zero when the magnetic field becomes larger than 500 mT. This result also emphasizes that the signal truly originates from the electrical spin generation by the $(Co/Pt)_3/Al_2O_3$ magnetic tunnel junction.

After one day of measurement, the current-voltage characteristic of the MTJ injection became linear, indicating that the tunnel barrier was destroyed. This prevented us to perform more measurements on this lateral spin valve.

To conclude and summarize, in this section, we exploited the PMA of the (Co/Pt) films to define magnetic tunnel junctions that can generate spin accumulation with out-of-plane orientation. We explored and developed new clean room processes to pattern devices with submicrometer critical range with a minimal use of e-beam lithography. The sample showed large variability and only one device exhibited tunneling conduction. On this specific device, we managed to observe a non-local spin signal in a lateral spin valve, demonstrating electrical spin generation and detection on the Ge channel.

The measured spin signals were very faint, these first results are very promising, although a intensive work of optimization will be required to stabilize the process and grow better tunnel barrier in the future.

5.3 Spin manipulation in spin transistor-like hybrid structures

In this section, I report one attempt at combining all the elements of the Ge-based spin-orbitronics platform in one device where the spin can be injected electrically or optically, detected using non-local spin voltage or the spin-to-charge conversion in the Bi_2Se_3/Ge (111) interfacial Rashba states and manipulated by a topgate voltage.
This type of devices is highly demanding in terms of nanofabrication steps and I could only make one batch of microstructures. This kind of structure, constitutes the main perspective of my PhD thesis.

5.3.1 Device design and nanofabrication

The design of the device is summarized in Fig. 5.18. The idea is to combine the developments of chapter 3 regarding the Bi_2Se_3/ Ge (111) heterostructure to the lateral spin valve architecture reported in the previous section.

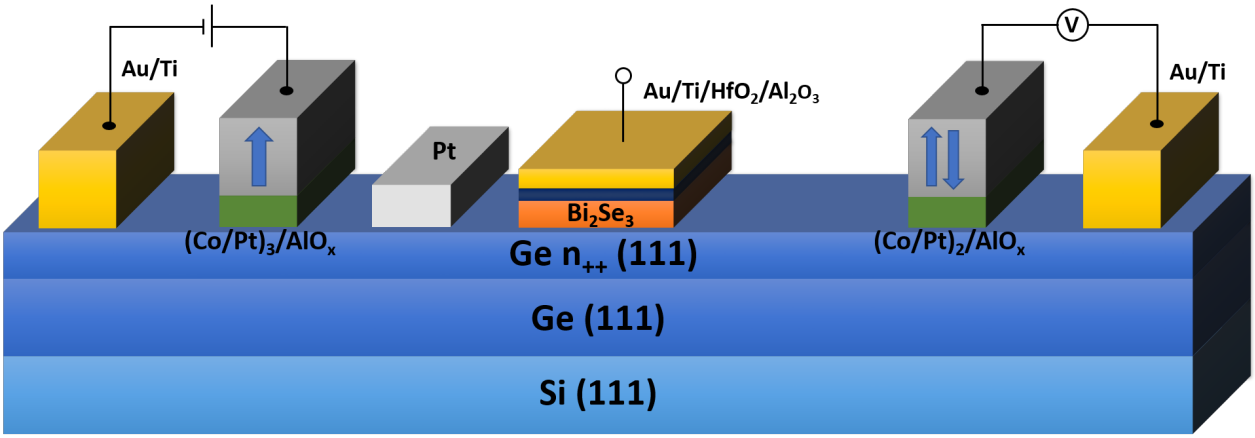

Figure 5.18 – Scheme of the proposed prototypical spin transistor that combines all the elements of the Ge-based spin platform.

We start by growing a 10 QL-thick Bi_2Se_3 film on a clean 2 μm-thick Ge(n++)/Ge(low-n)/Si (111) substrate using the molecular beam epitaxy procedure described in chapter 3. To pattern such complex devices we use 7 steps of laser lithography:
- Similarly to the process developed in the previous section, I define the alignment cross in a first exposure. Without developing, I expose the resist a second time to define the Bi_2Se_3 bar (orange in Fig. 5.18). After the second exposure, the sample is dipped in AZ developer 1:1 for 7 s and etched using ion beam etching for 3 minutes.
- The second step consists in defining the 15 nm-thick Pt stripe using e-beam evaporation and the lift-off technique. This part of the device will be used either as a reference for inverse spin Hall effect experiments or to generate spin accumulation with in-plane spin orientation using the techniques described in chapter 3.

- In a third step, a $(Co/Pt)_3/Al_2O_3$ *hard* magnetic tunnel junction is defined using the conditions developed in the two previous sections and a lift-off.
- In order to get a contrast of coercive fields for the two MTJs, the fourth step is dedicated to define the *soft* MTJ. Here, a $(Co/Pt)_3/Al_2O_3$ stack is deposited and lifted-off.
- The fifth step is used to pattern the passivation layer: a 70 nm-thick SiO_2 film is deposited by ion beam sputtering and lifted-off. This step ensures there is no short-circuits between the substrate and the future electrical contacts.
- The sixth step is the contact deposition: a Au(120 nm)/Ti(5 nm) film is deposited by e-beam evaporation and lifted-off.
- The last step is the topgate deposition. Here, we first deposit a HfO_2(40 nm)/Al_2O_3(5 nm) insulating stack by atomic layer deposition (ALD) at 200°C on the full sample area. Then, after the lithography, another Au(120 nm)/Ti(5 nm) electrode is deposited on the top of the Bi_2Se_3 bar, that acts as a topgate.

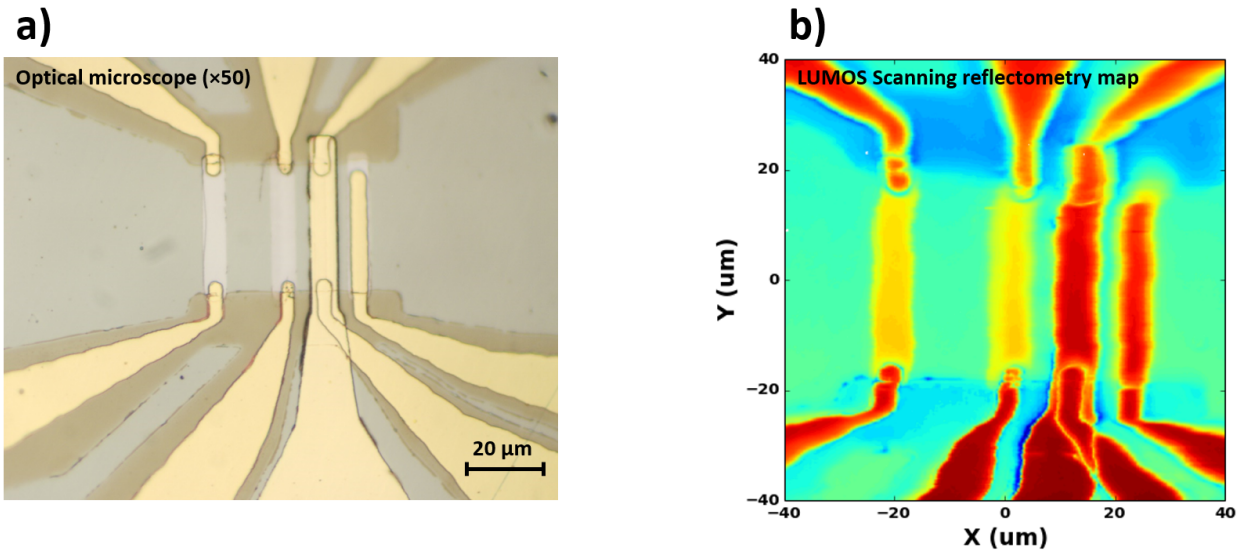

Figure 5.19 – a) Picture of the final prototypical spin transistor device taken with an optical microscope using a ×50 objective. b) Corresponding two-dimensional reflectivity map using scanning laser confocal microscopy in the LUMOS setup.

The final device picture taken with an optical microscope using a ×50 objective is shown in Fig. 5.19 a). Every layer is properly aligned and all electrical contacts are functional. Unfortunately, a problem occurred during the ALD deposition at the last step (the HfO_2 film was not deposited because of an issue with the gas precursor), resulting in the topgate leaking current for voltages above 1 V.

5.3.2 Perspectives: spin transistor effects

As I was not able to produce more batch of devices during the remaining time of my PhD thesis, I will let the investigation of the spin properties of the prototypical spin transistor as a perspective of my work. This short section aims to suggest the possible future experiments to perform with the devices.

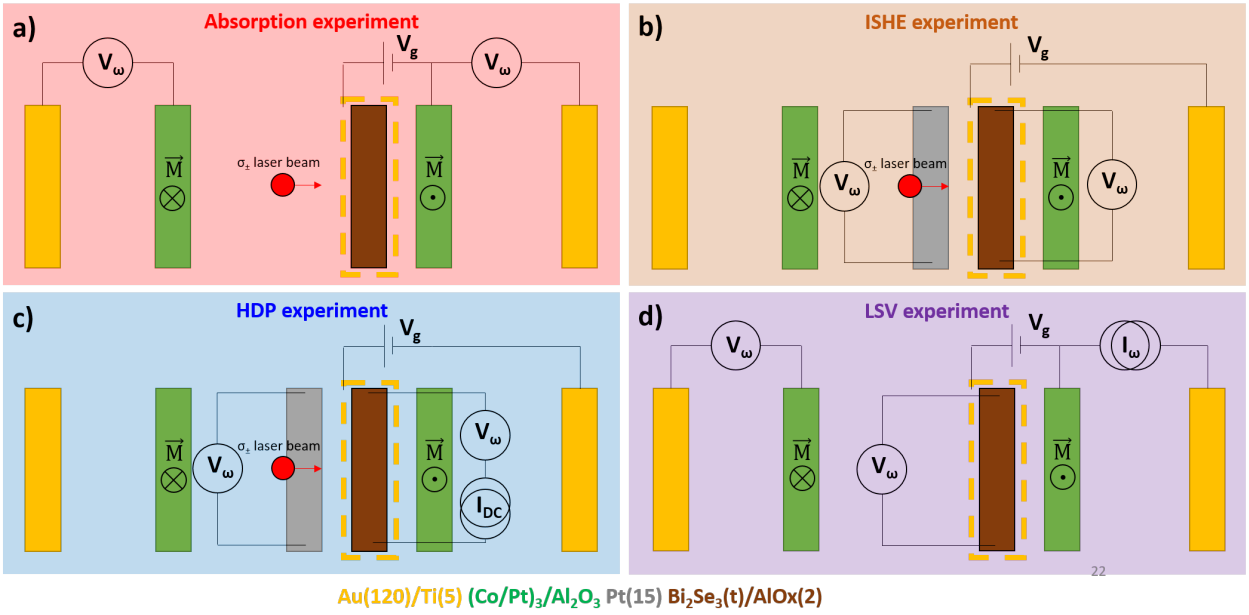

Figure 5.20 – Proposition of future experiments to perform with the prototypical spin transistor device. a) Precession and absorption experiment. b) Spin-to-charge conversion experiment. c) Helicity-dependent photovoltage experiment. d) All electrical spin generation, detection and manipulation using the lateral spin valve configuration.

Precession and absorption experiments

The first possibility of experiment to perform with the device is a spin absorption experiment. A spin population is generated by optical spin orientation using a circularly polarized laser beam. When the sample is illuminated at normal incidence, far away from the different metallic pads, the spin of the photogenerated electron is perpendicular to the sample plane. In this configuration, we can try to detect a non-local voltage between the MTJs and their associated ohmic contact. The idea then is to compare the non-local voltage magnitude between the two MTJs: the difference should come from the Bi_2Se_3 bar. The spin-polarization of the Bi_2Se_3/ Ge (111) interface states is in-plane, so the electrons with spins orientated perpendicular to the sample plane should not be absorbed but can eventually precess along the Rashba field generated by the passing of a current in the interface states. Alternatively, the experiment can be perform at oblique incidence, in order to allow the absorption of spin by the Bi_2Se_3 bar. This set of experiments could be repeated for different topgate voltages and at different temperatures in order to better disentangle the two effects: precession and absorption of spins.

Inverse spin Hall effect experiments

One of the main topic of chapter 3 was the quantification of the inverse spin Hall effect and inverse Rashba-Edelstein effect using optical spin orientation. Here, this device could be used to explore the topgate voltage dependence of the spin-to-charge conversion. Similarly to the experiments lead in chapter 3, an in-plane spin polarization could be generated using optical spin orientation at the edge of a Pt stripe. The latter also being contacted, a direct comparison of the signals sign and magnitude should be possible.

Helicity-dependent photovoltage experiments

The device can also be used to further investigate the helicity-dependent photovoltage that occurs when the Bi_2Se_3 bar is biased by a DC current. Again, studying the topgate voltage dependence of the effect should be very interesting and provide new information to better model the effect.

Lateral spin valve experiments

Finally, one could use the MTJs to electrically generate and detect a spin-accumulation with a perpendicular orientation. Then, the precession and absorption experiment described above could be performed again, in an all-electrical way.

To conclude this last section and chapter, we developed (Co/Pt) based perpendicularly magnetized magnetic tunnel junctions in order to develop a prototypical spin transistor based on semiconductors and topological insulators. We developed a new original microscopy technique to image magnetism in ultrathin ferromagnetic films that is a lot more sensitive than the Kerr effect. The technique is based on an (thermo)electrical detection of the magnetic circular dichroism of the (Co/Pt) film.

We developed advanced hybrid nanofabrication techniques that take advantage of the best of laser and e-beam lithography in order to pattern lateral spin valve with perpendicular magnetic anisotropy at reduced fabrication cost and time. We observed an all-electrical spin generation and detection in the Ge channel although the observed signals were very small and there is still room for optimization of the tunnel barrier properties.

Finally, we designed and fabricated a first spin transistor and proposed a set of future interesting experiments to perform on such devices.

Conclusion

This PhD thesis manuscript reported our advances in the implementation of a versatile spin-orbitronics platform based on Ge (111). My aim was to address the four critical principal technical issues of building a spin-based electronics: spin generation, transport, manipulation and detection. My work is based on the long run experience and knowledge of semiconductor spintronics developed by the team during the last 10 years. Electrical generation and detection of spin was already successfully realized at room temperature in Ge (100) substrate using lateral spin valves, optical spin orientation or spin pumping. However, Ge (100)-based platform is delicate to achieve as the instrinsic spin-orbit interaction is very small. The main part of my work focused on two approaches in order to tune the spin-orbit interaction (SOI) in the Ge-based platform. Both rely on the structural inversion asymmetry and the spin-orbit coupling at surfaces and interfaces with germanium (111).

In chapter 3, I performed the epitaxial growth of the topological insulator (TI) Bi_2Se_3 on Ge (111). I first develop the molecular beam epitaxy process that allowed us to grow high quality TI on Ge (111) and Al_2O_3 substrate. The structural properties of the heterostructure were extensively analyzed using electron and X-ray diffraction as well as transmission electron and atomic force microscopy. Then, the electrical properties were studied in low temperature and high magnetic field magnetotransport experiments. We showed that the electrical transport is two-dimensional in a single strongly coupled coherent channel in the presence of surface to bulk scattering using the Hall effect and the weak antilocalization signatures. We also showed that the conduction channel can be tuned between the Bi_2Se_3 film and the Ge layer underneath by adjusting a bias voltage which suggests that the Bi_2Se_3/Ge junction is a promising candidate for tuning spin-related phenomena at interfaces between TIs and semiconductors. Knowing that the structural and electrical properties of the bilayer were promising, we developed a ferromagnetic-free spin-to-charge conversion experiment. Indeed, it was shown that the chalcogenide species (Se or Te) can chemically react with the ferro-

magnetic film destroying the surface states and most of the current spin-to-charge conversion experiments rely on spin pumping from an adjacent ferromagnetic film. Here, we probe the spin-to-charge conversion states using a non-local generation/detection scheme. The spin population is generated by optical orientation in Ge, and diffuses towards the Bi_2Se_3 which acts as a spin detector. We compare the spin-to-charge conversion in Bi_2Se_3/Ge with the one taking place in Pt in the same experimental conditions. Interestingly, we observed that the sign of the spin-to-charge conversion given by the TI detector is reversed compared to the Pt one, while the efficiency is comparable, which is different from the current available results in literature. By exploiting first-principles calculations, we ascribed the sign reversal to the hybridization of the topological surface states of Bi_2Se_3 with the Ge bands. This work was done in strong collaboration with the semiconductor spintronics group of Politecnico di Milano, with Carlo Zucchetti, Adele Marchionni and Federico Bottegoni in particular. These results pave the way for the implementation of highly efficient spin detection in TI-based architectures compatible with semiconductor-based platforms.

In chapter 4, I reported the results from the second approach where we tried to exploit the intrinsic SOI of Ge (111). By investigating the electrical properties of a thin Ge (111) film epitaxially grown on Si(111), we found a large unidirectional Rashba magnetoresistance, which we ascribe to the interplay between the externally applied magnetic field and the current-induced pseudo-magnetic field applied in the spin-splitted subsurface states of Ge (111). As the UMR effect vanishes above liquid nitrogen temperature, I further studied the Fe/Ge (111) bilayer. The addition of the ultrathin Fe film bring ferromagnetism in the system, and resulted in a enhanced Rashba interaction. The unusual strength and tunability of this UMR effect open the door towards spin manipulation with electric fields in an all-semiconductor technology platform. This work was done in collaboration with the unité mixte de Physique CNRS-Thales in Palaiseau. Albert Fert strongly contributed to the theoretical framework and I performed a part of the early experiments with Jean-Marie George and Nicolas Reyren.

In chapter 5, I developed perpendicularly magnetized magnetic tunnel junctions on the Ge (111) platform. I first investigated the magnetic properties of Co/Pt multilayers grown by sputtering on Ge (111) by using three magnetometry techniques simultaneously: anomalous Hall effect, Kerr microscopy technique and a new original technique based on an electrical detection of the magnetic circular dichroism in (Co/Pt). These MTJs were then used to perform spin generation and detection in a lateral spin valve. The perpendicular magnetic anisotropy (PMA) allows to generate spin current with a spin orientation being also perpendicular to the sample plane.
Finally, I attempted to gather all the building block that were studied during my PhD work to build a prototypical spin transistor. Its principle relies on a gate voltage tunable Rashba spin-orbit field at the Bi_2Se_3/Ge (111) interface. Spin accumulations are generated either

optically by the optical spin orientation or electrically using the MTJ with PMA as a spin injector. Using perpendicularly magnetized spin injectors is interesting for the development of the spinFET as the spin orientation is orthogonal to the film plane, allowing to make the spins to precess around the Rashba field.

Perspectives

The development of topological insulators/semiconductors heterostructures realized in chapter 3 led to several interesting discoveries. The possibility to tune the conduction channel between Ge and Bi_2Se_3 in a vertical $p-n$ junction by applying a gate voltage is very interesting and further engineering of the bilayer could lead to new devices for spin-logic. The spin-to-charge conversion experiment probed by optical spin orientation brought a new landscape of experiments for topological insulators. As all bismuth-based TIs share similar structural properties, one perspective is to grow next generation TIs like BiSbTe and BiSbTeSe on Ge (111) by molecular beam epitaxy and apply the non-local optical spin orientation technique to measure the inverse Rashba-Edelstein in such system. We also showed that for the case Bi_2Se_3/Ge (111), the hybridization of states at the interface leads to a very strong Rashba spin splitting. One perspective would be to try to tune the spin-to-charge conversion by applying a gate voltage in this system. Also, the discovery of the helicity-dependent photovoltage in Bi_2Se_3/Ge (111), which we attributed to the interplay between two spin accumulations separated by a Schottky barrier should be the aim of a strong theoretical investigation in order to better catch the underlying microscopic mechanisms. This could pave the way to new interesting physics and original hybrid experiments.

In chapter 4, we discovered the unidirectional magnetoresistance in Ge (111) and Fe/Ge (111) system. We showed that the effect is a signature of the presence of spin-splitted Rashba states and that the addition of Fe atoms could increase the Rashba coupling. Further magneto-transport investigations should be pursued using ultrathin heavy atoms like Pt or Bi as a capping layer, and might give rise to room temperature UMR, which is promising for future spin transistor applications.

In chapter 5, we developed this new promising electro-optical technique to measure the magnetization state of ultra-thin ferromagnets. Advanced modeling of the effect would be interesting in order to further optimize the technique. The main perspective would be to try to measure the magnetization of two-dimensional ferromagnetic materials. In our team, we work on Mn-doped $MoSe_2$, $V_xPt_{1-x}Se_2$ alloys grown by molecular beam epitaxy, that could show ferromagnetism. Also, in a near future, we will grow the well-established FeGeTe 2D ferromagnet. We know from experience that measuring the magnetic properties of such

single atomic layer is difficult using standard magnetometry technique like SQUID, VSM or the Kerr effect. By growing those films on Ge (111) (or by transferring it), this new technique based on the electrical detection of the magnetic circular dichroism in the ferromagnet would provide an interesting solution and will be soon investigated in our group.

I also developed lateral spin valves based on perpendicularly magnetized magnetic tunnel junctions. Although small signals could be detected, there is room for optimization. An intensive work around the growth of single crystalline hexagonal tunnel barriers should enhance the spin injection efficiency by orders of magnitude and smaller devices using e-beam lithography could also reduce the variability between devices.

Finally, the prototypical spin transistor architecture I proposed and started developing should be the subject of more measurements and optimizations, as I was not able to fabricate proper devices within the available time. Nonetheless, all the work presented in this manuscript suggests that this architecture could be promising to achieve a spin transistor operation at room temperature.

Communications

Most of the work reported in my thesis manuscript are already published in peer-reviewed journals:
- T. Guillet, A. Marty, C. Beigné , C. Vergnaud, M.-T. Dau, P. Noël , J. Frigerio, G. Isella,and M. Jamet. "Magnetotransport in Bi_2Se_3 thin films epitaxially grown on Ge(111)". AIP Advances **8**, 115125 (2018).

- T. Guillet, C. Zucchetti, Q. Barbedienne, A. Marty, G. Isella, L. Cagnon, C. Vergnaud, H. Jaffrès, N. Reyren, J.-M. George, A. Fert, and M. Jamet. "Observation of Large Unidirectional Rashba Magnetoresistance in Ge(111)". Physical Review Letters **124**, 027201 (2020).

- T. Guillet, C. Zucchetti, A. Marchionni, A. Hallal, P. Biagioni, C. Vergnaud, A. Marty, H. Okuno, A. Masseboeuf, M. Finazzi, F. Ciccacci, M. Chshiev, F. Bottegoni, and M. Jamet. "Spin orbitronics at a topological insulator-semiconductor interface". Physical Review B **101**, 184406 (2020).

Three additional publications are in preparation:
- T. Guillet *et al.*, Electrical detection of magnetic circular dichroism: application to magnetic microscopy in ultra-thin ferromagnetic films

- T. Guillet*et al.*, Unidirectional magnetoresistance in Fe/Ge (111) grown by molecular beam epitaxy.

- T. Guillet *et al.*, Helicity-dependent photovoltage: two interacting spin accumulations.

I also contributed to additional works in international collaborations with other research groups that lead to other publications:

- C. Zucchetti, M.-T. Dau, F. Bottegoni, C. Vergnaud, T. Guillet, A. Marty, C. Beigné, S. Gambarelli, A. Picone, A. Calloni, G. Bussetti, A. Brambilla, L. Duo, F. Ciccacci, P. K. Das, J. Fujii, I. Vobornik, M. Finazzi, and M. Jamet. "Tuning spin-charge interconversion with quantum confinement in ultra-thin bismuth films". Physical Review B **98**, 184418 (2018).

- M. T. Dau, C. Vergnaud, A. Marty, C. Beigné, S. Gambarelli, V. Maurel, T. Journot, B. Hyot, T. Guillet, B. Grévin, H. Okuno, and M. Jamet. "The valley Nernst effect in WSe_2". Nature Communications 10, 5796 (2019).

I also had the opportunity to attend several national, european and international conferences where I gave multiple talks and poster presentations:
- *PASPS10*, Conference on Physics and Applications of Spin Phenomena in Solids, Linz (2018). Growth of Bi_2Se_3 on Ge (111), from surface states evidence to room temperature spin-to-charge conversion.
(Oral presentation)

- *JMC2018*, Journées de la matiè, Grenoble (2018). Growth of Bi_2Se_3 on Ge (111), from surface states evidence to room temperature spin-to-charge conversion.
(Oral presentation)

- *ESM2018*, The European School of Magnetism, Krakow (2018). Growth of Bi_2Se_3 on Ge (111), from surface states evidence to room temperature spin-to-charge conversion.
(Poster presentation)

- *EMRS2018*, The European Material Research Symposia, Warsaw (2018). Growth of Bi_2Se_3 on Ge (111), from surface states evidence to room temperature spin-to-charge conversion.
(Oral presentation)

- *CLN2019*, Colloque Louis Néel, Toulouse (2019). Spin-to-charge conversion in topological insulator/semiconductor heterostructures probed by optical spin orientation.
(Oral presentation)

- *JEMS2019*, The Joint European Magnetic Symposia, Uppsala (2019). Spin-to-charge conversion in topological insulator/semiconductor heterostructures probed by optical spin orientation.
(Oral presentation)

- *JEMS2019*, The Joint European Magnetic Symposia, Uppsala (2019). Observation of Large Unidirectional Rashba Magnetoresistance in Ge(111).

(Oral presentation)

- *MMM2019*, The Magnetism and Magnetic Materials conference, Las Vegas (2019). Spin-to-charge conversion in topological insulator/semiconductor heterostructures probed by optical spin orientation.
(Oral presentation)

- *MMM2019*, The Magnetism and Magnetic Materials conference, Las Vegas (2019). Observation of Large Unidirectional Rashba Magnetoresistance in Ge(111).
(Oral presentation)

- *MMM2019*, The Magnetism and Magnetic Materials conference, Las Vegas (2019). Helicity-dependent photo-induced magnetoresistance in topological insulator/semiconductor heterostructures.
(Poster presentation)

- *MMM2019*, The Magnetism and Magnetic Materials conference, Las Vegas (2019). Experimental evidence of the valley Nernst effect in WSe_2.
(Poster presentation)

- *SPIE Optics and Photonics*, The international society for optics and photonics, San Diego (2020). Germanium : a semiconducting platform for spin-orbitronics.
(Invited oral presentation)

Bibliography

[1] "ICT Energy Strategic Research Agenda" page 60.

[2] G. Moore. "Cramming More Components Onto Integrated Circuits". *Proceedings of the IEEE* **86**, 82 (1998).

[3] M. T. Bohr and I. A. Young. "CMOS Scaling Trends and Beyond". *IEEE Micro* **37**, 20 (2017).

[4] *The Historical Development of Quantum Theory 1-6*. The Historical Development of Quantum Theory. Springer-Verlag, New York (2001).

[5] J. Kübler. *Theory of Itinerant Electron Magnetism*. International Series of Monographs on Physics. Oxford University Press, Oxford, New York (2000).

[6] M. N. Baibich, J. M. Broto, A. Fert, F. N. Van Dau, F. Petroff, *et al.* "Giant Magnetoresistance of (001)Fe/(001)Cr Magnetic Superlattices". *Physical Review Letters* **61**, 2472 (1988).

[7] G. Binasch, P. Grünberg, F. Saurenbach, and W. Zinn. "Enhanced magnetoresistance in layered magnetic structures with antiferromagnetic interlayer exchange". *Physical Review B* **39**, 4828 (1989).

[8] M. Julliere. "Tunneling between ferromagnetic films". *Physics Letters A* **54**, 225 (1975).

[9] J. C. Slonczewski. "Current-driven excitation of magnetic multilayers". *Journal of Magnetism and Magnetic Materials* **159**, L1 (1996).

[10] P. M. Tedrow and R. Meservey. "Direct Observation of Spin-State Mixing in Superconductors". *Physical Review Letters* **27**, 919 (1971). Publisher: American Physical Society.

[11] P. M. Tedrow and R. Meservey. "Spin-Dependent Tunneling into Ferromagnetic Nickel". *Physical Review Letters* **26**, 192 (1971). Publisher: American Physical Society.

[12] J. S. Moodera, L. R. Kinder, T. M. Wong, and R. Meservey. "Large Magnetoresistance at Room Temperature in Ferromagnetic Thin Film Tunnel Junctions". *Physical Review Letters* **74**, 3273 (1995). Publisher: American Physical Society.

[13] M. Beth Stearns. "Simple explanation of tunneling spin-polarization of Fe, Co, Ni and its alloys". *Journal of Magnetism and Magnetic Materials* **5**, 167 (1977).

[14] J. C. Slonczewski. "Conductance and exchange coupling of two ferromagnets separated by a tunneling barrier". *Physical Review B* **39**, 6995 (1989). Publisher: American Physical Society.

[15] Y. Qi, D. Y. Xing, and J. Dong. "Relation between Julliere and Slonczewski models of tunneling magnetoresistance". *Physical Review B* **58**, 2783 (1998). Publisher: American Physical Society.

[16] W. H. Butler. "Tunneling magnetoresistance from a symmetry filtering effect". *Science and Technology of Advanced Materials* **9**, 014106 (2008). Publisher: Taylor & Francis _eprint: https://doi.org/10.1088/1468-6996/9/1/014106.

[17] D. C. Ralph and M. D. Stiles. "Spin Transfer Torques". *Journal of Magnetism and Magnetic Materials* **320**, 1190 (2008). ArXiv: 0711.4608.

[18] C. Chappert, A. Fert, and F. N. Van Dau. "The emergence of spin electronics in data storage". *Nature Materials* **6**, 813 (2007).

[19] S. Bhatti, R. Sbiaa, A. Hirohata, H. Ohno, S. Fukami, *et al.* "Spintronics based random access memory: a review". *Materials Today* **20**, 530 (2017).

[20] Z. Diao, Z. Li, S. Wang, Y. Ding, A. Panchula, *et al.* "Spin-transfer torque switching in magnetic tunnel junctions and spin-transfer torque random access memory". *Journal of Physics: Condensed Matter* **19**, 165209 (2007).

[21] S. Datta and B. Das. "Electronic analog of the electro-optic modulator". *Applied Physics Letters* **56**, 665 (1990).

[22] I. Žutić, J. Fabian, and S. Das Sarma. "Spintronics: Fundamentals and applications". *Reviews of Modern Physics* **76**, 323 (2004).

[23] S. A. Wolf, D. D. Awschalom, R. A. Buhrman, J. M. Daughton, S. von Molnár, *et al.* "Spintronics: a spin-based electronics vision for the future". *Science (New York, N.Y.)* **294**, 1488 (2001).

[24] A. Manchon, H. C. Koo, J. Nitta, S. M. Frolov, and R. A. Duine. "New perspectives for Rashba spin–orbit coupling". *Nature Materials* **14**, 871 (2015).

[25] T. Valet and A. Fert. "Theory of the perpendicular magnetoresistance in magnetic multilayers". *Physical Review B* **48**, 7099 (1993). Publisher: American Physical Society.

[26] A. Fert and H. Jaffrès. "Conditions for efficient spin injection from a ferromagnetic metal into a semiconductor". *Physical Review B* **64**, 184420 (2001). Publisher: American Physical Society.

[27] E. I. Rashba. "Theory of electrical spin injection: Tunnel contacts as a solution of the conductivity mismatch problem". *Physical Review B* **62**, R16267 (2000).

[28] M. Johnson and R. H. Silsbee. "Interfacial charge-spin coupling: Injection and detection of spin magnetization in metals". *Physical Review Letters* **55**, 1790 (1985). Publisher: American Physical Society.

[29] M. Johnson and R. H. Silsbee. "Spin-injection experiment". *Physical Review B* **37**, 5326 (1988). Publisher: American Physical Society.

[30] F. J. Jedema, A. T. Filip, and B. J. van Wees. "Electrical spin injection and accumulation at room temperature in an all-metal mesoscopic spin valve". *Nature* **410**, 345 (2001).

[31] F. J. Jedema, H. B. Heersche, A. T. Filip, J. J. A. Baselmans, and B. J. van Wees. "Electrical detection of spin precession in a metallic mesoscopic spin valve". *Nature* **416**, 713 (2002). Number: 6882 Publisher: Nature Publishing Group.

[32] D. Beckmann, H. B. Weber, and H. v. Löhneysen. "Evidence for Crossed Andreev Reflection in Superconductor-Ferromagnet Hybrid Structures". *Physical Review Letters* **93**, 197003 (2004). Publisher: American Physical Society.

[33] "Giant magnetoresistance in organic spin-valves | Nature".

[34] X. Lou, C. Adelmann, S. A. Crooker, E. S. Garlid, J. Zhang, *et al.* "Electrical detection of spin transport in lateral ferromagnet–semiconductor devices". *Nature Physics* **3**, 197 (2007). Number: 3 Publisher: Nature Publishing Group.

[35] H. C. Koo, H. Yi, J.-B. Ko, J. Chang, S.-H. Han, *et al.* "Electrical spin injection and detection in an InAs quantum well". *Applied Physics Letters* **90**, 022101 (2007). Publisher: American Institute of Physics.

[36] O. M. J. van 't Erve, A. T. Hanbicki, M. Holub, C. H. Li, C. Awo-Affouda, *et al.* "Electrical injection and detection of spin-polarized carriers in silicon in a lateral transport geometry". *Applied Physics Letters* **91**, 212109 (2007).

[37] T. Suzuki, T. Sasaki, T. Oikawa, M. Shiraishi, Y. Suzuki, *et al.* "Room-Temperature Electron Spin Transport in a Highly Doped Si Channel". *Applied Physics Express* **4**, 023003 (2011). Publisher: IOP Publishing.

[38] Y. Saito, T. Marukame, T. Inokuchi, M. Ishikawa, H. Sugiyama, *et al.* "Spin injection, transport, and read/write operation in spin-based MOSFET". *Thin Solid Films* **519**, 8266 (2011).

[39] Y. Zhou, W. Han, L.-T. Chang, F. Xiu, M. Wang, *et al.* "Electrical spin injection and transport in germanium". *Physical Review B* **84**, 125323 (2011).

[40] A. Jain, L. Louahadj, J. Peiro, J. C. Le Breton, C. Vergnaud, *et al.* "Electrical spin injection and detection at Al2O3/n-type germanium interface using three terminal geometry". *Applied Physics Letters* **99**, 162102 (2011).

[41] F. Rortais, S. Oyarzún, F. Bottegoni, J.-C. Rojas-Sánchez, P. Laczkowski, *et al.* "Spin transport inp-type germanium". *Journal of Physics: Condensed Matter* **28**, 165801 (2016).

[42] F. Rortais, C. Vergnaud, A. Marty, L. Vila, J.-P. Attané, *et al.* "Non-local electrical spin injection and detection in germanium at room temperature". *Applied Physics Letters* **111**, 182401 (2017).

[43] A. Jain, J.-C. Rojas-Sanchez, M. Cubukcu, J. Peiro, J. C. Le Breton, *et al.* "Crossover from Spin Accumulation into Interface States to Spin Injection in the Germanium Conduction Band". *Physical Review Letters* **109**, 106603 (2012).

[44] S. O. Valenzuela. "Nonlocal electronic spin detection, spin accumulation and the spin hall effect". *International Journal of Modern Physics B* **23**, 2413 (2009). Publisher: World Scientific Publishing Co.

[45] M. Shiraishi, Y. Honda, E. Shikoh, Y. Suzuki, T. Shinjo, *et al.* "Spin transport properties in silicon in a nonlocal geometry". *Physical Review B* **83**, 241204 (2011). Publisher: American Physical Society.

[46] T. Sasaki, Y. Ando, M. Kameno, T. Tahara, H. Koike, *et al.* "Spin Transport in Nondegenerate Si with a Spin MOSFET Structure at Room Temperature". *Physical Review Applied* **2**, 034005 (2014). Publisher: American Physical Society.

[47] J. Fabian, A. Matos-Abiague, C. Ertler, and P. Stano. "SEMICONDUCTOR SPINTRONICS". *Semiconductor Spintronics* page 343.

[48] S. P. Dash, S. Sharma, R. S. Patel, M. P. de Jong, and R. Jansen. "Electrical creation of spin polarization in silicon at room temperature". *Nature* **462**, 491 (2009).

[49] O. Txoperena and F. Casanova. "Spin injection and local magnetoresistance effects in three-terminal devices". *Journal of Physics D: Applied Physics* **49**, 133001 (2016). Publisher: IOP Publishing.

[50] F. Pezzoli, F. Bottegoni, D. Trivedi, F. Ciccacci, A. Giorgioni, *et al.* "Optical Spin Injection and Spin Lifetime in Ge Heterostructures". *Physical Review Letters* **108**, 156603 (2012). Publisher: American Physical Society.

[51] M. Jamet, T. Devillers, I.-S. Yu, A. Barski, P. Bayle-Guillemaud, *et al.* "(Ge,Mn): A ferromagnetic semiconductor for spin injection in silicon". *International Journal of Nanotechnology* (2010). Publisher: Inderscience Publishers.

[52] S. A. Crooker. "Imaging Spin Transport in Lateral Ferromagnet/Semiconductor Structures". *Science* **309**, 2191 (2005).

[53] J. Rioux and J. E. Sipe. "Optical injection and control in germanium: Thirty-band $\mathbf{k}\ensuremath{\cdot}\mathbf{p}$ theory". *Physical Review B* **81**, 155215 (2010). Publisher: American Physical Society.

[54] G. Lampel. "Nuclear Dynamic Polarization by Optical Electronic Saturation and Optical Pumping in Semiconductors". *Physical Review Letters* **20**, 491 (1968). Publisher: American Physical Society.

[55] F. Meier and B. P. Zakharchenya. *Optical orientation.* North-Holland ; Sole distributors for the U.S.A. and Canada, Elsevier Science Pub. Co., Amsterdam; New York; New York (1984). OCLC: 10925249.

[56] A. Ferrari, F. Bottegoni, G. Isella, S. Cecchi, and F. Ciccacci. "Epitaxial Si${}_{1\ensuremath{-}x}$Ge${}_{x}$ alloys studied by spin-polarized photoemission". *Physical Review B* **88**, 115209 (2013). Publisher: American Physical Society.

[57] E. J. Loren, J. Rioux, C. Lange, J. E. Sipe, H. M. van Driel, *et al.* "Hole spin relaxation and intervalley electron scattering in germanium". *Physical Review B* **84**, 214307 (2011). Publisher: American Physical Society.

[58] J. Sinova and I. Žutić. "New moves of the spintronics tango". *Nature Materials* **11**, 368 (2012). Number: 5 Publisher: Nature Publishing Group.

[59] T. Jungwirth, J. Wunderlich, and K. Olejník. "Spin Hall effect devices". *Nature Materials* **11**, 382 (2012). Number: 5 Publisher: Nature Publishing Group.

[60] M. I. Dyakonov and V. I. Perel. "Current-induced spin orientation of electrons in semiconductors". *Physics Letters A* **35**, 459 (1971).

[61] V. M. Edelstein. "Spin polarization of conduction electrons induced by electric current in two-dimensional asymmetric electron systems". *Solid State Communications* **73**, 233 (1990).

[62] I. M. Miron, K. Garello, G. Gaudin, P.-J. Zermatten, M. V. Costache, *et al.* "Perpendicular switching of a single ferromagnetic layer induced by in-plane current injection". *Nature* **476**, 189 (2011). Number: 7359 Publisher: Nature Publishing Group.

[63] L. Liu, C.-F. Pai, Y. Li, H. W. Tseng, D. C. Ralph, *et al.* "Spin-Torque Switching with the Giant Spin Hall Effect of Tantalum". *Science* **336**, 555 (2012). Publisher: American Association for the Advancement of Science Section: Research Article.

[64] I. M. Miron, T. Moore, H. Szambolics, L. D. Buda-Prejbeanu, S. Auffret, *et al.* "Fast current-induced domain-wall motion controlled by the Rashba effect". *Nature Materials* **10**, 419 (2011). Number: 6 Publisher: Nature Publishing Group.

[65] O. Boulle, J. Vogel, H. Yang, S. Pizzini, D. de Souza Chaves, *et al.* "Room-temperature chiral magnetic skyrmions in ultrathin magnetic nanostructures". *Nature Nanotechnology* **11**, 449 (2016). Number: 5 Publisher: Nature Publishing Group.

[66] J. E. Hirsch. "Spin Hall Effect". *Physical Review Letters* **83**, 1834 (1999). Publisher: American Physical Society.

[67] Y. K. Kato, R. C. Myers, A. C. Gossard, and D. D. Awschalom. "Observation of the Spin Hall Effect in Semiconductors". *Science* **306**, 1910 (2004).

[68] S. O. Valenzuela and M. Tinkham. "Direct electronic measurement of the spin Hall effect". *Nature* **442**, 176 (2006).

[69] E. Saitoh, M. Ueda, H. Miyajima, and G. Tatara. "Conversion of spin current into charge current at room temperature: Inverse spin-Hall effect". *Applied Physics Letters* **88**, 182509 (2006).

[70] T. Kimura, Y. Otani, T. Sato, S. Takahashi, and S. Maekawa. "Room-Temperature Reversible Spin Hall Effect". *Physical Review Letters* **98**, 156601 (2007). Publisher: American Physical Society.

[71] Y. Niimi, Y. Kawanishi, D. H. Wei, C. Deranlot, H. X. Yang, *et al.* "Giant Spin Hall Effect Induced by Skew Scattering from Bismuth Impurities inside Thin Film CuBi Alloys". *Physical Review Letters* **109**, 156602 (2012). Publisher: American Physical Society.

[72] N. Nagaosa, J. Sinova, S. Onoda, A. H. MacDonald, and N. P. Ong. "Anomalous Hall effect". *Reviews of Modern Physics* **82**, 1539 (2010).

[73] J. Sinova, S. O. Valenzuela, J. Wunderlich, C. H. Back, and T. Jungwirth. "Spin Hall effects". *Reviews of Modern Physics* **87**, 1213 (2015).

[74] Q. Hao, W. Chen, and G. Xiao. "Beta (β) tungsten thin films: Structure, electron transport, and giant spin Hall effect". *Applied Physics Letters* **106**, 182403 (2015). Publisher: American Institute of Physics.

[75] P. Laczkowski, J.-C. Rojas-Sánchez, W. Savero-Torres, H. Jaffrès, N. Reyren, *et al.* "Experimental evidences of a large extrinsic spin Hall effect in AuW alloy". *Applied Physics Letters* **104**, 142403 (2014). Publisher: American Institute of Physics.

[76] L. Vila, T. Kimura, and Y. Otani. "Evolution of the Spin Hall Effect in Pt Nanowires: Size and Temperature Effects". *Physical Review Letters* **99**, 226604 (2007). Publisher: American Physical Society.

[77] Y. Tserkovnyak, A. Brataas, and G. E. W. Bauer. "Enhanced Gilbert Damping in Thin Ferromagnetic Films". *Physical Review Letters* **88**, 117601 (2002). Publisher: American Physical Society.

[78] S. Oyarzún, A. K. Nandy, F. Rortais, J.-C. Rojas-Sánchez, M.-T. Dau, *et al.* "Evidence for spin-to-charge conversion by Rashba coupling in metallic states at the Fe/Ge(111) interface". *Nature Communications* **7**, 1 (2016).

[79] J. Kim, P. Sheng, S. Takahashi, S. Mitani, and M. Hayashi. "Spin Hall Magnetoresistance in Metallic Bilayers". *Physical Review Letters* **116**, 097201 (2016).

[80] H. Nakayama, M. Althammer, Y.-T. Chen, K. Uchida, Y. Kajiwara, *et al.* "Spin Hall Magnetoresistance Induced by a Nonequilibrium Proximity Effect". *Physical Review Letters* **110**, 206601 (2013). Publisher: American Physical Society.

[81] B. F. Miao, S. Y. Huang, D. Qu, and C. L. Chien. "Physical Origins of the New Magnetoresistance in Pt/YIG". *Physical Review Letters* **112**, 236601 (2014). Publisher: American Physical Society.

[82] Y. M. Lu, J. W. Cai, S. Y. Huang, D. Qu, B. F. Miao, *et al.* "Hybrid magnetoresistance in the proximity of a ferromagnet". *Physical Review B* **87**, 220409 (2013). Publisher: American Physical Society.

[83] Y.-T. Chen, S. Takahashi, H. Nakayama, M. Althammer, S. T. B. Goennenwein, *et al.* "Theory of spin Hall magnetoresistance". *Physical Review B* **87**, 144411 (2013). Publisher: American Physical Society.

[84] M. Althammer, S. Meyer, H. Nakayama, M. Schreier, S. Altmannshofer, *et al.* "Quantitative study of the spin Hall magnetoresistance in ferromagnetic insulator/normal metal hybrids". *Physical Review B* **87**, 224401 (2013). Publisher: American Physical Society.

[85] C. O. Avci, K. Garello, A. Ghosh, M. Gabureac, S. F. Alvarado, *et al.* "Unidirectional spin Hall magnetoresistance in ferromagnet/normal metal bilayers". *Nature Physics* **11**, 570 (2015).

[86] K. Olejník, V. Novák, J. Wunderlich, and T. Jungwirth. "Electrical detection of magnetization reversal without auxiliary magnets". *Physical Review B* **91**, 180402 (2015).

[87] K. Yasuda, A. Tsukazaki, R. Yoshimi, K. S. Takahashi, M. Kawasaki, *et al.* "Large Unidirectional Magnetoresistance in a Magnetic Topological Insulator". *Physical Review Letters* **117**, 127202 (2016).

[88] Y. Lv, J. Kally, D. Zhang, J. S. Lee, M. Jamali, *et al.* "Unidirectional spin Hall magnetoresistance in topological insulator/ferromagnetic layer heterostructures" page 10.

[89] Y. A. Bychkov and E. I. Rashba. "Oscillatory effects and the magnetic susceptibility of carriers in inversion layers". *Journal of Physics C: Solid State Physics* **17**, 6039 (1984). Publisher: IOP Publishing.

[90] S. LaShell, B. A. McDougall, and E. Jensen. "Spin Splitting of an Au(111) Surface State Band Observed with Angle Resolved Photoelectron Spectroscopy". *Physical Review Letters* **77**, 3419 (1996). Publisher: American Physical Society.

[91] C. R. Ast, J. Henk, A. Ernst, L. Moreschini, M. C. Falub, *et al.* "Giant Spin Splitting through Surface Alloying". *Physical Review Letters* **98**, 186807 (2007). Publisher: American Physical Society.

[92] K. v. Klitzing, G. Dorda, and M. Pepper. "New Method for High-Accuracy Determination of the Fine-Structure Constant Based on Quantized Hall Resistance". *Physical Review Letters* **45**, 494 (1980). Publisher: American Physical Society.

[93] K. von Klitzing. "25 Years of Quantum Hall Effect (QHE) A Personal View on the Discovery, Physics and Applications of this Quantum Effect". In B. Douçot, V. Pasquier, B. Duplantier, and V. Rivasseau, editors, "The Quantum Hall Effect", pages 1–21. Birkhäuser Basel, Basel (2005).

[94] S. Oh. "The Complete Quantum Hall Trio". *Science* **340**, 153 (2013). Publisher: American Association for the Advancement of Science Section: Perspective.

[95] M. Fruchart and D. Carpentier. "An introduction to topological insulators". *Comptes Rendus Physique* **14**, 779 (2013).

[96] L. Fu and C. L. Kane. "Topological insulators with inversion symmetry". *Physical Review B* **76**, 045302 (2007). Publisher: American Physical Society.

[97] F. D. M. Haldane. "Model for a Quantum Hall Effect without Landau Levels: Condensed-Matter Realization of the "Parity Anomaly"". *Physical Review Letters* **61**, 2015 (1988). Publisher: American Physical Society.

[98] X.-L. Qi and S.-C. Zhang. "The quantum spin Hall effect and topological insulators". *Physics Today* **63**, 33 (2010). ArXiv: 1001.1602.

[99] X.-L. Qi and S.-C. Zhang. "Topological insulators and superconductors". *Reviews of Modern Physics* **83**, 1057 (2011). Publisher: American Physical Society.

[100] C. L. Kane and E. J. Mele. "Quantum Spin Hall Effect in Graphene". *Physical Review Letters* **95**, 226801 (2005). Publisher: American Physical Society.

[101] M. König, S. Wiedmann, C. Brüne, A. Roth, H. Buhmann, *et al.* "Quantum Spin Hall Insulator State in HgTe Quantum Wells". *Science* **318**, 766 (2007). Publisher: American Association for the Advancement of Science Section: Research Article.

[102] M. Z. Hasan and C. L. Kane. "*Colloquium* : Topological insulators". *Reviews of Modern Physics* **82**, 3045 (2010).

[103] C. L. Kane and E. J. Mele. "$\{Z\}_\{2\}$ Topological Order and the Quantum Spin Hall Effect". *Physical Review Letters* **95**, 146802 (2005). Publisher: American Physical Society.

[104] D. Hsieh, D. Qian, L. Wray, Y. Xia, Y. S. Hor, *et al.* "A topological Dirac insulator in a quantum spin Hall phase". *Nature* **452**, 970 (2008). Number: 7190 Publisher: Nature Publishing Group.

[105] D. Hsieh, Y. Xia, D. Qian, L. Wray, J. H. Dil, *et al.* "A tunable topological insulator in the spin helical Dirac transport regime". *Nature* **460**, 1101 (2009).

[106] M. Neupane, A. Richardella, J. Sánchez-Barriga, S. Xu, N. Alidoust, *et al.* "Observation of quantum-tunnelling-modulated spin texture in ultrathin topological insulator Bi_2Se_3 films". *Nature Communications* **5**, 1 (2014).

[107] H. Wang, H. Liu, C.-Z. Chang, H. Zuo, Y. Zhao, *et al.* "Crossover between Weak Antilocalization and Weak Localization of Bulk States in Ultrathin Bi_2Se_3 Films". *Scientific Reports* **4**, 1 (2014).

[108] B. Irfan, B. P. Joshi, A. Thamizhavel, M. M. Deshmukh, and R. Chatterjee. "Gate tuned weak antilocalization effect in calcium doped Bi_2Se_3 topological insulators". *Solid State Communications* **220**, 45 (2015).

[109] Y. S. Kim, M. Brahlek, N. Bansal, E. Edrey, G. A. Kapilevich, *et al.* "Thickness-dependent bulk properties and weak antilocalization effect in topological insulator Bi_2Se_3". *Physical Review B* **84**, 073109 (2011).

[110] M. Brahlek, N. Koirala, M. Salehi, N. Bansal, and S. Oh. "Emergence of Decoupled Surface Transport Channels in Bulk Insulating Bi_2Se_3 Thin Films". *Physical Review Letters* **113**, 026801 (2014).

[111] J. Besbas, K. Banerjee, J. Son, Y. Wang, Y. Wu, *et al.* "Helicity-Dependent Photovoltaic Effect in Bi2Se3 Under Normal Incident Light". *Advanced Optical Materials* **4**, 1642 (2016). _eprint: https://onlinelibrary.wiley.com/doi/pdf/10.1002/adom.201600301.

[112] J. Yu, X. Zeng, L. Zhang, K. He, S. Cheng, *et al.* "Photoinduced Inverse Spin Hall Effect of Surface States in the Topological Insulator Bi_2Se_3". *Nano Letters* **17**, 7878 (2017).

[113] B. Yan, D. Zhang, and C. Felser. "Topological surface states of Bi2Se3 coexisting with Se vacancies". *physica status solidi (RRL) – Rapid Research Letters* **7**, 148 (2013). _eprint: https://onlinelibrary.wiley.com/doi/pdf/10.1002/pssr.201206415.

[114] S. Zhang and A. Fert. "Conversion between spin and charge currents with topological insulators". *Physical Review B* **94**, 184423 (2016). Publisher: American Physical Society.

[115] K. Shen, G. Vignale, and R. Raimondi. "Microscopic Theory of the Inverse Edelstein Effect". *Physical Review Letters* **112**, 096601 (2014). Publisher: American Physical Society.

[116] H. Geng, W. Luo, W. Y. Deng, L. Sheng, R. Shen, *et al.* "Theory of Inverse Edelstein Effect of The Surface States of A Topological Insulator". *Scientific Reports* **7**, 1 (2017). Number: 1 Publisher: Nature Publishing Group.

[117] M. Jamali, J. S. Lee, J. S. Jeong, F. Mahfouzi, Y. Lv, *et al.* "Giant Spin Pumping and Inverse Spin Hall Effect in the Presence of Surface and Bulk Spin-Orbit Coupling of Topological Insulator Bi $_2$ Se $_3$". *Nano Letters* **15**, 7126 (2015).

[118] S. Shi, A. Wang, Y. Wang, R. Ramaswamy, L. Shen, *et al.* "Efficient charge-spin conversion and magnetization switching through the Rashba effect at topological-insulator/Ag interfaces". *Physical Review B* **97**, 041115 (2018).

[119] H. Wang, J. Kally, J. S. Lee, T. Liu, H. Chang, *et al.* "Surface-State-Dominated Spin-Charge Current Conversion in Topological-Insulator–Ferromagnetic-Insulator Heterostructures". *Physical Review Letters* **117**, 076601 (2016).

[120] J.-C. Rojas-Sánchez, N. Reyren, P. Laczkowski, W. Savero, J.-P. Attané, *et al.* "Spin Pumping and Inverse Spin Hall Effect in Platinum: The Essential Role of Spin-Memory Loss at Metallic Interfaces". *Physical Review Letters* **112**, 106602 (2014). Publisher: American Physical Society.

[121] J. Zhang, C.-Z. Chang, Z. Zhang, J. Wen, X. Feng, *et al.* "Band structure engineering in (Bi 1-x Sb x) 2 Te 3 ternary topological insulators". *Nature Communications* **2**, 574 (2011). Number: 1 Publisher: Nature Publishing Group.

[122] H. Wang, J. Kally, C. Şahin, T. Liu, W. Yanez, *et al.* "Fermi level dependent spin pumping from a magnetic insulator into a topological insulator". *Physical Review Research* **1**, 012014 (2019). Publisher: American Physical Society.

[123] C. D. Spataru and F. Léonard. "Fermi-level pinning, charge transfer, and relaxation of spin-momentum locking at metal contacts to topological insulators". *Physical Review B* **90**, 085115 (2014).

[124] J. Zhang, J. P. Velev, X. Dang, and E. Y. Tsymbal. "Band structure and spin texture of ${\mathrm{Bi}}_{2}{\mathrm{Se}}_{3} 3d$ ferromagnetic metal interface". *Physical Review B* **94**, 014435 (2016). Publisher: American Physical Society.

[125] J.-C. Rojas-Sánchez, S. Oyarzún, Y. Fu, A. Marty, C. Vergnaud, *et al.* "Spin to Charge Conversion at Room Temperature by Spin Pumping into a New Type of Topological Insulator: $\ensuremath{\alpha}$-Sn Films". *Physical Review Letters* **116**, 096602 (2016).

[126] P. Noel, C. Thomas, Y. Fu, L. Vila, B. Haas, *et al.* "Highly Efficient Spin-to-Charge Current Conversion in Strained HgTe Surface States Protected by a HgCdTe Layer". *Physical Review Letters* **120**, 167201 (2018).

[127] J. C. R. Sánchez, L. Vila, G. Desfonds, S. Gambarelli, J. P. Attané, *et al.* "Spin-to-charge conversion using Rashba coupling at the interface between non-magnetic materials". *Nature Communications* **4**, 1 (2013). Number: 1 Publisher: Nature Publishing Group.

[128] P. Noël, F. Trier, L. M. Vicente Arche, J. Bréhin, D. C. Vaz, *et al.* "Non-volatile electric control of spin–charge conversion in a SrTiO 3 Rashba system". *Nature* **580**, 483 (2020). Number: 7804 Publisher: Nature Publishing Group.

[129] E. Gatti, F. Isa, D. Chrastina, E. Müller Gubler, F. Pezzoli, *et al.* "Ge/SiGe quantum wells on Si(111): Growth, structural, and optical properties". *Journal of Applied Physics* **116**, 043518 (2014).

[130] Y. Tsema, G. Kichin, O. Hellwig, V. Mehta, A. V. Kimel, *et al.* "Helicity and field dependent magnetization dynamics of ferromagnetic Co/Pt multilayers". *Applied Physics Letters* **109**, 072405 (2016).

[131] S. Mangin, M. Gottwald, C.-H. Lambert, D. Steil, V. Uhlíř, *et al.* "Engineered materials for all-optical helicity-dependent magnetic switching". *Nature Materials* **13**, 286 (2014).

[132] A. Soumyanarayanan, N. Reyren, A. Fert, and C. Panagopoulos. "Emergent phenomena induced by spin–orbit coupling at surfaces and interfaces". *Nature* **539**, 509 (2016). Number: 7630 Publisher: Nature Publishing Group.

[133] H. Zhang, C.-X. Liu, X.-L. Qi, X. Dai, Z. Fang, *et al.* "Topological insulators in Bi_2Se_3 , Bi_2Te_3 and Sb_2Te_3 with a single Dirac cone on the surface". *Nature Physics* **5**, 438 (2009).

[134] A. R. Mellnik, J. S. Lee, A. Richardella, J. L. Grab, P. J. Mintun, *et al.* "Spin-transfer torque generated by a topological insulator". *Nature* **511**, 449 (2014).

[135] J. Han, A. Richardella, S. A. Siddiqui, J. Finley, N. Samarth, *et al.* "Room-Temperature Spin-Orbit Torque Switching Induced by a Topological Insulator". *Physical Review Letters* **119**, 077702 (2017). Publisher: American Physical Society.

[136] Y. Fan, P. Upadhyaya, X. Kou, M. Lang, S. Takei, *et al.* "Magnetization switching through giant spin–orbit torque in a magnetically doped topological insulator heterostructure". *Nature Materials* **13**, 699 (2014).

[137] Y. Fan, X. Kou, P. Upadhyaya, Q. Shao, L. Pan, *et al.* "Electric-field control of spin–orbit torque in a magnetically doped topological insulator". *Nature Nanotechnology* **11**, 352 (2016). Number: 4 Publisher: Nature Publishing Group.

[138] M. Dc, M. Jamali, J.-Y. Chen, D. R. Hickey, D. Zhang, *et al.* "Room-temperature perpendicular magnetization switching through giant spin-orbit torque from sputtered BixSe(1-x) topological insulator material" page 14.

[139] F. Bottegoni, A. Ferrari, S. Cecchi, M. Finazzi, F. Ciccacci, *et al.* "Photoinduced inverse spin Hall effect in Pt/Ge(001) at room temperature". *Applied Physics Letters* **102**, 152411 (2013). Publisher: American Institute of Physics.

[140] F. Bottegoni, G. Isella, S. Cecchi, and F. Ciccacci. "Spin polarized photoemission from strained Ge epilayers". *Applied Physics Letters* **98**, 242107 (2011). Publisher: American Institute of Physics.

[141] J.-C. Rojas-Sánchez, M. Cubukcu, A. Jain, C. Vergnaud, C. Portemont, *et al.* "Spin pumping and inverse spin Hall effect in germanium". *Physical Review B* **88**, 064403 (2013).

[142] S. Kim, S. Lee, J. Woo, and G. Lee. "Growth of Bi_2Se_3 topological insulator thin film on Ge(111) substrate". *Applied Surface Science* **432**, 152 (2018).

[143] A. A. Taskin, S. Sasaki, K. Segawa, and Y. Ando. "Manifestation of Topological Protection in Transport Properties of Epitaxial Bi_2Se_3 Thin Films". *Physical Review Letters* **109**, 066803 (2012).

[144] N. Bansal, Y. S. Kim, M. Brahlek, E. Edrey, and S. Oh. "Thickness-Independent Transport Channels in Topological Insulator Bi_2Se_3 Thin Films". *Physical Review Letters* **109**, 116804 (2012).

[145] S. Nakajima. "The crystal structure of $Bi_2Te_{3-x}Se_x$". *Journal of Physics and Chemistry of Solids* **24**, 479 (1963).

[146] D. Kriegner, P. Harcuba, J. Veselý, A. Lesnik, G. Bauer, *et al.* "Twin domain imaging in topological insulator Bi_2Te_3 and Bi_2Se_3 epitaxial thin films by scanning X-ray nanobeam microscopy and electron backscatter diffraction". *Journal of Applied Crystallography* **50**, 369 (2017).

[147] F. Bonell, M. G. Cuxart, K. Song, R. Robles, P. Ordejón, *et al.* "Growth of Twin-Free and Low-Doped Topological Insulators on BaF_2 (111)". *Crystal Growth & Design* **17**, 4655 (2017).

[148] G. Renaud, A. Barbier, and O. Robach. "Growth, structure, and morphology of the Pd/MgO(001) interface: Epitaxial site and interfacial distance". *Physical Review B* **60**, 5872 (1999).

[149] T. Guillet, A. Marty, C. Beigné, C. Vergnaud, M.-T. Dau, *et al.* "Magnetotransport in Bi_2Se_3 thin films epitaxially grown on Ge(111)". *AIP Advances* **8**, 115125 (2018).

[150] S. Hikami, A. I. Larkin, and Y. Nagaoka. "Spin-Orbit Interaction and Magnetoresistance in the Two Dimensional Random System". *Progress of Theoretical Physics* **63**, 707 (1980).

[151] H.-Z. Lu and S.-Q. Shen. "Weak localization of bulk channels in topological insulator thin films". *Physical Review B* **84**, 125138 (2011).

[152] T. Chen, Q. Chen, K. Schouteden, W. Huang, X. Wang, *et al.* "Topological transport and atomic tunnelling–clustering dynamics for aged Cu-doped Bi_2Te_3 crystals". *Nature Communications* **5**, 1 (2014).

[153] J. Chen, H. J. Qin, F. Yang, J. Liu, T. Guan, *et al.* "Gate-Voltage Control of Chemical Potential and Weak Antilocalization in Bi_2Se_3". *Physical Review Letters* **105**, 176602 (2010).

[154] J. Chen, X. Y. He, K. H. Wu, Z. Q. Ji, L. Lu, *et al.* "Tunable surface conductivity in Bi_2Se_3 revealed in diffusive electron transport". *Physical Review B* **83**, 241304 (2011).

[155] W. J. Wang, K. H. Gao, and Z. Q. Li. "Thickness-dependent transport channels in topological insulator Bi_2Se_3 thin films grown by magnetron sputtering". *Scientific Reports* **6**, 1 (2016).

[156] D. Kim, P. Syers, N. P. Butch, J. Paglione, and M. S. Fuhrer. "Coherent topological transport on the surface of Bi_2Se_3". *Nature Communications* **4**, 1 (2013).

[157] M. Liu, C.-Z. Chang, Z. Zhang, Y. Zhang, W. Ruan, *et al.* "Electron interaction-driven insulating ground state in Bi_2Se_3 topological insulators in the two-dimensional limit". *Physical Review B* **83**, 165440 (2011).

[158] H. Steinberg, J.-B. Laloë, V. Fatemi, J. S. Moodera, and P. Jarillo-Herrero. "Electrically tunable surface-to-bulk coherent coupling in topological insulator thin films". *Physical Review B* **84**, 233101 (2011).

[159] R. V. Aldridge, K. Davis, and M. Holloway. "An investigation of the effect of a magnetic field on the forward characteristics of some silicon diodes at low temperatures". *Journal of Physics D: Applied Physics* **8**, 64 (1975).

[160] C. Wan, X. Zhang, X. Gao, J. Wang, and X. Tan. "Geometrical enhancement of low-field magnetoresistance in silicon". *Nature* **477**, 304 (2011).

[161] M. Liu, J. Zhang, C.-Z. Chang, Z. Zhang, X. Feng, *et al.* "Crossover between Weak Antilocalization and Weak Localization in a Magnetically Doped Topological Insulator". *Physical Review Letters* **108**, 036805 (2012).

[162] M. Lang, L. He, X. Kou, P. Upadhyaya, Y. Fan, *et al.* "Competing Weak Localization and Weak Antilocalization in Ultrathin Topological Insulators". *Nano Letters* **13**, 48 (2013).

[163] L. A. Walsh, C. M. Smyth, A. T. Barton, Q. Wang, Z. Che, *et al.* "Interface Chemistry of Contact Metals and Ferromagnets on the Topological Insulator Bi_2Se_3". *The Journal of Physical Chemistry C* **121**, 23551 (2017).

[164] T. Guillet, C. Zucchetti, A. Marchionni, A. Hallal, P. Biagioni, *et al.* "Spin orbitronics at a topological insulator-semiconductor interface". *Physical Review B* **101**, 184406 (2020). Publisher: American Physical Society.

[165] F. Bottegoni, M. Celebrano, M. Bollani, P. Biagioni, G. Isella, *et al.* "Spin voltage generation through optical excitation of complementary spin populations". *Nature Materials* **13**, 790 (2014).

[166] C. Lumerical Inc. "FDTD Solutions 2018b" .

[167] E. D. Palik. *Handbook of Optical Constants of Solids: Volume 2*. Academic Press (1991). Google-Books-ID: d4_kRYYS0H8C.

[168] C. Zucchetti, F. Bottegoni, C. Vergnaud, F. Ciccacci, G. Isella, *et al.* "Imaging spin diffusion in germanium at room temperature". *Physical Review B* **96**, 014403 (2017).

[169] C. H. Li, O. M. J. van 't Erve, J. T. Robinson, Y. Liu, L. Li, *et al.* "Electrical detection of charge-current-induced spin polarization due to spin-momentum locking in Bi_2Se_3". *Nature Nanotechnology* **9**, 218 (2014).

[170] J. S. Lee, A. Richardella, D. R. Hickey, K. A. Mkhoyan, and N. Samarth. "Mapping the chemical potential dependence of current-induced spin polarization in a topological insulator". *Physical Review B* **92**, 155312 (2015).

[171] C. Zucchetti, M. Bollani, G. Isella, M. Zani, M. Finazzi, *et al.* "Doping dependence of the electron spin diffusion length in germanium". *APL Materials* **7**, 101122 (2019).

[172] A. Dimoulas, P. Tsipas, A. Sotiropoulos, and E. K. Evangelou. "Fermi-level pinning and charge neutrality level in germanium". *Applied Physics Letters* **89**, 252110 (2006).

[173] S. Birner, T. Zibold, T. Andlauer, T. Kubis, M. Sabathil, *et al.* "nextnano: General Purpose 3-D Simulations". *IEEE Transactions on Electron Devices* **54**, 2137 (2007).

[174] E. Sagasta, Y. Omori, M. Isasa, M. Gradhand, L. E. Hueso, *et al.* "Tuning the spin Hall effect of Pt from the moderately dirty to the superclean regime". *Physical Review B* **94**, 060412 (2016).

[175] Y. Huo, F. L. Zeng, C. Zhou, and Y. Z. Wu. "Spin pumping and the inverse spin hall effect in single crystalline Fe/Pt heterostructure". *AIP Advances* **7**, 056024 (2017).

[176] P. Deorani, J. Son, K. Banerjee, N. Koirala, M. Brahlek, *et al.* "Observation of inverse spin Hall effect in bismuth selenide". *Physical Review B* **90**, 094403 (2014).

[177] Y. Liu, J. Besbas, Y. Wang, P. He, M. Chen, *et al.* "Direct visualization of current-induced spin accumulation in topological insulators". *Nature Communications* **9**, 2492 (2018).

[178] M. I. Dyakonov and V. I. Perel. "Current-induced spin orientation of electrons in semiconductors". *Physics Letters A* **35**, 459 (1971).

[179] W. Thomson. *On the Electro-Dynamic Qualities of Metals:–Effects of Magnetization on the Electric Conductivity of Nickel and of Iron*. Royal Society of London (1856).

[180] E. H. Hall. "On a New Action of the Magnet on Electric Currents". *American Journal of Mathematics* **2**, 287 (1879). Publisher: Johns Hopkins University Press.

[181] I. A. Campbell, A. Fert, and O. Jaoul. "The spontaneous resistivity anisotropy in Ni-based alloys". *Journal of Physics C: Solid State Physics* **3**, S95 (1970). Publisher: IOP Publishing.

[182] T. McGuire and R. Potter. "Anisotropic magnetoresistance in ferromagnetic 3d alloys". *IEEE Transactions on Magnetics* **11**, 1018 (1975). Conference Name: IEEE Transactions on Magnetics.

[183] G. Binasch, P. Grünberg, F. Saurenbach, and W. Zinn. "Enhanced magnetoresistance in layered magnetic structures with antiferromagnetic interlayer exchange". *Physical Review B* **39**, 4828 (1989).

[184] P. He, S. S.-L. Zhang, D. Zhu, Y. Liu, Y. Wang, *et al.* "Bilinear magnetoelectric resistance as a probe of three-dimensional spin texture in topological surface states". *Nature Physics* **14**, 495 (2018).

[185] P. He, S. M. Walker, S. S.-L. Zhang, F. Y. Bruno, M. S. Bahramy, *et al.* "Observation of Out-of-Plane Spin Texture in a ${\mathrm{SrTiO}}_{3}(111)$ Two-Dimensional Electron Gas". *Physical Review Letters* **120**, 266802 (2018).

[186] S. S.-L. Zhang and G. Vignale. "Theory of bilinear magneto-electric resistance from topological-insulator surface states". *Spintronics XI* page 40 (2018). ArXiv: 1808.06339.

[187] Y. Ohtsubo, S. Hatta, K. Yaji, H. Okuyama, K. Miyamoto, *et al.* "Spin-polarized semiconductor surface states localized in subsurface layers". *Physical Review B* **82**, 201307 (2010).

[188] Y. Ohtsubo, K. Yaji, S. Hatta, H. Okuyama, and T. Aruga. "Two-dimensional states localized in subsurface layers of Ge(111)". *Physical Review B* **88**, 245310 (2013).

[189] T. Aruga. "Different types of Rashba spin-split surface states on Ge(111)". *Journal of Electron Spectroscopy and Related Phenomena* **201**, 74 (2015).

[190] K. Yaji, Y. Ohtsubo, S. Hatta, H. Okuyama, R. Yukawa, *et al.* "Experimental evidence for two-dimensional states localized in subsurface region of Ge(111)". *Journal of Electron Spectroscopy and Related Phenomena* **201**, 92 (2015).

[191] T. Guillet, C. Zucchetti, Q. Barbedienne, A. Marty, G. Isella, *et al.* "Observation of Large Unidirectional Rashba Magnetoresistance in Ge(111)". *Physical Review Letters* **124**, 027201 (2020).

[192] W. Y. Choi, H.-j. Kim, J. Chang, G. Go, K.-J. Lee, *et al.* "Spin-polarization-induced anisotropic magnetoresistance in a two-dimensional Rashba system". *Current Applied Physics* **17**, 513 (2017).

[193] S. Sangiao, L. Morellon, G. Simon, J. M. De Teresa, J. A. Pardo, *et al.* "Anomalous Hall effect in Fe (001) epitaxial thin films over a wide range in conductivity". *Physical Review B* **79**, 014431 (2009). Publisher: American Physical Society.

[194] A. A. Taskin, H. F. Legg, F. Yang, S. Sasaki, Y. Kanai, *et al.* "Planar Hall effect from the surface of topological insulators". *Nature Communications* **8**, 1 (2017).

[195] N. Roschewsky, E. S. Walker, P. Gowtham, S. Muschinske, F. Hellman, *et al.* "Spin-orbit torque and Nernst effect in Bi-Sb/Co heterostructures". *Physical Review B* **99**, 195103 (2019).

[196] S.-H. Zheng, H.-J. Duan, J.-K. Wang, J.-Y. Li, M.-X. Deng, *et al.* "Origin of planar Hall effect on the surface of topological insulators: Tilt of Dirac cone by an in-plane magnetic field". *Physical Review B* **101**, 041408 (2020). Publisher: American Physical Society.

[197] J. Henk, M. Hoesch, J. Osterwalder, A. Ernst, and P. Bruno. "Spin–orbit coupling in the L-gap surface states of Au(111): spin-resolved photoemission experiments and first-principles calculations". *Journal of Physics: Condensed Matter* **16**, 7581 (2004). Publisher: IOP Publishing.

[198] T. Nakagawa, O. Ohgami, Y. Saito, H. Okuyama, M. Nishijima, *et al.* "Transition between tetramer and monomer phases driven by vacancy configuration entropy on $\mathrm{Bi}/\mathrm{Ag}(001)$". *Physical Review B* **75**, 155409 (2007). Publisher: American Physical Society.

[199] T. Liu, Y. Li, L. Gu, J. Ding, H. Chang, *et al.* "Nontrivial Nature and Penetration Depth of Topological Surface States in ${\mathrm{SmB}}_{6}$ Thin Films". *Physical Review Letters* **120**, 207206 (2018).

[200] S. Cai, J. Guo, V. A. Sidorov, Y. Zhou, H. Wang, *et al.* "Independence of topological surface state and bulk conductance in three-dimensional topological insulators". *npj Quantum Materials* **3**, 1 (2018).

[201] W. Y. Choi, J. Chang, H.-j. Kim, K.-J. Lee, and H. C. Koo. "Fermi surface distortion induced by interaction between Rashba and Zeeman effects". *Journal of Applied Physics* **117**, 17C111 (2015).

[202] Q. Barbedienne. "Etude d'états de surface topologiques en vue de leur intégration dans des dispositifs d'électronique de spin" page 174.

[203] C. Jeon, C. C. Hwang, T.-H. Kang, K.-J. Kim, B. Kim, *et al.* "Evidence from ARPES that the Ge(001) surface is semiconducting at room temperature". *Physical Review B* **74**, 125407 (2006).

[204] T. Ideue, K. Hamamoto, S. Koshikawa, M. Ezawa, S. Shimizu, *et al.* "Bulk rectification effect in a polar semiconductor". *Nature Physics* **13**, 578 (2017).

[205] "Physical properties of Germanium (Ge)".

[206] C. Zucchetti, M.-T. Dau, F. Bottegoni, C. Vergnaud, T. Guillet, *et al.* "Tuning spin-charge interconversion with quantum confinement in ultrathin bismuth films". *Physical Review B* **98**, 184418 (2018). Publisher: American Physical Society.

[207] C. Liu, Y. Park, and S. D. Bader. "Resistance minimum in ultrathin ferromagnetic films of Fe on MgO(100)". *Journal of Magnetism and Magnetic Materials* **111**, L225 (1992).

[208] F. Lacy. "Developing a theoretical relationship between electrical resistivity, temperature, and film thickness for conductors". *Nanoscale Research Letters* **6**, 636 (2011).

[209] J. Nogués and I. K. Schuller. "Exchange bias". *Journal of Magnetism and Magnetic Materials* **192**, 203 (1999).

[210] P. F. Carcia, A. D. Meinhaldt, and A. Suna. "Perpendicular magnetic anisotropy in Pd/Co thin film layered structures". *Applied Physics Letters* **47**, 178 (1985). Publisher: American Institute of Physics.

[211] G. H. O. Daalderop, P. J. Kelly, and F. J. A. den Broeder. "Prediction and confirmation of perpendicular magnetic anisotropy in Co/Ni multilayers". *Physical Review Letters* **68**, 682 (1992). Publisher: American Physical Society.

[212] M. T. Johnson, J. J. de Vries, N. W. E. McGee, J. aan de Stegge, and F. J. A. den Broeder. "Orientational dependence of the interface magnetic anisotropy in epitaxial Ni/Co/Ni sandwiches". *Physical Review Letters* **69**, 3575 (1992). Publisher: American Physical Society.

[213] S. Parkin and S.-H. Yang. "Memory on the racetrack". *Nature Nanotechnology* **10**, 195 (2015). Number: 3 Publisher: Nature Publishing Group.

[214] A. D. Kent and D. C. Worledge. "A new spin on magnetic memories". *Nature Nanotechnology* **10**, 187 (2015). Number: 3 Publisher: Nature Publishing Group.

[215] R. Sbiaa, H. Meng, and S. N. Piramanayagam. "Materials with perpendicular magnetic anisotropy for magnetic random access memory". *physica status solidi (RRL) – Rapid Research Letters* **5**, 413 (2011). _eprint: https://onlinelibrary.wiley.com/doi/pdf/10.1002/pssr.201105420.

[216] B. Dieny and M. Chshiev. "Perpendicular magnetic anisotropy at transition metal/oxide interfaces and applications". *Reviews of Modern Physics* **89**, 025008 (2017). Publisher: American Physical Society.

[217] S. Monso, B. Rodmacq, S. Auffret, G. Casali, F. Fettar, *et al.* "Crossover from in-plane to perpendicular anisotropy in Pt/CoFe/AlOx sandwiches as a function of Al oxidation: A very accurate control of the oxidation of tunnel barriers". *Applied Physics Letters* **80**, 4157 (2002). Publisher: American Institute of Physics.

[218] S. Peng, M. Wang, H. Yang, L. Zeng, J. Nan, *et al.* "Origin of interfacial perpendicular magnetic anisotropy in MgO/CoFe/metallic capping layer structures". *Scientific Reports* **5**, 18173 (2015).

[219] H. Nemoto and Y. Hosoe. "Analysis of interfacial magnetic anisotropy in Co/Pt and Co/Pd multilayer films". *Journal of Applied Physics* **97**, 10J109 (2005). Publisher: American Institute of Physics.

[220] M. Ota, M. Itou, Y. Sakurai, A. Koizumi, and H. Sakurai. "Perpendicular magnetic anisotropy in Co/Pt multilayers studied from a view point of anisotropy of magnetic Compton profiles". *Applied Physics Letters* **96**, 152505 (2010). Publisher: American Institute of Physics.

[221] K. Yakushiji, T. Saruya, H. Kubota, A. Fukushima, T. Nagahama, *et al.* "Ultrathin Co/Pt and Co/Pd superlattice films for MgO-based perpendicular magnetic tunnel junctions". *Applied Physics Letters* **97**, 232508 (2010). Publisher: American Institute of Physics.

[222] L. Grenet, C. Arm, P. Warin, S. Pouget, A. Marty, *et al.* "Origin of perpendicular anisotropy in thin Co/Pt bilayers grown on alumina". *arXiv:1110.2628 [cond-mat]* (2011). ArXiv: 1110.2628.

[223] A. D. Kent, B. Özyilmaz, and E. del Barco. "Spin-transfer-induced precessional magnetization reversal". *Applied Physics Letters* **84**, 3897 (2004). Publisher: American Institute of Physics.

[224] K. J. Lee, O. Redon, and B. Dieny. "Analytical investigation of spin-transfer dynamics using a perpendicular-to-plane polarizer". *Applied Physics Letters* **86**, 022505 (2005). Publisher: American Institute of Physics.

[225] C. Papusoi, B. Delaët, B. Rodmacq, D. Houssameddine, J.-P. Michel, *et al.* "100 ps precessional spin-transfer switching of a planar magnetic random access memory cell with perpendicular spin polarizer". *Applied Physics Letters* **95**, 072506 (2009). Publisher: American Institute of Physics.

[226] M. Gottwald. "New model systems with perpendicular magnetic anisotropy for spin transfer torque experiments" page 177.

[227] S. Mangin, D. Ravelosona, J. A. Katine, M. J. Carey, B. D. Terris, *et al.* "Current-induced magnetization reversal in nanopillars with perpendicular anisotropy". *Nature Materials* **5**, 210 (2006). Number: 3 Publisher: Nature Publishing Group.

[228] R. Sbiaa, S. Y. H. Lua, R. Law, H. Meng, R. Lye, *et al.* "Reduction of switching current by spin transfer torque effect in perpendicular anisotropy magnetoresistive devices (invited)". *Journal of Applied Physics* **109**, 07C707 (2011). Publisher: American Institute of Physics.

[229] I. Mihai Miron, G. Gaudin, S. Auffret, B. Rodmacq, A. Schuhl, *et al.* "Current-driven spin torque induced by the Rashba effect in a ferromagnetic metal layer". *Nature Materials* **9**, 230 (2010). Number: 3 Publisher: Nature Publishing Group.

[230] P. Gambardella and I. M. Miron. "Current-induced spin–orbit torques". *Philosophical Transactions of the Royal Society A: Mathematical, Physical and Engineering Sciences* **369**, 3175 (2011).

[231] K.-F. Huang, D.-S. Wang, H.-H. Lin, and C.-H. Lai. "Engineering spin-orbit torque in Co/Pt multilayers with perpendicular magnetic anisotropy". *Applied Physics Letters* **107**, 232407 (2015). Publisher: American Institute of Physics.

[232] J.-C. Rojas-Sánchez, P. Laczkowski, J. Sampaio, S. Collin, K. Bouzehouane, *et al.* "Perpendicular magnetization reversal in Pt/[Co/Ni]3/Al multilayers via the spin Hall effect of Pt". *Applied Physics Letters* **108**, 082406 (2016). Publisher: American Institute of Physics.

[233] B. Jinnai, H. Sato, S. Fukami, and H. Ohno. "Scalability and wide temperature range operation of spin-orbit torque switching devices using Co/Pt multilayer nanowires". *Applied Physics Letters* **113**, 212403 (2018). Publisher: AIP Publishing LLC.

[234] G. P. Zhang and W. Hübner. "Laser-Induced Ultrafast Demagnetization in Ferromagnetic Metals". *Physical Review Letters* **85**, 3025 (2000). Publisher: American Physical Society.

[235] M. Cinchetti, M. Sánchez Albaneda, D. Hoffmann, T. Roth, J.-P. Wüstenberg, *et al.* "Spin-Flip Processes and Ultrafast Magnetization Dynamics in Co: Unifying the Microscopic and Macroscopic View of Femtosecond Magnetism". *Physical Review Letters* **97**, 177201 (2006). Publisher: American Physical Society.

[236] B. Koopmans, G. Malinowski, F. Dalla Longa, D. Steiauf, M. Fähnle, *et al.* "Explaining the paradoxical diversity of ultrafast laser-induced demagnetization". *Nature Materials* **9**, 259 (2010). Number: 3 Publisher: Nature Publishing Group.

[237] J.-H. Shim, A. Ali Syed, C.-H. Kim, K. M. Lee, S.-Y. Park, *et al.* "Ultrafast giant magnetic cooling effect in ferromagnetic Co/Pt multilayers". *Nature Communications* **8**, 1 (2017). Number: 1 Publisher: Nature Publishing Group.

[238] J. Walowski and M. Münzenberg. "Perspective: Ultrafast magnetism and THz spintronics". *Journal of Applied Physics* **120**, 140901 (2016). Publisher: American Institute of Physics.

[239] J. Gorchon, C.-H. Lambert, Y. Yang, A. Pattabi, R. B. Wilson, *et al.* "Single shot ultrafast all optical magnetization switching of ferromagnetic Co/Pt multilayers". *Applied Physics Letters* **111**, 042401 (2017).

[240] G. Kichin, M. Hehn, J. Gorchon, G. Malinowski, J. Hohlfeld, *et al.* "From Multiple- to Single-Pulse All-Optical Helicity-Dependent Switching in Ferromagnetic Co/Pt Multilayers". *Physical Review Applied* **12**, 024019 (2019). Publisher: American Physical Society.

[241] S. Bandiera, R. C. Sousa, B. Rodmacq, and B. Dieny. "Enhancement of perpendicular magnetic anisotropy through reduction of Co-Pt interdiffusion in (Co/Pt) multilayers". *Applied Physics Letters* **100**, 142410 (2012). Publisher: American Institute of Physics.

[242] B. D. Hermsmeier, R. F. C. Farrow, C. H. Lee, E. E. Marinero, C. J. Lin, *et al.* "Magnetic anisotropy and structural characterization of Co/Pt superlattices grown along selected orientations by molecular-beam epitaxy". *Journal of Applied Physics* **69**, 5646 (1991). Publisher: American Institute of Physics.

[243] C. H. Lee, R. F. C. Farrow, C. J. Lin, E. E. Marinero, and C. J. Chien. "Molecular-beam-epitaxial growth and magnetic properties of Co-Pt superlattices oriented along the [001], [110], and [111] axes of Pt". *Physical Review B* **42**, 11384 (1990). Publisher: American Physical Society.

[244] Y. Nie, X. Yang, P. Zhang, and H. Sang. "Magnetization and coercivity in Co/Pt multilayers with constant total Co layer thickness". *Transactions of Nonferrous Metals Society of China* **20**, 819 (2010).

[245] S. Egelkamp and L. Reimer. "Imaging of magnetic domains by the Kerr effect using a scanning optical microscope". *Measurement Science and Technology* **1**, 79 (1990). Publisher: IOP Publishing.

[246] R. A. Fry, L. H. Bennett, and E. Della Torre. "Kerr imaging of a Co/Pt bimodal magneto-optical medium". *Journal of Applied Physics* **85**, 5169 (1999). Publisher: American Institute of Physics.

[247] F. Romanens, S. Pizzini, F. Yokaichiya, M. Bonfim, Y. Pennec, *et al.* "Magnetic relaxation of exchange biased Pt/Co multilayers studied by time-resolved Kerr microscopy". *Physical Review B* **72**, 134410 (2005). Publisher: American Physical Society.

[248] P. J. Stephens. "Theory of Magnetic Circular Dichroism". *The Journal of Chemical Physics* **52**, 3489 (1970). Publisher: American Institute of Physics.

[249] B. T. Thole, P. Carra, F. Sette, and G. van der Laan. "X-ray circular dichroism as a probe of orbital magnetization". *Physical Review Letters* **68**, 1943 (1992). Publisher: American Physical Society.

[250] P. Schattschneider, S. Rubino, C. Hébert, J. Rusz, J. Kuneš, *et al.* "Detection of magnetic circular dichroism using a transmission electron microscope". *Nature* **441**, 486 (2006). Number: 7092 Publisher: Nature Publishing Group.

[251] W. C. Law, T. L. Jin, X. T. Zhu, R. R. Nistala, N. Thiyagarajah, *et al.* "Perpendicular magnetic anisotropy in Co/Pt multilayers induced by hcp-Ho at 400 C". *Journal of Magnetism and Magnetic Materials* **477**, 124 (2019).

[252] Z. Fei, B. Huang, P. Malinowski, W. Wang, T. Song, *et al.* "Two-dimensional itinerant ferromagnetism in atomically thin Fe 3 GeTe 2". *Nature Materials* **17**, 778 (2018). Number: 9 Publisher: Nature Publishing Group.

[253] N. Bansal, Y. S. Kim, E. Edrey, M. Brahlek, Y. Horibe, *et al.* "Epitaxial growth of topological insulator Bi2Se3 film on Si(111) with atomically sharp interface". *Thin Solid Films* **520**, 224 (2011).

[254] M. Brahlek, N. Bansal, N. Koirala, S.-Y. Xu, M. Neupane, *et al.* "Topological-Metal to Band-Insulator Transition in $({\mathrm{Bi}}_{1\ensuremath{-}x}{\mathrm{In}}_{x}{)}_{2}{\mathrm{Se}}_{3}$ Thin Films". *Physical Review Letters* **109**, 186403 (2012). Publisher: American Physical Society.

[255] Y. Wang, D. Zhu, Y. Wu, Y. Yang, J. Yu, *et al.* "Room temperature magnetization switching in topological insulator-ferromagnet heterostructures by spin-orbit torques". *Nature Communications* **8**, 1364 (2017).

[256] S. Olive-Mendez, A. Spiesser, L. A. Michez, V. Le Thanh, A. Glachant, *et al.* "Epitaxial growth of Mn5Ge3/Ge(111) heterostructures for spin injection". *Thin Solid Films* **517**, 191 (2008).

[257] C. Zeng, Y. Yao, Q. Niu, and H. H. Weitering. "Linear Magnetization Dependence of the Intrinsic Anomalous Hall Effect". *Physical Review Letters* **96**, 037204 (2006). Publisher: American Physical Society.

APPENDIX A

MBE growth and magnetotransport study of Bi_2Se_3/Al_2O_3

We investigated the properties of Bi_2Se_3/Ge (111) heterostructure in the third chapter of this manuscript [3]. The interpretation we proposed to account for the spin-to-charge conversion results involved the hybridization between the topological surface states (TSS) of Bi_2Se_3 and the states of Ge.[164] As a control experiment, we grew Bi_2Se_3 thin films on a sapphire substrate using a similar molecular beam epitaxy procedure. The results showed that Ge is essential to observe spin-to-charge conversion and the helicity-dependent photovoltage reported in the third chapter [3.4]. The aim of this appendix is to present the structural and magnetotransport properties of the Bi_2Se_3 film grown on sapphire, as we were able to reach higher cristalline quality on this substrate than on Ge (111).

A.1 Bi_2Se_3/Al_2O_3 growth by molecular beam epitaxy

We start with the substrate preparation. The $\sim 10 \times 10$ mm^2 sapphire substrate is first cleaned in acetone and isopropanol in an ultrasonic bath for 5 minutes to remove organic species. Then the substrate is annealed at 1000°C in air conditions for 90 minutes in order to obtain large atomic terraces. The substrate is then introduced into the ultra-high vacuum molecular beam epitaxy chamber and annealed at 850°C for 30 min in order to degas remaining species and obtain a clean surface. Then, we proceed the growth the 10 QL-thick Bi_2Se_3 film by co-depositing Bi and Se at a substrate temperature of ∼230°C as illustrated by Fig. A.1 a). Bi and Se were evaporated using an e-beam evaporator and a Knudsen cell operating at ∼200°C, respectively. Bi and Se evaporation rates were adjusted in order to reach a high Se:Bi ratio of about 15:1 and limit the presence of Se vacancies in the film. The lamellar crystal structure is schematically shown in Fig. A.1 b). Finally, the sample is capped with 1.5 nm-thick Al film that transform into AlO_x when exposed to air. Fig. A.1 c) shows the characteristic RHEED patterns obtained along two different azimuths of the crystal lattice, we note that the observed lines are typically sharper than for Bi_2Se_3/Ge (111),

indicating a higher crystalline quality.

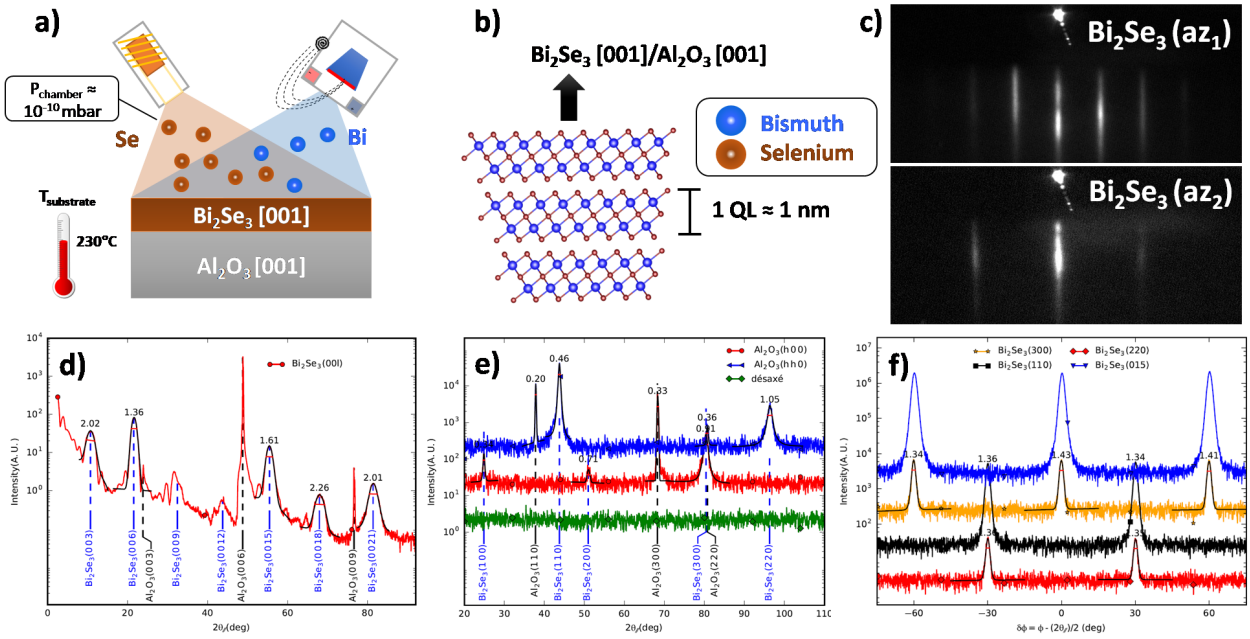

Figure A.1 – a) Schematics of the codeposition growth of Bi_2Se_3/Al_2O_3 by molecular beam epitaxy. b) Quintuple layer structure of Bi_2Se_3, Bi and Se atoms are represented in blue and brown color, respectively. c) RHEED patterns recorded along two azimuths separated by 30° during the growth of Bi_2Se_3 on Al_2O_3. d) Out-of-plane symmetric $\theta/2\theta$ X-ray diffraction spectrum. b) In-plane grazing incidence XRD (GIXD) radial scans along different reciprocal directions. c) In-plane GIXD azimuthal scans for two peaks families {300} and {110}.

Similarly to the Bi_2Se_3/Ge (111) samples, a thorough XRD analysis was performed to characterize the crystal structure properties. Fig. A.1 b) shows the symmetric out-of-plane $\theta/2\theta$ diffraction spectrum along the Al_2O_3 $(0,0,3h)$ reciprocal space direction. In addition to the Al_2O_3 (100) substrate peaks, the 5 other peaks can be attributed to the rhombohedral structure $R\bar{3}m$ of Bi_2Se_3.[145] They are indexed in the hexagonal unit cell ($a = b = 0.4143$ nm and c =2.8636 nm) which consists of three Se-Bi-Se-Bi-Se quintuple layers separated from each other by a van der Waals gap (see Fig. 3.1 b)). The relative intensities of the peaks are consistent with the calculated structure factors.
Fig. A.1 e) and f) show GIXD measured with an optimized incidence angle of 0.32°. Radial scans (Fig. A.1 e)) along the two 30° apart in-plane directions Al_2O_3 $(h\,0\,0)$ and Ge$(h\,h\,0)$ give the epitaxial relationship between Bi_2Se_3 and the Al_2O_3 substrate: Bi_2Se_3 (001)$\|Al_2O_3$(001). The peak positions corresponding to the bulk Bi_2Se_3 ones show that there is no substrate induced in-plane strain. Azimuthal scans around the Bi_2Se_3 (hk0) Bragg peaks (Fig. A.1 f)) show that 30° rotational domains are completely absent. However, like in the case of Bi_2Se_3/Ge (111), pure in-plane measurements cannot exclude twinning which generally occurs due to the simultaneous nucleation of twinned domains on lattice mismatched substrates but with the same in-plane symmetries.[146] Indeed, the ABCAB and ACBAC stackings of the quintuple layer structure give in-plane diffraction peaks {hk0} at the same positions. Nevertheless, the 3-fold symmetry of the out-of-plane {015} reflections allows

to quantify the degree of twinning.[147] The measurement shows that the film is composed of both twins in equal proportions.

Overall, the extracted diffraction linewidth are sharper than for Bi_2Se_3 grown on Ge (111), suggesting a larger grain size. Also, the presence of satellite peaks on the out-of-plane spectrum indicates sharp interfaces with limited roughness.

Then, we pattern Hall bars in the Bi_2Se_3 film with the usual two-step microfabrication process. We first define the conduction channel using laser lithography and ion-beam etching to etch the 10 QL-thick Bi_2Se_3 and deposit Au(120 nm)/Ti(5 nm) electrical contacts after etching the alumina layer beneath.

A.2 Magnetotransport measurements

Following this structural analysis, I characterized the electrical properties of the Bi_2Se_3 film. The Hall bar dimensions are $L = 100$ µm and $w = 10$ µm as shown in Fig. A.2 a). The Hall bar aspect ratio is then defined as: $Z = L/w = 10$. We report in Fig. A.2 b) the temperature dependence of the four-probe longitudinal resistance $R_{xx} = U_{xx}/I_{\mathrm{DC}}$ using a 1 µA DC current. The resistance of the film decreases monotonously when lowering the temperature and is almost constant below 20 K, indicating that the conduction is metallic.

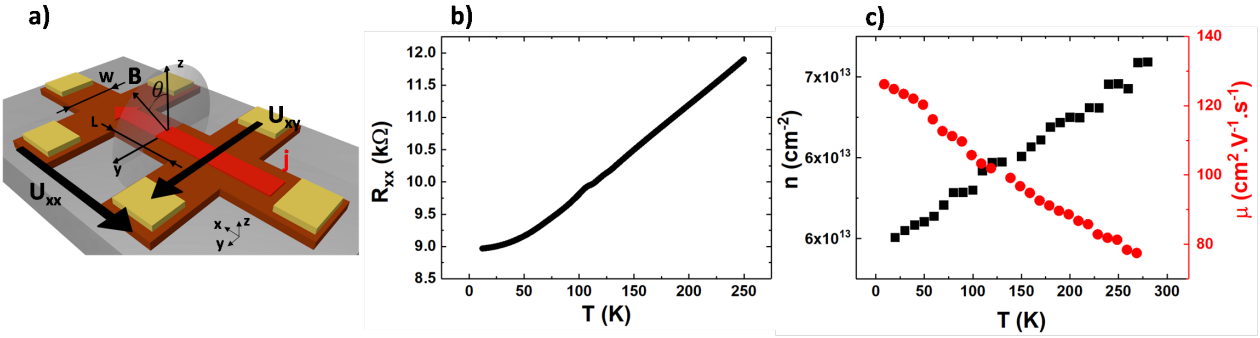

Figure A.2 – a) Sketch of the Hall bar and description of the four-probe measurements geometry. A 1 µA DC current I_{DC} is applied along x and the external magnetic field direction in the zy plane, characterized by the polar angle θ. The longitudinal and transverse resistance are defined as: $R_{xx(xy)} = U_{xx(xy)}/I_{\mathrm{DC}}$ b) Temperature dependence of the four-probe longitudinal resistance exhibiting a typical metallic behavior. c) Carrier density (black squares) and mobility (red dots) as a function of temperature, extracted from Hall effect measurements.

We characterize the carrier density and mobility as a function of the temperature using the Hall effect. We apply an external magnetic field $\mathbf{B}$ along z and record the longitudinal $R_{xx} = U_{xx}/I_{\mathrm{DC}}$ and transverse $R_{xy} = U_{xy}/I_{\mathrm{DC}}$ resistances. The resulting Hall resistance is linear with the applied field, indicating that there is a single type of carrier contributing to the electrical conduction. The negative slope confirms the electron nature of the carriers. Fig. A.2 c) reports the evolution of the carriers concentration and mobility. The carrier density is almost independent of the temperature,

as expected for a metallic conduction. We find $n \approx 6 \times 10^{13}$ cm^{-2}, which is almost the same as in Bi_2Se_3/Ge (111) films, indicating that even if the structural quality is better, the amount of Se vacancies is comparable. The carrier mobility however, reaches 130 cm^2.V^{-1}.s^{-1}, which about three times larger than Bi_2Se_3/Ge (111) films. This can be understood as a consequence of the increased grain size and the smoother surfaces.

We proceed to the measurement of the low temperature magnetoresistance (MR) response. Similarly to the case of Bi_2Se_3/Ge (111), the positive MR dip is the signature of the weak anti-localization effect (see sect. [3.2.2]).

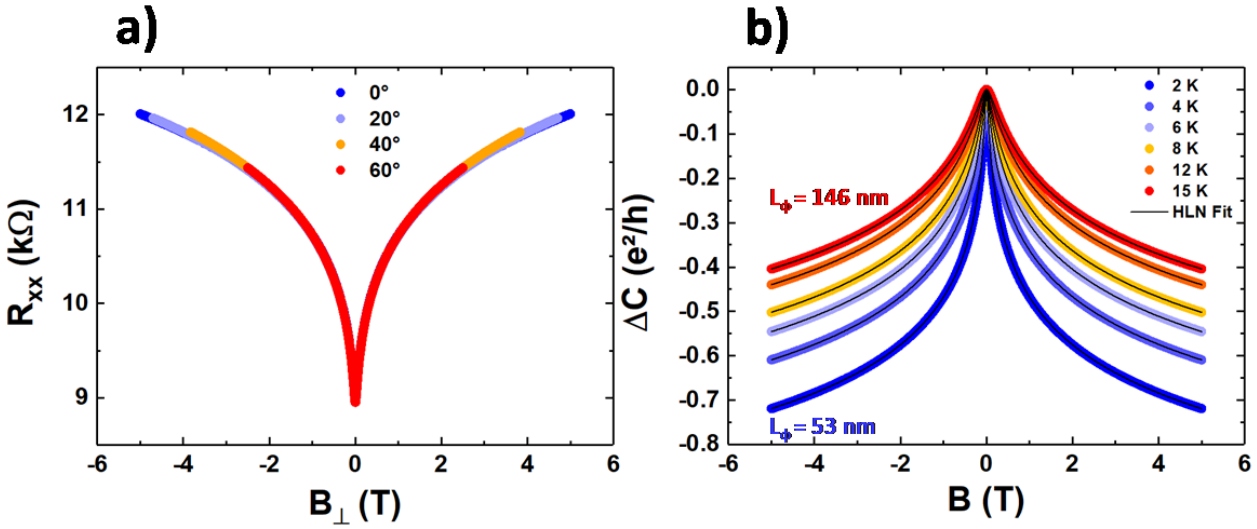

Figure A.3 – a) R_{xx} as a function of $B_\perp = B \times \cos\theta$. b) Magnetoconductance ΔC normalized to the quantum of conductance e^2/h as a function of temperature. Black solid lines are fits using the HLN model. The extracted phase coherence length decays as $T^{-1/2}$, from 146 nm at 2 K to 53 nm at 15 K.

The observation of WAL suggests a two-dimensional electrical conduction in the presence of spin-orbit coupling.[150,151] This is supported by the temperature and angular dependences of the magnetoresistance. Fig. A.3 a) presents MR measurements as a function of the projected magnetic field $B_\perp = B \times cos(\theta)$ using a 1 μA DC current. All the curves perfectly overlap at low fields which is the signature of WAL.[152] Fig. A.3 b) shows the film magnetoconductance at temperatures varying from 2 K to 6 K, the data are fitted using the Hikami-Larkin-Nagaoka (HLN) two-dimensionnal quantum diffusion model[107,108,150]:

$$\Delta C = -\frac{\alpha e^2}{2\pi^2\hbar}\left[\psi\left(\frac{\hbar}{4eBL_\phi^2}+\frac{1}{2}\right) - ln\left(\frac{\hbar}{4eBL_\phi^2}\right)\right] \tag{A.1}$$

where ψ is the digamma function, B is the applied magnetic field perpendicular to the film, L_Φ is the effective phase coherence length and α a parameter related to the number of channels contributing to the transport.[153,154] $\alpha = 0.5$ is for one channel contributing to the transport and $\alpha = 1$ for two channels contributing. In the literature, α varies from 0.25 to 1 depending on the thickness,[109,110] or

the film fabrication technique.[155] Using the HLN model, we can extract a temperature independent α value of 0.52. This value is very close to 0.5 which corresponds to a single conducting channel. For a 10 QL-thick Bi_2Se_3 film, bulk states are quantized and we can exclude pure magnetotransport into those 2D bulk states since they should give rise to a weak localization (WL) signal as predicted by Shen *et al.*[151] Considering the high electron density extracted from Hall measurements, the Fermi energy is larger than the energy spacing between the quantized bulk states of the 10 QL-thick Bi_2Se_3 film. Hence, those bulk states are energetically accessible for electron transport and scattering (non-TI regime). As a consequence, magnetotransport and the WAL take place in a single coherent channel corresponding to strongly coupled surface and bulk states.[156]
We find an effective phase coherence length L_ϕ of 156 nm at 2 K which is 1.5 larger than in Bi_2Se_3/Ge (111). L_ϕ decreases with increasing the temperature as $T^{-0.49}$, which is in good agreement with the theory predicting $L_\phi \propto T^{-0.50}$.

To conclude, we develop a one-step process to grow high quality Bi_2Se_3 thin films on a Al_2O_3 substrate. Even if this set of samples was meant to be used as a reference where the topological insulator Bi_2Se_3 is decoupled from the Ge (111) substrate, the films were found of higher structural and electrical quality. In the literature, Bi_2Se_3/Al_2O_3 is often grown using a two-steps MBE process where a low quality 1-2 QL-thick Bi_2Se_3 film is deposited at low temperature and acts as a seed layer, followed by a second deposition at a comparable temperature (i.e $\sim$230°C).[253] Although this method leads to high crystalline quality, it is also correlated with the observation of two types of carriers contributing to the electrical transport[144] and Cu or In doping has to be used to observe a single carrier type.[152,254] Our simplified process allows to grow high quality films with only one type of carriers.

APPENDIX B

Bi_2Se_3/Mn_5Ge_3/Ge (111): a fully epitaxial SOT devices

In this second appendix, I report the first results we obtained on the Bi_2Se_3/ Mn_5Ge_3/Ge (111) all-epitaxial system. Topological insulators exhibit spin-momentum locked surface states that leads to strong spin-charge interconversion.[102,114–116,132] By depositing a thin ferromagnetic film on top, one can use the efficient spin current generation of the TI to control the magnetization of the FM by spin-orbit torque (SOT).

Also, in such systems, we can expect to measure spin-dependent magnetoresistance (MR) effects like the (unidirectional) spin Hall MR.[85–88] . In the literature, the most studied system is the Bi_2Se_3 (10 nm)/NiFe(10 nm) bilayer.[255] Applying an electrical current in such bilayer results in an almost complete shunting in the FM because of the large difference of resistivity between the two materials. In this work, we take advantage of the fact that we can grow Mn_5Ge_3, which is a high resistivity ferromagnet, directly on Ge (111).[256] The lattice parameter of the reconstructed Mn_5Ge_3 surface matches almost perfectly the one of Bi_2Se_3 [ref]. We aim at growing a fully epitaxial heterostructure on Ge (111), which could operate as a SOT memory in future applications. Nevertheless, this is still an undergoing work and neither SOT nor USMR could be observed yet. Further optimization of the material thicknesses and the quality of the growth will be necessary to observe such effects. Here, I report the structural and magnetotransport characterizations of a first sample.

B.1 Bi_2Se_3/Mn_5Ge_3/Ge (111) growth by molecular beam epitaxy

The heterostructure was grown on a low p-doped 2 µm-thick Ge/Si(111) substrate by MBE, the surface quality and structure were followed by reflection high-energy electron diffraction (RHEED) during the different steps of the growth. We prepare the Ge (111) surface using annealing (850°C) and ion beam etching cycles in UHV to remove the native Ge oxide layer and smooth the surface. We obtain the Ge(2×8) surface reconstruction shown in Fig. B.1 a). Then, we deposit a 10 nm-thick Mn film at room temperature at a fixed rate of 0.5 $\AA.s^{-1}$. At this stage, the film is rough and poorly crystalline as indicated by the RHEED pattern in Fig. B.1 b).

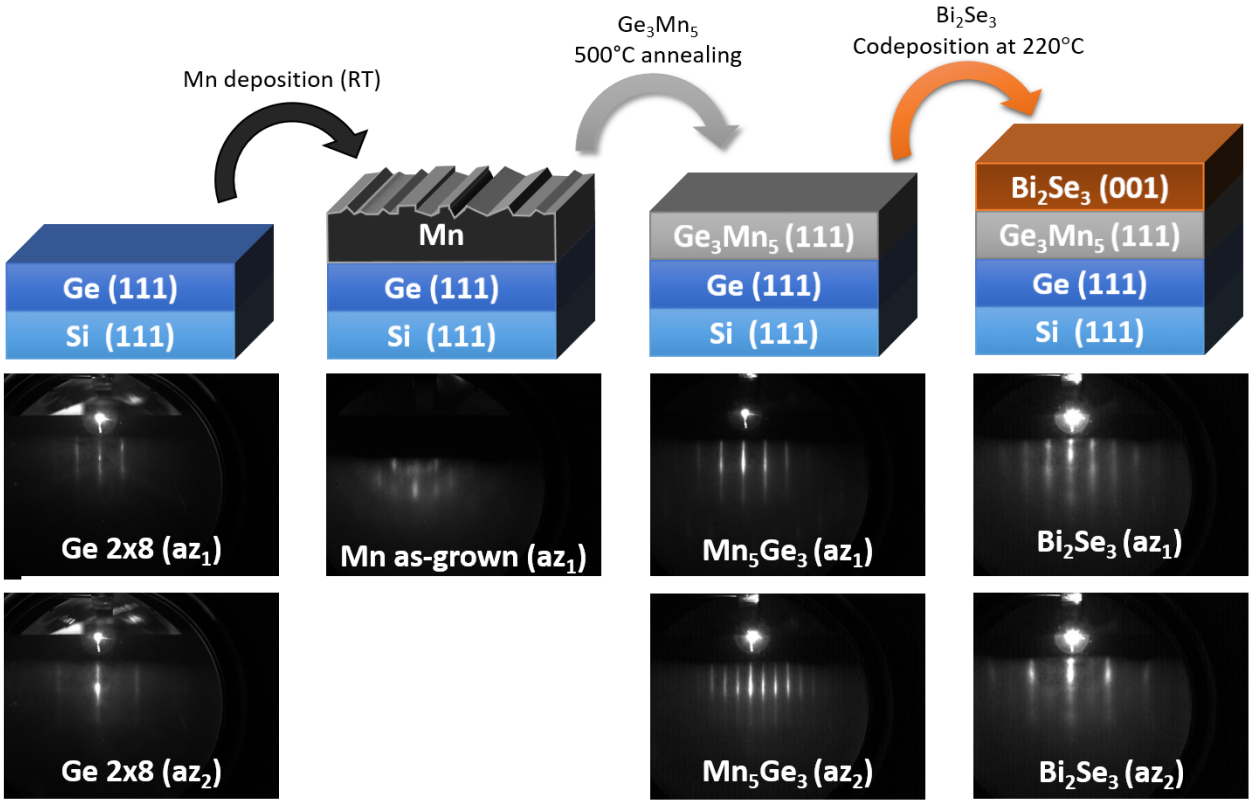

Figure B.1 – From left to right: Initial Ge (2×8) surface reconstruction. After depositing 10 nm of Mn at room temperature, the RHEED pattern changes as the film roughness is important and the crystalline quality is low. We then anneal the substrate to 500°C, the Mn diffuses in the Ge lattice leading to the formation of a highly-ordered Mn_5Ge_3 thin film. Finally, we deposit the Bi_2Se_3 film at 220°C following the usual codeposition procedure.

The substrate is then annealed at 500°C for 30 min. As a result, Mn atoms diffuse in the Ge lattice and recrystallize, forming the Mn_5Ge_3 ferromagnetic compound. As suggested by the RHEED pattern in Fig. B.1 c). The film crystalline quality is very good, the surface is smooth and is characterized by the $(\sqrt{3}\times\sqrt{3})R30°$ reconstruction. The lattice parameter of Mn_5Ge_3 being $a_{\mathrm{GeMn}} = 0.714$ nm, we obtain $a_{\mathrm{GeMn,rec}} = a/\sqrt{3} = 0.412$ nm, which almost perfectly matches the lattice parameter of Bi_2Se_3: $a_{\mathrm{BiSe}} = 0.413$ nm. This should favor an epitaxial growth of Bi_2Se_3 on Mn_5Ge_3. We then proceed the growth of a 10 QL-thick Bi_2Se_3 film using the usual codeposition technique. The Se:Bi

flux ratio is maintained above 15:1 and the substrate temperature is 220°C. Fig. B.1 d) shows the resulting RHEED patterns, the film quality is comparable to the one of Bi_2Se_3/Ge (111) films. The sample is finally capped using a 1.5 nm-thick Al layer which transforms into AlO_x when exposed to air.

In order to better understand the magnetotransport properties of this heterostructure, we also grew a simple 10 nm-thick Mn_5Ge_3/Ge/Si (111) sample as a reference.

It was pointed out in the manuscript that the interface between a TI and a FM film is not perfect as the chalchogen atoms (Se here) are likely to react with the FM atoms (Mn here). A more sophisticated approach would be to grow an additional ultra-thin epitaxial Ge (111) diffusion barrier between Bi_2Se_3 and Mn_5Ge_3. Unfortunately, we are not able to grow such heterostructure with our current setup. A novel molecular beam epitaxy setup currently in development in our group will allow to investigate this approach.

B.2 Magnetotransport measurements

We pattern 100×10 mm^2 Hall bars in the Bi_2Se_3/Mn_5Ge_3/Ge (111) film in two steps: we first define the conduction channel using laser lithography, we etch the metallic layers (Bi_2Se_3 and Mn_5Ge_3) using ion-beam etching and we etch the 2 μm-thick Ge film using ion-coupled plasma etching. Using a second step of laser lithography, we define the electrical leads and deposit Au(120 nm)/Ti(5 nm) by e-beam evaporation.

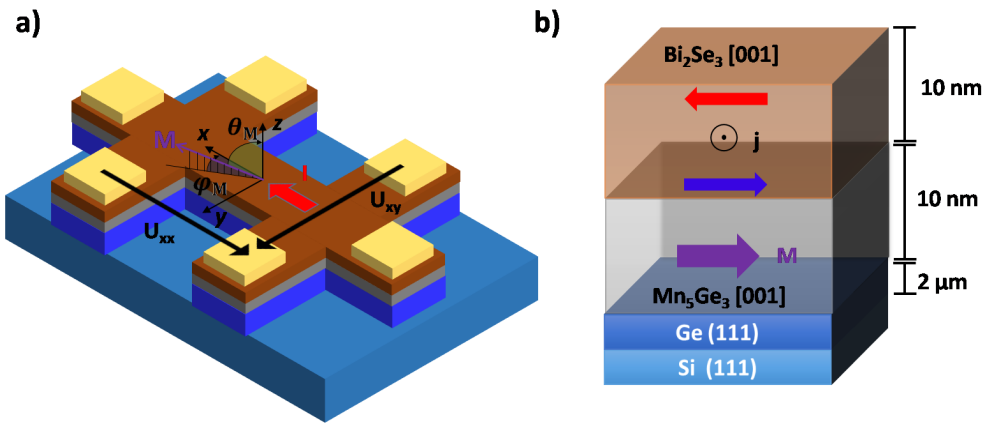

Figure B.2 – a) Sketch of the Hall bar and description of the four-probe measurements geometry. The current is applied along x and the external magnetic field direction is given by the azimuthal and polar angles (φ, θ). b) Schematic representation of the Bi_2Se_3/ Mn_5Ge_3/Ge/Si (111) stack, the Mn_5Ge_3 magnetization direction is in-plane (in purple), and the blue and red arrows show the spin accumulation induced by the Rashba-Edelstein effect (or the spin Hall effect) when a current is flowing in the heterostructure.

The sample stack and the Hall bar geometry are summarized in Fig. B.2 a). The current is applied along x and the external magnetic field direction is set by the azimuthal and polar angles (φ, θ). As illustrated in Fig. B.2 b), passing a charge current j in such topological insulator/ferromagnetic

metal (TI/FM) bilayer results in spin accumulations (blue and red arrows) induced by either the spin Hall effect (SHE) in Bi_2Se_3 bulk states or by the Rashba-Edelstein effect (REE) in the spin-momentum locked surface states. In this TI/FM system, one can expect to detect the current-independent spin Hall magnetoresistance (SMR) as well as the current-dependent unidirectional spin Hall magnetoresistance (USMR) and eventually, spin-orbit torque-induced magnetization switching.

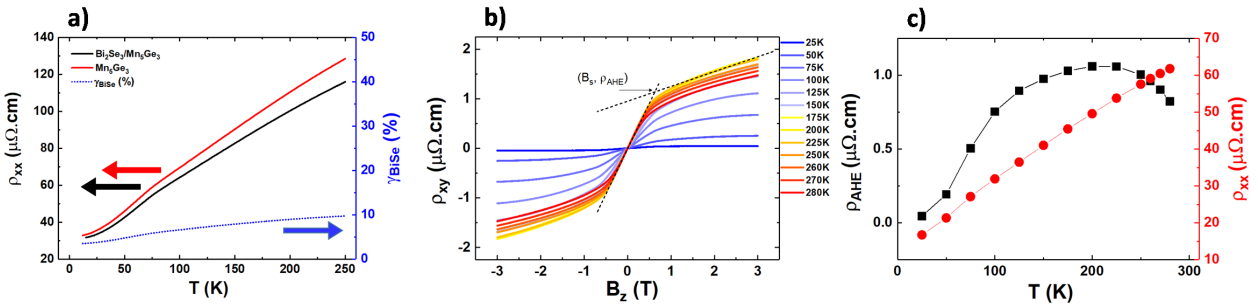

Figure B.3 – a) Temperature dependence of the longitudinal resistance. b) Anomalous Hall effect measurements at different temperatures. c) Extracted longitudinal and transverse resistivities temperature dependences.

We first measure the resistivity of the Bi_2Se_3/Mn_5Ge_3 and the Mn_5Ge_3 samples in order to estimate the proportion of current shunting into the Mn_5Ge_3 film. Fig. B.3 a) reports the two samples temperature dependence of the longitudinal resistivity, we observe that the resistivity of the TI/FM stack (in black) is slightly lower than the FM alone (in red), indicating that a small fraction of the current flows in the TI. We analyze the current shunting using a simple model of two parallel conduction channels:

$$\gamma_{\mathrm{BiSe}} = \frac{\rho_{xx}^{\mathrm{GeMn}}}{\rho_{xx}^{\mathrm{BiSe}} + \rho_{xx}^{\mathrm{GeMn}}} \tag{B.1}$$

The shunting ratio γ_{BiSe} represents the proportion of current flowing in the Bi_2Se_3 film. It is plotted as a function of temperature on a second axis in Fig. B.3 a) (dotted blue line). It is maximum at room temperature ($\sim$ 10 %) and decreases monotonously when lowering the temperature ($\sim$ 4.5 % at 15 K). This is a consequence of the larger temperature dependence of the Mn_5Ge_3 film longitudinal resistivity compared to the Bi_2Se_3 one. The value at room temperature represents a first improvement from the typical < 1 % found in Bi_2Se_3/NiFe bilayers.[255] Moreover, it could be increased by one order of magnitude by reducing the Mn_5Ge_3 film thickness.

Fig. B.3 b) displays the field and temperature dependences of the transverse resistance of the Bi_2Se_3/Mn_5Ge_3 bilayer in the Hall configuration (**B** along z). We identify the contributions from the ordinary and anomalous Hall effects, . The transverse resistivity can be written as:

$$\rho_{xy} = R_0 B_z + R_s M_z \tag{B.2}$$

Where R_0 (R_s) accounts for the ordinary (anomalous) contribution. The non-linear behaviour of $\rho_{\mathrm{xy}}(B)$ in Fig. B.3 b) is a fingerprint the anomalous Hall effect in the FM film. The exact saturation

field (B_s and corresponding AHE resitivity ρ_{AHE} is found at the intersection between the linear fits of the ordinary ($|B|> B_s$) and anomalous ($|B|< B_s$) components. The sign of the ordinary Hall effect indicates that the parallel conduction channel is n-type so we can conclude that there is no conduction in the Ge substrate, which is p-type.

The extracted longitudinal and AHE resistivity ρ_{AHE} temperature dependencies are reported in Fig. B.3 c). Interestingly, ρ_{AHE} is minimum at low temperature and increases with the temperature until it reaches the Curie temperature. This was already observed in Mn_5Ge_3 and was attributed to the intrinsic AHE conductivity being proportional to the total magnetization as a consequence of the long wavelength fluctuations of the spin orientation at finite temperatures.[257] The same behavior was observed in the Mn_5Ge_3 reference sample.

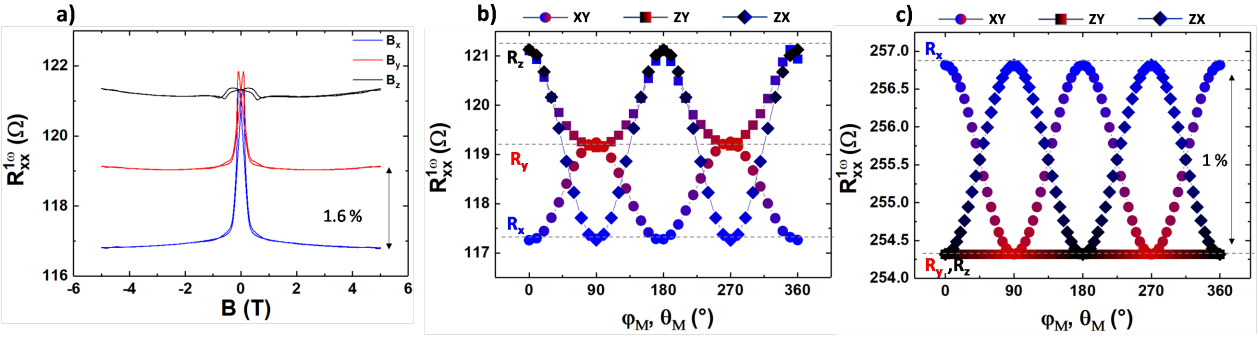

Figure B.4 – a) Bi_2Se_3/ Mn_5Ge_3 bilayer first harmonic longitudinal resistance $R^{1\omega}_{xx}$ for different external magnetic directions, measured at 15 K, applying an AC current of 500 μA. b) Corresponding $R^{1\omega}_{xx}$ angular dependencies recorded at $T = 15$ K using an applied current of $I = 500$ μA and an external field of $B = 1.5$ T,the color code indicates the magnetic field projection along: x (blue), y (red), z (black). c) Same measurements for the Mn_5Ge_3/Ge (111) reference sample, a pure anisotropic magnetoresistance (AMR) behavior is observed.

We then analyze the different harmonic comonents of the magnetoresistance. We first investigate the dependence of the first harmonic longitudinal resistance $R^{1\omega}_{xx}$ with the magnetic field orientation. The measurements are performed at 15 K, we apply a 500 μA AC current at a frequency $f = 177$ Hz and apply an external magnetic field up to 5 T along the x, y and z direction. As shown in Fig. B.4 a), we observe MR peaks at low magnetic field corresponding to the magnetization reversals. We notice that when $\mathbf{M}$ is saturated, we obtain $R_z > R_y > R_x$ where R_x, R_y and R_z are the resistances measured at saturation along x, y and z respectively. This behavior cannot be attributed to the classical anisotropic magnetoresistance (AMR) where the $\mathbf{M} \perp \mathbf{j}$ state is more resistive than the $\mathbf{M} \parallel \mathbf{j}$ state. We further have to consider the contribution from the spin Hall Magnetoresistance (SMR). The addition of the two effects gives the following expression (see sect. [4.1]):

$$R^{1\omega}_{xx} = \alpha \left(R_{M_x} - R_{M_z}\right) . \sin^2\theta_{\mathrm{M}} \cos^2\varphi_{\mathrm{M}} + \beta \left(R_{M_y} - R_{M_z}\right) . \sin^2\theta_{\mathrm{M}} \sin^2\varphi_{\mathrm{M}} \tag{B.3}$$

where the first term accounts for the AMR and the second for the SMR. Using this expression, we found that half of the measured MR can be attributed to the AMR, and half to the SMR:

$\Delta_{AMR} \approx \Delta_{SMR} \approx 0.7$ % (the Δ notation refers to the amplitude of each effect here). This MR behavior is specific to the bilayer and was not observed in the Mn_5Ge_3 reference sample. As shown in Fig. B.4 c), the angular dependence of $R_{xx}^{1\omega}$ in the Mn_5Ge_3 sample only shows the AMR contribution. This result suggests that a large spin accumulation generated in the Bi_2Se_3 film diffuses toward the Mn_5Ge_3 film. That spin current reflects at the interface and is converted back into a charge current. This SMR value is unusually large as compared to typical systems in the literature: 0.01 % for YIG/Pt, 0.1 % for CoFeB/W and ~0.15 % for Bi_2Se_3/ CoFeB. This could be explained by the fact that the TI/FM structure is epitaxial, but further theoretical work is required to explain this large increase of the SMR.

Finally, we measured the second harmonic MR terms to investigate the unidirectional spin Hall MR (USMR) and possibly the spin-orbit torque (SOT) contributions to the current-dependent MR.

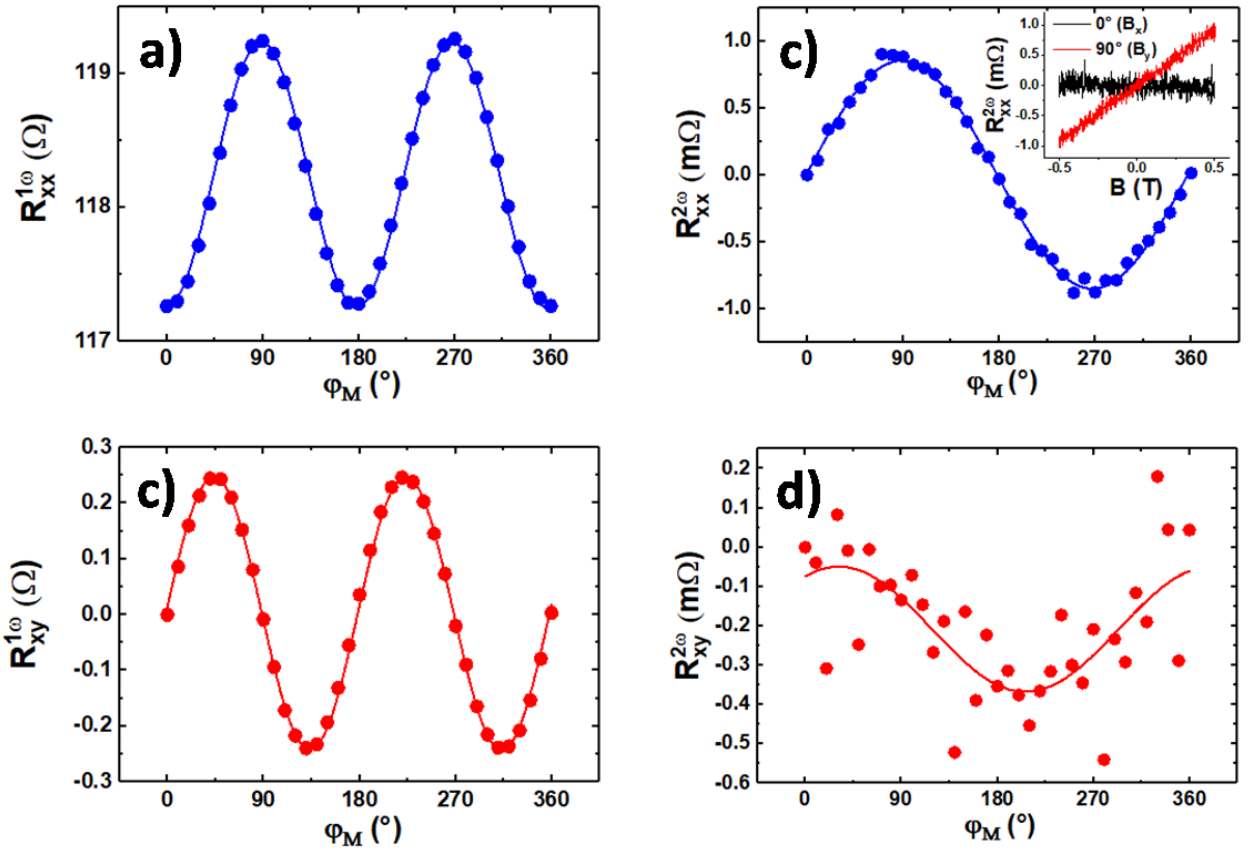

Figure B.5 – a) Angular dependencies of the longitudinal and transverse MR signals in the xy plane: a) $R_{xx}^{1\omega}$ b) $R_{xy}^{1\omega}$ c) $R_{xx}^{2\omega}$ and d) $R_{xy}^{2\omega}$, measured at 15 K, with an applied magnetic field of 0.5 T and a current of 1 mA. The inset of c) shows the field dependence of $R_{xx}^{2\omega}$ at $\varphi_M = 0°$ and $\varphi_M = 90°$.

We report in Fig. B.5 the in-plane angular dependence of the four MR components recorded at 15 K, with an applied magnetic field $B = 0.5$ T and a current $I = 1$ mA. At this magnetic field, the Mn_5Ge_3 magnetization is saturated, the angular dependencies of $R_{xx}^{1\omega}$ is due to the sum of AMR of SMR as shown prevously whereas $R_{xy}^{1\omega}$ is a consequence of the planar Hall effect. In Fig. B.5 c) and d), we report the angular dependences of $R_{xx}^{2\omega}$ and $R_{xy}^{2\omega}$ simultaneously recorded. We observe a

very small unidirectional MR for the longitudinal resistance which is proportional to the external magnetic field as shown in the inset. Hence, we attribute this term to a very small UMR contribution or to the Nernst effect resulting from the out-of-plane thermal gradient induced by Joule heating. The fact that we do not observe an hysteresis loop in $R_{xx}^{2\omega}$ indicates that the USMR is not detectable in this configuration.

To conclude, we grew a full-epitaxial topological insulator/ferromagnetic metal heterostructure by molecular beam epitaxy. We characterized the magnetic properties of the Mn_5Ge_3 film by performing anomalous Hall effect measurements. Aside from the usual anisotropic magnetoresistance, we found an additional quadratic magnetoresistance term which is comparable in magnitude corresponding to the spin Hall magnetoresistance. The effect is rather large in this system and is characteristic of a large spin-charge interconversion in Bi_2Se_3. Further optimizations of the thicknesses and interfaces could allow to detect more spin-related phenomena. In particular, it could be very interesting to grow an additional epitaxial Ge layer betwen Mn_5Ge_3 and Bi_2Se_3 to limit the suspected atomic interdiffusion.

APPENDIX C

Development of a universal and versatile control interface: MSB

In the chapter 2 of the manuscript, I presented the two experimental setups I developed: the SpectromagPT cryostat and the LUMOS optical bench. These two equipments were key tools for my thesis work.

I designed and mounted all the elements of the two setups, and created a very powerful control software that allows to automate the measurements through rigorous control of the available degrees of freedom (DOFs). This control interface is called *Measurement Sequence Builder* (MSB), it is now used on several magnetotransport and magneto-optical setups in the lab. This appendix aims at introducing the program architecture and capabilities.

As a reminder, Fig. C.1 summarizes the two experimental setups main components. The SpectromagPT is schemed in Fig. C.1 a), it can be used to apply an intense magnetic field up to 7 T and to control the sample temperature from 1.5 K to room temperature within a mK temperature stability. It is different from other superconducting magnet cryostats for the presence of four windows to access optically to the sample: the sample can be illuminated by a laser beam which adds several degrees of freedom to our measurements like the laser power, wavelength and polarization. The sample holder located at the bottom of the measurement probe can be plugged either in-plane or out-of-plane with respect to the magnetic field, allowing to perform full angular dependencies (Fig. C.1 a)).

LUMOS is a homemade confocal microscope that can operate at variable temperatures (4.2 K-300 K), its strength resides in the amount of DOFs that can be controlled to perform original experiments. Fig. C.1 b) shows a schematic top view of the optical bench, the light source is coming from a laser diode out of an optical fiber, the wavelength can be changed easily by changing the diode without moving any part of the setup. The beam emerging from the fiber is strongly divergent so it first passes through a convergent $f = 5$ cm lens that shapes it into a 1 cm-diameter collimated beam. Dynamic circular polarization is obtained by combining a wollaston biprism

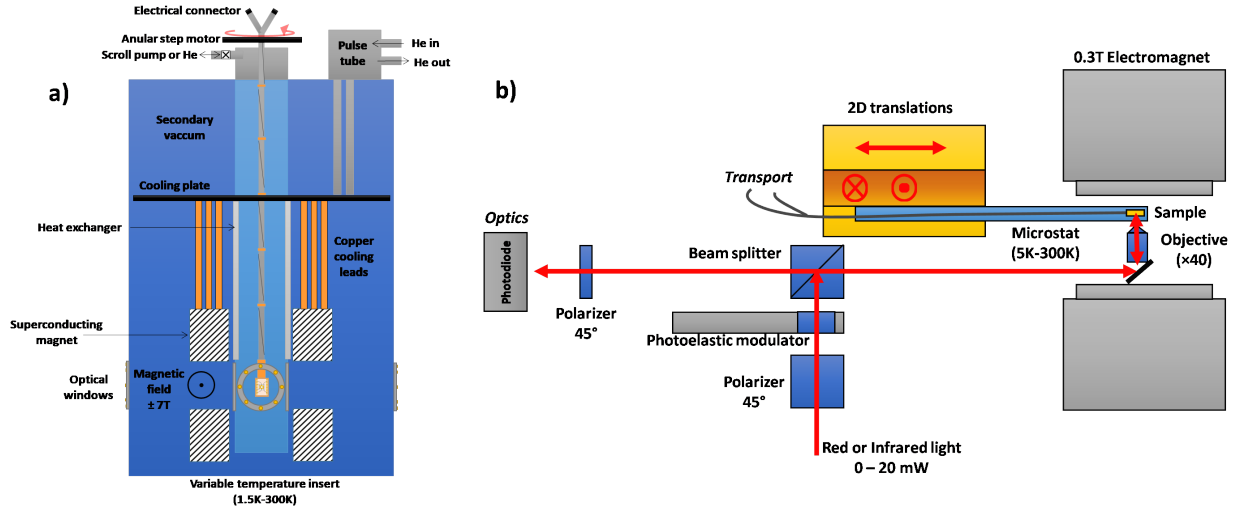

Figure C.1 – a) Scheme of the SpectromagPT superconducting magnet cryostat. b) Schematic top view of the LUMOS optical bench showing its main components: cryostat, electromagnet, the scanning x-y stage and the polarized light path.

with a photoelastic modulator (PEM). This circularly polarized light beam is reflected on a beam splitter (BS) to enter the microscope objective (×40). This objective is unique, it is completely non-magnetic and thanks to its long focal length (2 mm), it allows to focus the beam on the sample through the cryostat quartz optical windows. The cryostat can be cooled down to liguid nitrogen or liquid helium temperatures (77 K and 4.2 K respectively) in a continuous nitrogen or helium gas flow. Like in the SpectromagPT setup, the sample is glued on a sample holder mounted on a measurement probe that allows to perform electrical measurements using 10 electrical contacts. The sample lies at the center of a 0.3 T electromagnet with a 10^{-4} T resolution. The whole cryostat is mounted on a x-y translation stage that brings the additional spatial DOF: the sample position can be adjusted within a 300 nm resolution, allowing to perform optical microscopy and detect in the meantime any physical signal at each laser spot position.

The following table summarizes all the degrees of freedom that are available in the two setups, their range and resolution are also given.

Setup	**Oxford**			**LUMOS**		
DOF	**Range**	**Resolution**	**Comment**	**Range**	**Resolution**	**Comment**
Temperature	1.5 - 300 K	1 mK	Closed-loop	4.2 - 300 K	5 mK	Helium flux
Field	± 7 T	10^{-4} T	Superconducting	± 0.3 T	10^{-4} T	Electromagnet
Current source	2 pA - 200 mA	1 pA	DC, AC, ± I	2 pA - 200 mA	1 pA	DC, AC, ± I
Voltage source	20 mV - 200 V	1 mV	Gate	20 mV - 200 V	1 mV	Gate
Angle	0-360°	0.05°	xy, zy,zx planes	∅	∅	Perpendicular
Position X	∅	∅	∅	26 mm	150 nm	∅
Position Y	∅	∅	∅	26 mm	150 nm	∅
Laser power	0.5 - 200 mW	< 1 %	∅	1 - 20 mW	< 0.01 %	∅
Laser wavelength	400 - 2000 nm	1 nm	∅	661, 1550nm	5 nm	∅
Laser polarization	Linear, circular	∅	∅	Linear, circular	∅	∅
Laser incidence	Normal, grazing	∅	∅	Normal, oblique	< 1°	Motorized

Table C.1 – Summary of the controllable DOFs of the SpectromagPT superconducting magnet cryostat setup and LUMOS optical bench.

From my previous experience of experimental physics, one type of measurement usually requires one specific program that is used to control the DOFs and acquire the data. This implies that a minor change in the experimental setup such as an additional instrument, or the control of a supplemental DOF often results in the development of an additional control program. My guideline was to design a versatile and modular control software that can be used for any kind of experiments without having to change the source code. I developed this program using the National Instrument graphic programming environment LabView 2014. I will not give too many details about the numerous functions of the program but I will attempt to explain its architecture and core functions as well as its main features.

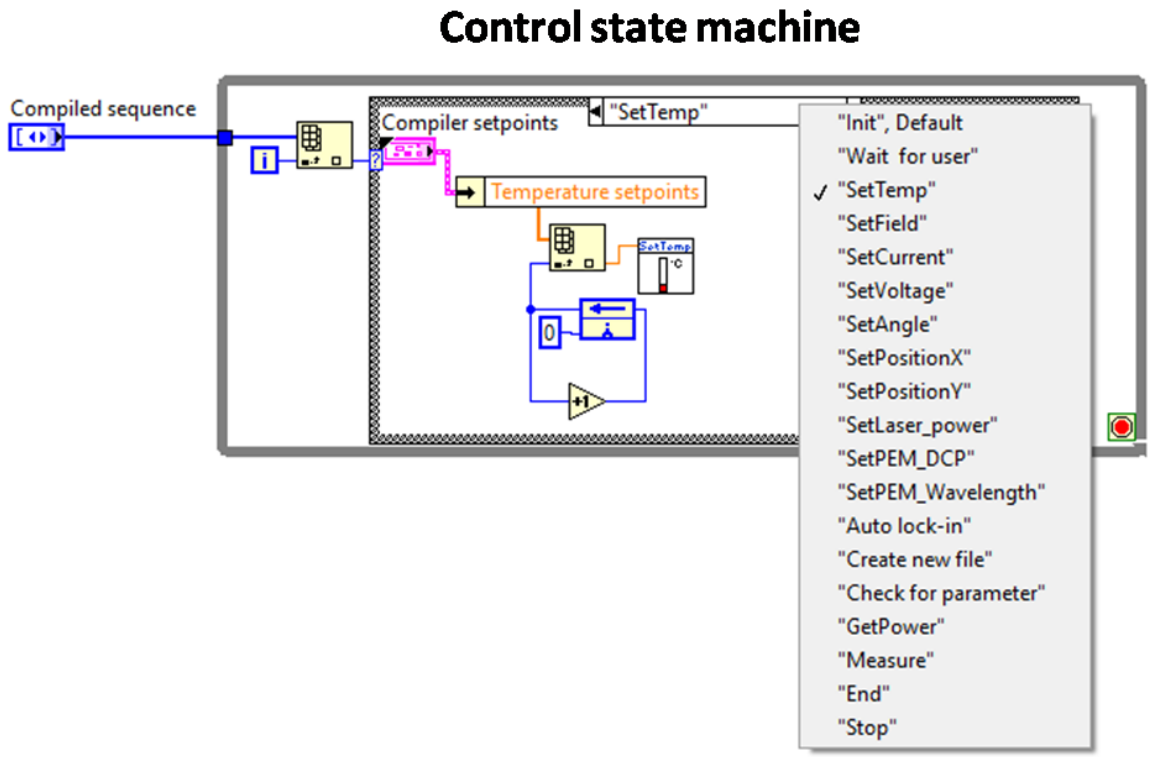

Figure C.2 – Labview diagram of the state machine, it consists of a *while* loop and a *condition* structure wired to the state enumeration. Each condition corresponds to the control of one DOF. Here, the example of the temperature control state is given.

The program is based on two main core functions: the state machine and the sequence builder. The state machine (Fig. C.2) contains all the controls of the different DOFs using an independent VI that can be considered as a black box here. This function only takes a setpoint as an input and some specific settings (sweep rate, stabilization time ...). When the state is called, the setpoint is fed to the cryostat and the program waits for a stabilization critera that is worked out by a DOF-dependent algorithm. We can take the example of the temperature control, a setpoint (15 K for instance) is fed to the control function, the cryostat controler (ITC Mercury) takes the setpoint and adjust the heater power to regulate the temperature. Meanwhile, the stabilization algorithm compares the measured temperature to the numerical setpoint (simplified picture). When the temperature is

estimated as stable, the function ends and the state machine moves to the next state.

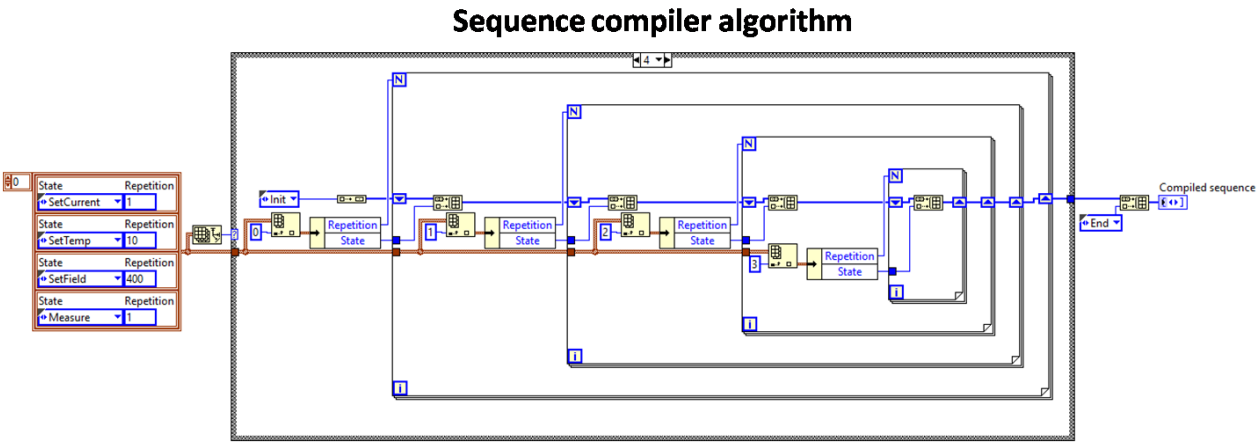

Figure C.3 – Labview diagram of the sequence builder algorithm, the nested *For* loop repeats the *build array* function, adding the n^{th} state corresponding to the n^{th} level of the nested loop.

The navigation between the different states is controlled by the sequence builder, this algorithm lies at the heart of the program. All the available states are encoded in a enumeration control. The sequence is an array of the states enumeration and is set by the user in the front panel. A sequence is composed of one or more DOFs to set and always finishes by the *Measure* state.

Considering N DOFs, the sequence builder consists of $N+1$ nested *For* loops. For each level, the n^{th} element of the sequence array is indexed and concatenated to the *compiled sequence*. Each n^{th} *For* loop runs R times, this number is given by the amount of setpoints calculated from the settings cluster of each DOF, that the user fills in the front panel.

Let's now consider the example given in Fig. C.3. Here the sequence is: SetCurr, SetTemp, SetField, Measure. The corresponding number of setpoints is determined from the individual DOF settings cluster shown in Fig. C.4. The sequence builder gives us the following compiled sequence: Init, SetCurr, [SetTemp [SetField, Measure]$_{400}$]$_{10}$, End. When the user presses the start button, this compiled sequence is fed to the state machine: it first starts by initializing all the instruments and controller, then it sets the current to the desired value, then it sets the temperature and waits for the stability criteria to be fulfilled. Then it performs a sequential field sweep: it sets the magnetic field value and records the different measurement instrument outputs (here the two nanovoltmeters giving the longitudinal and transverse resistance of the sample). This type of sequence is typically used to perform Hall effect measurements at various temperatures.

This architecture allows to edit and perform any type of measurements without having to update the code. One can perform Hall effect measurements, then do temperature and gate dependencies of the resistance or magnetic field angular dependencies. This versatility allows for enhanced phase-space exploration using a single protocol.

Fig. C.4 shows the front panel of MSB. The sequence control is on the top left corner. The corresponding settings cluster automatically appears when a DOF is chosen. In a simplified picture, the

user has to set the control mode for each DOF: one point, linear sweep or a setpoint array. The program compiles in real time the setpoints array (R) for each DOF and feeds it to the sequence builder.

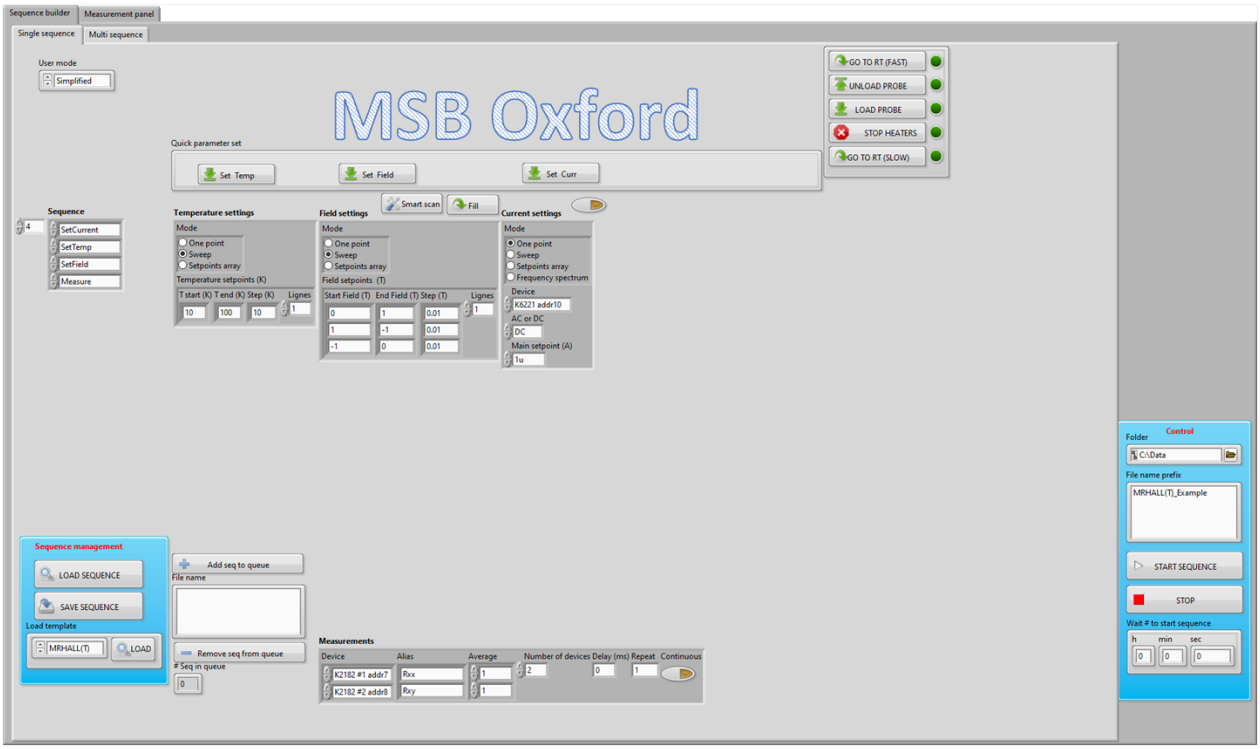

Figure C.4 – Measurement Sequence Builder settings front panel.

The instrumentation is selected by the user on the *Measurements* settings on the bottom. Each time the state machine goes into the *Measure* state, data points from these instruments are acquired. Additional settings allow to take several data points and perform averaging. One very practical feature that I implemented in the program is the ability to save and load sequences. A headline is systematically generated at the start of every data file, this headline can then be read by MSB, loading all the measurement settings. Also, as some measurements can be rather long, I added the possibility to queue up several sequences. For example, one can measure the resistance temperature dependence by slowly cooling down the cryostat, which can last several hours, and queue up a Hall effect measurement. When the first sequence is done, the program will load the second sequence: set the current applied in the sample, stabilize the desired temperature and perform field sweeps. When the user presses the *Start* button, the sequence is compiled and the state machine performs the measurement. The program automatically switches to the real time data display front panel (Fig. C.5). Here, four modular display clusters allow to plot the data in real time. One can plot a regular XY graph but also two-dimensional XYZ maps. An algorithm computes an estimation of the remaining measurement time (top blue panel) and indications on the state of the program are also given in top right blue panel.

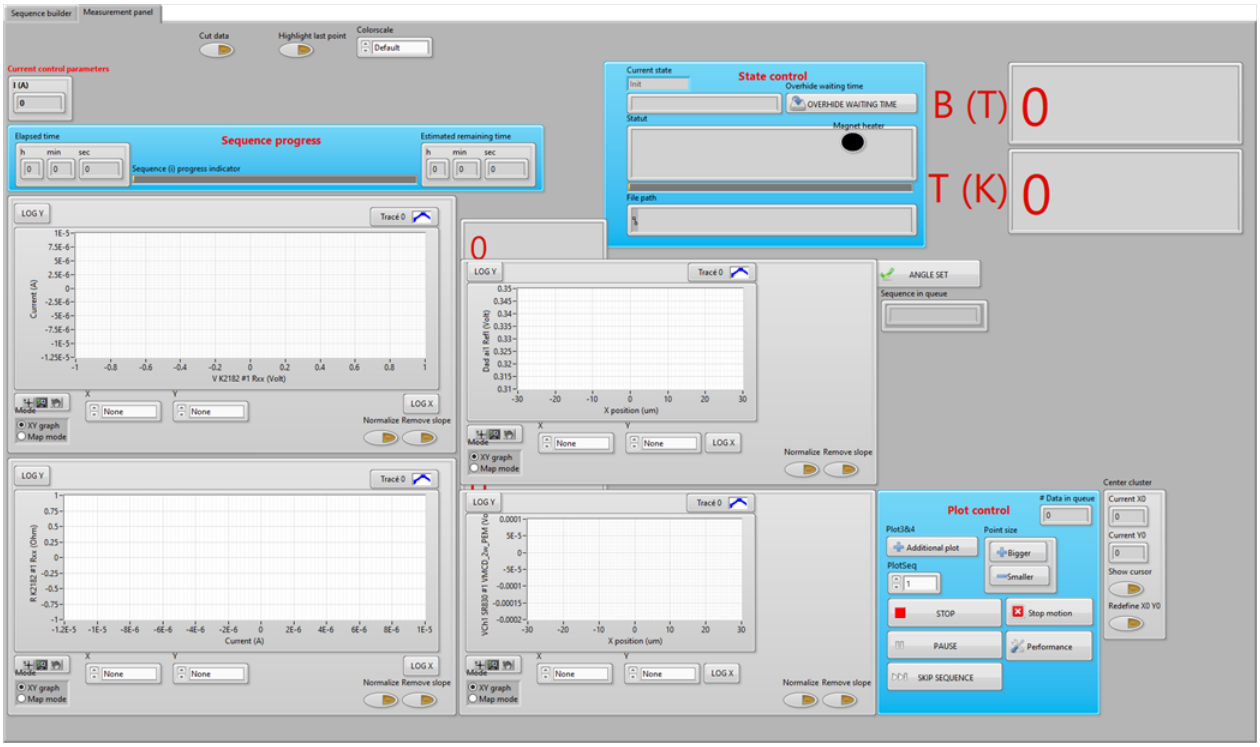

Figure C.5 – Measurement Sequence Builder real time data display front panel.

Fig. C.6 shows a schematic representation of the main LabView diagram.

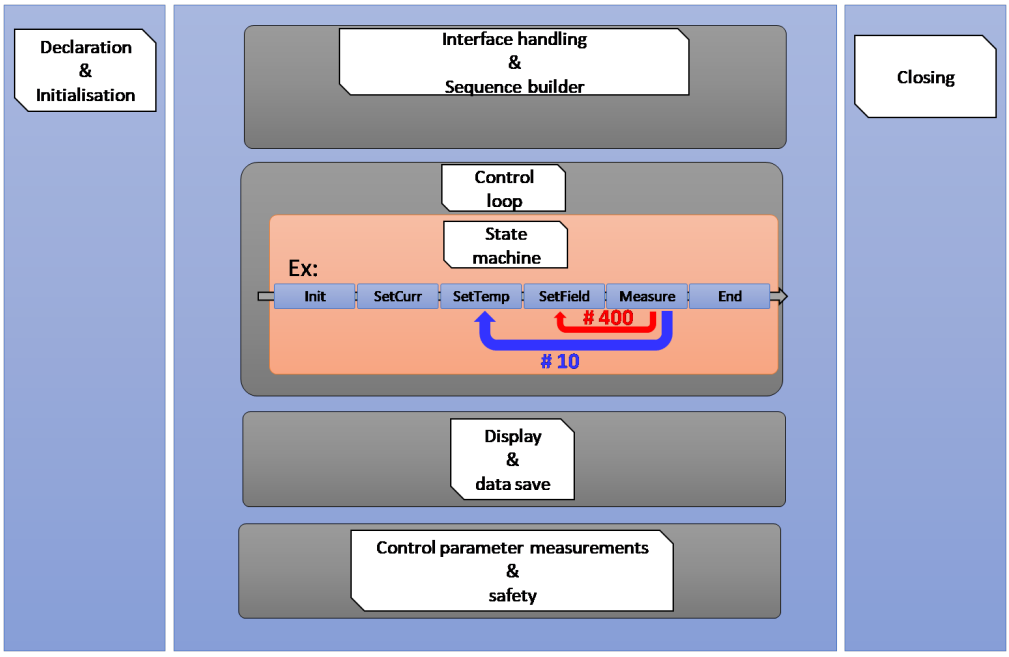

Figure C.6 – Scheme of the main program diagram architecture.

The blue panels represent the three successive blocks of a *sequence* structure, the first is used to declare most variables and gather clusters of their *reference*, which are used to manipulate the variables properties (values, size of the arrays, visibility...). The main frame is composed of four

parallel *while* loops. The first one is always active, it handles the interface: it automatically shows and hides the relevant front panel controls depending on the sequence configuration chosen by the user. It also contains the sequence builder algorithm. The second one hosts the state machine: it controls all the degrees of freedom and performs the measurements. Each time the *Measure* state is called, the data points are passed to the third loop: Display and Data Saving using a queue implementation. The latter first saves the acquired data into a file on the hard-disk drive and transmits it to the display function. The fourth loop constantly measures the critical cryostat parameters (magnetic field and temperature) to ensure the safety of the setup. The last panel takes care of properly closing all the communications with the different control and measurement instruments.

This short appendix aimed at introducing the MSB program through its core functions and architecture. More details can be found in the program documentation I wrote.

To conclude, the MSB software versatility and modularity allowed me and several other reseachers in the lab to perform automated measurements with rigorous control of the DOFs during the nights and weekends, not only saving time and efforts but also allowing to explore more physics through extensive phase-space exploration.

Abstract

One of the main goals of spintronics is to achieve the spin transistor operation and for this purpose, one has to successfully implement a platform where spin currents can be easily injected, detected and manipulated at room temperature. In this sense, this thesis work shows that Germanium is a very good candidate thanks to its unique spin and optical properties as well as its compatibility with Silicon-based nanotechnology. Throughout the years, several spin injection and detection schemes were achieved in Ge but the electrical manipulation of the spin orientation is still a missing part. Recently we focused on two approaches in order to tune the spin-orbit interaction (SOI) in a Ge-based platform. Both rely on the structural inversion asymmetry and the spin-orbit coupling at surfaces and interfaces with germanium (111). First, we performed the epitaxial growth of the topological insulator (TI) Bi_2Se_3 on Ge (111). After characterizing the structural and electrical properties of the Bi_2Se_3/Ge heterostructure, we developed an original method to probe the spin-to-charge conversion at the interface between Bi_2Se_3 and Ge by taking advantage of the Ge optical properties. The results showed that the hybridization between the Ge and TI surface states could pave the way for implementing an efficient spin manipulation architecture. The latter approach is to exploit the intrinsic SOI of Ge (111). By investigating the electrical properties of a thin Ge (111) film epitaxially grown on Si (111), we found a large unidirectional Rashba magnetoresistance, which we ascribe to the interplay between the externally applied magnetic field and the current-induced pseudo-magnetic field in the spin-splitted subsurface states of Ge (111). The unusual strength and tunability of this UMR effect open the door towards spin manipulation with electric fields in an all-semiconductor technology platform. In a last step, I integrated perpendicularly magnetized (Co/Pt) multilayers-based magnetic tunnel junctions on the Ge (111) platform. I developed an original electro-optical hybrid technique to detect electrically the magnetic circular dichroism in (Co/Pt) and perform magnetic imaging. These MTJs were then used to perform spin injection and detection in a lateral spin valve device. The perpendicular magnetic anisotropy (PMA) allowed to generate spin currents with the spin oriented perpendicular to the sample plane. Finally, I assembled all these building blocks that were studied during my PhD work to build a prototypical spin transistor. The spin accumulation was generated either optically or electrically, using optical spin orientation in germanium or the injection from the magnetic tunnel junction.

Résumé

L'un des principaux objectifs de la spintronique est de réaliser le transistor à spin et pour y parvenir, il faut mettre en œuvre avec succès une plateforme où les courants de spin peuvent être facilement injectés, détectés et manipulés à température ambiante. Dans cette optique, ce travail de thèse montre que le germanium est un très bon candidat grâce à ses propriétés optiques et de spin ainsi qu'à sa compatibilité avec les nanotechnologies à base de silicium. Au fil des années, plusieurs schémas d'injection et de détection de spin ont été réalisés dans Ge, mais la manipulation électrique de l'orientation du spin est toujours une pièce manquante. Dans cette thèse, nous nous sommes concentrés sur deux approches afin de manipuler l'interaction spin-orbite (SOI) dans le germanium. Les deux s'appuient sur l'absence de symétrie d'inversion structurale et le couplage spin-orbite aux surfaces et aux interfaces avec le germanium (111). Tout d'abord, nous avons effectué la croissance épitaxiale de l'isolant topologique Bi_2Se_3 sur Ge (111). Après avoir caractérisé les propriétés structurales et électriques de l'hétérostructure Bi_2Se_3/ Ge, nous avons développé une méthode originale pour sonder la conversion courant de spin-courant de charge à l'interface entre Bi_2Se_3 et Ge en tirant profit des propriétés optiques du Ge. Les résultats ont montré que l'hybridation entre les états de surface de Bi_2Se_3 et du Ge pourrait permettre la manipulation électrique de l'orientation du spin dans un transistor. La seconde approche consiste à exploiter le SOI intrinsèque de Ge (111). J'ai étudié les propriétés électriques d'un film mince de Ge (111) et découvert que le passage du courant dans des états de sous-surface où l'interaction Rashba est forte, induit un effet de magnétorésistance très particulier que nous avons appelé la magnétorésistance Rashba unidirectionnelle. Elle est due à l'interaction entre le champ magnétique appliqué extérieur et le pseudo champ magnétique induit par le courant appliquée dans les états polarisés en spin du Ge (111). La forte intensité et modularité de cet effet nous mène à penser que ces états pourraient être également mis à profit dans la réalisation d'un transistor à spin tout semi-conducteur. Parallèlement, j'ai intégré des jonctions tunnel magnétiques à anisotropie perpendiculaire à base de multicouches (Co/Pt) sur la plateforme de Ge (111). J'ai développé une technique hybride électro-optique originale basée sur une détection électrique du dichroïsme magnétique circulaire du (Co/Pt) pour faire de l'imagerie magnétique Ces jonctions tunnel magnétiques ont ensuite été utilisées pour effectuer la génération et la détection de spin dans un dispositif de type vanne de spin latérale. L'anisotropie magnétique perpendiculaire permet de générer un courant de spin avec une orientation de spin perpendiculaire au plan de l'échantillon. Enfin, j'ai rassemblé tous ces éléments développés pendant ma thèse dans un dispositif ultime : un prototype de transistor à spin où une accumulation de spin peut être générée et détectée optiquement et/ou électriquement, en utilisant l'orientation optique de spin dans le germanium ou les jonctions tunnel magnétiques.